Université Gustave Eiffel

PARIS EST SUP — ÉCOLE DOCTORALE Sciences, Ingénierie et Environnement

Modeling, Numerical Simulation and Measurements of Cracking in the Corrosion Process of the Steel/Concrete Interface

Thèse de doctorat de l'Université Gustave Eiffel

École doctorale N° 531: Science, Ingénierie et Environnements (SIE)

Spécialité : **Génie Civil**

Thèse présentée et soutenue à l'Université Gustave Eiffel le 15 Janvier 2026 par

JANA ABOU EID

Composition du jury:

Wanqing SHEN Maitre de Conférence, Université de Lille	Rapporteur
Syed-Yasir ALAM Maître de Conférences, École Centrale de Nantes	Rapporteur
Véronique BOUTEILLER Directrice de Recherche, Université Gustave Eiffel	Directrice de thèse
Julien YVONNET Professeur des Universités, Université Gustave Eiffel	Co-directeur de thèse
Frédéric RAGUENEAU Professeur des Universités, EPF	Examinateur (Président du jury)
Lucas ADELAIDE Chargé de Recherche, Université Gustave Eiffel	Examinateur
Marc QUIERTANT Directeur de Recherches, ESTP	Invité

Université Gustave Eiffel — LABORATOIRE EMGCU EXPÉRIMENTATION ET MODÉLISATION POUR LE GÉNIE CIVIL ET URBAIN

MSME — LABORATOIRE MODÉLISATION ET SIMULATION MULTI ÉCHELLE
Sous la co-tutelle de : CNRS, UNIVERSITÉ GUSTAVE EIFFEL, UPEC • UNIVERSITÉ PARIS-EST CRÉTEIL

Acknowledgements

As this three-year journey comes to an end, I would like to embrace the person it has shaped me into through moments of doubt and discovery, frustration, and fulfillment- and I am deeply grateful to those who stood by me through every twist and turn. First and foremost, I would like to express my deepest gratitude to my thesis directors.

To Prof. Julien YVONNET, my co-director — thank you from the bottom of my heart for your generosity, professionalism, and continuous guidance. You have been not only a mentor, but also a true source of inspiration. Your guidance has been a cornerstone in the realization of this work.

To Lucas ADELAIDE, my supervisor — thank you sincerely for your warmth, availability, and for always being approachable. Your support throughout this journey has been sincerely appreciated.

To Véronique BOUTEILLER, my director — I would like to extend my acknowledgement for your contributions and for the professional perspective, insightful feedback, and high standards of scientific rigor that greatly enriched this work.

I am also grateful to all the members of the EMGCU laboratory, for the stimulating and friendly environment that made my research years rich in learning and exchange. My sincere thanks also go to my colleagues from the MSME laboratory, especially Zakaria and Souhail, for always being there and generously offering their time, advice, and support whenever I needed it. Their willingness to assist and share their knowledge has been deeply appreciated.

To my mom and dad: the two who were there at every A I got since elementary and always pushed me forward towards success, seeing this day long before I did. I remain the little girl who seeks your pride in everything she achieves, and I only stand here because of the faith you put in me. Everything I have achieved is because of you and for you– I love you both endlessly and am forever grateful.

To my brothers, Rabih and Wassim, although life has kept us apart for many years — each of us living in different countries — our bond has never weakened. We grew up separated by distance but united by love. You have always been only a call away, encouraging me, supporting me, and reminding me of home.

And to my sister Aya — you are not only my sister, but my best friend and my biggest cheerleader. You have always seen the best in me, even when I couldn't see it myself. I love you deeply.

My heartfelt thanks also go to my sisters-in-law, Rokaya and Fatima. You are a precious part of our family, and I am deeply grateful for the love and unity you bring into our lives.

I dedicate this thesis to the souls of my beloved grandparents — my two grandmothers and my grandfather — whose prayers have always guided me from above. I wish they were here today to share this moment of pride. I also dedicate it to my grandfather Nehme, who is still with us, and who has lovingly called me "Dr. Jana" long before this dream became real.

To my three friends Shaymaa, Ghida and Reem who have been with me in France since day one. We started together, and we reached this milestone together. Your friendship has been a true blessing.

To my family of friends in and around Champs-sur-Marne: Kassem, Houda, Hussein, Marwa, Karen and Haidar— you are the ones who became my chosen family here. Thank you for turning stress into joy, loneliness into warmth, and foreign streets into home. You made this journey not only bearable, but truly unforgettable.

To my closest friend since school, Kawthar — thank you for being my constant through all these years. Across time and distance, your unwavering presence has always been a gift in my life.

Finally, to Ahmad — who was once my colleague, then my best friend, and is now the love of my life and my future partner. I dedicate this thesis to you. It is ours — you and I. Thank you for all the love. If this work represents chapters of research and study, then you are the eternal chapter of my life — the one that never ends, and the one I will always keep writing with love.

Abstract

This thesis develops a robust computational framework for modeling corrosion-induced cracking in reinforced concrete structures, grounded in the variational phase-field approach to fracture. The primary objective is to simulate the progressive degradation caused by reinforcement corrosion and to bridge the gap between physical damage mechanisms and predictive structural assessment tools.

At the core of the proposed methodology is a phase-field formulation that treats damage as a continuous and thermodynamically consistent process, enabling the simulation of complex crack patterns without explicit crack tracking. Corrosion-induced damage is represented through two complementary approaches: an eigenstrain-based expansion model that simulates the internal pressure generated by rust formation, and a displacement-driven formulation that enforces expansion along the steel–concrete interface. These strategies enable modeling both the early nucleation of cracks and the long-term evolution of crack openings in response to corrosion progression.

A significant contribution of the work lies in integrating image-based modeling of heterogeneous concrete microstructures into the simulation process. Two-dimensional models are constructed from experimental tomography using AI-assisted segmentation tools, allowing the phase-field framework to capture the influence of realistic aggregate shapes and voids on crack propagation. These simulations provide insight into how mesostructural heterogeneity affects the damage process and demonstrate the added value of coupling computational modeling with experimental imaging.

Furthermore, the thesis incorporates experimental data to calibrate and validate a time-dependent corrosion expansion law. By correlating electrochemical parameters with observed crack openings, a generalized model is formulated to predict the evolution of damage as a function of corrosion exposure. This formulation enables the simulation of time-dependent fracture processes in reinforced concrete and supports the connection between experimental testing and numerical prediction.

Overall, this research establishes a unified numerical approach for analyzing corrosion-induced cracking in reinforced concrete, offering a pathway toward predictive durability analysis of RC structures under aggressive environments, laying the groundwork for future extensions involving multiphysics coupling, uncertainty quantification, inverse approaches and three-dimensional simulations.

Résumé

Cette thèse développe un cadre numérique robuste pour la modélisation de la fissuration induite par la corrosion dans les structures en béton armé, basé sur l'approche variationnelle par champ de phase pour la fissuration. L'objectif principal est de simuler la dégradation progressive provoquée par la corrosion des armatures et de faire le lien entre les mécanismes physiques de détérioration et les outils prédictifs d'évaluation structurelle.

Au cœur de cette méthodologie se trouve une formulation par champ de phase qui traite l'endommagement comme un processus continu et thermodynamiquement cohérent, permettant la simulation de fissures complexes sans suivi explicite. La corrosion est représentée à travers deux approches complémentaires : un modèle d'expansion basé sur une déformation propre (eigenstrain), simulant la pression interne générée par la formation de rouille, et une formulation par déplacement imposé au niveau de l'interface acier-béton. Ces stratégies permettent de modéliser à la fois la nucléation des fissures et l'évolution de leur ouverture au cours du temps.

Une contribution majeure de ce travail réside dans l'intégration de microstructures hétérogènes de béton, issues d'images expérimentales, dans le processus de simulation. Des modèles bidimensionnels sont construits à partir de tomographies expérimentales, segmentées à l'aide d'outils d'intelligence artificielle, permettant au champ de phase de capturer l'influence des agrégats et vides réels sur la propagation des fissures. Ces simulations offrent une meilleure compréhension du rôle de l'hétérogénéité sur les mécanismes de fissuration et illustrent l'intérêt du couplage entre modélisation numérique et imagerie expérimentale.

Par ailleurs, la thèse propose un modèle d'expansion dépendant du temps, calibré à partir de données expérimentales. En corrélant les paramètres électrochimiques à l'ouverture des fissures observées, un modèle généralisé est formulé pour prédire l'évolution de la fissuration en fonction de l'exposition à la corrosion. Cette formulation permet de simuler les processus de fissuration évolutifs dans le béton armé et de renforcer le lien entre essais expérimentaux et simulations numériques.

En résumé, cette recherche établit une approche numérique unifiée pour analyser la fissuration induite par la corrosion dans le béton armé, ouvrant la voie à une analyse prédictive de la durabilité des structures soumises à des environnements agressifs, et posant les bases d'extensions futures en couplage multiphysique, quantification d'incertitudes, identification inverse et simulations tridimensionnelles.

Contents

Acknowledgements **1**

Abstract **3**

Résumé **4**

1 General Introduction **15**

2 State of the Art on Corrosion-Induced Cracking in Reinforced Concrete **18**

2.1 Introduction 18

2.2 Economic and Societal Impact of Corrosion: Motivation for Predictive Modelling 19

2.3 Corrosion Mechanisms in Reinforced Concrete 20

2.3.1 Carbonation-Induced Corrosion 20

2.3.2 Chloride-Induced Corrosion 21

2.3.3 Uniform and Non-Uniform Expansion of Corrosion Products . . 23

2.4 Stages of the Corrosion Process 25

2.5 Models for Corrosion-Induced Cracking 26

2.5.1 Experimental test methods to induce cracking due to corrosion . 27

2.5.2 Empirical Models 29

2.5.3 Numerical Models 33

2.6 Phase Field Method 47

2.6.1 Regularized representation of free discontinuities 47

2.6.2 Phase Field Formulation: Regularized variational framework . . 50

2.6.3 Formulation for unilateral contact 51

2.6.4 Finite Element Discretization 55

2.7 Conclusion 58

3 Phase-Field Modeling of Corrosion-Induced Cracking: numerical investigations **60**

3.1 Introduction 60

3.2 Implementation of the phase field method in classical fracture tests . . . 60

3.3 Corrosion-induced fracture model 64

3.3.1 Formulation and numerical implementation 64

3.3.2 Comparison of strain split models to account for crack closure . 67

3.3.3 Numerical investigations: mesh sensitivity analysis 69

3.3.4 Non-Uniform Expansion model for corrosion products 71
3.3.5 Geometrical parameter sensitivity analysis 74
3.4 Conclusion 78

4 Modelling of corrosion-induced cracking in experimental-image based heterogeneous concrete models 80
4.1 Introduction 80
4.2 Crack simulations on segmented images of 2D concrete microstructures obtained from micro CT-scans 80
4.2.1 Traction tests 81
4.2.2 Corrosion-induced fracture in image-based models 88
4.3 Corrosion cracking in optical-based image models with AI-based segmentation tools 90
4.3.1 Dragonfly ORS Imaging Software 92
4.3.2 K-means Clustering for Phase Classification 93
4.3.3 Mesh Construction 94
4.3.4 Corrosion-Induced Cracking Simulations 97
4.4 Conclusion 105

5 Modeling of the corrosion kinetics: Time-dependent corrosion-induced expansion 106
5.1 Introduction 106
5.2 Approach description of the modelling of the corrosion kinetics 106
5.2.1 Radial Displacement: A non-linear exponential model 108
5.2.2 Crack Opening Finding Methodology 109
5.3 Necessary experimental data for the modeling 110
5.3.1 Corrosion product thickness 110
5.3.2 Data Processing Methodology 115
5.3.3 Comparison Across Current Densities 116
5.3.4 Selection of Experimental Slices for Numerical Modeling and Validation 117
5.3.5 Experimental evaluation of horizontal crack widths 123
5.4 Application of the approach: Test case 128
5.4.1 Numerical Analysis of a Selected Microstructure 128
5.4.2 Qualitative Comparison of Simulated and Experimental Crack Patterns 129
5.4.3 Quantitative Comparison and Parametric Sensitivity 131
5.5 Results for the three current densities 138

5.5.1 Current Density: 200 µA/cm² 139
5.5.2 Current Density: 100 µA/cm² 140
5.5.3 Current Density: 50 µA/cm² 149
5.6 Generalized Model 152
5.6.1 Introduction and motivation 152
5.6.2 Physical interpretation and calibration of model parameters . . . 153
5.6.3 Relationship between effective expansion and total charge 154
5.6.4 Generalized modelling framework 154
5.6.5 Formulation of a physically-based generalized exponential law . 155
5.6.6 Parameter identification and model validation 156
5.7 Conclusion 159

6 General Conclusions and Perspectives 161

List of Figures

1 Corrosion-induced cracking originating from rebars embedded in concrete. Reproduced from [1] 15

2 Schematic sketch of steel corrosion sequence in concrete (reproduced from [31]). 23

3 Photographs showing uniform and localized corrosion of reinforcement bars (reproduced from [32]). 23

4 Schematic representation of the initiation and propagation phases of corrosion in reinforced concrete (adapted from Tuutti [5]). 26

5 Idealization of cover concrete as a thick-walled cylinder [75]. (a) Initial unrestrained RC specimen, (b) deformation of concrete, (c) deformation of corrosion products, and (d) rust deposited within open cracks. 31

6 Concrete elements in RBSM with rigid body degrees of freedom and interaction springs [84]. 35

7 Computational flow of steel corrosion model [110]. 38

8 (a) Cohesive elements inserted in mortar, aggregates, and interfaces, (b) Cracking due to corrosion in reinforced concrete [115] 39

9 Enriched nodes in XFEM method for tracking crack 41

10 Comparison between element-based enrichment in EFEM (left) and nodal enrichment in XFEM (right) [127]. 42

11 Strain convolution non-local model principle with the typical bell-shaped function [142]. 45

12 Regularized representation of a crack: 1D case: (a) sharp crack model, taking unitary value of $d(x)$ at $x = x_\Gamma = L/2$ (crack); (b) regularized representation through phase field (adapted from [150]). 50

13 Regularized representation of a crack: 2D case: (a) sharp crack model; (b) regularized representation through phase field (adapted from [150]). 50

14 Illustration of phase-field fracture simulation in concrete microstructure. Adapted from [153]. 58

15 Locally refined meshes near the notch for both tests. 61

16 Schematic representation of applied boundary conditions. 61

17 Tensile crack evolution at different loading steps (steps 4, 170, 180, and final). 62

18 Shear crack evolution at different loading steps (steps 4, 180, 250, and final). 62
19 Force–displacement responses under Amor formulation for tension and shear tests. 62
20 Final damage pattern in tension using Miehe's formulation. 63
21 Pure tension loading: damage pattern of the phase field simulation in a) Ref. [146], b) Ref. [156], c) present work 63
22 Force-displacement response: (left) present work, (right) reference [156] showing their force-displacement curve with Miehe's [146] curve. 64
23 Structural problem with reinforcement and expansive corrosive layer. . . 65
24 Global mesh of the reinforced concrete domain showing concrete (blue), steel (red), and corrosion layer (green) 67
25 Damage patterns from corrosion-induced expansion using Amor and Miehe formulations 68
26 Finite element mesh with centered steel rebar ($r_s = 0.1$ mm) and corrosion layer ($t_c = 0.015$ mm). Case shown: mesh size $e = \ell/2$. 69
27 Convergence study: maximum damage $d_{\max}$ versus corrosion eigenstrain parameter h, for five mesh sizes. 70
28 Effect of mesh refinement on damage evolution using Miehe's formulation with fixed $\ell = 0.02$ mm. 70
29 One-sided corrosion expansion: localized damage on the left side of the rebar 72
30 Elliptical expansion profile representing corrosion product accumulation 72
31 Damage evolution under elliptical corrosion expansion 73
32 Mesh displacement under uniform and non-uniform expansion 73
33 Damage comparison between uniform and localized expansion 74
34 Experimental crack orientations from Loukil's thesis (Slice: P11-d100-35j-T11-D). Horizontal (H), vertical (V), and oblique (O) cracks emerge from the corner reinforcement. 75
35 Simulated damage field with corner rebar positioning. Cracks appear in horizontal, vertical, and oblique orientations. 76
36 Damage pattern for corner rebar, cover = 20 mm. 77
37 Damage pattern for side rebar, cover = 20 mm. 77
38 Effect of concrete cover thickness on damage development. 78
39 2D tomography-image-based concrete models extracted from a full 3D model. 82

40 Boundary conditions: vertical traction applied at the top boundary, fully fixed at the bottom boundary (both U_x and U_y). 83
41 Damage patterns in the 2D image-based models of concrete under tension, corresponding to the geometries shown in Fig. 39. 84
42 Force-displacement curves for the 9 samples under traction. 85
43 Models defined by increasing size in the original image. 86
44 Damage patterns in traction for the cropped subdomains of slice 100 . . 87
45 Damage patterns in traction for the full slice 100 87
46 Force-displacement curves for all cropped and full domains of slice 100 . 88
47 Tomography-based heterogeneous sample meshes with embedded corroded rebar. 89
48 Damage patterns due to corrosion-induced expansion in nine heterogeneous concrete slices. 91
49 Original experimental slice: P11-d100-35j-T11-D [Concrete section with color disturbances and visual noise] 93
50 Comparison of image-based data extraction before and after pre-processing. 94
51 Experimental slice P11-d100-35j-T11-D (a), segmented image after pre-processing and classification of material phases (b), and the corresponding constructed triangular mesh (c) used for numerical simulation 96
52 Damage pattern due to traction loading – Slice P11-d100-35j-T11-D . . . 97
53 Validation of corrosion-induced cracking in slice P11-d100-35j-T11-D. Top row: experimental image and corresponding mesh. Bottom row: damage patterns from simulation for increasing expansion values. 98
54 Experimental slice and corresponding numerical mesh for P11-d100-35j-T12-D 100
55 Damage field evolution under corrosion expansion for slice P11-d100-35j-T12-D at different h_{max} values. 100
56 Experimental photo of P27-d50-70j-T15-D 101
57 Segmented mesh for P27-d50-70j-T15-D 101
58 Damage at $h_{\max} = 0.5$ 101
59 Damage at $h_{\max} = 1$ 101
60 Damage at $h_{\max} = 1.5$ 101
61 Division of the steel–concrete interface into eight corrosion dials (C1–C8), where each dial represents a zone between two adjacent points on the steel perimeter. This segmentation enables selective application of expansion in semi-uniform modeling [37]. 103
62 Slice: P11-d100-35j-T11-D (experimental crack pattern) 104

63 Expansion Creating Cracking (whole rust contour); $h_{max} = 1$ 105
64 Expansion Creating Cracking (C1C2); $h_{max} = 1$ 105

65 Radial Displacement Scheme 108
66 Exponential growth model used to describe corrosion layer thickness over time 108
67 a) External cracking (Faces T and F), b) Reinforced prism cutting plan (100x12.5x10, dimensions in cm), c) Slice location, d) Slices T10, T13 and T16 (12.5x10), e) Samples E10, E13 and E16 (4x4), f) Dial delimitation methodology from C1 to C8 (reproduced from Loukil's thesis [37], Fig. II-18.) 114
68 Evolution of average corrosion product thickness over time for three current densities (50, 100, and 200$\mu A/cm^2$) 115
69 Corrosion Product Thickness vs. Time for Equal Total Charge (Q = 700 $\mu Ad/cm^2$) 117
70 Experimental slices for prism P23 (a) P23-d50-14d-T12-D and (b) P23-d50-14d-T13-D 118
71 Experimental slices for prism P25 (a) P25-d50-28d-T16-D and (b) P25-d50-28d-T13-D 119
72 Experimental slices for prism P27 (a) P27-d50-70d-T9-D and (b) P27-d50-70d-T13-D 119
73 Experimental slices for prism P31 (a) P31-d100-7d-T11-D and (b) P31-d100-7d-T16-D 120
74 Experimental slices for prism P05 (a) P05-d100-14d-T14-D and (b) P05-d100-14d-T10-D 120
75 Experimental slices for prism P08 (a) P08-d100-21d-T12-D and (b) P08-d100-21d-T17-D 121
76 Experimental slices for prism P09 (a) P09-d100-28d-T10-D and (b) P09-d100-28d-T15-D 121
77 Experimental slices for prism P11 (a) P11-d100-35d-T14-D and (b) P11-35d-T11-D 122
78 Experimental slices for prism P14 (a) P14-d200-3.5d-T11-D and (b) P14-d200-3.5d-T10-D 122
79 Experimental slices for prism P16 (a) P16-d200-7d-T14-D and (b) P16-d200-7d-T16-D 123
80 Experimental slices for prism P17 (a) P17-d200-17.5d-T16-D and (b) P17-d200-17.5d-T13-D 123

81 Location (in T and/or F) and maximum opening of the external crack for the current densities: (a) 50 µA/cm², (b) 100 µA/cm², (c) 200 µA/cm². . . . 125
82 Average horizontal crack openings over time for the current densities: (a) 50 µA/cm², (b) 100 µA/cm², (c) 200 µA/cm². 126
83 Experimental slice P14-d200-3.5j-T11-D (a) and its corresponding mesh (b) 129
84 (a) Experimental Cracks, (b) Numerical Damage Pattern 130
85 Crack opening over time for different values of β (with fixed $A = 0.233$ mm and $B = 0.2$), ℓ = 2*element size and before extension of curve duration range. The red curve represents the experimental results curve for $200\mu A/cm^2$. 134
86 Crack opening evolution over time for various values of β with increased regularization length ($\ell = 3\times$ element size) and extension of curve duration. The red curve represents the experimental results curve for $200\mu A/cm^2$. 135
87 Crack opening over time for smaller g_c value 137
88 Close correlation between the simulated curve (β = 11.6) and the experimental reference 138
89 Comparison of experimental, meshed, and numerical damage pattern for two different slices P16–T14–D (a, b, c) and P17–T16–D (d, e, f) after 7 and 17.5 days of corrosion respectively under 200 $\mu A/cm^2$. 141
90 Combined crack opening curves of all slices with the experimental results curve for the current density equal to 200 $\mu A/cm^2$. 142
91 Calibrated expansion A×β vs. total charge for 200 µA/cm². 142
92 Comparison of experimental, meshed, and numerical damage pattern for two different slices P05–T14–D (a, b, c) and P05–T10–D (a', b', c') after 14 days of corrosion under 100 $\mu A/cm^2$. 144
93 Comparison of experimental, meshed, and numerical damage pattern for two different slices P08–T12–D (a, b, c) and P08–T17–D (a', b', c') after 21 days of corrosion under 100 $\mu A/cm^2$. 145
94 Comparison of experimental, meshed, and numerical damage pattern for two different slices P09-T10-D (a, b, c) and P09-T15-D (a', b', c') after 28 days of corrosion under 100 $\mu A/cm^2$. 146
95 Comparison of experimental, meshed, and numerical damage pattern for two different slices P11-T11-D (a, b, c) and P11-T14-D (a', b', c') after 35 days of corrosion under 100 $\mu A/cm^2$. 147
96 Combined crack opening curves of all slices with the experimental results curve for the current density equal to 100 µA/cm². 148
97 Calibrated expansion A×β vs. total charge for 100 µA/cm². 148

98 Experimental slice, image-based mesh, and numerical damage pattern for microstructure P23–T13-D after 14 days of corrosion under 50 $\mu A/cm^2$. 150
99 Experimental slice, image-based mesh, and numerical damage pattern for microstructure P25–T16-D after 28 days of corrosion under 50 $\mu A/cm^2$. 150
100 Experimental slice, image-based mesh, and numerical damage pattern for microstructure P27–T9-D after 70 days of corrosion under 50 $\mu A/cm^2$. 150
101 Combined crack opening curves of all slices with the experimental results curve for the current density equal to 50 µA/cm². 151
102 Calibrated expansion A×β vs. total charge for 50 µA/cm². 152
103 Calibrated effective displacement ($A \cdot \beta$) versus total charge Q for the three current densities. 154
104 Verification of the generalized $A\beta(Q)$ model for two new current densities (75 and 150 $\mu A/cm^2$) 158

List of Tables

1 Material parameters used in the simulations 60
2 Material parameters used in the expansion simulations 68
3 Mechanical properties assigned to the three phases in the heterogeneous concrete domain. 83
4 Material properties used in the simulations for each phase in the heterogeneous reinforced concrete domain. 95
5 Maximum and minimum thicknesses (µm) of corrosion products for a current density of $50\mu A/cm^2$ (reproduced from Table IV-1 from Loukil's thesis [37]) 111
6 Maximum and minimum thicknesses (µm) of corrosion products for a current density of $100\mu A/cm^2$ (reproduced from Table IV-2 from Loukil's thesis [37]) 112
7 Maximum and minimum thicknesses (µm) of corrosion products for a current density of $200\mu A/cm^2$ (reproduced from Table IV-3 from Loukil's thesis[37]) 113
8 Corrosion expansion parameters calibrated for the microstructures extracted from experimental specimens exposed to a current density of $200\ \mu A/cm^2$. 140
9 Corrosion expansion parameters calibrated for the microstructures extracted from experimental specimens exposed to a current density of $100\ \mu A/cm^2$. 143
10 Corrosion expansion parameters calibrated for the microstructures extracted from experimental specimens exposed to a current density of $50\ \mu A/cm^2$. 149
11 Computed values of the corrosion expansion parameter $A\beta(i, Q)$ for different current densities i and corrosion charges Q. 158

Chapter 1
General Introduction

Concrete has been a cornerstone of construction for thousands of years. From ancient Roman structures that have withstood millennia to modern skyscrapers and bridges, the evolution of concrete has shaped the built environment in enduring ways. In particular, the advent of reinforced concrete (RC)—the combination of a cementitious matrix with steel reinforcement—revolutionized structural engineering, enabling greater load-bearing capacity, improved flexibility, and wider applications in public infrastructure. Its widespread use stems from its favorable mechanical properties, cost-effectiveness, and adaptability to complex forms and functions.

Yet, despite its ubiquity, the long-term durability of reinforced concrete structures has increasingly come into question. What was once assumed to be an ”eternal” material has shown vulnerabilities over time, particularly in aging infrastructure exposed to aggressive environments. Corrosion of embedded steel reinforcement has emerged as one of the most critical and widespread causes of deterioration (example in Figure 1), resulting in premature damage, costly repairs, and even structural failures in severe cases. The implications of this degradation are not only technical but also economic and societal, affecting the safety, serviceability, and sustainability of vital infrastructure.

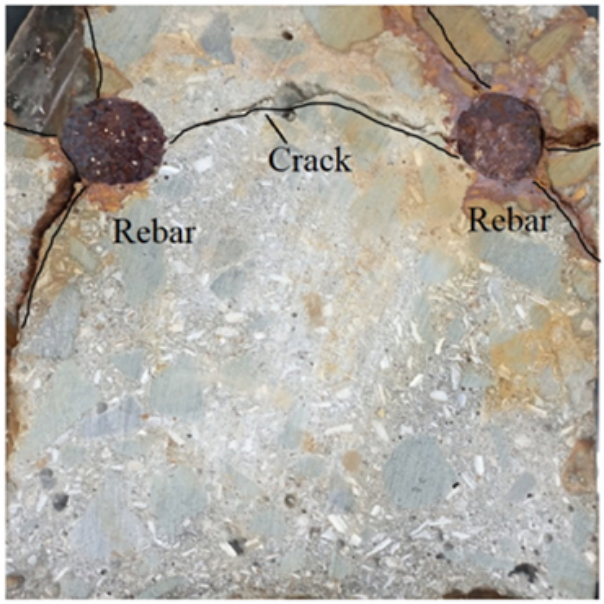

Figure 1: Corrosion-induced cracking originating from rebars embedded in concrete. Reproduced from [1]

Recent national evaluations in France have cast a stark light on this issue. In 2019, the French Senate estimated that more than 25,000 bridges across the country were in poor structural condition, representing approximately 10–12% of the total road bridge stock [2]. Just three years later, in 2022, this number had risen to between 30,000 and 35,000 bridges—an increase of over 30% [3]. The deterioration is particularly severe among locally managed infrastructures, with 23% of communal and inter-communal bridges and 10% of departmental bridges now deemed structurally deficient. These trends underscore not only the natural aging of materials but also systemic shortcomings in inspection, diagnosis, and maintenance strategies.

From a financial perspective, the situation is equally alarming. While the annual maintenance budget for state-managed bridges was tripled between 2018 and 2022—from an average of €45 million to €120 million—the accumulated maintenance backlog remains significant. Estimates suggest that restoring the deficient local bridges alone would require investments exceeding €2 billion. Furthermore, many municipalities lack the technical expertise or resources to assess the condition of their bridges, let alone to implement appropriate repair measures. The gap between structural degradation and the capacity to respond is widening.

These developments have prompted policymakers, engineers, and researchers alike to call for a paradigm shift in how infrastructure is monitored, maintained, and managed. Central to this shift is the urgent need for predictive tools capable of anticipating deterioration before it becomes visible or irreversible. Diagnostic models, numerical simulations, and digital frameworks can play a transformative role in moving from reactive to preventive maintenance strategies—an approach that is not only more cost-effective but also essential for ensuring public safety and extending service life.

It is within this context that the present thesis is situated. The objective of this research is to contribute to the development of an advanced modeling tool for predicting damage in reinforced concrete structures, with a particular focus on corrosion-induced cracking. At the core of this work lies the implementation and application of the phase-field method, a robust numerical framework for simulating fracture processes. Rather than treating damage as a static or isolated phenomenon, the proposed phase-field model enables a continuous and time-dependent representation of crack initiation and propagation resulting from corrosion-induced expansion. This model is specifically designed to bridge the gap between physical deterioration mechanisms and engineering-scale assessment tools, providing a unified and flexible approach for analyzing the long-term structural performance of reinforced concrete infrastructure.

This thesis manuscript is structured into six chapters:

Chapter 1 provides the general introduction and contextual background that mo-

tivates the research.

Chapter 2 presents the state of the art on corrosion-induced cracking in reinforced concrete, covering corrosion mechanisms and existing modeling approaches from empirical to numerical frameworks.

Chapter 3 introduces the phase-field method for modeling corrosion-induced cracking, including validation on standard benchmarks and implementation details.

Chapter 4 applies the developed phase-field model to heterogeneous concrete microstructures obtained from experimental imaging, including AI-based segmentation and tomography data, enabling realistic representation of the material's microstructure.

Chapter 5 incorporates time dependency into the simulation of corrosion-induced expansion, linking corrosion kinetics with crack opening evolution and comparing numerical predictions with experimental data.

Chapter 6 concludes the thesis by summarizing the main findings and contributions and outlining perspectives for future research in this field.

Chapter 2
State of the Art on Corrosion-Induced Cracking in Reinforced Concrete

2.1 Introduction

Reinforced concrete (RC) is the most widely used structural material worldwide, forming the backbone of modern and historical infrastructure. Its success lies in the composite action between two fundamentally different materials: concrete, which provides compressive strength and environmental protection, and steel reinforcement, which ensures tensile resistance and ductility. The durability and long-term performance of RC depend on the integrity of this composite system — that is, on both the quality of the concrete matrix and the preservation of the embedded steel. As emphasized by Gehlen, Andrade, Bartholemew, and Papworth [4], deterioration mechanisms in RC structures can be broadly divided into those affecting the durability of the concrete and those affecting the reinforcement. The interaction between these two domains largely governs the service life and maintenance needs of RC structures.

However, the long-term durability of RC remains a major engineering concern. Environmental exposure, combined with progressive physicochemical degradation of both concrete and steel, gradually compromises structural performance over time. While structural design ensures that elements meet prescribed mechanical requirements, durability design is more complex because it must account for evolving environmental conditions and time-dependent deterioration processes. Predicting how these processes develop, interact, and lead to visible distress is therefore a central challenge in extending the service life of reinforced concrete infrastructure.

Reinforced concrete is subjected to multiple degradation mechanisms that act at different scales and can be grouped into *mechanical*, *physical*, and *chemical* categories. *Mechanical mechanisms* include fatigue, creep, and cracking under sustained or cyclic loading; *physical mechanisms* comprise freeze–thaw cycles, thermal stresses, and shrinkage-induced cracking; while *chemical mechanisms* arise from interactions with aggressive agents such as carbon dioxide, chlorides, and sulfates, which alter the chemistry and microstructure of the material. Among these, the corrosion of embedded steel reinforcement is universally recognized as the most critical cause of deterioration and the main factor limiting the service life of RC structures.

Considering the vulnerability of reinforced concrete structures to aggressive environments and the progressive nature of their deterioration, understanding the mechanisms of corrosion and predicting its effects are of paramount importance. Corrosion of reinforcement not only reduces the cross-sectional area of the steel but also generates expansive corrosion products that induce cracking and spalling of the concrete cover, thereby accelerating further degradation. Modeling corrosion-induced cracking thus provides a crucial scientific and engineering tool for anticipating damage, optimizing maintenance strategies, and enhancing the service life of existing and future reinforced concrete structures.

This chapter first highlights the global economic and societal impact of corrosion, establishing the motivation for durability modelling. It then discusses the fundamental corrosion mechanisms in reinforced concrete—namely carbonation and chloride ingress—and describes the stages of corrosion evolution as described by Tuutti [5]. After, the chapter reviews the wide range of models developed over recent decades to simulate corrosion-induced cracking, including empirical formulations, diffusion- and expansion-based approaches, and numerical methods ranging from classical to advanced computational frameworks. Finally, the chapter culminates in the presentation of the phase-field method (PFM) as a promising and unifying framework for corrosion-induced cracking modeling.

2.2 Economic and Societal Impact of Corrosion: Motivation for Predictive Modelling

Corrosion is not only a technical degradation process but also a major economic and societal challenge that affects virtually every industrial sector. From transportation and energy infrastructure to cultural heritage and manufacturing, metallic and reinforced concrete structures are continuously exposed to environmental agents that cause deterioration over time [6].

The global cost associated with corrosion is exceptionally high. Estimates by international organizations, including the U.S. National Institute of Standards and Technology and the NACE International IMPACT report, indicate that corrosion-related expenses amount to approximately **3–4% of the gross national product (GNP)** of industrialized countries and nearly **USD 2.5 trillion annually**, corresponding to **3.4% of the global GDP** [7]. These figures include both direct costs—such as repairs, replacements, and protection systems—and indirect costs related to production loss, environmental damage, and safety risks. Notably, it is estimated that applying established corrosion prevention and monitoring techniques could reduce these losses by **15–35%**, represent-

ing potential global savings of up to **USD 875 billion per year** [6].

Beyond the economic burden, corrosion has far-reaching societal and environmental implications. It accelerates material consumption, increases energy demand for repair and reconstruction, and can compromise public safety through structural failures. Preventive corrosion management, on the other hand, contributes to sustainability by extending the service life of infrastructure, conserving resources, and reducing greenhouse gas emissions associated with new material production.

In this context, **predictive modelling of corrosion-induced cracking** in reinforced concrete emerges as an essential engineering tool. By simulating the initiation and propagation of cracks resulting from reinforcement corrosion, numerical models allow for more accurate predictions of service life, maintenance scheduling, and performance deterioration. Such models support the shift from reactive maintenance to *proactive durability design*, optimizing life-cycle costs while enhancing the safety and reliability of civil infrastructure.

2.3 Corrosion Mechanisms in Reinforced Concrete

Reinforcing steel embedded in concrete is typically protected by a thin, adherent film composed of iron oxyhydroxides, known as the passive layer. This film forms naturally in the highly alkaline pore solution of concrete, where pH values typically range between 12.5 and 13.5 [8, 9]. In this environment, corrosion rates are negligible, and the reinforcement remains electrochemically stable. However, certain environmental or chemical processes can disrupt this equilibrium, resulting in depassivation and the onset of corrosion. The two primary mechanisms responsible for this are carbonation and chloride ingress.

2.3.1 Carbonation-Induced Corrosion

Carbonation is the process through which carbon dioxide CO_2 from the atmosphere diffuses into the porous structure of concrete and reacts with calcium hydroxide ($Ca(OH)_2$), one of the principal hydration products of Portland cement. The governing chemical reaction can be represented as:

$$Ca(OH)_2 + CO_2 \longrightarrow CaCO_3 + H_2O. \tag{2.1}$$

This transformation reduces the alkalinity of the pore solution by consuming hydroxide ions and producing calcium carbonate. As a result, the pH gradually drops from

approximately 13 to below 9, a level at which the passive layer on steel becomes unstable and dissolves. When the carbonation front reaches the depth of the reinforcing bar, depassivation occurs, and uniform corrosion initiates in the presence of oxygen and moisture.

The carbonation rate is influenced by the concrete's microstructure, its moisture state, and the environmental exposure. In very dry conditions, the reaction slows because insufficient pore water is available for ionic transport; in saturated concrete, the ingress of CO_2 is limited by the low diffusivity of gas through water-filled pores. Consequently, carbonation progresses most rapidly at intermediate relative humidities of 50–70%. Papadakis et al. [10] formulated a mathematical model expressing the carbonation depth as $x_c = k_c \sqrt{t}$, where k_c depends on the diffusivity of carbon dioxide and the concrete's microstructural parameters. Subsequent experimental work by Kropp and Hilsdorf [11] confirmed that cracking and surface degradation significantly accelerate carbonation by increasing the effective diffusion paths. Recent numerical developments coupling diffusion, chemical reaction, and fracture—such as those using the phase-field method—further emphasize the strong interaction between cracking and carbonation front propagation [12, 13, 14, 15].

2.3.2 Chloride-Induced Corrosion

Chloride-induced corrosion represents the most aggressive and structurally significant degradation mechanism in reinforced concrete. Unlike carbonation, this process can occur even when the concrete remains highly alkaline. Chlorides—originating from de-icing salts, seawater exposure, or contaminated aggregates—penetrate the concrete through diffusion, absorption, or capillary suction. Once sufficient chloride ions accumulate at the steel surface, they locally break down the passive film, initiating localized electrochemical activity known as pitting corrosion.

The transport of chloride ions within the concrete is generally described by Fick's second law of diffusion:

$$\frac{\partial C}{\partial t} = D_{eff} \nabla^2 C, \tag{2.2}$$

where C is the chloride concentration and D_{eff} is the effective diffusion coefficient, dependent on temperature, humidity, and the microstructural properties of the concrete. The pioneering work of Collepardi [16] and Tuutti [5] introduced the concept of chloride ingress as a time-dependent initiation process leading to corrosion, while Andrade and Page [17] validated chloride concentration profiles experimentally for cracked and uncracked concrete. Modern approaches, such as those by Bastidas-Arteaga [18], have incorporated probabilistic and stochastic parameters to account for variability in diffu-

sion coefficients, binding capacities, and chloride thresholds.

The concentration of chloride ions necessary to destroy the passive film—known as the *critical chloride threshold* (CTL)—varies widely in the literature. The concept of a critical chloride threshold (CCT) was first introduced by Hausmann [19], who proposed that corrosion initiates when the chloride concentration at the steel surface exceeds a critical ratio relative to hydroxide ions, typically around $[Cl^-]/[OH^-] \approx 0.6$. Glass and Buenfeld [20] defined it as the total chloride content by mass of cement. Alonso et al. [21] determined a CTL of approximately 0.4%, whereas Melchers and Li [22] reported a range of 0–2.5%, reflecting differences in exposure severity. The large scatter of CTL data, summarized in the review by Angst et al. [23], illustrates the complexity of quantifying chloride-induced depassivation. Factors such as cement type, steel surface condition, and environmental humidity strongly affect CTL [24, 25]. Moreover, investigations have shown that chloride accumulation near anodic sites may exceed bulk concentrations due to ionic migration effects, complicating measurement and interpretation [26, 27].

Once depassivation occurs, corrosion is activated as an electrochemical process consisting of anodic iron dissolution and cathodic oxygen reduction [28, 29]:

$$\mathrm{Fe} \rightarrow \mathrm{Fe}^{2+} + 2e^-, \tag{2.3}$$

$$\mathrm{H_2O} + \tfrac{1}{2}\mathrm{O_2} + 2e^- \rightarrow 2\mathrm{OH}^-. \tag{2.4}$$

The overall sequence of corrosion reactions and ion transport phenomena is illustrated schematically in Figure 2.

In uniform corrosion, both anodic and cathodic reactions are distributed evenly over the rebar surface. In localized corrosion, however, anodic dissolution occurs within pits, while cathodic reduction takes place on adjacent passive regions. As the pit environment becomes deoxygenated, hydrolysis of ferrous ions lowers the pH, and ion migration maintains charge balance: positively charged ions (Fe^{2+}, H^+) move outward, while aggressive anions (Cl^-, $SO_4{}^{2-}$, OH^-) migrate inward [27, 30]. This establishes a macrocell current that sustains pit growth and promotes a self-propagating (auto-catalytic) corrosion mechanism.

A visual distinction between uniform and localized corrosion can be seen in Figure 3, which presents representative photographs of reinforcement bars subjected to both mechanisms. In practical terms, uniform corrosion caused by carbonation tends to produce widespread but shallow material loss. Conversely, chloride-induced pitting corrosion is more insidious, causing deep and localized penetration with significant cross-section loss before visible cracking appears. This makes chloride-induced corro-

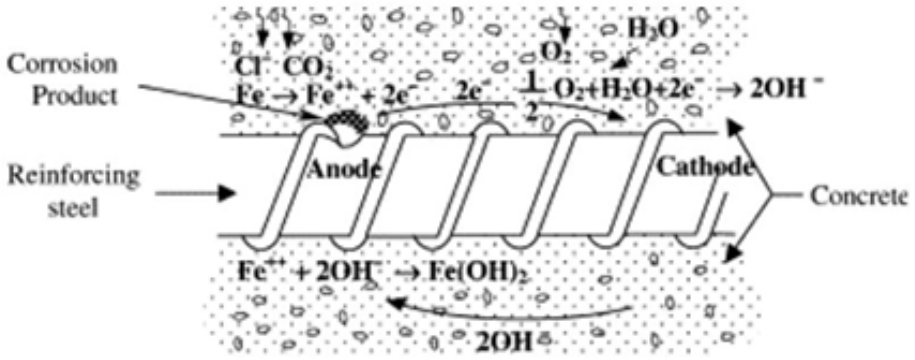

Figure 2: Schematic sketch of steel corrosion sequence in concrete (reproduced from [31]).

sion particularly dangerous for structural safety and the primary focus of this research.

2.3.3 Uniform and Non-Uniform Expansion of Corrosion Products

Corrosion of steel reinforcement in concrete generates expansive iron oxides and hydroxides, which exert radial pressure on the surrounding matrix. The spatial distribution of these corrosion products, whether uniform or non-uniform, governs the stress development and cracking morphology of the concrete cover. The distinction between uniform and localized expansion is essential to understand the initiation and propagation of corrosion-induced damage.

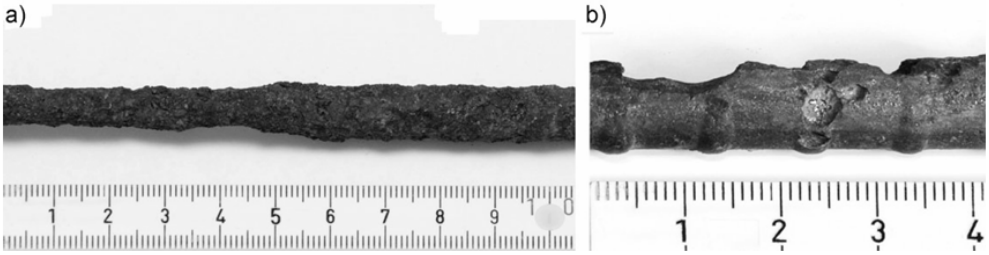

Figure 3: Photographs showing uniform and localized corrosion of reinforcement bars (reproduced from [32]).

2.3.3.1 Uniform Expansion of Corrosion Products

Uniform or generalized corrosion leads to an even distribution of corrosion products around the steel surface. As described by Pedeferri [6] and standardized in ASTM references [33], such expansion typically occurs under stable environmental exposure and results in a homogeneous radial pressure acting on the concrete cover. The induced

tensile stresses are axisymmetric, leading to a single dominant circumferential crack that propagates perpendicularly toward the surface once the cover tensile strength is exceeded. This mechanism produces a relatively predictable cracking pattern, with the rate of propagation depending on the corrosion rate and concrete tensile capacity.

Finite element simulations by Zhao et al. [34] confirmed that under uniform corrosion, the concrete cover experiences symmetric crack propagation and nearly simultaneous surface cracking across the rebar perimeter. The rust expansion pressure is evenly distributed, leading to uniform tensile stress and early formation of a continuous crack front. However, because of the homogeneous nature of this stress field, once the cover crack forms, further propagation is rapid and can cause spalling. Uniform corrosion, therefore, is often used in simplified analytical and numerical models due to its symmetric stress field and direct relation between rust layer thickness and crack initiation.

2.3.3.2 Non-Uniform Expansion of Corrosion Products

In contrast, localized or non-uniform corrosion results in uneven accumulation of rust products over the rebar perimeter, typically on the side closer to the chloride ingress path [6]. This non-uniform rust growth produces asymmetric pressure distribution on the concrete, resulting in highly localized stress concentrations. According to ASTM guidelines [33], this leads to pitting-type expansion and irregular cracking patterns often oriented toward the zone of highest corrosion intensity. Experimental and modeling evidence by Zhao et al. [35] demonstrated that such non-uniform expansion generates inclined and branched cracks that propagate obliquely toward the surface. The Gaussian characterization of the corrosion front used in their finite element model revealed that even small asymmetries in corrosion depth substantially increase localized damage and accelerate concrete delamination.

Recent investigations by Vu et al. [36] using a phase-field modeling framework further emphasized the significance of the corrosion pattern on the fracture behavior of reinforced concrete. The study compared uniform and non-uniform corrosion-induced cracking in various rebar configurations, showing that uniform expansion tends to produce direct, singular cracks leading rapidly to cover failure, whereas non-uniform expansion causes complex, multi-branch cracking and delayed but more extensive degradation of the cover layer. These simulations also revealed that the rust expansion displacement required to reach full cracking is larger in non-uniform cases due to localized strain redistribution.

As the core modeling approach of the present thesis also relies on the phase-field method, the findings of Vu et al. [36] are particularly relevant. While the experimental data considered herein are derived from the thesis of Olfa Loukil considering in their

work a chloride-induced corrosion (non-uniform expansion) [37, 38, 39], the numerical simulations in this work assume uniform expansion for simplification. Nevertheless, future extensions may incorporate non-uniform rust expansion to improve realism and capture the anisotropic stress fields that arise under localized corrosion conditions.

2.4 Stages of the Corrosion Process

To effectively model corrosion-induced cracking in reinforced concrete, it is essential to first understand the sequence of physical and chemical processes that govern corrosion development. The deterioration of steel reinforcement does not occur instantaneously but rather evolves progressively through distinct stages. Each stage—beginning with the initiation of corrosion and followed by its propagation—introduces specific mechanisms that influence the durability and structural performance of reinforced concrete. Among the various conceptual frameworks proposed, the two-stage corrosion model introduced by Tuutti [5] remains the most widely accepted and serves as the foundation for many subsequent durability models. Figure 4 schematically illustrates the time-dependent evolution of corrosion damage.

During the initiation phase, aggressive species such as CO_2 or chloride ions diffuse through the pore network of the concrete until they reach the steel surface in concentrations sufficient to destroy the passive layer. This phase is largely governed by transport phenomena—diffusion, absorption, and permeability—and can last for several years or decades, depending on exposure conditions and material quality [40, 41].

The propagation phase begins once the passive film is broken and active corrosion commences. Corrosion products (iron oxides and hydroxides) form and accumulate at the steel–concrete interface, creating internal pressures that can exceed the tensile strength of the surrounding concrete. These pressures induce microcracking, which can evolve into visible longitudinal cracks, delamination, and ultimately spalling of the cover concrete. Studies focusing on this phase have investigated the chemical composition and expansion properties of rust, which directly influence the rate of cracking and structural degradation [42, 43, 44].

As the corrosion advances, the cross-sectional area of the steel is reduced, decreasing its load-carrying capacity, while cracking weakens the bond between steel and concrete. This dual degradation mechanism affects both the serviceability and the ultimate limit states of RC elements [45, 46, 47]. Understanding these effects is vital for evaluating residual strength and structural safety.

While research on the initiation phase provides valuable insights into preventive measures and durability enhancement [24, 25, 48], studies on the propagation phase

offer a deeper understanding of structural behavior under progressive corrosion [49, 50]. The present thesis focuses primarily on the propagation phase, where corrosion-induced expansion and cracking are modeled within a phase-field framework.

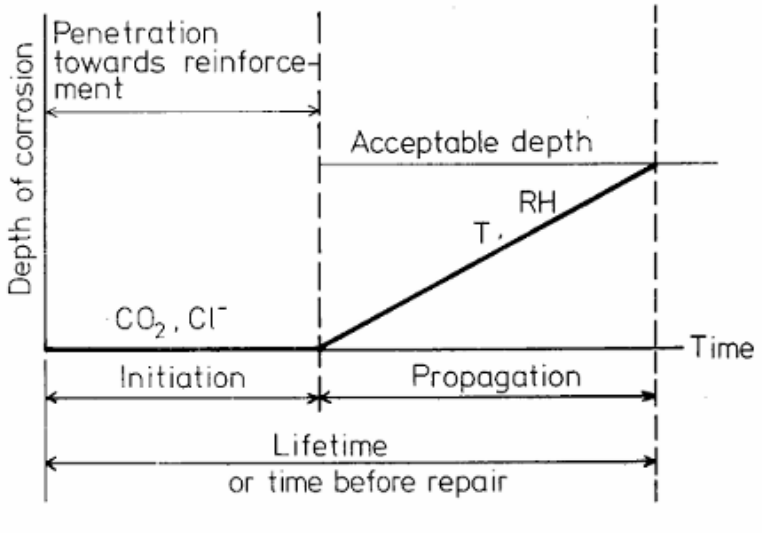

Figure 4: Schematic representation of the initiation and propagation phases of corrosion in reinforced concrete (adapted from Tuutti [5]).

2.5 Models for Corrosion-Induced Cracking

Corrosion-induced cracking in reinforced concrete has long been a central topic in durability research, owing to its significant implications for the safety, serviceability, and maintenance of concrete infrastructure. Over the past five decades, extensive experimental and theoretical efforts have been dedicated to understanding and predicting this complex phenomenon. As corrosion remains one of the principal causes of deterioration in reinforced concrete, modeling its induced cracking is essential for both fundamental insight and practical assessment of structural performance.

A wide range of models has been proposed in the literature to describe the initiation, evolution, and mechanical consequences of corrosion-induced damage. These models vary in their complexity, underlying assumptions, and physical representation of the corrosion process, reflecting the progressive refinement of scientific understanding and computational capabilities. Broadly, they can be classified into two main families:

1. **Empirical models**, which are based on experimental observations and statistical correlations, providing simplified relationships between corrosion parameters and crack formation;

2. **Numerical models,** corrosion kinetics, and the expansive behavior of rust products to simulate stress development and cracking, which use computational methods to simulate fracture and damage phenomena in a coupled mechanical and physical framework.

This section reviews each family of models in chronological order, highlighting their conceptual development, the main contributors, and how successive studies have addressed the limitations of earlier approaches. The objective is to establish a coherent understanding of the state of the art and to identify the key gaps that motivate the adoption of advanced modeling strategies such as the phase-field method.

2.5.1 Experimental test methods to induce cracking due to corrosion

Empirical models for corrosion-induced cracking are primarily grounded in experimental investigations, which provide the quantitative data necessary to relate corrosion rate, crack width, and steel mass loss. Over the years, numerous studies have explored corrosion mechanisms through laboratory and field testing under varying environmental conditions and exposure regimes. These experiments can be broadly categorized into two major groups: (i) natural corrosion experiments and (ii) artificial corrosion experiments, the latter encompassing accelerated corrosion testing as the most widely used approach.

2.5.1.1 Natural Corrosion Experiments

Natural corrosion experiments aim to capture the corrosion process under real environmental conditions without external acceleration. They are typically carried out on structural components extracted directly from existing reinforced concrete structures [51] or through long-term on-site monitoring of exposed elements [52, 53]. These experiments provide highly realistic insights into the corrosion mechanisms by reflecting true variations in temperature, humidity, and chloride ingress. However, the primary drawback of such studies is their duration, as it can take several years or even decades before measurable levels of corrosion damage appear.

To partially overcome this limitation, laboratory-based setups have been developed to simulate marine or atmospheric exposure conditions while maintaining natural corrosion kinetics. These configurations often employ salt chambers or wetting–drying cycles to mimic environmental variations [54, 55, 56]. Such experiments retain the realism of natural corrosion but still require extended testing periods to achieve advanced degradation states.

2.5.1.2 Artificial Corrosion Experiments

Artificial corrosion tests, in contrast, are designed to replicate the corrosion process under controlled environmental conditions within shorter timeframes. They allow precise adjustment of critical parameters such as temperature, humidity, chloride concentration, and exposure duration [57]. These experiments bridge the gap between realism and practicality, enabling systematic study of how specific variables affect corrosion initiation and propagation.

Within this group, the most common and efficient technique is the *accelerated corrosion experiment*, which induces corrosion by applying an external electrical current to the reinforcement, as discussed below.

Accelerated corrosion experiments by imposing a current

Accelerated corrosion experiments are among the most widely used laboratory methods for studying the mechanical and durability consequences of reinforcement corrosion. In these tests, a direct current (DC) is applied to the reinforcing bar (serving as the anode) while an external cathode—typically made of stainless steel or copper—is immersed in an electrolyte solution, usually a sodium chloride (NaCl) solution [58, 59, 60, 61, 62]. This setup accelerates the oxidation of steel, thereby producing measurable corrosion damage within days or weeks instead of years.

For example, Elgarf [60] reported achieving approximately 10% steel mass loss within 96 hours using a current density of 4 mA/cm^2. Despite their practicality, accelerated corrosion tests must be interpreted with caution, as they tend to generate more uniform corrosion patterns rather than the localized pitting commonly found in real structures.

Moreover, the applied current densities in laboratory conditions often exceed those measured in natural exposure environments. Field observations indicate corrosion current densities between 0.1 and 100 μA/cm^2 [63, 64, 65, 66], whereas accelerated laboratory tests typically employ 59–200 μA/cm^2 [67]. In certain cases, much higher values—up to 4 mA/cm^2 [58, 59, 60] or even 6.6 mA/cm^2 [62]—have been used to speed up corrosion kinetics. However, excessive current densities can lead to unrealistic rust formation and cracking behavior.

El-Maaddawy et al. [68] compared the resulting crack widths and side strains of specimens subjected to current densities ranging from 100 to 500 μA/cm^2, concluding that notable increases in expansion and cracking occur above 200 μA/cm^2 due to the accumulation of rust at the steel–concrete interface. Below this threshold, part of the corrosion products diffuses into concrete pores, reducing pressure buildup. Malumbela et al. [69] and Feng et al. [70] further demonstrated that the geometry and placement of

the cathode, as well as concrete type, salt concentration, and current intensity, strongly affect the corrosion and cracking patterns.

Experimental setups vary considerably across studies. The NaCl concentration typically ranges between 3% and 5%, while cathodes may be made of copper or stainless steel and arranged either in contact with or separated from the specimen surface. Some setups include sustained flexural loading to simulate in-service conditions, which facilitates chloride ingress through existing cracks. Others introduce salt directly into the concrete mix to trigger depassivation and initiate corrosion. These variations underscore that while accelerated corrosion provides efficiency and control, it must be carefully calibrated to ensure realistic damage evolution.

2.5.2 Empirical Models

Empirical models have played a central role in the early development of corrosion-induced cracking theories, serving as the first quantitative tools to relate experimental observations to predictive design expressions. Derived from controlled laboratory and field data, these models established the fundamental relationships between corrosion penetration, corrosion rate, cover thickness, and time-to-cracking. While they were later superseded by mechanistic and numerical formulations, empirical approaches remain crucial for calibrating and validating more advanced models, particularly in practical service-life prediction frameworks.

2.5.2.1 Early Empirical Corrosion–Cracking Relationships (1990s–2000s)

The pioneering empirical models aimed to establish a link between corrosion rate (i_{corr}), concrete cover thickness (c), bar diameter (d), and the time required for surface crack initiation (t_{cr}). Liu and Weyers [71] were among the first to present a physically based empirical formulation combining electrochemical kinetics with experimental data. They divided the corrosion process into three stages—corrosion initiation, accumulation of corrosion products in the porous zone, and mechanical cracking.

They derived a time-to-cracking equation based on the accumulation of corrosion products, expressed as:

$$W_{\text{rust}}^2 = 2 \int_0^t k_p \, dt \tag{2.5}$$

Assuming constant corrosion rate, this becomes:

$$t_{cr} = \frac{W_{\text{crit}}^2}{2k_p} \tag{2.6}$$

where W_{crit} is the critical amount of rust products required to initiate cracking, and k_p is the rate of rust production [71].

They also expressed the time-to-cracking using Faraday's law, linking it to corrosion current density and penetration depth:

$$t_{cr} = \frac{zF\rho_{Fe}(x_{cr} - x_0)}{M_{Fe}i_{corr}} \tag{2.7}$$

where z is the number of electrons exchanged per iron atom, F is Faraday's constant, ρ_{Fe} and M_{Fe} are the density and molar mass of iron, and x_{cr}, x_0 are the critical and initial corrosion penetration depths, respectively.

Pantazopoulou and Papoulia [72] introduced a semi-empirical analytical model that accounted for both radial and tangential stress development in the concrete cover. Their work emphasized the nonlinear relationship between rust volume expansion and concrete stress response, suggesting that the pressure at the steel–concrete interface evolves nonlinearly with corrosion penetration. Williamson and Clark [73] complemented this by experimentally quantifying the pressure required to cause cracking and by linking it to rust expansion ratios and tensile strength of the cover concrete.

2.5.2.2 Development of the Thick-Walled Cylinder Analogy (2005–2011)

The most significant step forward in empirical modeling came with the introduction of the *thick-walled cylinder analogy*, which idealizes the concrete cover as an elastic cylindrical shell subjected to internal pressure induced by rust expansion. This concept allowed closed-form derivations for cracking pressure, radial displacement, and stress evolution, forming the basis for almost all subsequent corrosion-cracking models.

Bhargava et al. [74] refined the analogy by dividing the corrosion process into three distinct phases: unrestrained rust accumulation, stress build-up within the cover, and crack propagation. Their model incorporated the porosity of the rust layer and the nonuniform pressure transfer between steel and concrete, significantly improving the accuracy of time-to-cracking predictions.

They expressed the critical amount of rust required to cause cracking as:

$$W_{\text{crit}} = \rho_r(x_{cr} - x_0) \tag{2.8}$$

and the critical corrosion penetration depth x_{cr} using mechanics-based parameters:

$$x_{cr} = \frac{t_c\,(1 + \nu_c)}{E_c} \cdot \frac{\sigma_t}{k_p} \tag{2.9}$$

where t_c is the concrete cover thickness, ν_c and E_c are the Poisson's ratio and elastic

modulus of concrete, σ_t is the tensile strength of concrete, and k_p is the rust expansion coefficient [74].

Lu et al. [75] extended the model by coupling the thick-walled cylinder theory with experimental observations of crack propagation. They also introduced a conceptual model describing the mechanical interaction between corrosion products, steel loss, and concrete deformation in the form of a thick-walled cylinder, as illustrated in Figure 5.

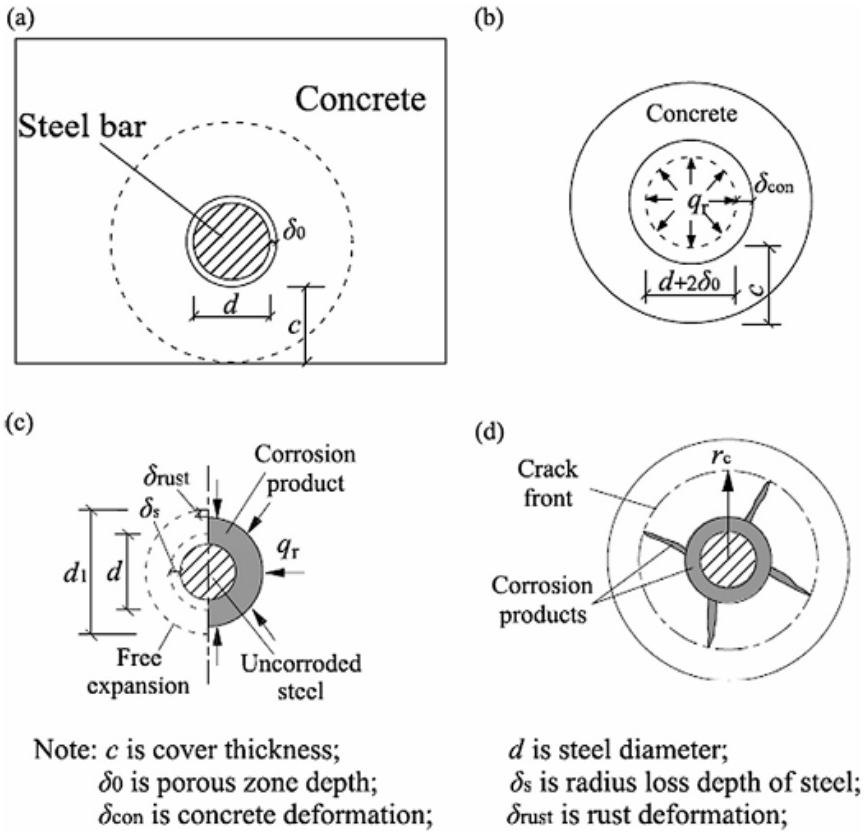

Figure 5: Idealization of cover concrete as a thick-walled cylinder [75]. (a) Initial unrestrained RC specimen, (b) deformation of concrete, (c) deformation of corrosion products, and (d) rust deposited within open cracks.

To model deformation compatibility, they proposed:

$$\delta_{\text{rust}} = \beta\, \delta_s + \delta_{\text{con}} \tag{2.10}$$

$$p = \frac{E_c}{(1+\nu_c)(1-2\nu_c)} \cdot \left(\frac{\delta_{\text{rust}}}{c - \frac{d}{2}} \right) \tag{2.11}$$

where δ_{rust}, δ_s, and δ_{con} are the deformations of rust, steel, and concrete, respectively; β is the rust expansion ratio; p is the internal pressure acting on the concrete cover; c

and d are the concrete cover and rebar diameter, respectively.

2.5.2.3 Empirical Validation and Refinements (Post-2010)

Mullard and Stewart [76] provided extensive experimental validation for existing corrosion–cracking models, deriving updated empirical equations for both crack width and mass loss evolution. They emphasized that environmental exposure, bar geometry, and confinement conditions significantly influence the rate of cover deterioration. Zhao and Jin [77] introduced a mechanical–empirical relationship to estimate the critical corrosion amount at first cracking.

Zhao, Xu, and Jin [35] also proposed a pressure-based cracking criterion using hoop stress theory:

$$\sigma_\theta = \frac{p \cdot r_i^2}{r_o^2 - r_i^2} \left(1 + \frac{r_o^2}{r^2}\right) \tag{2.12}$$

where r_i and r_o are the inner and outer radii of the concrete cylinder, r is the radial location, and p is the internal pressure from rust expansion.

Zhang, Castel, and François [78] further examined the influence of corrosion pattern—uniform versus localized—on empirical crack width evolution, demonstrating that nonuniform corrosion produces wider, asymmetric cracks for the same level of steel mass loss.

A major contribution to the validation of the thick-walled cylinder model was made by Roshn et al. [79], who compared the analytical predictions from multiple empirical formulations against experimental data. Their work confirmed that most existing cylinder-based models tend to slightly overpredict cracking time when uniform corrosion is assumed. They also proposed a modification factor to account for the transition from uniform to pitting corrosion, bridging empirical and probabilistic reliability models.

Recent developments continue to refine empirical relationships for specialized materials. Liu et al. [80] developed an empirical model for lightweight aggregate concrete, highlighting the role of internal pore structure in mitigating rust-induced stress buildup. Their findings suggest that the reduced stiffness and higher porosity of lightweight aggregates delay crack initiation despite faster chloride diffusion.

2.5.2.4 Critical Discussion and Limitations

Despite their historical and practical significance, empirical models remain constrained by simplifying assumptions. Most treat rust expansion as a uniform internal pressure and neglect the spatial variability of corrosion, load-induced microcracking, or multi-

axial stress effects. Zhao, Xu, and Jin [35] comprehensively reviewed these models, concluding that empirical formulations provide accurate predictions only under controlled conditions and cannot capture localized phenomena such as pitting or nonuniform expansion. Consequently, these limitations have driven the development of numerical and chemo-mechanical approaches, which can simulate crack initiation, propagation, and interaction with environmental processes.

2.5.3 Numerical Models

Numerical modeling has long served as a foundational framework for simulating damage and fracture in materials, with methods evolving from early mechanical formulations to sophisticated multi-scale approaches. These models were originally developed to capture generalized damage mechanisms in quasi-brittle and brittle solids, including crack initiation, propagation, and material degradation under diverse loading and environmental conditions. Over time, various numerical families—such as discrete models, continuum damage formulations, micromechanical theories, cohesive zone models, and enriched finite element techniques—have been refined to account for complex material responses. While each method was initially proposed within broader contexts of fracture and failure analysis, many have since been adapted or extended to study corrosion-induced cracking in reinforced concrete. In the subsections that follow, each modeling strategy is presented from its theoretical foundation, followed by its specific contributions and applications in the context of corrosion-related deterioration.

2.5.3.1 Discrete Approaches

The Discrete Element Method (DEM), introduced by Cundall and Strack [81], is a numerical approach that models materials as assemblies of rigid particles interacting through contact laws. These laws encompass cohesive and frictional behavior, allowing simulation of both elastic deformation and failure processes, including crack initiation and propagation. When the cohesive bonds between particles break, the system can simulate material degradation realistically. The macroscopic mechanical response of the model emerges from the stiffness and force transmission characteristics between discrete elements.

The behavior of DEM systems is greatly influenced by the size and shape of the discrete particles. Circular or spherical particles are frequently used due to simplicity, but they tend to underestimate the friction angle and shear strength in granular materials, as shown by Rothenburg and Bathurst [82]. Moreover, such geometries lead to unrealistic pore distributions and are less representative of crack surfaces, which typically

involve broader contact zones than point contacts.

To define elastic interactions, a linear spring model is often used, where normal and tangential stiffnesses are represented by springs with stiffness constants k_n and k_t, respectively, as per Cundall et al. [81]. To incorporate energy dissipation, Tavarez et al. [83] proposed an extension that adds a viscous term to the linear-elastic interaction law. The resulting contact forces are decomposed into normal and tangential components, calculated based on the relative motion of particles.

DEM simulations proceed through a three-step loop: contact detection, computation of interaction forces, and time integration. Using Newton's second law, accelerations are determined from the sum of internal and external forces. These accelerations update the positions of particles, forming new contact pairs for the next cycle. Stability requires very small time steps, and simulations continue until a convergence criterion or maximum time is reached.

Discrete cracking approaches treat cracks as explicit geometric discontinuities. In this context, model topologies are updated as cracks propagate, requiring remeshing or the addition of new nodes to simulate opening displacement. Adaptive remeshing enables modeling of dynamic crack growth with high fidelity. The method is especially well-suited for modeling fracture behavior in brittle or quasi-brittle materials, such as concrete. Many DEM-based fracture models use tensile strength thresholds to define bond failure.

The Discrete Element Method (DEM) has been effectively utilized to model corrosion-induced cracking in reinforced concrete by capturing the granular nature and discrete fracture behavior of the cementitious matrix. Jiradilok et al. [84] developed a 3D discrete meso-scale RBSM framework for modeling cover cracking caused by non-uniform corrosion. In this method, the concrete is discretized into randomly shaped polyhedral rigid bodies generated via Voronoi tessellation. Each rigid body possesses six degrees of freedom — three translational and three rotational — and is interconnected with neighboring elements via three springs: one normal and two shear springs. These springs govern the mechanical interaction and failure behavior of the material. The general configuration of these elements is illustrated in Fig. 6.

In this approach, compressive failure is excluded in the normal spring, while tensile and shear failure are explicitly modeled. The shear springs follow an elasto-plastic constitutive law, with the maximum shear stress $\tau_{\max}$ governed by the nonlinear expressions:

$$\tau_{\max} = \pm \left(1.6 f_{\text{telem}}^2 (-\sigma + f_{\text{telem}})^{0.4} + 0.15 f_{\text{telem}}\right), \quad \text{if} \quad \sigma \geq 3 f_{\text{telem}} \tag{2.13}$$

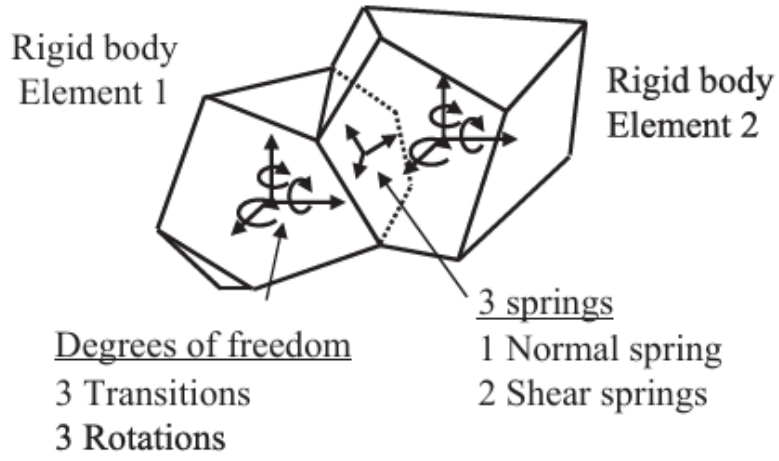

Figure 6: Concrete elements in RBSM with rigid body degrees of freedom and interaction springs [84].

$$\tau_{max} = \pm \left(1.6 f_{telem}^2 (-3 f_{telem} + f_{telem})^{0.4} + 0.15 f_{telem}\right), \quad \text{if} \quad \sigma < 3 f_{telem} \tag{2.14}$$

Similarly, Qiao and Nakamura [85] implemented a three-dimensional Rigid Body Spring Model (RBSM), a discrete modeling approach, to simulate cover spalling induced by localized corrosion expansion. Their model utilized Voronoi-based element generation and spring-based interaction laws to capture crack initiation and propagation, directly linking corrosion kinetics to mechanical deterioration. These studies highlight the strength of discrete methods in representing crack localization, opening widths, and progressive failure under the influence of internal expansive forces from rust growth.

2.5.3.2 Continuum Damage Models (CDM)

Continuum Damage Mechanics (CDM) provides a powerful theoretical framework for simulating fracture and degradation in materials. Initially proposed by Kachanov [86] in 1958, CDM introduces the concept of a scalar continuity variable ψ, also known as the integrity index, defined as the ratio of the differential intact area to the original cross-sectional area. This index quantifies the progressive damage of a material and forms the basis of effective stress formulations used to represent low-stress brittle creep damage.

Kachanov proposed the evolution equation of integrity as:

$$\dot{\psi} = B\left(\frac{\sigma}{\psi}\right)^{v} = B\bar{\sigma}^{v} \tag{1.1}$$

where ψ is the continuity variable, B and v are material constants, σ is the Cauchy stress, and $\bar{\sigma}$ denotes the effective stress acting on the undamaged material portion.

Building on this foundation, Rabotnov et al. [87] introduced the damage variable $D = 1-\psi$ in 1970, and coupled it with stress to develop the well-known Kachanov–Rabotnov constitutive equations:

$$\dot{\varepsilon}_{cr} = A\left(\frac{\sigma}{1-D}\right)^{n} \tag{1.2}$$

$$\dot{D} = B\frac{\sigma^{v}}{(1-D)^{\mu}} \tag{1.3}$$

Here, $\dot{\varepsilon}_{cr}$ is the creep strain rate, A and n are Norton power law parameters, and μ is the tertiary creep-damage exponent.

Kachanov and Rabotnov's foundational work was further developed through the contributions of researchers such as Lemaitre [88], Murakami [89] and Ju [90]. These works expanded CDM from its origins in creep to encompass elastic, plastic, brittle, and fatigue damage, and extended its applicability from metals to rocks, ceramics, composites, and other quasi-brittle or brittle non-metallic materials.

Common CDM models for brittle concrete-like materials include those by Løland [91] and Mazars [92]. These models provide explicit macroscopic damage formulations that are practical for engineering applications and relatively easy to implement. However, they suffer from key limitations: many model parameters lack physical meaning, some formulations are not rigorously derived, and microstructural aspects of damage are often overlooked.

Continuum Damage Mechanics (CDM) has proven to be a robust theoretical framework for simulating the deterioration of concrete due to corrosion-induced cracking. This approach captures the coupling between mechanical degradation and expansive internal stresses caused by rust formation. For instance, Zreid and Brühwiler [93] proposed a CDM-based model to simulate corrosion-induced cracking and cover spalling, validated against experimental data. Pan [94] extended this approach through a multiphysics micromechanical model, accounting for ionic transport and suction effects in unsaturated concrete. Similarly, Zeng et al. [95] incorporated CDM within a poromechanical framework to analyze corrosion-induced crack patterns under sustained loads. Seetharam et al. [96] applied a mesoscale CDM formulation to assess structural degradation in large RC components exposed to chloride ingress. Additionally, Qiao et al.

[97] integrated a Rigid Body Spring Model (RBSM) with a damage mechanics formulation to simulate electrochemical-mechanical coupling in corroded concrete. These contributions demonstrate the capability of CDM to realistically simulate the progressive cracking process induced by reinforcement corrosion, offering predictive tools for service life assessment and durability design.

2.5.3.3 Micro-Mechanical Damage Models

Micromechanical damage models provide a fundamental approach for understanding material deterioration by linking macroscopic behavior to microstructural evolution. These models emerged as an alternative to macroscopic phenomenological approaches, offering more physically meaningful insights. The pioneering work in this area was conducted by Gurson [98], who developed a micromechanical framework to characterize material porosity and its influence on deformation and failure. Such models have since gained popularity due to their capacity to relate local microstructural changes (e.g., microcrack growth, pore evolution) to overall mechanical responses [99].

Micromechanical models utilize various homogenization schemes to bridge the micro-to-macro scale. These include the sparse scheme [100], Mori-Tanaka scheme [101], self-consistent scheme [102, 103], and differential scheme [104, 105]. The resulting models allow for detailed representation of heterogeneous microstructures, enabling more accurate predictions of damage evolution in concrete materials.

A notable advantage of micromechanical approaches is the physical clarity of damage variables. These models can explicitly represent microcrack interactions and their effects on material behavior, making them particularly suitable for quasi-brittle materials such as concrete. Zhu et al. [106] derived a thermodynamic micromechanics formulation accounting for microcrack opening–closure transitions based on Eshelby's inclusion theory. Furthermore, models developed by Zhu and Shao [107, 108] incorporate frictional sliding and unilateral effects in crack behavior, capturing the complex mechanisms of damage accumulation more realistically.

Despite their strengths, micromechanical models still face practical challenges. High model complexity often requires advanced numerical techniques and calibration through microstructural testing. Additionally, the transition from diffuse microcracking to localized macrocracks (damage bands) remains a computational and theoretical challenge [109].

Micromechanical damage models, while traditionally developed for modeling quasi-brittle fracture and ductile failure, have also found significant applications in simulating corrosion-induced damage in reinforced concrete. A notable implementation is the micro-mechanics-based corrosion model developed by Song et al. [110], which com-

bines a chloride penetration model, an electrochemical corrosion cell model, and an oxygen diffusion model to evaluate both the initiation and propagation of corrosion (see Figure 7. This comprehensive framework is then integrated with a cracking model to assess the critical rust product accumulation required to trigger cover concrete cracking. Their model demonstrates time- and space-dependent predictions of corrosion effects in RC structures exposed to chloride environments, effectively bridging micromechanical analysis and durability assessment. Furthermore, Rios [111] extends micromechanical principles to the study of corrosion-fatigue crack growth in steels, which—while not specific to concrete—offers critical insights applicable to reinforcement deterioration. His model integrates microstructural fracture mechanics to account for crack tip plasticity, pit-induced stress concentrations, and environmental effects, providing a multi-scale pathway to simulate the corrosion-driven fatigue process at the crack initiation and propagation levels.

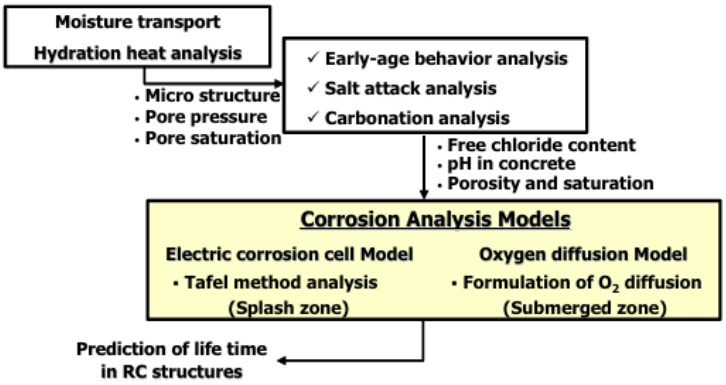

Figure 7: Computational flow of steel corrosion model [110].

2.5.3.4 Cohesive Zone Models

Cohesive Zone Models (CZMs) were initially introduced by Dugdale [112] and Barenblatt [113] in the 1960s to simulate fracture propagation in materials. These models address limitations in Griffith's theory by accounting for crack initiation in the absence of geometric singularities. Later, Hillerborg et al. [114] extended the cohesive zone concept to simulate crack propagation in concrete, introducing the notion of fracture energy G_c as the critical energy release rate controlling crack growth. The principle of the cohesive crack is illustrated in Figure 8 In this formulation, the fracture process occurs in a localized region ahead of the crack tip, known as the *cohesive zone*.

Within this cohesive zone, a fictitious interface is established where displacement jumps can occur while still transmitting cohesive forces. The total energy of the system

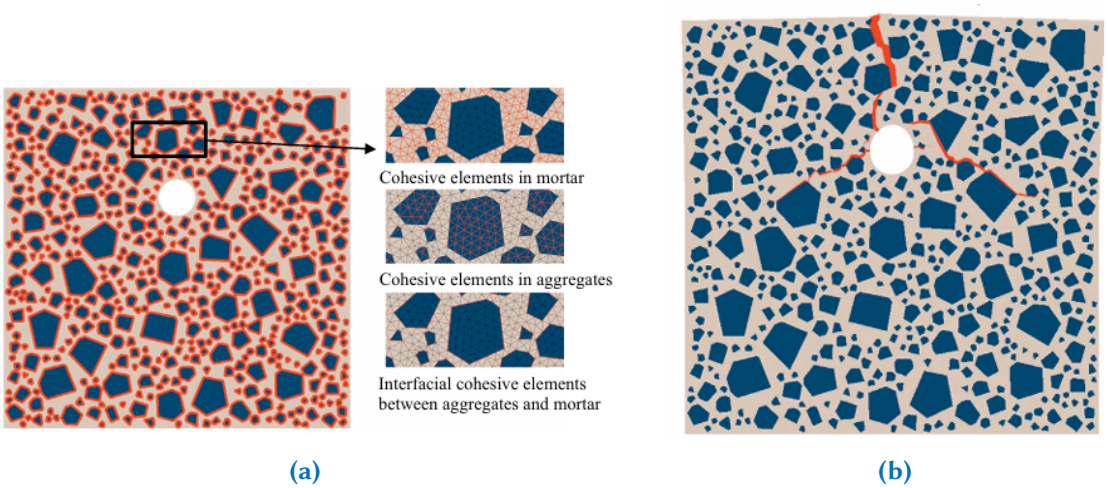

Figure 8: (a) Cohesive elements inserted in mortar, aggregates, and interfaces, (b) Cracking due to corrosion in reinforced concrete [115]

Ω with cohesive interface Γ is expressed as:

$$E = \int_{\Omega} \psi_e(\varepsilon(u))\, d\Omega + \int_{\Gamma} \psi_c(u)\, dS - \int_{\Omega} f^* \cdot u\, d\Omega - \int_{\partial\Omega_F} F^* \cdot u\, dS \tag{2.15}$$

Here, ψ_e represents the elastic strain energy, and $\psi_c(u)$ denotes the surface energy controlling the displacement jump u across the interface. The constitutive behavior of the cohesive zone is described by the traction-separation law, which governs the relation between the cohesive traction vector and displacement separation vector. The traction reaches a maximum $\sigma_{\max}$ at the onset of separation and degrades to zero at the critical opening u_c. Multiple forms of traction-separation laws exist, including bilinear, exponential, trapezoidal, and parabolic laws.

CZM can be implemented in two forms:

- **Intrinsic formulation:** Cohesive elements are inserted along pre-defined potential crack paths before the simulation begins. The major limitation is that the crack trajectory cannot be predicted in advance.
- **Extrinsic formulation:** Cohesive elements are adaptively inserted during the simulation once a predefined criterion is satisfied. This method allows crack paths to evolve freely but requires remeshing, making it computationally intensive.

The cohesive approach effectively simulates progressive damage, fracture initiation, and propagation in quasi-brittle materials. Originally limited to Mode I fracture (tensile cracks), further developments have extended it to mixed-mode cracking, dynamic rupture, and irreversible deformations [116, 117]. The cohesive law parameters such as $\sigma_{\max}$ and u_c are typically determined through experimental calibration.

The intrinsic cohesive formulation may lead to mesh-dependency, as crack growth tends to follow element boundaries. However, this issue can be mitigated by coupling CZM with the Extended Finite Element Method (X-FEM), which allows cracks to propagate independently of mesh topology [118, 119].

Cohesive zone models (CZMs) have demonstrated strong potential in simulating corrosion-induced cracking in reinforced concrete structures. A key application was developed by Guzmán et al. [120], who implemented a two-dimensional finite element model with an embedded cohesive crack formulation to reproduce the internal cracking and spalling behavior caused by reinforcement corrosion. The model estimates the time to surface cracking with reasonable accuracy by considering corrosion rate, rust expansion, and partial accommodation of corrosion products within cracks. Importantly, it was validated through application to a real bridge deck, where simulated crack patterns matched practical observations. Complementing this, Yang et al. [121] introduced a CZM-based numerical model capable of simulating nonuniform corrosion along reinforcement. By embedding cohesive elements within a fine discretized mesh, the model successfully predicted time-dependent surface crack widths under realistic corrosion progression scenarios. Their simulations showed strong agreement with experimental results from literature, highlighting the model's potential for service life estimation and maintenance planning of corrosion-affected structures. Together, these contributions illustrate that cohesive zone modeling, particularly when enhanced by embedded or finely-meshed formulations, is a robust approach for capturing complex fracture behavior driven by corrosion expansion.

2.5.3.5 Extended Finite Element Method (X-FEM)

The Extended Finite Element Method (X-FEM) is a numerical technique developed as an extension of the classical Finite Element Method (FEM), rooted in the Partition of Unity Finite Element Method (PUFEM). Originally proposed by Belytschko and Black in 1999 [122], X-FEM was introduced to effectively model discontinuities such as cracks without requiring mesh alignment to the discontinuity geometry. Its most distinctive advantage lies in its ability to simulate arbitrary crack growth paths independently of the mesh topology, thereby offering greater flexibility and accuracy in fracture simulations.

X-FEM retains the computational framework and strengths of FEM, but overcomes one of its primary limitations—namely, the need for fine mesh discretization around regions of high stress concentration, such as crack tips. This is achieved by enriching the finite element approximation space with additional functions that capture the behavior of discontinuities.

Within the X-FEM framework, two classes of enrichment functions are utilized: one

set captures strong discontinuities across crack faces (designated as the K set), while another set introduces singularity functions at crack tips (the J set)(Figure 9).

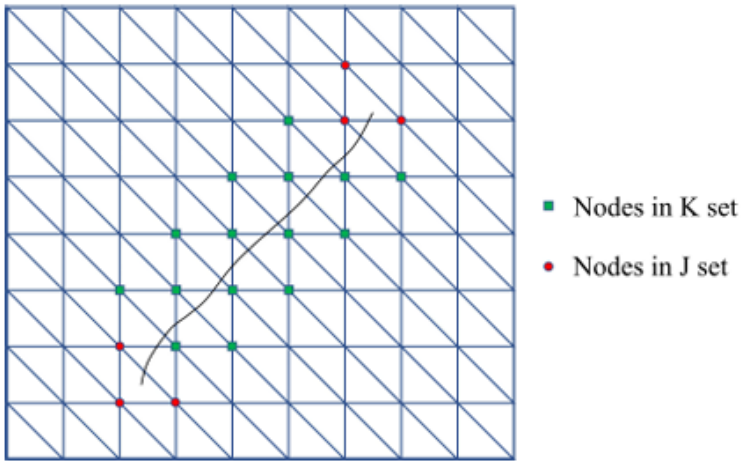

Figure 9: Enriched nodes in XFEM method for tracking crack

To address the discontinuity in the displacement field across crack surfaces, Moës et al. (1999) incorporated the Heaviside function [118], enhancing the accuracy of the method near crack faces. The resulting displacement field approximation takes the form:

$$u^h = \sum_{i \in I} u_i N_i + \sum_{j \in J} b_j N_j H(x) + \sum_{k \in K} N_k \sum_{l=1}^{4} c_k^l F_l(x) \tag{2.16}$$

Here, u^h represents the approximated displacement field, N are shape functions, $H(x)$ is the Heaviside function, and $F_l(x)$ are asymptotic crack-tip enrichment functions. Coefficients b_j and c_k^l are additional degrees of freedom associated with the enriched nodes.

Since its inception, X-FEM has been significantly expanded and applied to a range of fracture problems. Despite its advantages, X-FEM has certain limitations, particularly when dealing with problems involving multiple evolving cracks. The increasing number of enriched nodes in such scenarios can significantly complicate implementation and computational efficiency [123].

X-FEM has been effectively applied to simulate corrosion-induced cracking phenomena where the crack paths evolve independently of the mesh topology, offering a key advantage in modeling damage in reinforced concrete and metallic systems under aggressive environments. Duddu et al. [124] developed an XFEM-based sharp-interface model to simulate crevice and pitting corrosion in metallic alloys, combin-

ing the Nernst–Planck electrochemical framework with level set methods to represent evolving corrosion fronts. Their results successfully captured species transport and morphological evolution in crevice environments, particularly in Al–Mg alloys. Jin and Yu [125] introduced an improved CDM-XFEM framework that integrates continuum damage mechanics (CDM) and water transport modeling to simulate corrosion-induced cracking in concrete with pre-existing transverse cracks. The study showed that crack width and propagation angle are significantly influenced by the geometry of the transverse cracks, and their model was validated against experimental observations. Additionally, Mirzaee et al. [126] assessed the XFEM implementation in ABAQUS for modeling corrosion-induced crack propagation in marine concrete structures. The simulated crack patterns were found to correlate well with experimental data, reinforcing XFEM's reliability for such applications in harsh coastal environments.

2.5.3.6 Embedded Finite Element Method (EFEM)

The Embedded Finite Element Method (EFEM) is a numerical approach that extends classical FEM to allow for arbitrary crack initiation and propagation independently of mesh alignment, similar in objective to XFEM but based on a fundamentally different formulation [127, 128]. Unlike XFEM, which enriches nodes globally, EFEM treats enrichment parameters as local element-wise variables, eliminated at the element level using static condensation techniques.

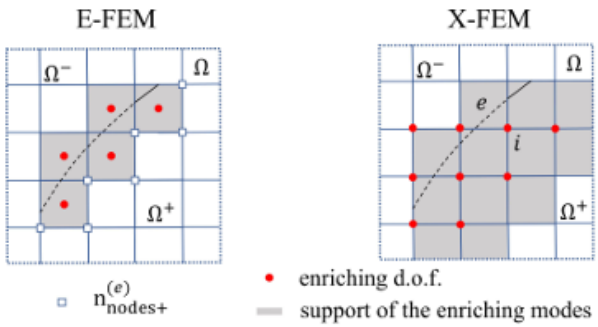

Figure 10: Comparison between element-based enrichment in EFEM (left) and nodal enrichment in XFEM (right) [127].

The EFEM displacement field includes a standard finite element component and an enrichment term that accounts for displacement discontinuities within cracked elements using a Heaviside function [127]. The method originated from the works of Ortiz [129] and Xu and Needleman [130], and was further developed to represent softening bands and strong discontinuities in the early 1990s [131, 132]. Huespe et al. [133] ex-

tended EFEM to dynamic fracture problems with cohesive models, while Armero and Linder [134] enhanced it to capture strong discontinuities using linear displacement jumps.

EFEM is particularly suited to modeling multiple crack formations due to its ability to condense local discontinuities, but it suffers from mesh dependency and approximation errors, especially where displacement continuity across elements is poorly represented [127, 135].

2.5.3.7 Local damage models

Local damage models represent material degradation by introducing a scalar damage variable $d \in [0, d_c]$, where $d = 0$ denotes the intact state and $d = d_c$ denotes full degradation. This internal variable modifies the material stiffness and leads to energy dissipation through strain-softening. As outlined in [136], constructing a local damage model requires the definition of:

- a scalar damage variable d,
- a constitutive law relating stress, strain, and damage via the elastic potential $\psi_e(\varepsilon, d)$, with stress computed as $\sigma = \partial\psi_e/\partial\varepsilon$,
- and a damage evolution law governed by a yield function $f(\varepsilon, d)$, constrained by the Kuhn–Tucker conditions:

$$\dot{d} \geq 0, \quad f(\varepsilon, d) \leq 0, \quad \dot{d} f(\varepsilon, d) = 0,$$

  expressing irreversibility, admissibility, and consistency, respectively.

The evolution of d is typically driven by the choice of the threshold function f which controls the damaged material behavior, such as $f(\tilde{\varepsilon}, \kappa) = \tilde{\varepsilon} - \kappa$, as noted in [137]. The damage law may be expressed by:

$$d = \begin{cases} 0 & \text{if } \kappa < \kappa_0, \\ 1 - \frac{\kappa}{\kappa_0}\left[(1-\alpha) + \alpha e^{-\beta(\kappa-\kappa_0)}\right] & \text{otherwise,} \end{cases}$$

where κ_0 is the damage initiation threshold, and α, β control the residual state in the post-peak stage and the softening behavior respectively.

Within the Standard Generalized Materials framework, the threshold function f can be linked to the dissipated energy via the postulate of Drucker–Ilyushin, which ensures non-negative strain work in any strain cycle [136].

However, local damage models are highly mesh dependent which stands as a key limitation of these models application when implemented with numerical approaches as finite element methods. As shown in [138], the energy dissipated tends to vanish with mesh refinement, which is not physically realistic. To overcome this, non-local formulations have been proposed.

2.5.3.8 Non-local damage models

Non-local damage models are based on the premise that the mechanical response at a given point is not solely governed by the local stress state but also by the surrounding material neighborhood. This behavior is attributed to the interaction between microcracks within a damaged region [139]. In continuum damage mechanics, this is captured by introducing an internal regularization length that accounts for such non-local effects. Below, two common non-local damage models are presented.

Strain Convolution Regularisation Based Damage Model

Often referred to as the integral damage model [139, 140, 141], this approach replaces the local strain field with a non-local averaged strain field $\bar{\varepsilon}(\mathbf{x})$ obtained via a convolution product:

$$\bar{\varepsilon}(\mathbf{x}) = \frac{1}{V} \int_{\Omega} \phi(\mathbf{s}) \varepsilon(\mathbf{x} + \mathbf{s}) \, dV. \tag{2.17}$$

Here, $\phi(\mathbf{s})$ is the weight function controlling the influence of surrounding points, and V is the volume of the interaction domain. The function $\phi(\mathbf{s})$ typically decays with distance $r = \|\mathbf{x} - \mathbf{s}\|$ and must satisfy the normalization condition:

$$\frac{1}{V} \int_{\Omega} \phi(\mathbf{s}) \, dV = 1. \tag{2.18}$$

Two common definitions for $\phi(\mathbf{s})$ were proposed in the literature, the Gauss weighting function:

$$\phi(\mathbf{s}) = \exp\left(-\frac{4\|\mathbf{x} - \mathbf{s}\|^2}{\ell_0^2} \right), \tag{2.19}$$

and the bell-shaped function (see Fig. 11):

$$\phi(\mathbf{s}) = \begin{cases} 1 - \frac{r^2}{\ell_0^2}, & \text{if } r \leq \ell_0, \\ 0, & \text{if } r > \ell_0, \end{cases} \tag{2.20}$$

where ℓ_0 is the internal length parameter. These formulations allow modeling of crack nucleation and propagation as functions of energy release in a distributed neighborhood.

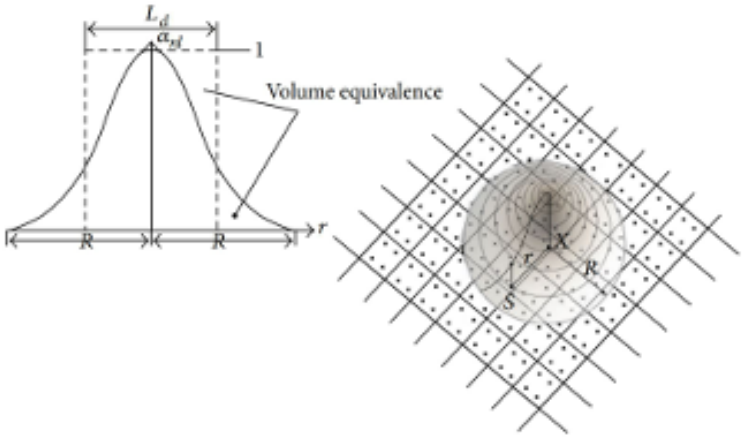

Figure 11: Strain convolution non-local model principle with the typical bell-shaped function [142].

Gradient-Enhanced Damage Model

Gradient-enhanced models (also known as differential non-local models) [143, 144] employ higher-order spatial derivatives of the strain tensor to regularize the strain field. Using a Taylor expansion of $\varepsilon(\mathbf{x}+\mathbf{s})$ around $\mathbf{x}$, the effective strain becomes:

$$\bar{\varepsilon}(\mathbf{x}) = \varepsilon(\mathbf{x}) + \sum_{n=1}^{\infty} a_{2n} \nabla^{(2n)} \varepsilon(\mathbf{x}), \tag{2.21}$$

where a_{2n} are coefficients. Truncating after the second-order term gives:

$$\bar{\varepsilon}(\mathbf{x}) = \varepsilon(\mathbf{x}) + a \nabla^2 \varepsilon(\mathbf{x}), \tag{2.22}$$

where $a = a_2$ is a scalar parameter which is of the dimension length squared and ∇^2 is the Laplacian operator.

To eliminate the C^1 continuity requirement in FEM implementations, the equation is differentiated twice:

$$\nabla^2 \varepsilon(\mathbf{x}) = \nabla^2 \bar{\varepsilon}(\mathbf{x}) - \sum_{n=2}^{\infty} a_{2n} \nabla^{(2n)} \varepsilon(\mathbf{x}). \tag{2.23}$$

Substituting back yields:

$$\varepsilon(\mathbf{x}) - a\nabla^2\bar{\varepsilon}(\mathbf{x}) = \varepsilon(\mathbf{x}) + (a_4 - a^2)\nabla^4\varepsilon(\mathbf{x}) + \sum_{n=3}^{\infty}(a_{2n} - a_{2(n-1)}a)\nabla^{(2n)}\varepsilon(\mathbf{x}). \tag{2.24}$$

Neglecting higher-order terms, the final simplified form becomes:

$$\varepsilon(\mathbf{x}) = \bar{\varepsilon}(\mathbf{x}) - a\nabla^2\bar{\varepsilon}(\mathbf{x}). \tag{2.25}$$

To solve this partial differential equation, appropriate boundary conditions related to the effective strain must be applied. These include either the prescription of $\bar{\varepsilon}$ or its normal derivative:

$$\nabla\bar{\varepsilon}\cdot\mathbf{n} = 0 \quad \text{on } \partial\Omega, \tag{2.26}$$

where $\mathbf{n}$ is the external unit normal vector.

2.5.3.9 Towards Phase-Field Modeling

The modeling of corrosion-induced cracking has evolved through multiple paradigms, each addressing specific aspects of the phenomenon while revealing limitations that hinder predictive accuracy and numerical robustness. Empirical or experimental-based models provide valuable but isolated insights into corrosion or cracking states. These models alone cannot predict the future progression of damage, as they lack the ability to simulate the temporal and spatial evolution of cracking under varying environmental and loading conditions. Classical fracture theories, such as the Griffith model, have provided foundational insights into brittle fracture under quasi-static conditions, yet they inherently fail to describe phenomena like crack nucleation, crack branching, or the complex interaction of multiple cracks.

Numerical methods have been introduced to overcome these limitations, but each class of models carries inherent drawbacks. Direct crack front tracking requires frequent and complex re-meshing procedures, rendering it impractical for three-dimensional structures or evolving crack topologies.

Advanced techniques such as the Extended Finite Element Method (X-FEM) circumvent re-meshing by enriching the displacement field, but they depend heavily on level set functions to track crack surfaces. This leads to challenges in modeling crack initiation, branching, and the interaction of multiple crack fronts. Cohesive zone models (CZMs), though capable of capturing crack nucleation and propagation along multiple fronts, enforce crack paths along predefined element boundaries and exhibit convergence issues with mesh refinement.

These limitations collectively motivate the need for a more robust and unified approach—one that can naturally model crack initiation, propagation, branching, and merging, while being grounded in variational principles and avoiding mesh bias. The *Phase-Field Method (PFM)* has emerged as a powerful solution, offering a regularized representation of discontinuities through a diffusive damage variable and an internal length scale. It seamlessly integrates fracture mechanics into a variational energy minimization framework, unifying elastic deformation, fracture energy, and damage evolution into a single formulation. As such, phase-field modeling represents the frontier of computational fracture mechanics, particularly suited for the complex, multi-physical nature of corrosion-induced cracking.

2.6 Phase Field Method

In this section, the theoretical foundation of the phase field method as a tool for fracture modeling in materials is introduced. The method transforms discrete crack representations into continuous functions, enabling regularized descriptions of crack propagation. Starting with the fundamental variational framework and its Euler-Lagrange formulation, the chapter discusses the energy decomposition into elastic and fracture components. Variants of the method, such as Amor's [145] and Miehe's [146] formulations, are explored, focusing on their treatment of strain energy splits and damage evolution under tensile and compressive forces. The finite element discretization of both damage and displacement problems is detailed, providing a comprehensive basis for subsequent numerical simulations.

2.6.1 Regularized representation of free discontinuities

In phase field fracture modeling, the damage variable $d(x)$ serves as a regularized representation of cracks, transitioning smoothly from undamaged ($d = 0$) to fully damaged ($d = 1$) material. This method eliminates the need for explicit crack tracking by using energy minimization principles and a diffuse interface to approximate the crack morphology. Several formulations of the phase field method, such as AT1, AT2, and their variants, cater to different fracture behaviors.
The Ambrosio-Tortorelli (AT) [147] functional was introduced by Luigi Ambrosio and Vincenzo M. Tortorelli as an elliptic regularization of free-discontinuity problems, particularly in the context of fracture mechanics. This work laid the mathematical foundation for phase-field models of fracture, including the later development of the AT1 and AT2 models [147, 146].

The AT1 model is tailored for brittle fracture and enforces a strict elastic phase prior to damage initiation. The energy density function for AT1 is characterized by a linear degradation function $w(d) = d$, ensuring a sharp response upon crack initiation. The crack density function is defined as:

$$\gamma(d, \nabla d) = \frac{1}{c\ell}(d + \ell^2 |\nabla d|^2). \tag{2.27}$$

where $c = 8/3$ is a scaling constant and ℓ is the regularization parameter controlling the diffused crack width. This formulation ensures brittle fracture behavior by concentrating the energy dissipation within the crack zone. However, the AT1 model can be computationally expensive due to the strict enforcement of elastic behavior before crack propagation [148, 146]
In contrast, the AT2 model is designed for ductile fracture and introduces a smoother damage evolution. It uses a quadratic degradation function $w(d) = d^2$, resulting in a more gradual transition between undamaged and damaged states. The crack density function for AT2 is expressed as:

$$\gamma(d, \nabla d) = \frac{1}{c\ell}(d^2 + \ell^2 |\nabla d|^2). \tag{2.28}$$

where $c = 2$ is a scaling constant. The AT2 model is computationally efficient and well-suited for materials with ductile or mixed fracture behavior, although it may overestimate damage progression in highly brittle materials [148, 149].

To address specific limitations, modifications such as the AT2 with a threshold have been developed. These incorporate a threshold strain energy density $H(d)$, ensuring that damage only evolves when the energy release rate exceeds a critical value. This hybrid approach combines the simplicity of AT2 with improved accuracy for brittle fractures [149].

In this thesis, the AT2 model is adopted due to its computational efficiency and its suitability for capturing the progressive damage and crack propagation typically observed in reinforced concrete structures. Reinforced concrete often exhibits mixed-mode fracture behavior, where tensile cracking in the concrete matrix combines with localized plasticity near reinforcement elements. The quadratic degradation function $w(d) = d^2$ in the AT2 model allows for a smoother transition between undamaged and damaged states, providing a practical balance between computational feasibility and the ability to simulate the complex fracture mechanisms inherent in reinforced concrete under corrosion and mechanical loading conditions.

So, following this model, the function d(x) can be determined by solving the follow-

ing boundary value problem [146]:

$$\begin{cases} d - \ell^2 \Delta d = 0 & in\ \Omega \\ d(\boldsymbol{x}) = 1 & on\ \Gamma \\ \nabla d(\boldsymbol{x}).\boldsymbol{n} = 0 & on\ \partial\Omega \end{cases} . \tag{2.29}$$

where d is the damage variable, ℓ is a regularization parameter describing the actual size of the damaged zone, Δ is the Laplacian, $\partial\Omega$ is a characteristic length equivalent to the size of an elementary volume representative of the microstructure, and n the outward normal to $\partial\Omega$. In 2D and 3D dimensions, the solution of (2.29) produces a representation of the crack morphology. It can be demonstrated that (2.29) is the Euler-Lagrange equation associated with the variational problem:

$$d(\boldsymbol{x}) = Arg\left\{ inf_{d\in\delta_d}\Gamma_l(d)\right\}, \tag{2.30}$$

such that:

$$\Gamma_l(d) = \int_\Omega \gamma(d, \nabla d) d\Omega, \tag{2.31}$$

$$\delta_d = \{d \mid d(\boldsymbol{x}) = 1\ on\ \Gamma\ \forall \boldsymbol{x} \in \Gamma\}, \tag{2.32}$$

and

$$\gamma(d, \nabla d) = \frac{1}{2\ell}(d^2 + \ell^2 |\nabla d|^2) \tag{2.33}$$

where γ is the crack density function per unit volume, and $\Gamma_\ell(d)$ is the total crack length.

$$\lim_{l\to 0}\left\{ inf_{d\in\delta_d}\Gamma_\ell(d)\right\} = |\Gamma|, \tag{2.34}$$

We define the functional derivative $\delta_\gamma(d)$ such that:

$$D_{\delta d}\Gamma_\ell(d) = \int_\Omega \gamma(d, \nabla d)\ \delta d\ \partial\Omega \tag{2.35}$$

where

$$D_{\delta d}\Gamma_\ell(d) = \left\{ \frac{d}{d\alpha}(\Gamma_l(d + \alpha\delta d))\right\}_{\alpha=0} \tag{2.36}$$

is known as the Gateaux or directional derivative. By applying the divergence theorem

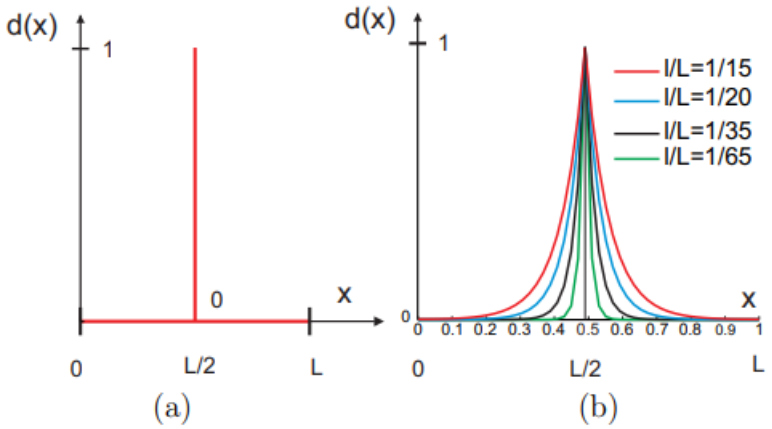

Figure 12: Regularized representation of a crack: 1D case: (a) sharp crack model, taking unitary value of $d(x)$ at $x = x_\Gamma = L/2$ (crack); (b) regularized representation through phase field (adapted from [150]).

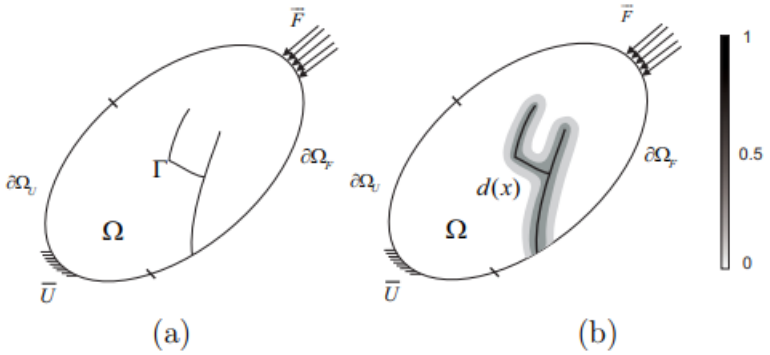

Figure 13: Regularized representation of a crack: 2D case: (a) sharp crack model; (b) regularized representation through phase field (adapted from [150]).

to (2.62), and assuming $\nabla d.n = 0$ on $\partial\Omega$, we obtain:

$$\delta_\gamma(d) = \frac{d}{\ell} - \ell\Delta d. \tag{2.37}$$

2.6.2 Phase Field Formulation: Regularized variational framework

We consider a linear elastic body Ω , with a crack Γ, where we neglect the external forces. As part of the phase field method (regularization), the energy of a cracked body can be written as the sum of the elastic (free) energy and the dissipated (fracture) energy.

The variational approach to fracture mechanics defined by Francfort and Marigo [151]

introduces this energy as follows:

$$E(\boldsymbol{u},\Gamma) = E_u(\boldsymbol{u},\Gamma) + E_s(\Gamma) = \int_{\Omega\setminus\Gamma} W_u(\boldsymbol{\varepsilon}(\boldsymbol{u})d\Omega + g_c H^{d-1}(\Gamma) \tag{2.38}$$

where W_u is the energy density function, u is the displacement field, $\boldsymbol{\varepsilon} = \frac{1}{2}(\nabla u + \nabla u^T)$ is the strain field, g_c is the fracture resistance, and H^{d-1} is the Hausdorff surface measure giving the crack length ($d = 2$) or surface ($d = 3$). $E_u(\boldsymbol{u},\Gamma)$ represents the elastic energy stored in the cracked body, and $E_s(\Gamma)$ is the energy required to create the crack according to the Griffith criterion. In a regularized framework (phase field method), the above functional becomes the following:

$$E(\boldsymbol{u}, d) = \int_\Omega W_u(\boldsymbol{\varepsilon}(\boldsymbol{u}), d)d\Omega + g_c \int_\Omega \gamma(d)d\Omega, \tag{2.39}$$

where $\gamma(d)$ is defined by eq. (2.33). The total energy is then rewritten as $E = \int_\Omega W d\Omega$ where

$$W = W_u(\boldsymbol{\varepsilon}(\boldsymbol{u}), d) + g_c\gamma(d) \tag{2.40}$$

can be identified as the free energy.

2.6.3 Formulation for unilateral contact

In the early stages of the modelling work, Amor's formulation [145] of the phase field method was used as a preliminary validation of the approach. After, we moved to Miehe's formulation [146, 152] for the rest of implemented modelling of corrosion-induced cracking. To avoid crack opening in compression in both formulations, we assume an isotropic elastic behavior of the body taking into account the damage caused by tension only [152, 150]. We then choose the following form for W_u:

$$W_u(\boldsymbol{u}, d) = \Psi^+(\boldsymbol{\varepsilon}(\boldsymbol{u}))\{g(d) + kres\} + \Psi^-\boldsymbol{\varepsilon}(\boldsymbol{u}). \tag{2.41}$$

Another aspect that was actually introduced by Amor [145] and then Miehe [146, 152] was the splitting of the strain energy ψ. In Amor's split, it is to discriminate between volumetric and deviatoric strain energy terms. While in Miehe's split, it is to discriminate between tension and compression energy modes.

2.6.3.1 *Amor Formulation*

The strain energy terms, introduced by Amor [145], are as the following:

$$\Psi^{+}(\boldsymbol{\varepsilon}) = \frac{1}{2}k(< Tr(\boldsymbol{\varepsilon}) >_{+})^{2} + \mu\ dev(\boldsymbol{\varepsilon}) : dev(\boldsymbol{\varepsilon}), \tag{2.42}$$

$$\Psi^{-}(\boldsymbol{\varepsilon}) = \frac{1}{2}k(< Tr(\boldsymbol{\varepsilon}) >_{-})^{2}, \tag{2.43}$$

Ψ^{+} and Ψ^{-} are the energies of the traction and compression modes respectively.

dev is the deviatoric operator and $k = \lambda + \frac{2}{n}\mu\ \ (n = 2, 3)$ is the compression modulus.

The stress is expressed as follows:

$$\boldsymbol{\sigma} = \frac{\partial W_u}{\partial \boldsymbol{\varepsilon}} \tag{2.44}$$

or as:

$$\boldsymbol{\sigma}(\boldsymbol{u}, d) = g(d)\frac{\partial \Psi^{+}}{\partial \boldsymbol{\varepsilon}}(\boldsymbol{u}) + \frac{\partial \Psi^{-}}{\partial \boldsymbol{\varepsilon}}(\boldsymbol{u}) \tag{2.45}$$

$\Longrightarrow$

$$\boldsymbol{\sigma}(\boldsymbol{\varepsilon}, d) = ((1-d)^{2} + kres)(k < Tr(\boldsymbol{\varepsilon}) >_{+} I + 2\mu dev(\boldsymbol{\varepsilon})) + k < Tr(\boldsymbol{\varepsilon}) >_{-} I \tag{2.46}$$

$g(d)$ is the degradation function. It takes into account the effect of damage on the rigidity of material and have the following form:

$$g(d) = (1-d)^{2}. \tag{2.47}$$

It is chosen such that $g'(1) = 0$ to guarantee obtaining a finite value of the strain energy density function particularly in the cracked domain, and $g(0) = 1$ to guarantee that the material is initially undamaged, and $g(1) = 0$ for fully damaged zones. The small parameter $kres \ll 1$ is the residual stiffness and is introduced to avoid any singular stiffness in the fully damaged state ($d = 1$).

2.6.3.2 *Miehe Formulation*

On the other hand, in Miehe's formulation [146], the strain energy terms are as the following:

$$\Psi^{+}(\boldsymbol{\varepsilon}) = \frac{1}{2}\lambda < Tr(\boldsymbol{\varepsilon}) >_{+}^{2} + \mu Tr\{(\boldsymbol{\varepsilon}^{+})^{2}\} \tag{2.48}$$

$$\Psi^{-}(\boldsymbol{\varepsilon}) = \frac{1}{2}\lambda < Tr(\boldsymbol{\varepsilon}) >_{-}^{2} + \mu Tr\{(\boldsymbol{\varepsilon}^{-})^{2}\}. \tag{2.49}$$

The stress is now expressed as follows:

$$\boldsymbol{\sigma}(u,d) = g(d)\frac{\partial \Psi^{+}}{\partial \boldsymbol{\varepsilon}}(u) + \frac{\partial \Psi^{-}}{\partial \boldsymbol{\varepsilon}}(u) \tag{2.50}$$

$\Longrightarrow$

$$\boldsymbol{\sigma}(\boldsymbol{\varepsilon},d) = ((1-d)^{2} + kres)(\lambda < Tr(\boldsymbol{\varepsilon}) >_{+} I + 2\mu\boldsymbol{\varepsilon}^{+}) + \lambda < Tr(\boldsymbol{\varepsilon}) >_{-} I + 2\mu\boldsymbol{\varepsilon}^{-} \tag{2.51}$$

Another split that was introduced by Miehe [146] is the strain field split. The strain field is decomposed into extensive and compressive modes:

$$\boldsymbol{\varepsilon} = \boldsymbol{\varepsilon}^{+} + \boldsymbol{\varepsilon}^{-} \tag{2.52}$$

where

$$\boldsymbol{\varepsilon}^{\pm} = \sum_{i=1}^{D} < \boldsymbol{\varepsilon}^{i} >_{\pm} \boldsymbol{n}^{i} \otimes \boldsymbol{n}^{i} \tag{2.53}$$

where $\boldsymbol{\varepsilon}^{i}$ and $\boldsymbol{n}^{i}$ are the eigenvalues and eigenvectors of $\boldsymbol{\varepsilon}$, i.e. satisfying $\boldsymbol{\varepsilon}\boldsymbol{n}^{i} = \boldsymbol{\varepsilon}^{i}\boldsymbol{n}^{i}$. In (2.53) $< x >_{+} = (x + |x|)/2$ and $< x >_{-} = (x - |x|)/2$.

To satisfy non-reversible evolution of cracks, and to handle loading and unloading histories, the strain history functional H is proposed by Miehe et al.[146] such that:

$$H(\boldsymbol{x},t) = \max_{\tau \in [0,t]} \{\Psi^{+}(\boldsymbol{x},\tau)\} \tag{2.54}$$

which is to be substituted to the tensile energy Ψ^{+} in the above equations. The minimization of the energy $E(u,d)$ with respect to d ($\delta_{d}E(u,d) = 0 \ \forall \ \delta d$) and the consideration of this irreversibility condition yields the following phase field problem which is to be solved:

$$\begin{cases} 2(1-d)H - \frac{g_c}{\ell}\left\{d - \ell^{2}\Delta d\right\} = 0 & in\ \Omega \\ d(\boldsymbol{x}) = 1 & on\ \Gamma \\ \nabla d(\boldsymbol{x}).\boldsymbol{n} = 0 & on\ \partial\Omega \end{cases} \tag{2.55}$$

Shifted Strain Split Algorithm

To avoid the nonlinearity related to the decomposition of the strain field at time t^{n+1},

two shifted strain tensor split algorithms were introduced.

Split Algorithm 1:

$$\boldsymbol{\varepsilon}^{+}_{n+1} \simeq P^{+}_{n} \,:\, \boldsymbol{\varepsilon}_{n+1}, \qquad \boldsymbol{\varepsilon}^{-}_{n+1} \simeq P^{-}_{n} \,:\, \boldsymbol{\varepsilon}_{n+1} \tag{2.56}$$

where P^{+} and P^{-} are fourth order projectors and can be expressed, thanks to the algorithm presented in Miehe and Lambrecht [152], as $P^{\pm}_{n} = \frac{\partial \boldsymbol{\varepsilon}^{\pm}_{n}}{\partial \boldsymbol{\varepsilon}_{n}}$. Such a simplification might induce small load increments to maintain a good accuracy of the solution. To overcome this drawback, a second algorithm is proposed, described as follows:

Split Algorithm 2:

$$\boldsymbol{\varepsilon}^{+}_{n+1} \simeq P^{+}_{n} + 1 \,:\, \boldsymbol{\varepsilon}_{n+1}, \qquad \boldsymbol{\varepsilon}^{-}_{n+1} \simeq P^{-}_{n} + 1 \,:\, \boldsymbol{\varepsilon}_{n+1} \tag{2.57}$$

where

$$P^{+}_{n+1} \simeq P^{+}_{n} + \Delta t_{n} \frac{\partial P^{+}_{n}}{\partial t} \tag{2.58}$$

$$P^{-}_{n+1} \simeq I - P^{-}_{n+1} \tag{2.59}$$

with $\Delta t_{n} = t_{n+1} - t_{n}$, and $\frac{\partial P^{+}_{n}}{\partial t} \simeq \frac{\partial P^{+}_{n} - P^{+}_{n-1}}{\partial \Delta t_{n-1}}$. We then allow load increments to be adapted, as when cracks begin nucleating and propagating smaller load increments might be required. Furthermore, in the broken zone ($d \simeq 1$), the decomposition (2.53) might lead unphysical values of $\boldsymbol{\varepsilon}^{\pm}$. To alleviate this issue, we introduce a weight function $\beta(d)$ such that $\beta(d=0) = 1, \beta(d=1) = 0, e.g.\ \beta(d) = (1-d)^2$ then:

$$P^{+}_{n+1} \simeq P^{+}_{n} + \beta(d_{n}) \Delta t_{n} \frac{\partial P^{+}_{n}}{\partial t}. \tag{2.60}$$

This ensures that for $\beta(d=0)$ the behavior is linear and that the projector tensor is well defined. For $d=1$, the property $\beta(d=1) = 0$ leads to compute the projector tensor as the projector from the previous load increment.

2.6.4 Finite Element Discretization

2.6.4.1 Damage Problem

Weak Form

The weak form of the damage problem is obtained by multiplying the above equation (2.55_1) by a test function δd and integrating over Ω:

$$\int_\Omega \left\{ 2(1-d)H\delta d - \frac{g_c}{\ell}(d - \ell^2\Delta d)\delta d \right\} d\Omega = 0 \tag{2.61}$$

with the help of the following property:

$$(\Delta d)\delta d = \nabla.(\nabla d\delta d) - \nabla d.\nabla(\delta d) \tag{2.62}$$

and the divergence theorem, and by assuming $\nabla d.n = 0$ on $\partial\Omega$, we finally obtain:

$$\int_\Omega \left\{ (2H + \frac{g_c}{\ell})d\delta d + g_c\ell\nabla d.\nabla(\delta d) \right\} d\Omega = \int_\Omega 2H\delta d d\Omega. \tag{2.63}$$

In the present work, the computations are done in quasi-static conditions. The time steps introduced after that refer to load increments, so that the problem to be solved at time t^{n+1} is expressed by seeking $d(x) \in \delta_d$, such that:

$$\int_\Omega \left\{ (2H_n + \frac{g_c}{\ell})d_{n+1}\delta d + g_c\ell\nabla d_{n+1}.\nabla(\delta d) \right\} d\Omega = \int_\Omega 2H_n\delta d d\Omega. \tag{2.64}$$

$\forall\delta d(x) \in H_0^1(\Omega)$. where $H_n = H(\boldsymbol{u}_n)$ is calculated at the time of the previous loading by:

$$\begin{cases} H_{n+1}(\boldsymbol{x}) = \Psi^+_{n+1}(\boldsymbol{x}) \quad if \quad \Psi^+_{n+1}(\boldsymbol{x}) > \Psi^+_n(\boldsymbol{x}), \\ H_{n+1}(\boldsymbol{x}) = \Psi^+_n(\boldsymbol{x}) \quad if \quad \Psi^+_{n+1}(\boldsymbol{x}) \leq \Psi^+_n(\boldsymbol{x}). \end{cases} \tag{2.65}$$

Discretization of the Damage Problem

In this work, 2D problems are considered where a mesh of linear 3-node triangles has been used. The phase field and phase field gradient in one element are estimated by:

$$d(\mathbf{x}) = \mathbf{N}_d(\mathbf{x})\mathbf{d}_i \quad and \quad \nabla d(\mathbf{x}) = \mathbf{B}_d(\mathbf{x})\mathbf{d}_i \tag{2.66}$$

where $\mathbf{d}_i$ are the nodal values of d_{n+1}. The same discretization is done for the variations:

$$\delta d(\mathbf{x}) = \mathbf{N}_d(\mathbf{x})\delta\mathbf{d}_i \quad and \quad \nabla\delta d(\mathbf{x}) = \mathbf{B}_d(\mathbf{x})\delta\mathbf{d}_i \tag{2.67}$$

where $\boldsymbol{N}_d(x)$ and $\boldsymbol{B}_d(x)$ are the shape functions and shape functions derivatives respectively. By introducing the above FEM discretization in the weak form, we get the following linear system of equations:

$$\mathbf{K}_d\mathbf{d} = \mathbf{F}_d \tag{2.68}$$

where $\mathbf{d}$ is the vector containing all nodal damage variables.

$$\mathbf{K}_d = \int_\Omega \left\{ (\frac{g_c}{\ell} + 2H_n)\mathbf{N}_d^T\mathbf{N}_d + g_c\ell\mathbf{B}_d^T\mathbf{B}_d \right\} d\Omega \tag{2.69}$$

and

$$\mathbf{F}_d = \int_\Omega 2\mathbf{N}_d^T H_n d\Omega \tag{2.70}$$

H_n is evaluated at the Gauss points by (2.65).

2.6.4.2 Displacement Problem

Weak Form

The weak form for the displacement problem is derived by solving the variational problem:

$$\boldsymbol{u}(\boldsymbol{x}) = Arg\left\{ \inf_{u\in\delta u}(E(\boldsymbol{u}, d) - W^{ext}) \right\} \tag{2.71}$$

where $\delta\boldsymbol{u} = \left\{ \boldsymbol{u} | \boldsymbol{u}(\boldsymbol{x}) = \bar{\boldsymbol{u}}\ on\ \partial\Omega_u, \boldsymbol{u} \in H^1(\Omega) \right\}$ and $W_{ext} = \int_\Omega f.ud\Omega + \int_{\partial\Omega F}\bar{F}.ud\Gamma$ with f and $\bar{F}$ body forces and prescribed traction over the boundary $\partial\Omega_F$. The classical weak form for $\boldsymbol{u}(\boldsymbol{x}) \in \delta\boldsymbol{u}$ is obtained:

$$\int_\Omega \boldsymbol{\sigma} : \boldsymbol{\varepsilon}(\delta\boldsymbol{u})d\Omega = \int_\Omega \boldsymbol{f}.\delta\boldsymbol{u}d\Omega + \int_{\partial\Omega\boldsymbol{F}} \bar{\boldsymbol{F}}.\delta\boldsymbol{u}d\Gamma \quad \forall\delta\boldsymbol{u} \in H_0^1(\Omega), \tag{2.72}$$

where $\boldsymbol{\sigma}$ is expressed in both equations (2.46) and (2.51) for Amor and Miehe respectively.

Discretization of the Displacement Problem

Amor's displacement equation

Following Amor's equation (2.46), the stress expression is as follows:

$$\boldsymbol{\sigma} = ((1-d)^2 + kres)(k < Tr(\boldsymbol{\varepsilon}) >_+ I + 2\mu dev(\boldsymbol{\varepsilon})) + k < Tr(\boldsymbol{\varepsilon}) >_- I \tag{2.73}$$

We propose the following approximation:

$$< Tr\boldsymbol{\varepsilon}_{n+1} >_+ \simeq R^+(\boldsymbol{\varepsilon}_n) Tr\boldsymbol{\varepsilon}_{n+1}, \qquad < Tr\boldsymbol{\varepsilon}_{n+1} >_- \simeq R^-(\boldsymbol{\varepsilon}_n) Tr\boldsymbol{\varepsilon}_{n+1} \tag{2.74}$$

with:

$$R^+(\boldsymbol{\varepsilon}_n) = \frac{1}{2}(sign(Tr\boldsymbol{\varepsilon}_n) + 1), \qquad R^-(\boldsymbol{\varepsilon}_n) = \frac{1}{2}(sign(-Tr\boldsymbol{\varepsilon}_n) + 1). \tag{2.75}$$

Using the Voigt's notation: $[\boldsymbol{\varepsilon}] = \{\boldsymbol{\varepsilon}_{11}; \boldsymbol{\varepsilon}_{22}; 2\boldsymbol{\varepsilon}_{12}\}^T$, $[\boldsymbol{\sigma}] = \{\boldsymbol{\sigma}_{11}; \boldsymbol{\sigma}_{22}; \boldsymbol{\sigma}_{12}\}^T$, $[\mathbf{1}] = \{1; 1; 0\}^T$

The expression of the stress tensor becomes:

$$[\boldsymbol{\sigma}_{n+1}] = ((1-d_{n+1})^2 + kres)(kR_n^+([\boldsymbol{\varepsilon}_{n+1}].[\mathbf{1}])[\mathbf{1}] + 2\mu(I - 0.5[\mathbf{1}][\mathbf{1}]^T)) + kR_n^-([\boldsymbol{\varepsilon}_{n+1}].[\mathbf{1}])[\mathbf{1}] \tag{2.76}$$

Introducing the FEM discretization, we get the following linear system of equations:

$$\{\boldsymbol{K}_1(d_{n+1}, \boldsymbol{u}_n) + \boldsymbol{K}_2(\boldsymbol{u}_n)\}\, \boldsymbol{u}_{n+1} = \boldsymbol{F}_{n+1} \tag{2.77}$$

with:

$$\begin{cases} \boldsymbol{K}_1(d_{n+1}) = \int_\Omega \boldsymbol{B}^T \left\{ ((1-d_{n+1})^2 + kres)(kR_n^+[\mathbf{1}]^T[\mathbf{1}] + 2\mu(I - 0.5[\mathbf{1}][\mathbf{1}]^T)) \right\} \boldsymbol{B} d\Omega, \\ \boldsymbol{K}_2 = \int_\Omega \boldsymbol{B}^T \left\{ kR_n^-[\mathbf{1}]^T[\mathbf{1}] \right\} \boldsymbol{B} d\Omega, \\ \boldsymbol{F}_{n+1} = \int_\Omega \boldsymbol{N}^T \boldsymbol{f} d\Omega + \int_{\partial\Omega F} \boldsymbol{N}^T \bar{\boldsymbol{F}}_{n+1} d\Gamma. \end{cases} \tag{2.78}$$

Miehe's displacement equation

While using Miehe's equation (2.51), the stress equation is:

$$\boldsymbol{\sigma}(\boldsymbol{\varepsilon}, d) = ((1-d)^2 + kres)(\lambda < Tr(\boldsymbol{\varepsilon}) >_+ I + 2\mu\boldsymbol{\varepsilon}^+) + \lambda < Tr(\boldsymbol{\varepsilon}) >_- I + 2\mu\boldsymbol{\varepsilon}^- \tag{2.79}$$

Following the same previous Voigt's notation and by introducing the expressions of the fourth order projectors $\boldsymbol{P}^+$ and $\boldsymbol{P}^-$, the stress can be expressed at time t_{n+1} by:

$$[\boldsymbol{\sigma}_{n+1}] = ((1-d_{n+1})^2 + kres)(\lambda R_n^+([\boldsymbol{\varepsilon}_{n+1}].[\mathbf{1}])[\mathbf{1}] + 2\mu\boldsymbol{P}_n^+[\boldsymbol{\varepsilon}_{n+1}]) + \lambda R_n^-([\boldsymbol{\varepsilon}_{n+1}].[\mathbf{1}])[\mathbf{1}] + 2\mu\boldsymbol{P}_n^-[\boldsymbol{\varepsilon}_{n+1}]. \tag{2.80}$$

and the linear system of equations is obtained:

$$\{\boldsymbol{K}_1(d_{n+1}, \boldsymbol{u}_n) + \boldsymbol{K}_2(\boldsymbol{u}_n)\}\, \boldsymbol{u}_{n+1} = \boldsymbol{F}_{n+1} \tag{2.81}$$

with:

$$\begin{cases} \boldsymbol{K}_1(d_{n+1}) = \int_\Omega \boldsymbol{B}^T \left\{ ((1-d_{n+1})^2 + kres)(\lambda R_n^+[\mathbf{1}]^T[\mathbf{1}] + 2\mu \boldsymbol{P}_n^+) \right\} \boldsymbol{B} d\Omega, \\ \boldsymbol{K}_2 = \int_\Omega \boldsymbol{B}^T \left\{ \lambda R_n^-[\mathbf{1}]^T[\mathbf{1}] + 2\mu \boldsymbol{P}_n^- \right\} \boldsymbol{B} d\Omega, \\ \boldsymbol{F}_{n+1} = \int_\Omega \boldsymbol{N}^T \boldsymbol{f}\, d\Omega + \int_{\partial\Omega F} \boldsymbol{N}^T \bar{\boldsymbol{F}}_{n+1} d\Gamma. \end{cases} \tag{2.82}$$

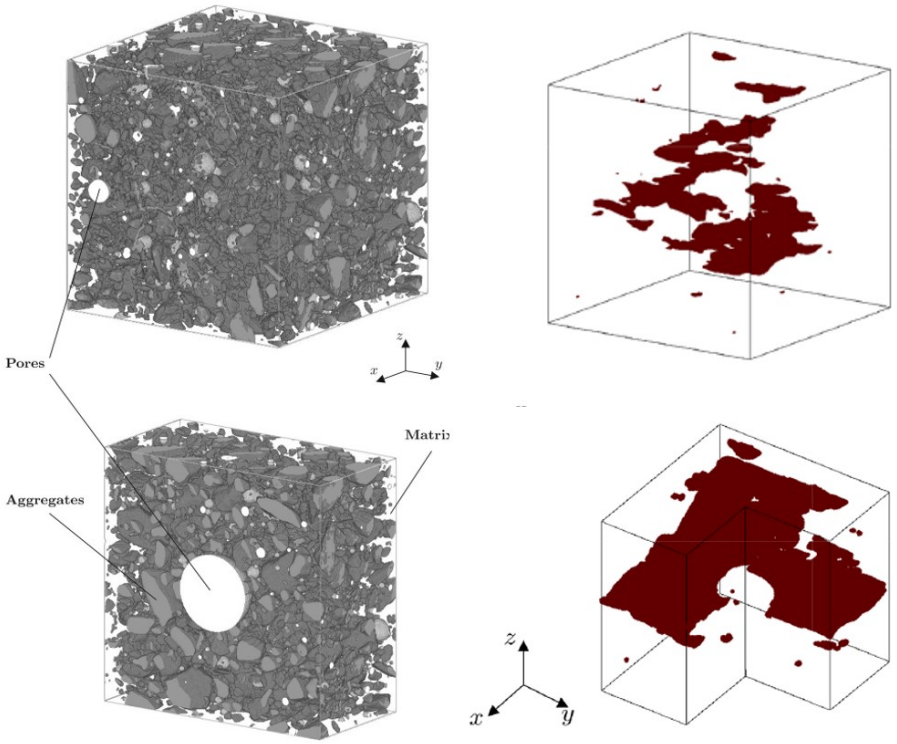

Figure 14: Illustration of phase-field fracture simulation in concrete microstructure. Adapted from [153].

2.7 Conclusion

This chapter has provided a summary state-of-the-art review of modeling strategies for corrosion-induced cracking in RC structures. Beginning with the socio-economic significance and physical mechanisms of corrosion, we have tracked the historical and methodological progression from empirical and experimental models to more mechanically and numerically grounded approaches. While empirical models offer useful diag-

nostics and experimental support, their lack of generalization limits their use in predictive simulations.

Classical fracture theories, such as Griffith's criterion, provide foundational insights but are insufficient for modeling complex crack phenomena like branching or nucleation in heterogeneous concrete media. Numerical strategies, including discrete element, continuum damage, and cohesive zone models, have significantly advanced our ability to simulate crack initiation and growth. However, they each face limitations, such as mesh-dependence, remeshing complexity, or difficulties in handling multiple cracks and complex geometries.

As demonstrated, the phase-field method emerges as a robust, thermodynamically consistent, and variationally grounded alternative that naturally regularizes crack topology, removes the need for explicit tracking, and allows for multiphysics coupling. It represents a paradigm shift in fracture modeling and forms the backbone of the computational strategy adopted in this thesis.

The following chapters will build upon this foundation, providing the application and validation of a phase-field model for corrosion-induced cracking in reinforced concrete, aimed at enhancing predictive durability assessments of RC structures. An illustration of phase-field fracture simulation in concrete microstructure is shown in Fig. 14.

Chapter 3
Phase-Field Modeling of Corrosion-Induced Cracking: numerical investigations

3.1 Introduction

In this chapter, fracture models based on the phase field method for corrosion-induced cracks are developed and implemented. First, the phase field is implemented on state-of-the-art benchmarks to validate the developed in-house code constructed during this thesis. Then, a model able to describe cracks induced by the expansion of corrosion products is presented and implemented. Finally, numerical investigations are conducted to determine the influence of modeling and numerical parameters.

3.2 Implementation of the phase field method in classical fracture tests

We first present implementations of the phase field method to fracture as presented in Chapter 2 and illustrations on classical benchamrks of the literature.

First, we consider a plate defined in a square domain of dimensions 1×1 mm^2, containing an initial horizontal notch emanating from the left edge. Two different loading scenarios are simulated: pure tension and pure shear. The mesh is refined locally around the notch to enhance accuracy in crack initiation and propagation regions. Figures 15 and 16 illustrate the refined meshes and applied boundary conditions, respectively.

The model assumes a homogeneous and isotropic elastic behavior with the following parameters:

Symbol	Description	Value
E	Young's modulus	210 GPa
ν	Poisson's ratio	0.3
g_c	Fracture toughness	2.7×10^{-3} kN/mm
λ	First Lamé parameter	121.1538 GPa
μ	Shear modulus (Second Lamé parameter)	80.76923 GPa

Table 1: Material parameters used in the simulations

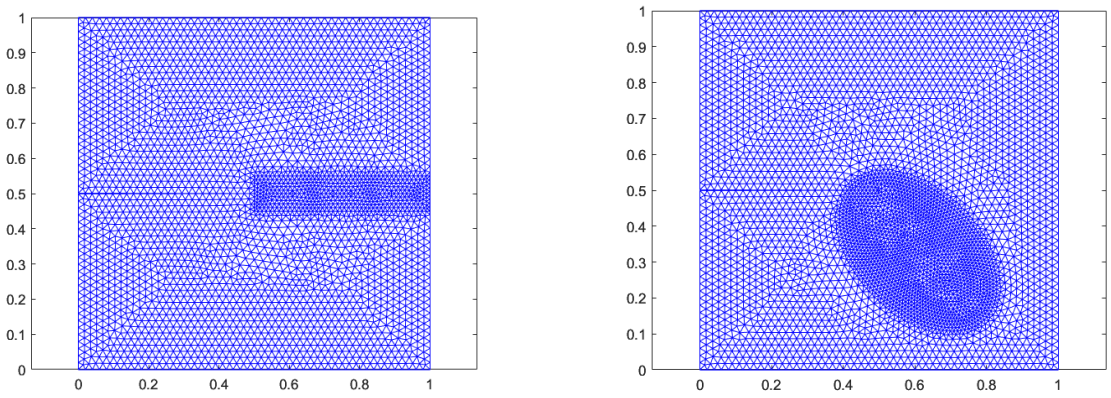

(a) Refined mesh for tension **(b)** Refined mesh for shear

Figure 15: Locally refined meshes near the notch for both tests.

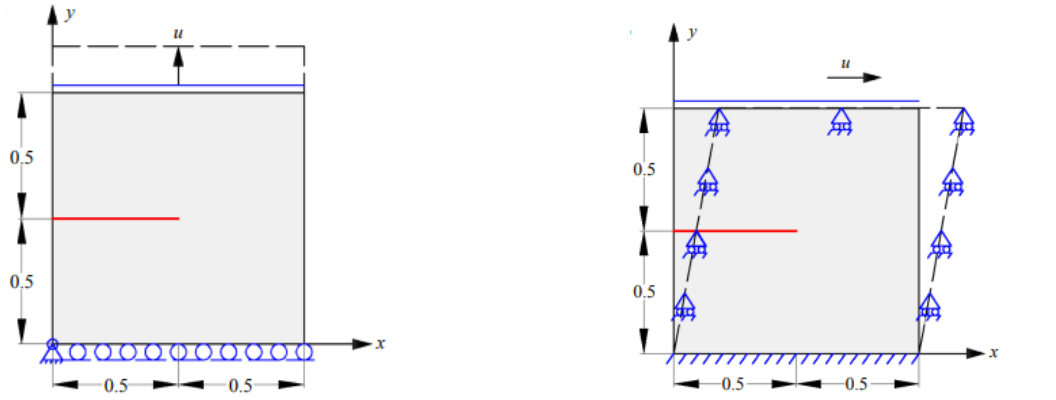

(a) Boundary conditions for tension loading **(b)** Boundary conditions for shear loading

Figure 16: Schematic representation of applied boundary conditions.

The domain is discretized using triangular finite elements, of size $e = 0.02$ mm and a refined zone mesh size of $e = 0.01$ mm (see Fig. 15.b). The regularization length ℓ is taken as $\ell = 2e = 0.02$ mm. A displacement is applied incrementally with:

$$U_{\max} = 0.015 \text{ mm}, \quad N = 500 \quad \Rightarrow \quad \Delta u = \frac{U_{\max}}{N-1}$$

The propagation of the crack is simulated during loading using the phase field method with the Amor model (see Sections 2.6.3 & 2.6.4) to take into account unilateral contact in the cracked region [145]. The evolution of the damage field at selected increments is shown in Figs. 17 and 18 for tension and shear loading, respectively.

The global force-displacement curves for both loading types are plotted in Figure 19. As anticipated, the tension curve exhibits a brittle response with a sudden drop post-peak, while the shear case demonstrates a more irregular post-peak softening.

The corresponding crack paths are also consistent with literature benchmarks: a

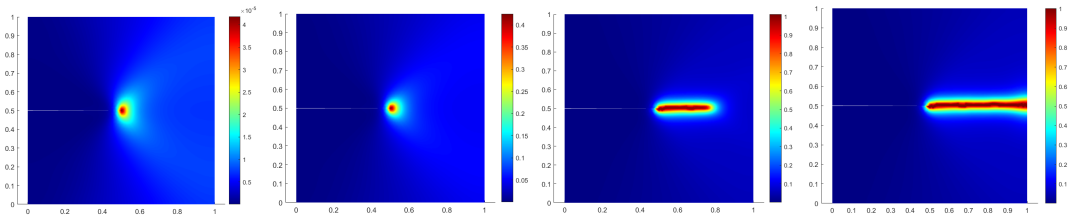

Figure 17: Tensile crack evolution at different loading steps (steps 4, 170, 180, and final).

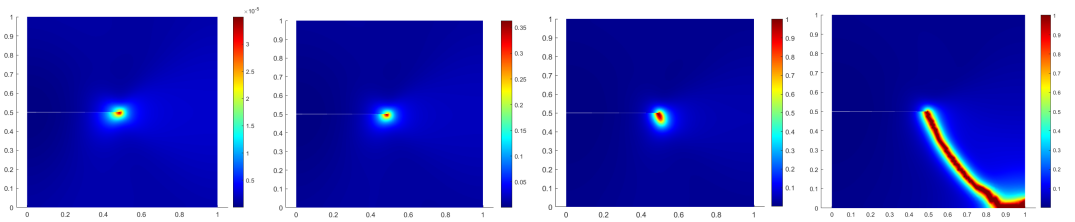

Figure 18: Shear crack evolution at different loading steps (steps 4, 180, 250, and final).

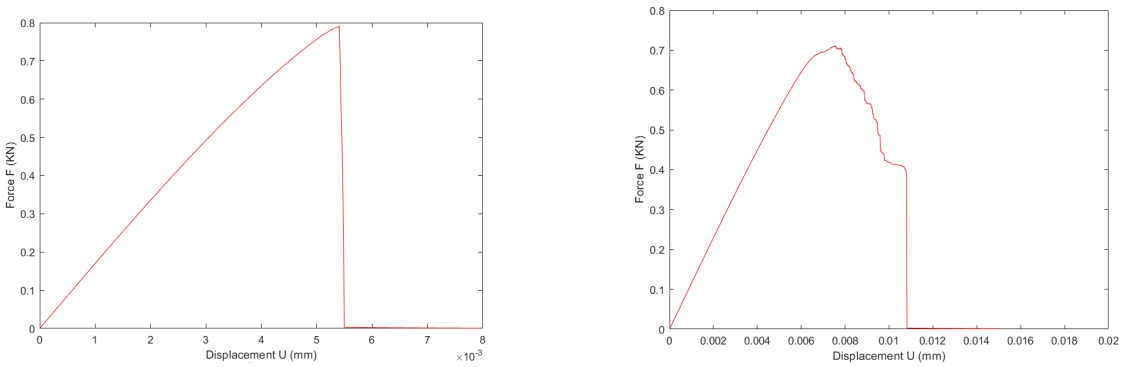

(a) Tension **(b)** Shear

Figure 19: Force–displacement responses under Amor formulation for tension and shear tests.

horizontal crack develops under uniaxial tension, while an inclined crack forms under shear loading. These results are in qualitative agreement with previous studies [149, 154, 155] and confirm that Amor's volumetric–deviatoric split can reproduce the expected fracture modes in pure mode-I and shear-dominated cases. These findings pave the way for the following simulations using Miehe's energy-split formulation.

To further validate the implementation, an exact comparison is made with a state-of-the art solution using Miehe's energy-decomposition phase-field model [156].

A square domain 1 mm × 1 mm is used with the same boundary conditions as in Figure 16. The regularization length is taken as $\ell = 0.0075$ mm as in [146], with a mesh refined accordingly. The loading is applied in a monotonic, displacement-controlled manner, following the approach described in Miehe et al. [146]. To ensure numerical stability during the simulation of crack propagation, especially in the post-peak regime,

the total loading is divided into two stages. In the initial phase, a constant displacement increment of $\Delta u = 10^{-5}$ mm is applied for the first 500 steps. After this point, the increment is refined to $\Delta u = 10^{-6}$ mm in order to capture the abrupt nature of the crack evolution and to improve convergence behavior.

The damage pattern and force-displacement response obtained from the simulation are shown in Figures 20 and 22. The numerical results are in excellent agreement with the reference results from both Miehe et al. [146] (Fig.21 a) and Lu et al. [156] (Fig.21 b).

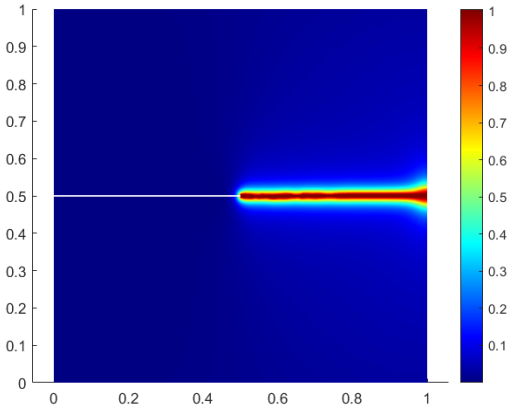

Figure 20: Final damage pattern in tension using Miehe's formulation.



Figure 21: Pure tension loading: damage pattern of the phase field simulation in a) Ref. [146], b) Ref. [156], c) present work

The results confirm that the phase-field implementation accurately captures the fracture response under mechanical loading, and matches well with literature benchmarks. This provides a validated foundation of the in-house code developed in this thesis for the upcoming corrosion-induced cracking simulations.

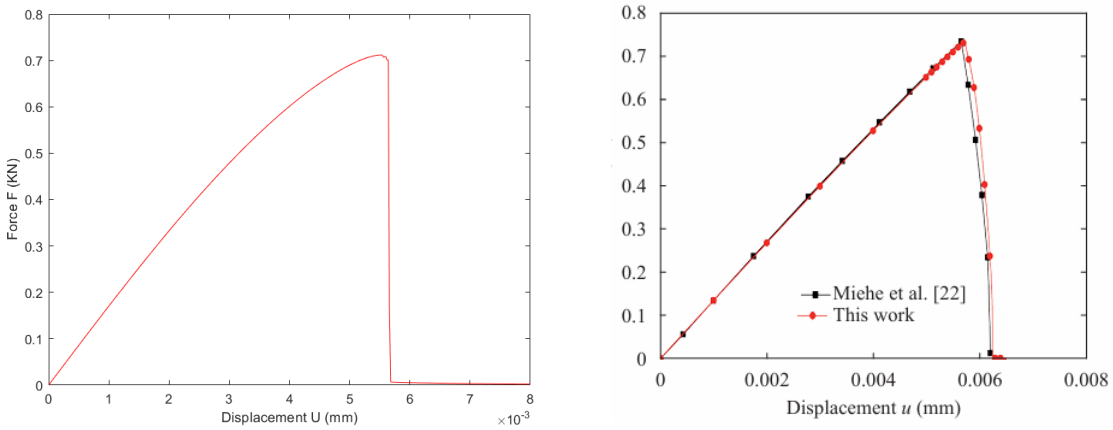

Figure 22: Force-displacement response: (left) present work, (right) reference [156] showing their force-displacement curve with Miehe's [146] curve.

3.3 Corrosion-induced fracture model

In this section, a corrosion-induced cracking model is developed and implemented for reinforced concrete structures. The primary objective is to simulate the expansive effects of reinforcement corrosion and study the resulting fracture patterns within the concrete matrix. Unlike previous mechanical loading simulations, this part of the work integrates the influence of internal volumetric expansion due to rust formation at the steel-concrete interface.

In this chapter, the concrete is modeled as a homogeneous, isotropic, quasi-brittle material. The steel reinforcement is modelled as a stiff, elastic phase. Corrosion is modelled in a layer around the reinforcement with specific elastic properties and a corrosion parameter expansion eigenstrain. During expansion of the layer, local stress concentration induces local traction states which initiate cracks.

3.3.1 Formulation and numerical implementation

To model the corrosion process, the total strain tensor is additively decomposed into elastic and corrosion expansion strains as:

$$\boldsymbol{\varepsilon} = \boldsymbol{\varepsilon}^e + \boldsymbol{\varepsilon}^h \tag{3.1}$$

where $\boldsymbol{\varepsilon}$ is the total strain tensor, $\boldsymbol{\varepsilon}^e$ is the elastic strain due to mechanical equilibrium and $\boldsymbol{\varepsilon}^h$ is the corrosion-induced expansion strain.

The expansion strain $\boldsymbol{\varepsilon}^h$ models the internal volumetric growth resulting from rust formation. In this study, an isotropic and uniform expansion assumption is adopted for

simplicity and computational feasibility. It is expressed as:

$$\boldsymbol{\varepsilon}^h = h\,\boldsymbol{I}. \tag{3.2}$$

Here, h is the scalar expansion parameter representing the intensity of the corrosion effect and $\boldsymbol{I}$ is the second-order identity tensor. Note that in this chapter, the evolution law for the parameter h is given by a linear function of time, to demonstrate the feasibility of the approach. A time-dependent model calibrated on experiments is described in Chapter 5. In the present model, the corrosion expansion strain plays the role of thermal expansion in classical thermoelastic models. Then, the local elastic problem is given by:

$$\nabla \cdot \mathbb{C}(d) \,:\, \left(\boldsymbol{\varepsilon}(\mathbf{u}) - \boldsymbol{\varepsilon}^h\right) \tag{3.3}$$

whose corresponding weak form is expressed by:

$$\int_\Omega \mathbb{C}(d) \,:\, \boldsymbol{\varepsilon}(\mathbf{u}) \,:\, \boldsymbol{\varepsilon}(\delta\mathbf{u}) d\Omega = \int_\Omega \mathbb{C}(d) \,:\, \boldsymbol{\varepsilon}^h d\Omega \tag{3.4}$$

In this work, the expansion is applied in a region around the rebar, supposed to model the corrosion layer (see Fig. 23). In the different performed simulations of this chapter, a rectangular domain is made of a quasi-brittle matrix, an elastic rebar, and an elastic expansive corrosion layer. The displacements on the bottom end are fixed, while the other boundaries are stress-free. Under the expansion of the layer, crack is formed in the matrix due to local traction.

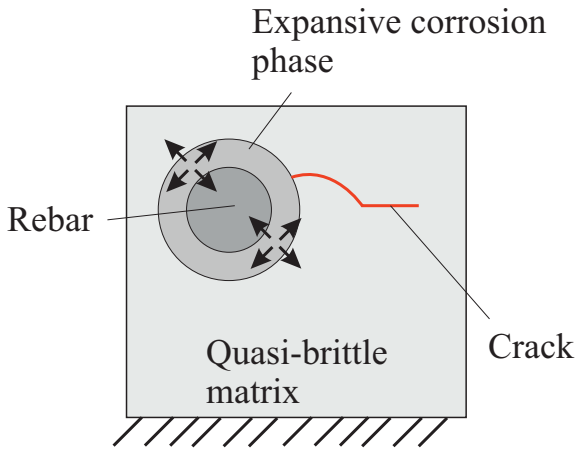

Figure 23: Structural problem with reinforcement and expansive corrosive layer.

The stress relation is given by

$$\boldsymbol{\sigma} = g(d)\frac{\partial \Psi^+}{\partial \boldsymbol{\varepsilon}^e} + \frac{\partial \Psi^-}{\partial \boldsymbol{\varepsilon}^e}, \qquad g(d) = (1-d)^2 + k_{res},$$

but is now evaluated as a function of $\boldsymbol{\varepsilon}^e = \boldsymbol{\varepsilon} - \boldsymbol{\varepsilon}^h$.

Accordingly, the operators $R^{\pm}$ and $P^{\pm}$ are also computed from the elastic strain:

$$R^{\pm} = R^{\pm}(\mathrm{Tr}\,\boldsymbol{\varepsilon}^e), \qquad P^{\pm} = P^{\pm}(\boldsymbol{\varepsilon}^e).$$

In this context, the expression of the stress is given in the Amor's model by

$$[\boldsymbol{\sigma}_{n+1}] = g(d_{n+1})\Big(kR_n^+[\mathbf{1}][\mathbf{1}]^T + 2\mu\big(\boldsymbol{I} - 0.5[\mathbf{1}][\mathbf{1}]^T\big)\Big)([\boldsymbol{\varepsilon}_{n+1}] - [\boldsymbol{\varepsilon}^h]) + kR_n^-[\mathbf{1}][\mathbf{1}]^T([\boldsymbol{\varepsilon}_{n+1}] - [\boldsymbol{\varepsilon}^h]). \tag{3.5}$$

and in the Miehe's model by:

$$[\boldsymbol{\sigma}_{n+1}] = g(d_{n+1})\Big(\lambda R_n^+[\mathbf{1}][\mathbf{1}]^T + 2\mu\boldsymbol{P}_n^+\Big)([\boldsymbol{\varepsilon}_{n+1}] - [\boldsymbol{\varepsilon}^h]) + \Big(\lambda R_n^-[\mathbf{1}][\mathbf{1}]^T + 2\mu\boldsymbol{P}_n^-\Big)([\boldsymbol{\varepsilon}_{n+1}] - [\boldsymbol{\varepsilon}^h]). \tag{3.6}$$

Since $\boldsymbol{\varepsilon}^h$ is constant and independent of $\boldsymbol{u}$, the tangent stiffness tensor has the same split as in the original case, but evaluated at $\boldsymbol{\varepsilon}^e$:

In the Amor's model:

$$[C(d)] = g(d)\Big(kR^+[\mathbf{1}][\mathbf{1}]^T + 2\mu(\boldsymbol{I} - 0.5[\mathbf{1}][\mathbf{1}]^T)\Big) + kR^-[\mathbf{1}][\mathbf{1}]^T. \tag{3.7}$$

In the Miehe's model:

$$[C(d)] = g(d)\Big(\lambda R^+[\mathbf{1}][\mathbf{1}]^T + 2\mu\boldsymbol{P}^+\Big) + \lambda R^-[\mathbf{1}][\mathbf{1}]^T + 2\mu\boldsymbol{P}^-. \tag{3.8}$$

The stress update is then written in compact form as

$$[\boldsymbol{\sigma}_{n+1}] = [C(d_{n+1})][\boldsymbol{\varepsilon}_{n+1}] - [C(d_{n+1})][\boldsymbol{\varepsilon}^h]. \tag{3.9}$$

The first term corresponds to the original operator, while the second is the corrosion expansion contribution.

Introducing FEM discretization in (3.4) leads to the linear system:

$$\big(\boldsymbol{K}_1(d_{n+1}) + \boldsymbol{K}_2\big)\boldsymbol{u}_{n+1} = \boldsymbol{F}_{ext} + \boldsymbol{F}_h, \tag{3.10}$$

where $\mathbf{K}_1$ and $\mathbf{K}_2$ have been provided in Eq. (2.78) & (2.82) and where F_h takes the form for the Amor's model as:

$$\boldsymbol{F}_{h,Amor} = \int_\Omega \boldsymbol{B}^T[C_{Amor}(d_{n+1})][\boldsymbol{\varepsilon}^h]\,d\Omega. \tag{3.11}$$

and for Miehe's model:

$$\boldsymbol{F}_{h,Miehe} = \int_{\Omega} \boldsymbol{B}^T [C_{Miehe}(d_{n+1})][\boldsymbol{\varepsilon}^h] \, d\Omega. \tag{3.12}$$

The formulation of the damage problem remains the same as in the previous general case (see Eq. (2.68)). The only modification lies in the evaluation of the history field:

$$H_{n+1}(\boldsymbol{x}) = \max \Big(\Psi^+(\boldsymbol{\varepsilon}(u_{n+1}) - \boldsymbol{\varepsilon}^h), \, H_n(\boldsymbol{x}) \Big). \tag{3.13}$$

3.3.2 Comparison of strain split models to account for crack closure

In this section, we compare damage patterns when using Amor's and Miehe's model in corrosion-induced cracking in simple academic configurations.

The studied domain is described in Fig. 24, where the mesh is depicted for the different phases. A square domain of 1×1 mm is used. The steel rebar has a radius of $r = 0.05$ mm and is located near the top of the domain, centered at $(0.5, 0.8)$. The corrosion product layer forms a ring of thickness 0.015 mm, giving an outer radius of 0.065 mm. A triangular mesh is employed with a regularization length $\ell = 0.02$mm sufficient to accurately capture the stress concentration and crack initiation.

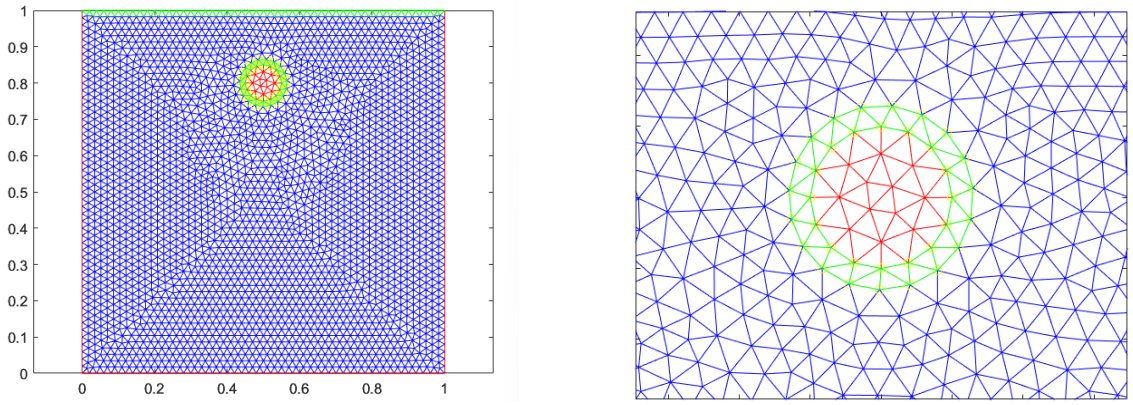

Figure 24: Global mesh of the reinforced concrete domain showing concrete (blue), steel (red), and corrosion layer (green)

The material properties used for the different phases are listed in Table 2. The only difference between the concrete and corrosion product layer lies in the fracture toughness g_c, which is set to a very high value for the corrosion layer as well as in the rebar to ensure it does not crack during simulation.

The boundary conditions are defined as follows: The bottom-left corner node are fully fixed ($u_x = u_y = 0$); All other nodes along the bottom edge: constrained vertically ($u_y = 0$).

Table 2: Material parameters used in the expansion simulations

Phase	E (GPa)	ν	g_c (kN/mm)
Concrete matrix	34.5	0.1	0.2
Steel rebar	110	0.3	2.0
Corrosion layer	34.5	0.1	3000

The expansion parameter h is increased incrementally within the corrosion layer using:

$$\Delta h = 0.02 \quad \text{for 120 steps} \quad \Rightarrow \quad h_{\max} = 2.4$$

Figure 25 illustrates the final damage fields obtained using Amor and Miehe formulations under the same expansion conditions.

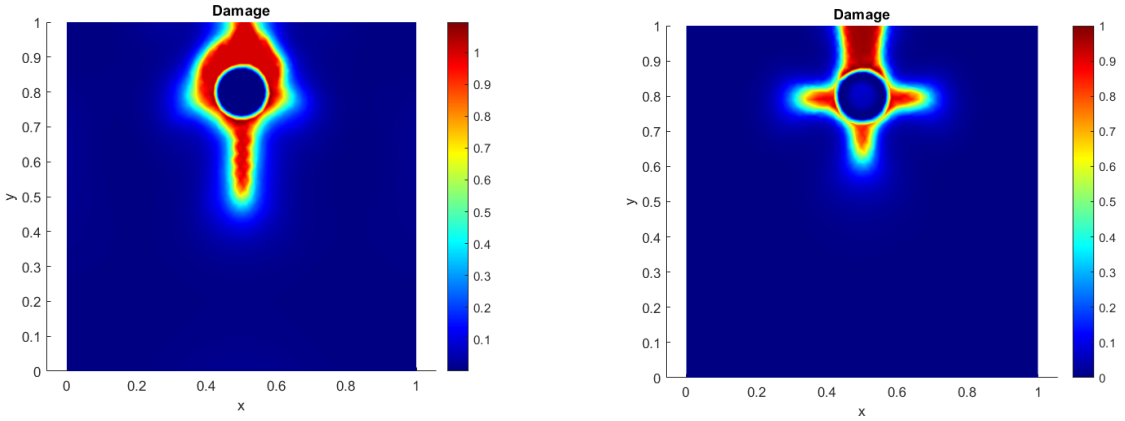

(a) Amor formulation **(b)** Miehe formulation

Figure 25: Damage patterns from corrosion-induced expansion using Amor and Miehe formulations

Comparing the results obtained with both models (Amor's and Miehe, see section 3.3.1), we can note that different damage patterns are obtained, showing a significant influence of the strain split model, due to local traction and compression states in the neighborhood of the corrosion zone. In the case of corrosion-induced expansion, the imposed eigenstrain generates a mixed stress state: radial compression develops at the steel–concrete interface, while tensile hoop stresses arise in the surrounding cover. These coexisting tensile and compressive directions cannot be consistently resolved by Amor's volumetric split, which only distinguishes volumetric tension and compression based on the trace of the strain tensor. As a result, tensile components may be masked when the volumetric response is dominated by compression, leading to an underestimation of crack driving forces. By contrast, Miehe's spectral decomposition separates

each principal strain into its tensile and compressive parts, preserving the directionality of stresses and enabling a more realistic representation of crack nucleation and branching. Therefore, in Fig. 25 (a) (Amor's model), it can be noted that the crack remains roughly unidirectional and emerges from a diffuse damage zone around the reinforcement, while in Fig. 25 (b) (Miehe's model), several cracks propagate from the corrosion zone, in agreement with the expected stress field. This is consistent with the arguments reported in [157], where the ability of spectral splits to resolve complex mixed states was emphasized.

In the following, Miehe's model will be adopted for the corrosion-induced simulations.

3.3.3 Numerical investigations: mesh sensitivity analysis

The sensitivity of the crack path to the mesh size is investigated. The Miehe's strain split is adopted. A new configuration is studied. A centered reinforcement with circular cross section is considered in a square domain, as depicted in Fig. 26. The steel rebar has a radius of $r_s = 0.1$ mm, and the corrosion layer has the same thickness as before, $t_c = 0.015$ mm, giving an outer radius of $r_c = 0.115$ mm.

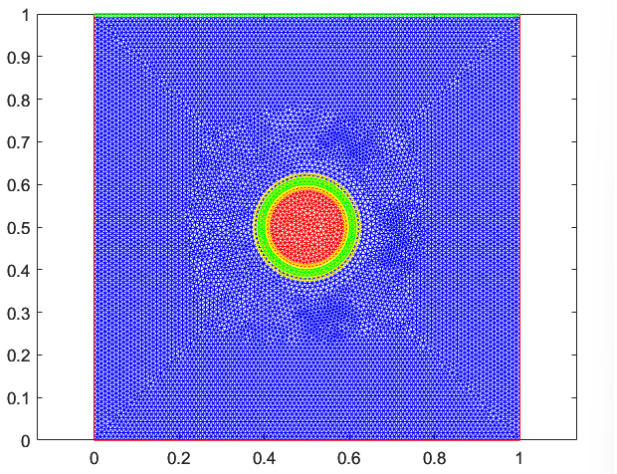

Figure 26: Finite element mesh with centered steel rebar ($r_s = 0.1$ mm) and corrosion layer ($t_c = 0.015$ mm). Case shown: mesh size $e = \ell/2$.

Five simulations are performed using increasing mesh densities and triangular meshes. The domain is constrained by symmetry boundary conditions: vertical displacements are fixed along the horizontal edges, while horizontal displacements are fixed along the vertical edges, ensuring that the response is driven solely by the corrosion-induced eigenstrain. The material and phase-field parameters are: fracture toughness $g_c =$

2.7×10^{-3} (kN/mm) and regularization length $\ell = 0.02$ mm (kept fixed for all cases). The corrosion-induced expansion is applied through an incremental increase in the expansion parameter h, with step increments $\Delta h = 0.015$ up to a maximum value of $h_{\max} = 1.5$ over 100 loading steps.

Five simulations are performed with a fixed regularization length $\ell = 0.02$ mm and different mesh sizes:

$$e = \ell, \quad e = \frac{\ell}{1.5}, \quad e = \frac{\ell}{2}, \quad e = \frac{\ell}{3}, \quad e = \frac{\ell}{4}.$$

The convergence of the results is analyzed by plotting the maximum damage $d_{\max}$ against the eigenstrain parameter h (Fig. 27) and by comparing the corresponding damage fields at the end of loading (Fig. 28).

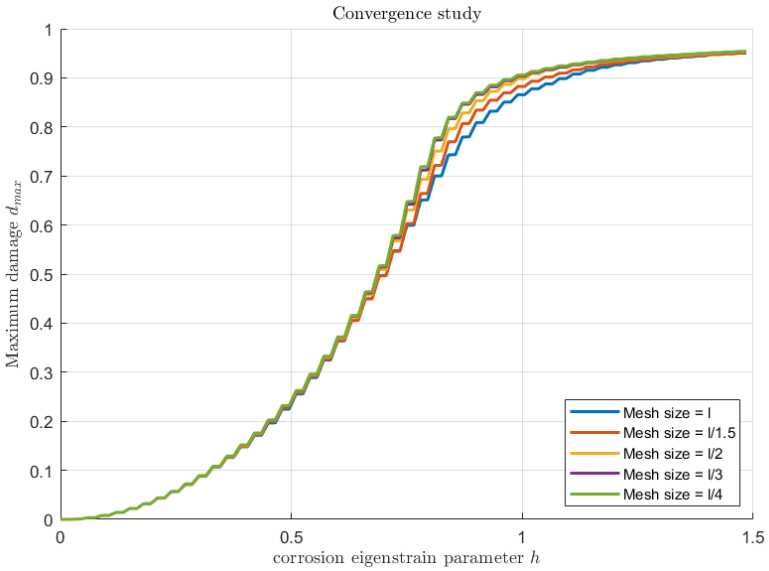

Figure 27: Convergence study: maximum damage $d_{\max}$ versus corrosion eigenstrain parameter h, for five mesh sizes.

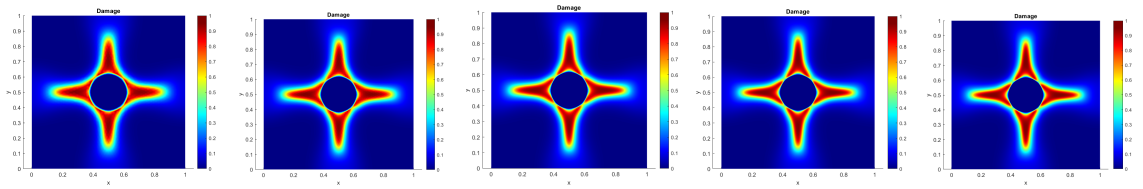

(a) $e = \ell$ **(b)** $e = \ell/1.5$ **(c)** $e = \ell/2$ **(d)** $e = \ell/3$ **(e)** $e = \ell/4$

Figure 28: Effect of mesh refinement on damage evolution using Miehe's formulation with fixed $\ell = 0.02$ mm.

From Fig. 27 and Fig. 28, we can note that both the damage patterns and the $d_{\max}(h)$

response converge as the mesh is refined, which illustrates the convergence properties of the phase-field method with respect to the mesh size.

3.3.4 Non-Uniform Expansion model for corrosion products

The previous simulations assumed a uniform expansion of corrosion products around the circumference of the steel reinforcement. While this simplification facilitates the analysis, it does not adequately reflect the complexity of realistic corrosion phenomena. In practice, corrosion rarely occurs uniformly, but depends on factors such as chloride ion penetration, surface defects, heterogeneous material properties, and environmental exposure, all of which lead to non-uniform accumulation of corrosion products around the steel perimeter.

Several studies have highlighted the importance of modeling non-uniform corrosion to accurately capture cracking patterns in reinforced concrete. For example, Molina [158] and De Koster [159] initially explored uniform corrosion, but later works (e.g., [160, 161, 162]) emphasized the need for more realistic representations. Non-uniform expansion can be described using different spatial distributions, such as elliptical profiles [163], Gaussian distribution [34], or discrete activation angles [161]. These approaches produce more accurate damage propagation paths and reflect the real-life cracking behavior observed in corroded concrete.

In this section, three different types of non-uniform expansion are investigated: (a) Uni-directional expansion (left-side corrosion), (b) Elliptical expansion (higher intensity along horizontal axis) and (c) Random peak expansion (localized corrosion with discrete activation).

We first assume Uni-directional Corrosion Expansion. This configuration assumes that corrosion products accumulate only on one side of the reinforcement, simulating a chloride penetration from one face (e.g., left) of the concrete cover. Mathematically, the expansion strain is defined as:

$$\boldsymbol{\varepsilon}^h = h \cdot \alpha(\boldsymbol{x}) \cdot \boldsymbol{I} \tag{3.14}$$

where $\alpha = 1$ on the left side of the corrosion layer, and $\alpha = 0$ elsewhere. This causes the corrosion expansion to activate on half of the circular boundary only. The resulting mesh displacement and damage patterns are shown in Figure 29.
As expected, damage is concentrated on the left side of the steel, where the corrosion pressure is applied. Cracks nucleate and propagate in the expansion direction, with no damage observed on the right side. Three main crack branches emerge, unlike the four symmetrical cracks observed in uniform corrosion scenarios.

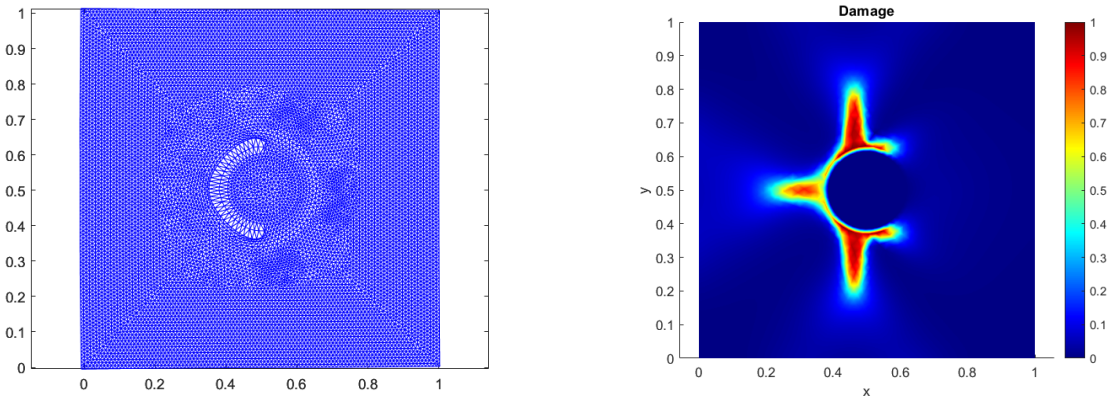

(a) Mesh displacement

(b) Damage pattern

Figure 29: One-sided corrosion expansion: localized damage on the left side of the rebar

Several studies have suggested elliptical expansion profiles to reflect the observed shape of section loss in corroded rebars [163, 164]. Next, we prescribe an elliptical expansion distribution, where corrosion products accumulate more significantly along the horizontal axis (left–right) of the rebar, while vertical regions (top–bottom) experience minimal expansion. In this elliptical case, the eigenstrain tensor retains the same original form $\varepsilon^h = h\,\mathbf{I}$, but the set of elements on which it is applied is no longer circular. Instead, h is imposed over the elliptical corrosion layer, leading to greater expansion along the horizontal axis and reduced expansion along the vertical one.

The elliptical shape of the corrosion products layer is illustrated in Figure 30, followed by the corresponding damage evolution.

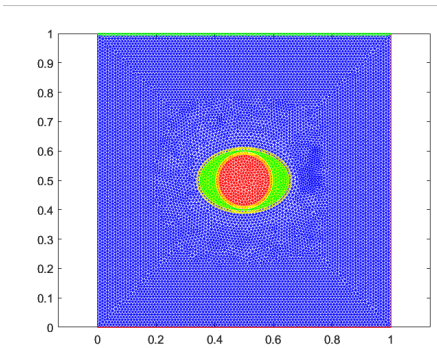

Figure 30: Elliptical expansion profile representing corrosion product accumulation

Initially, cracks emerge along the left and right faces of the reinforcement, where expansion is maximal. As the corrosion progresses, weaker cracks appear vertically, following the lower expansion intensity in those regions. The progressive nature of the damage validates the model's ability to replicate realistic corrosion-induced failure

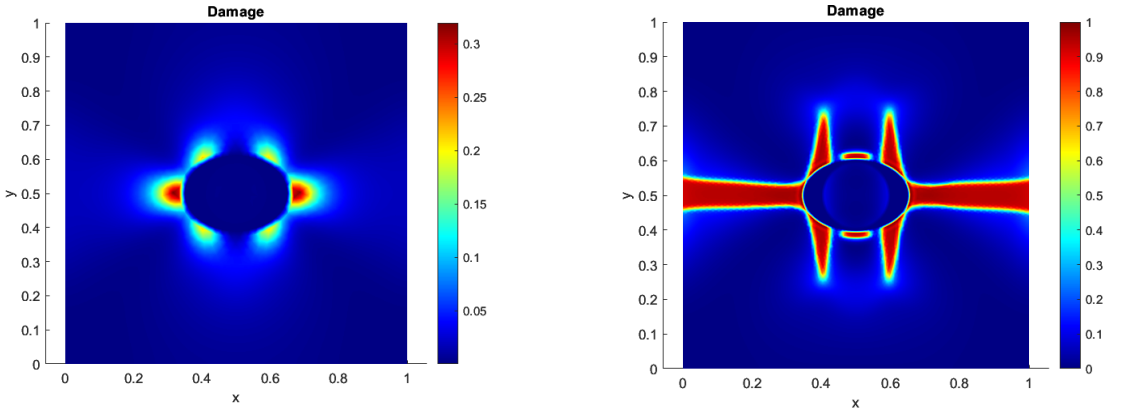

(a) Early stage of damage

(b) Advanced damage propagation

Figure 31: Damage evolution under elliptical corrosion expansion

patterns.

Finally, a random distribution of expansion in the corrosion layer is investigated, where a maximum value (peak) is located arbitrarily in the layer. This case simulates the highly localized corrosion behavior typically observed in practice due to chloride pitting or heterogeneity in the concrete matrix. The expansion strain is again defined according to eq. (3.14) where α randomly takes values 0 or 1 at each element in the corrosion layer. Fig. 32 shows the mesh displacements due to uniform and non-uniform expansion, followed by the damage distributions in both cases.

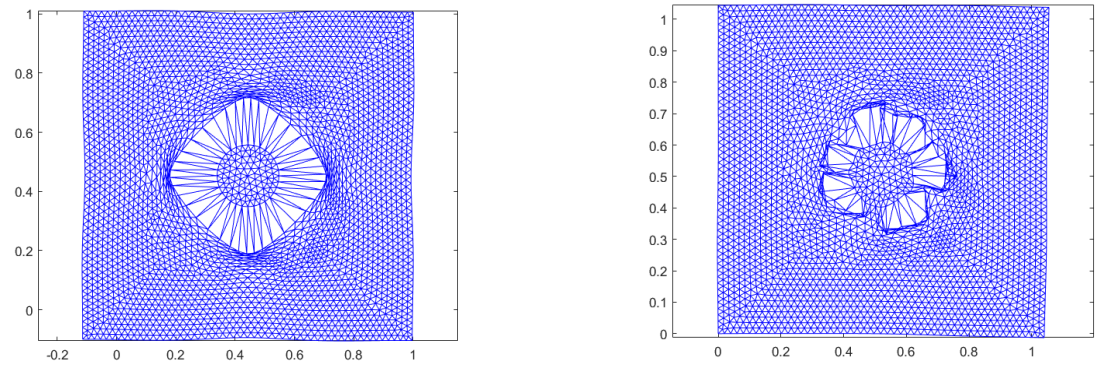

(a) Uniform expansion

(b) Localized expansion

Figure 32: Mesh displacement under uniform and non-uniform expansion

The results show that random localized corrosion produces more severe internal damage at lower expansion pressures compared to uniform corrosion. This behavior aligns with experimental findings reported by Jang [161] and Šavija [162], who found

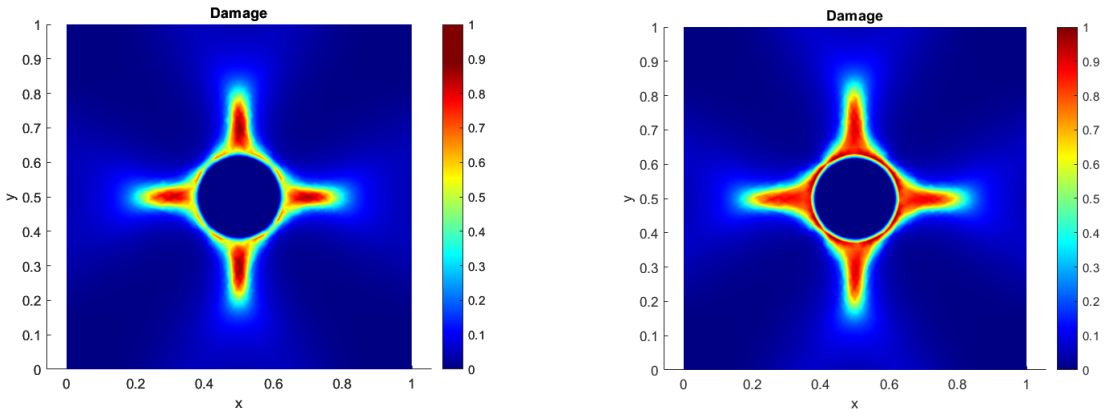

(a) Uniform expansion

(b) Random expansion

Figure 33: Damage comparison between uniform and localized expansion

that non-uniform corrosion expansion can reduce the required cracking pressure by up to 60%, and create internal cracks that propagate undetected toward the surface.

These results show that the solution is strongly dependent on the expansion distribution model around the rebar, suggesting to identify this distribution from experimental results to accurately model the crack paths in realistic simulations.

3.3.5 Geometrical parameter sensitivity analysis

In the following the influence of the position of the rebar, and its distance with the boundaries of the sample, is investigated. In regular applications, steel reinforcements are most often positioned near boundaries to resist to traction during bending. Then, we investigate different configurations in the following.

- **Corner positioning of reinforcement** — commonly used in practice to provide structural integrity.
- **Effect of variable positioning of reinforcement with fixed concrete cover thickness** — commonly used in practice to provide structural integrity.
- **Effect of variable concrete cover thickness** — a key design parameter influencing corrosion initiation and crack propagation.

A constant expansion loading effect is applied to all of the following simulations with different rebar positioning and concrete cover thickness scenarios.

Corner positioning of reinforcement:
Due to higher stress concentrations at corners, reinforcements are frequently placed at these locations in RC structures. Experimental observations from Loukil's thesis [37] show characteristic crack paths—namely horizontal (H), vertical (V), and oblique (O)—developing from the reinforcement toward the concrete boundary.

The image used for comparison in this study corresponds to the experimental slice labeled **P11-d100-35j-T11-D**, extracted from Loukil's dataset. This specimen featured a corner-positioned reinforcement and exhibited a distinctive crack network involving three orientations (H, V, O), as shown in Figure 34. These crack orientations are especially relevant for validating numerical simulations under corrosion-induced expansion scenarios.

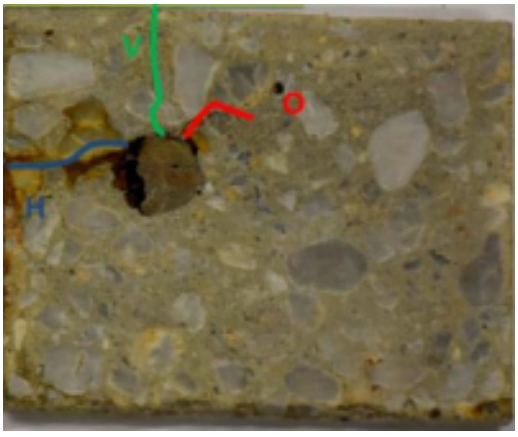

Figure 34: Experimental crack orientations from Loukil's thesis (Slice: P11-d100-35j-T11-D). Horizontal (H), vertical (V), and oblique (O) cracks emerge from the corner reinforcement.

To replicate this behavior, a simulation was performed with the steel rebar positioning at the corner of the square domain corresponding to a concrete cover of 20 mm and a steel radius of 10 mm. The resulting damage pattern is shown in Figure 35.

This result shows good qualitative agreement with the experimental crack orientations observed in the P11-d100-35j-T11-D slice from Loukil's thesis [37], confirming that the model can accurately reproduce the behavior of corner reinforcement under corrosion-induced expansion. In particular, two prominent cracks are observed in the simulation: one horizontal (H) and one vertical (V), both propagating from the reinforcement toward the nearest edges of the concrete domain. The difference in the formation of the oblique (O) crack arise from the modeling assumptions. In particular, the uniform eigenstrain expansion leads to symmetric horizontal and vertical cracks, while the oblique cracks observed experimentally are absent. This discrepancy is due to the uniform corrosion and homogeneous concrete assumptions, which will be refined in later

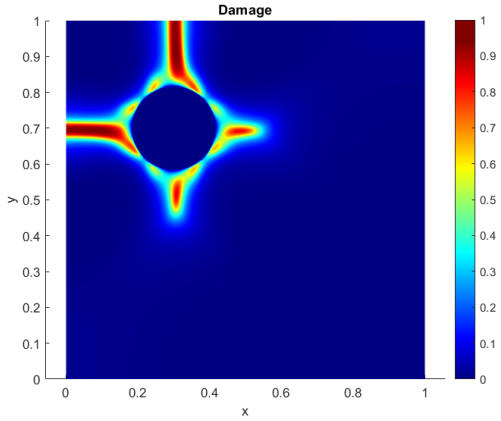

Figure 35: Simulated damage field with corner rebar positioning. Cracks appear in horizontal, vertical, and oblique orientations.

chapters.

Compared to the case of centered reinforcement—where corrosion-induced expansion is applied symmetrically around the rebar and four major crack orientations typically emerge (upward, downward, leftward, and rightward)—the corner positioning leads to asymmetrical crack propagation. This difference arises because, in the corner configuration, the reinforcement is positioned closer to two concrete boundaries, making these boundaries the preferred paths for crack propagation. As a result, cracks tend to initiate and grow in the directions of shortest cover distance, i.e., toward the top and left edges in this case. This behavior demonstrates the critical role that rebar positioning plays in influencing the directionality and severity of corrosion-induced cracking, and it validates the ability of the phase-field model to capture such effects accurately.

Effect of rebar positioning at fixed cover thickness:
To isolate the influence of positioning, two cases were considered with the same cover thickness of 20 mm but different rebar locations (Figures 36 and 37). Despite the identical cover, the resulting damage patterns differ: in the corner configuration, both vertical and horizontal cracks propagate toward the nearest boundaries, while in the side configuration, cracks develop preferentially along the closest edge. This shows that, even with fixed cover, the rebar position has a strong effect on the crack path.

Effect of concrete cover thickness:
Concrete cover thickness plays a major role in both the corrosion initiation time and the subsequent crack propagation due to rust expansion. A larger cover delays chloride ion penetration and provides better confinement to resist internal pressures. This section investigates three cases with increasing cover thicknesses: 20 mm, 30 mm and 40 mm.

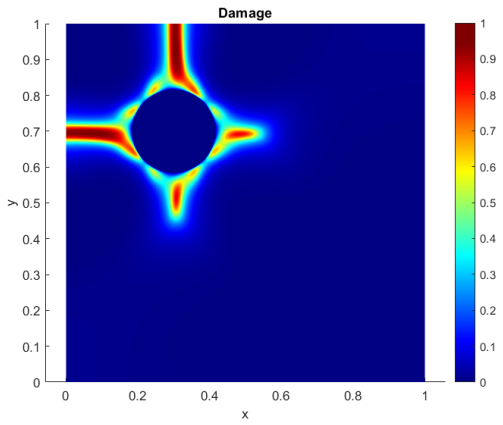

Figure 36: Damage pattern for corner rebar, cover = 20 mm.

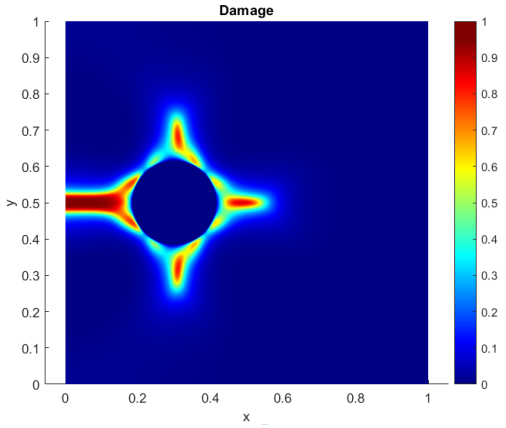

Figure 37: Damage pattern for side rebar, cover = 20 mm.

In this series of simulations, the domain size is kept fixed ($L = H = 1$), and the cover thickness is varied by shifting the position of the rebar while keeping its radius constant. All are loaded under the same expansion parameter effect as before. In this way, the main parameter under investigation is the distance between the reinforcement and the concrete boundary (the cover). The corresponding results are shown in Figure 38. As the cover increases from 20 mm to 40 mm, the cracks remain more confined around the rebar and do not reach the boundaries, whereas for smaller cover values cracks propagate earlier to the edges. This confirms the governing role of cover thickness in resisting corrosion-induced stresses.

It should be noted that, with this modeling choice, varying the cover thickness necessarily modifies the absolute position of the rebar. An alternative approach would be to fix the rebar position and vary the cover thickness by enlarging the domain. However, this would also change the ratio of the rebar diameter to the domain size, introducing an additional parameter that influences the cracking behavior. In practice, such parameters cannot always be separated cleanly, since the geometry of reinforced concrete elements inherently couples rebar position, cover thickness, and structural dimensions.

Altogether, these effects highlight the importance of both rebar placement and concrete cover as coupled design parameters. A thicker cover provides a mechanical buffer that distributes tensile stresses over a broader region, while deeper embedment postpones the development of critical tensile stress states at the reinforcement–concrete interface. These findings are consistent with experimental and micromechanical investigations in the literature. Jang and Oh [161] observed that higher concrete cover increases the pressure threshold for crack initiation. Moreover, Šavija and Schlangen [162] reported that thicker covers lead to delayed cracking and reduced crack widths due to the enhanced confinement provided by the surrounding concrete. Collectively, the re-

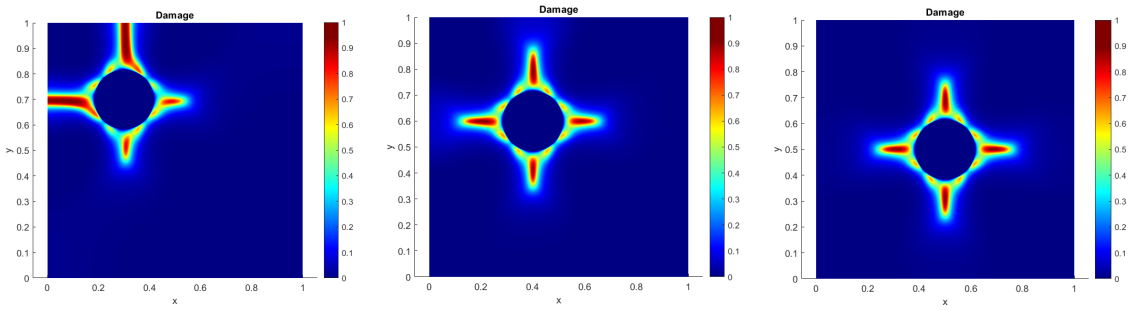

(a) Cover = 20 mm **(b)** Cover = 30 mm **(c)** Cover = 40 mm

Figure 38: Effect of concrete cover thickness on damage development.

sults confirm that optimizing both the cover thickness and the positioning of reinforcement is essential for extending the service life of RC structures exposed to corrosive environments.

3.4 Conclusion

In this chapter, the phase-field method was applied to corrosion-induced cracking in reinforced concrete through an eigenstrain-based expansion model. First, we have implemented an in-house phase field code to state-of-the art numerical tests for validation. Then, we have proposed an expansion model for the corrosion layer, which coupled with the phase field problem allows modelling the nucleation of cracks due to the corrosion expansion. In this chapter, we have restricted to academic tests to show the feasibility of the approach. Several numerical investigations have been performed to test the sensitivity of the crack paths to numerical and geometrical parameters. Comparisons between Amor's volumetric split and Miehe's spectral split highlighted that while Amor favors nearly unidirectional cracks, Miehe's formulation better captures branching and multiple crack orientations, making it more appropriate for corrosion problems, and has then been adopted in the following. Mesh sensitivity tests confirmed convergence of results with respect to the mesh size, which is an advantage of the phase field method due to its natural regularization properties. Non-uniform expansion modes (unidirectional and elliptical) have been proposed to model the effects of proximity of the reinforcement to external boundaries and diffusion of corrosive species, reflecting the dependent trait of the damage patterns on the location and distribution of corrosion products around the rebar. Geometrical effects, including rebar positioning and concrete cover thickness, were shown to strongly affect crack paths: small covers led to early cracks reaching the boundary, while thicker covers confined damage near the reinforcement. Finally, these results demonstrate that the phase field method is a technique appropriate to consider

corrosion-induced cracking.

Chapter 4
Modelling of corrosion-induced cracking in experimental-image based heterogeneous concrete models

4.1 Introduction

Concrete is a highly heterogeneous material whose mechanical response depends on numerous factors, including its formulation (binder type, the water-to-cement ratio and binder content), aggregate distribution, hydration gradients, porosity, and the presence of microstructural defects. This inherent variability leads to complex and non-uniform mechanical behavior that cannot be fully captured by homogenized macroscopic models. This complexity is particularly critical when simulating deterioration mechanisms driven by corrosion-induced expansion, where cracking is highly sensitive to local material differences and stress concentrations around the reinforcement.

In this chapter, realistic models of concrete structures obtained from experimental imaging techniques are used to simulate corrosion-induced cracking. In contrast with synthetic models of heterogeneous concrete or cementitious materials where idealized inclusions with ellipsoidal shapes are considered, experimental images allow describing the complex shapes of aggregates and pores. First, available segmented images of concrete microstructures are used, available from experimental micro tomography images. Second, optical images obtained at EMGCU lab. are considered, showing cracks due to corrosion. In each case, we demonstrate the use of the phase field method to fracture in such realistic models, and apply it to corrosion-induced fracture. For optical images, we present a methodology using AI-based segmentation to efficiently extract the different phases in the structure.

4.2 Crack simulations on segmented images of 2D concrete microstructures obtained from micro CT-scans

First, realistic microstructures of concrete, obtained from 3D micro CT-scans experimental images are used. A segmentation procedure was conducted (not performed in this thesis) to extract the matrix, aggregates and pores. The data consists into a 500×500×600

file of indices associated to phases. For numerical simulations, 2D 500×600 slices are extracted. For each one, a regular mesh of triangular elements is constructed and the local properties are mapped on the elements. Examples of $9 \times$ 2D models extracted from the 3D dataset are shown in Fig. 39.

4.2.1 Traction tests

To investigate the effects of heterogeneities on the crack paths and force-displacement curves, traction tests are first conducted on several 2D models without reinforcement and without corrosion-induced cracks. Here, the cracks are solely created by the external traction. These tests are introduced to investigate the convergence of numerical crack simulations with respect to the domain size and number of samples on 9 2D models, corresponding to slices in the full 3D model, are used for the analysis (see Fig. 39).

Boundary conditions are depicted in Fig. 40. A vertical traction is prescribed on the top end, while the displacements are fully constrained on the bottom end.

Once the original tomography-based data matrices are meshed, the material properties are assigned to each element on the basis of its phase index.

4.2.1.1 Loading Parameters and Simulation Setup

In the simulations presented below, the mechanical load is applied by imposing a vertical displacement denoted by U_Y, which represents the total prescribed displacement (in millimeters) on the upper edge of the concrete section. This displacement serves as the driving force for crack initiation and propagation under tensile loading conditions. The loading is applied incrementally over a series of steps, with $N = 100$ representing the total number of load increments used in each simulation. For each traction testing case, the maximum imposed displacement is set to $U_Y = 0.5$ mm, applied gradually over the 100 increments. The heterogeneous slices used in the following simulations are composed of three distinct phases. In Fig. 39, the cement matrix is depicted in light green. The aggregates are depicted in dark blue while voids are depicted in yellow. The corresponding material properties are defined in Table 3. Note that the pores are modeled by a material with very low mechanical properties to maintain a regular mesh of elements throughout the whole domain.

The phase field method to fracture, as presented in Chapter 3, is applied. Results of damage patterns are depicted in Fig. 41 for the 9 corresponding samples depicted in Fig. 39. The results highlight the strong effects of heterogeneity on damage development and the stochastic nature of the crack path in realistic models of cementitious materials.

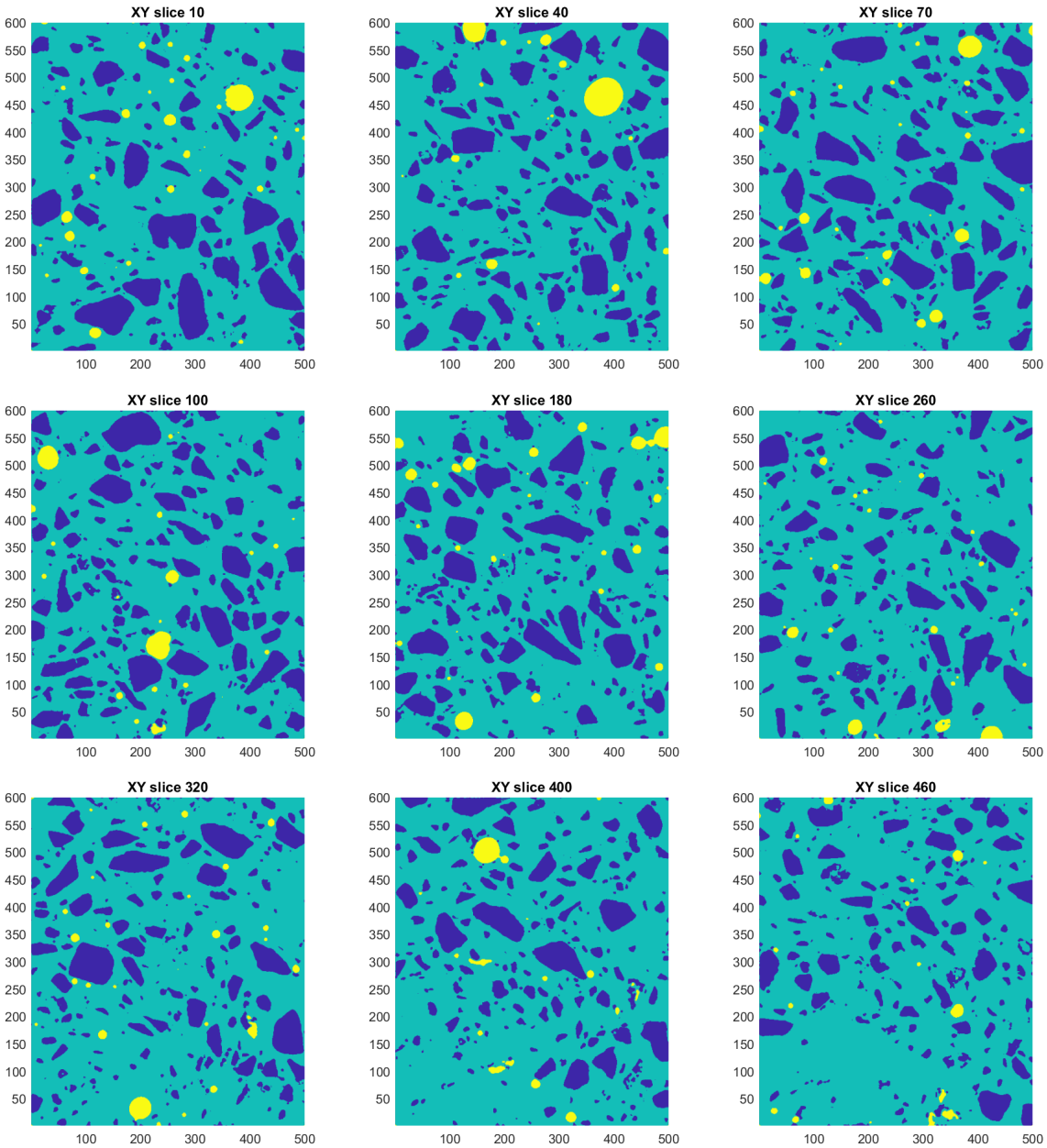

Figure 39: 2D tomography-image-based concrete models extracted from a full 3D model.

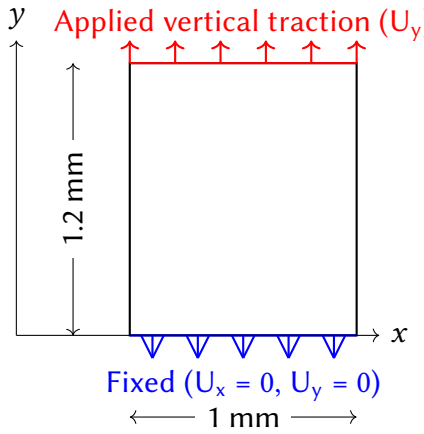

Figure 40: Boundary conditions: vertical traction applied at the top boundary, fully fixed at the bottom boundary (both U_x and U_y).

Material Phase	Young's Modulus, E (GPa)	Fracture Energy, g_c (kN/mm)
Cement matrix	34.5	$2.5 * 10^{-4}$
Aggregates (inclusions)	10^4	10^4
Voids	10^{-6}	10^4

Table 3: Mechanical properties assigned to the three phases in the heterogeneous concrete domain.

From Fig. 41, we can note qualitatively that the simulations reflect some experimentally observed features, like roughly perpendicular crack with respect to the loading direction, barrier effects of the aggregates on the crack paths, and nucleation of cracks within the domain, due to stress concentrations around voids and aggregates created by material properties heterogeneities.

These results confirm that heterogeneities strongly affect crack paths when the size of inclusions or voids is large with respect to the sample size, inducing a stochastic distribution of crack paths. In the following, we also investigate the effects of these heterogeneities on the mechanical response of the material.

4.2.1.2 Force-Displacement curves

To quantify the mechanical response under uniaxial tension, force-displacement curves are plotted for each of the nine tomography-based slices. These curves help evaluating the overall stiffness and peak load capacity of each slice, which are affected by the internal distribution of aggregates and voids.

The force–displacement curves for the nine tomography-based slices in Fig. 42 show the variability of the response, as a direct consequence of the local material distribution.

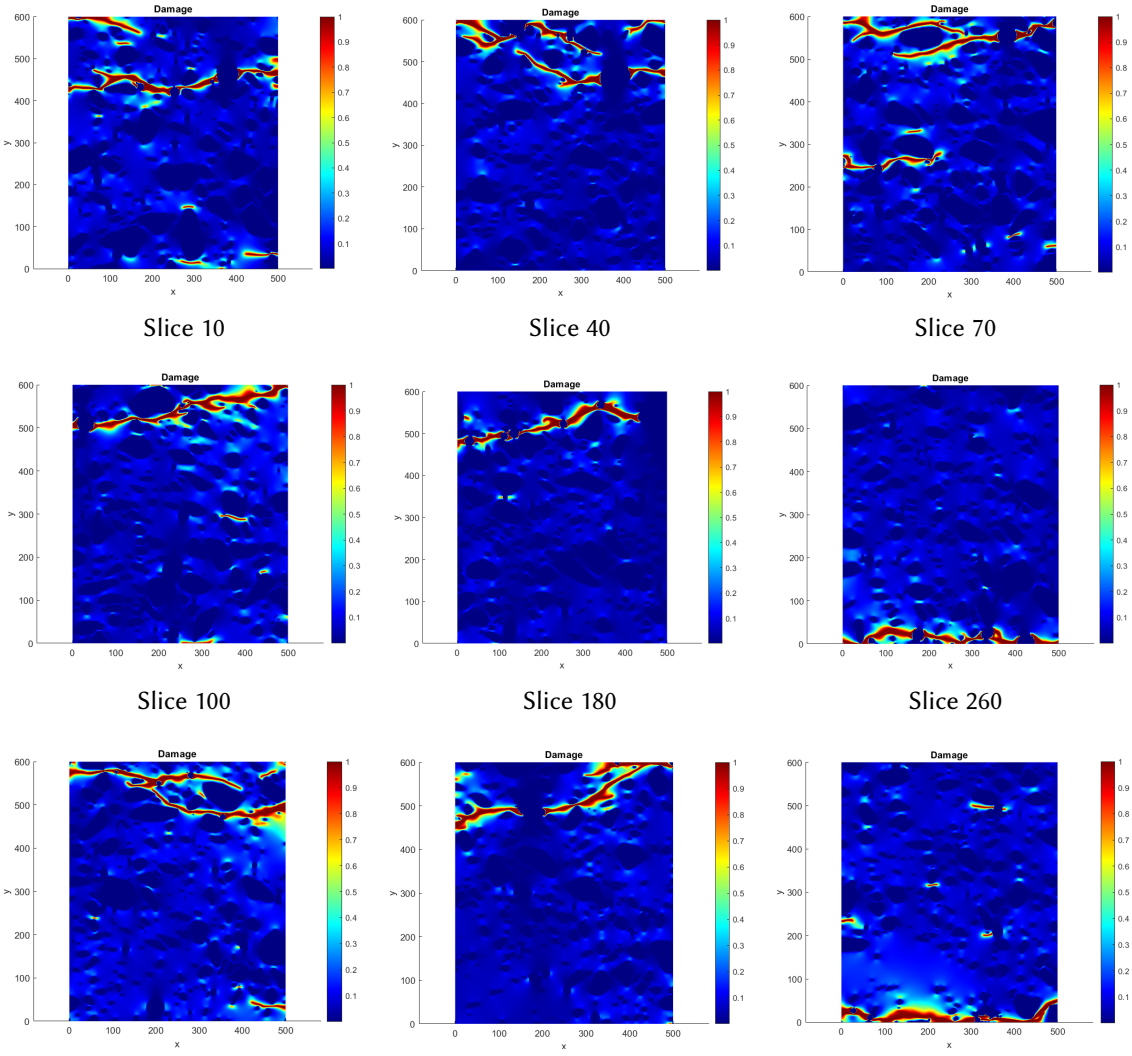

Slice 10 Slice 40 Slice 70

Slice 100 Slice 180 Slice 260

Slice 320 Slice 400 Slice 460

Figure 41: Damage patterns in the 2D image-based models of concrete under tension, corresponding to the geometries shown in Fig. 39.

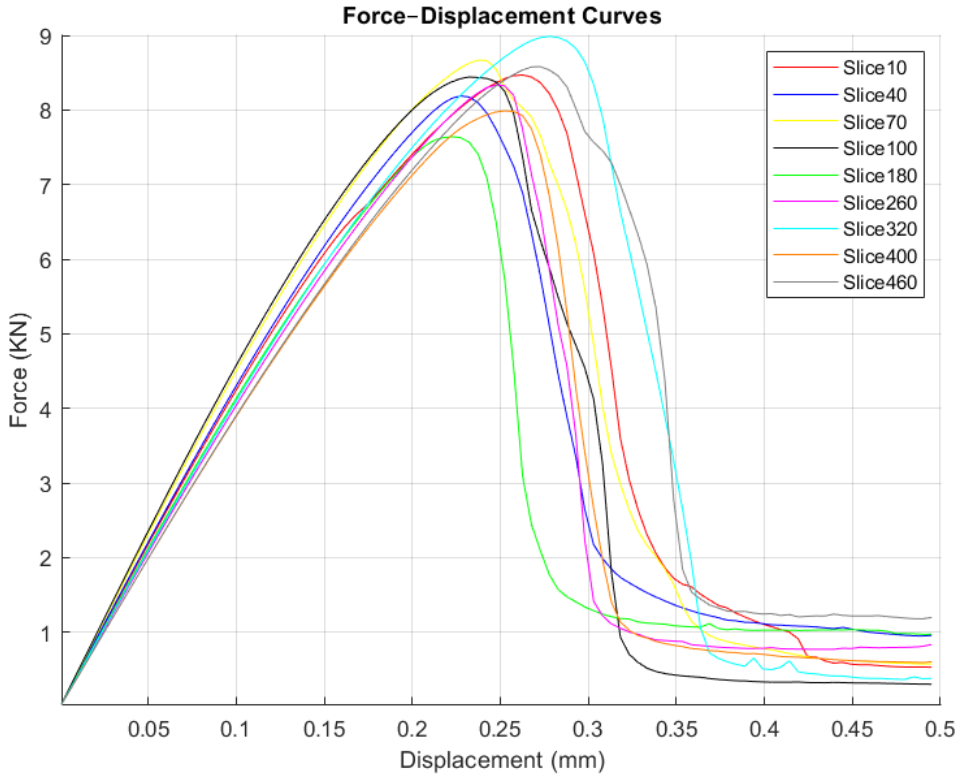

Figure 42: Force-displacement curves for the 9 samples under traction.

To evaluate the effects of the domain size on the fracture response of the sample, four meshes with increasing number of elements, corresponding to pixels in the original model, are cropped in the 2D sample labeled as number 100 in the database. The sizes of the domain contain 100×200, 200×300, 300×400 and 400×500 pixels, respectively. In each case, the dimensions of heterogeneities is unchanged, only their number vary with respect to the increasing size of the domain. Identical loading conditions are applied for all cases (imposed vertical displacement $U = 0.5$ mm, over 100 loading increments) and damage patterns are observed. See Figures 43, 44 and 45.

Force-displacement curves shown in Fig. 46 show a qualitative convergence of the results, indicating that a sufficiently large domain can provide an average estimate for the mechanical response of the material, despite of the heterogeneities.

These results show that including heterogeneities in the model induce stochastic effects, depending on the domain size and on the number of included heterogeneities.

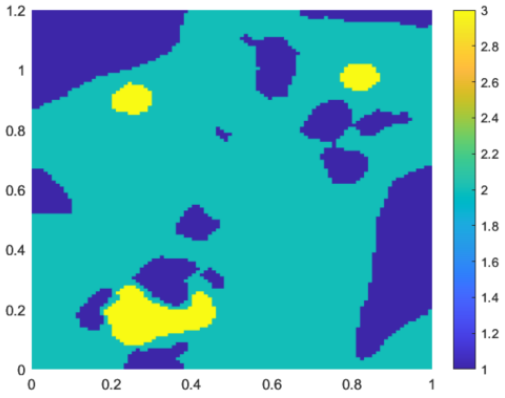

Slice 100: (100 x 200) cropped section

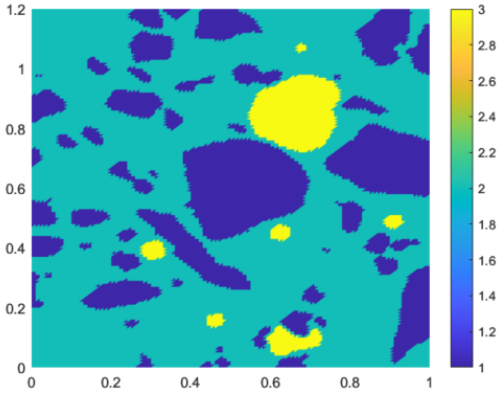

Slice 100: (200 x 300) cropped section

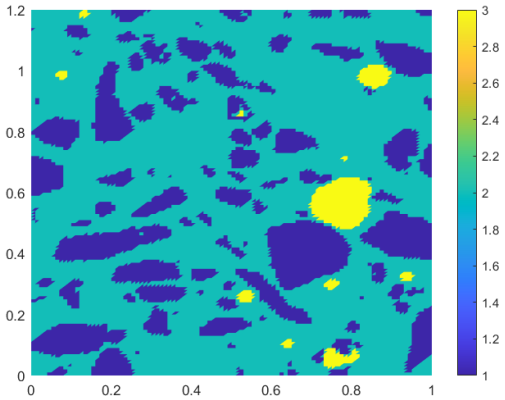

Slice 100: (300 x 400) cropped section

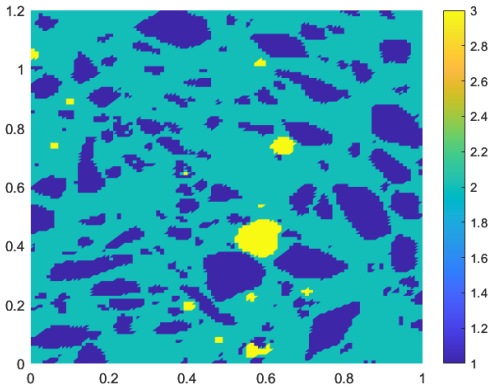

Slice 100: (400 x 500) cropped section

Figure 43: Models defined by increasing size in the original image.

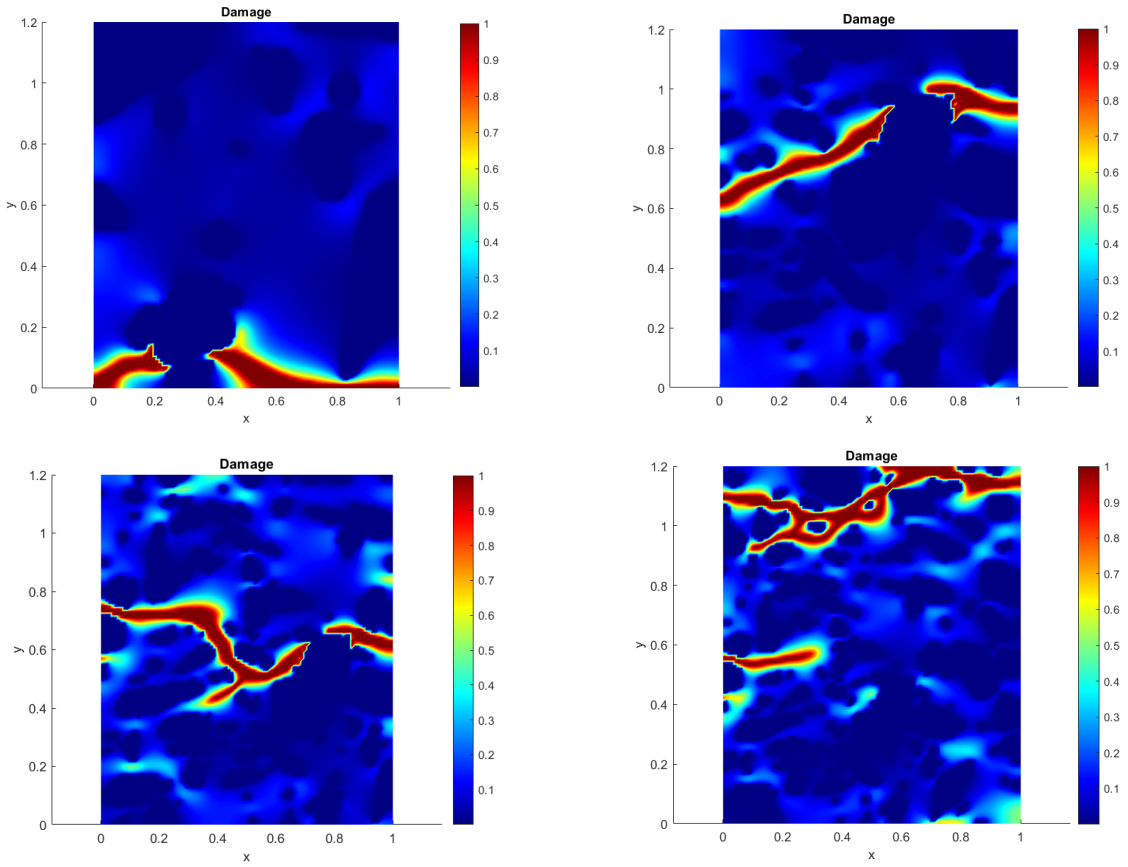

Figure 44: Damage patterns in traction for the cropped subdomains of slice 100

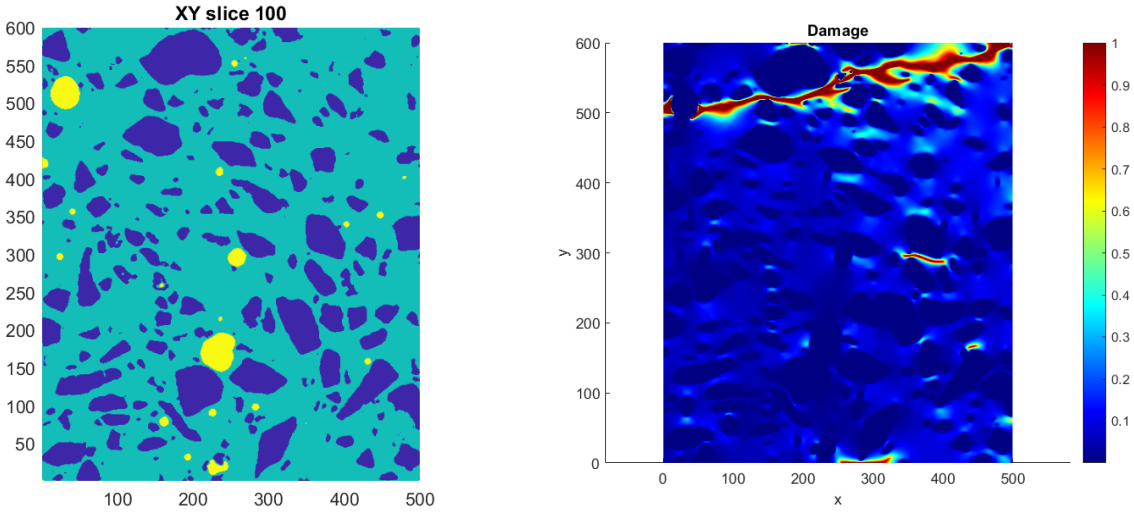

Figure 45: Damage patterns in traction for the full slice 100

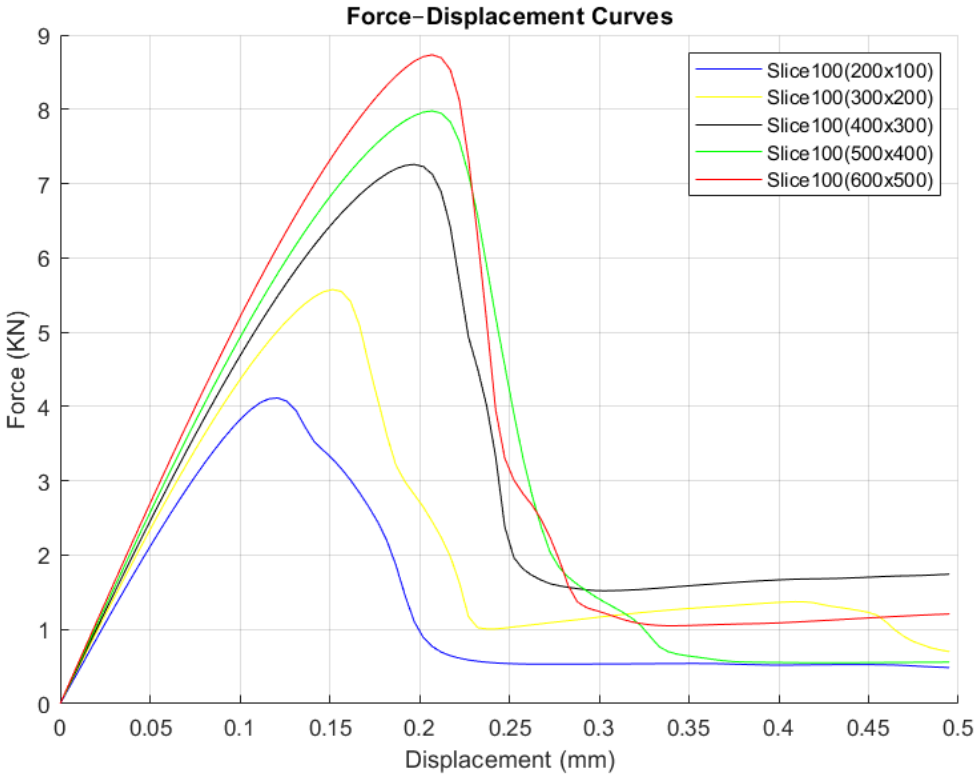

Figure 46: Force-displacement curves for all cropped and full domains of slice 100

4.2.2 Corrosion-induced fracture in image-based models

To simulate corrosion-cracking induced by expansion, a steel reinforcement bar is artificially incorporated in the realistic heterogeneous 2D models. For this purpose, a new material phase, denoted by index 4, is associated to a circular region centered in the domain. The steel phase is generated by marking all points within a radius of 50 matrix units from the center of the matrix. This circular region simulates a reinforcement embedded in concrete. Surrounding the steel region, a corrosion layer is defined by assigning another material phase, denoted by index 5, to a concentric circular ring of thickness $h_0 = 10$ pixels. This creates a ring of corrosion products that encircles the steel bar, representing the region where expansion occurs due to rust formation.

The remaining matrix retains its heterogeneous nature, with phase values corresponding to the original concrete constituents: cement paste (light blue), aggregates (dark blue), and voids (light green). By integrating this steel-corrosion system into the heterogeneous matrix, the model enables the study of crack initiation and propagation due to corrosion-induced expansion within a semi-realistic concrete environment using the model described in section 3.3.

Note that this model is not a realistic one, in view of the steel bar diameter with re-

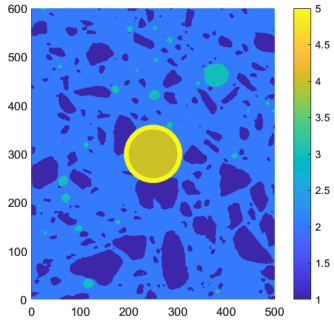

Slice 10

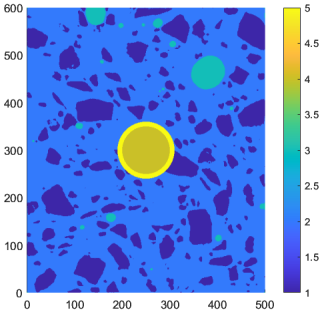

Slice 40

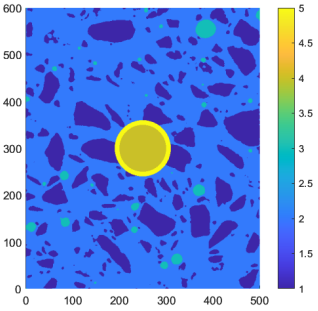

Slice 70

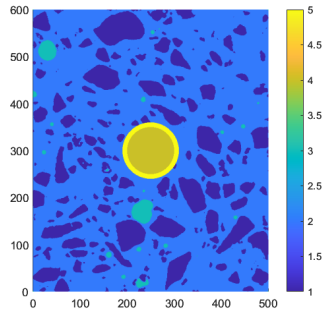

Slice 100

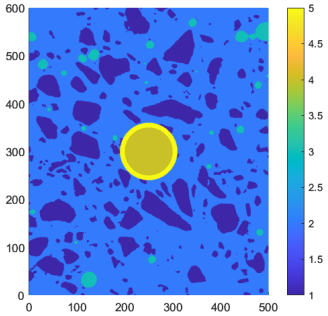

Slice 180

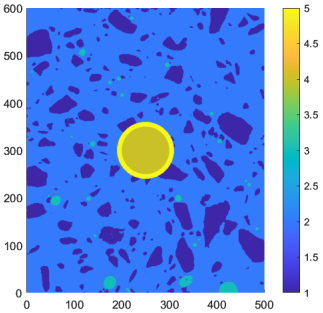

Slice 260

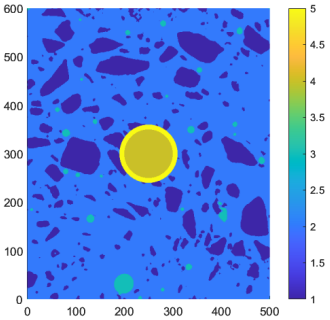

Slice 320

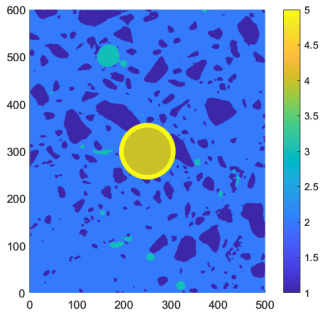

Slice 400

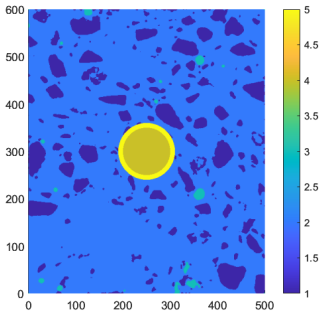

Slice 460

Figure 47: Tomography-based heterogeneous sample meshes with embedded corroded rebar.

spect to the inclusions size, which are in the original images associated with a material closer to a cement paste. However, this preliminary example is used to illustrate the applicability of the phase field fracture model combined with corrosion expansion in a complex geometrical configuration, possibly arising from an experimentally characterized image.

The model described in section 3.3 is used. The expansion parameter h of the corrosion layer reaches a maximum value $h = 10$ (no units)), with 100 intermediate increments.

In Fig. 47, 9 configurations are tested. Each one uses a subdomain of 2D layers in the 3D database describing the micro CT tomography, where a steel bar and a corrosion layer has been added.

Results of cracks induced by the expansion of the corrosion layer after 100 time steps (here taken as quasi-static expansion increments) are shown in Fig. 48. We can note a stochastic distribution of cracks, but in all cases, damage initiates at the steel–corrosion interface, where expansion stresses are concentrated. The cracks propagate radially outward, consistent with the globally radial loading nature of the expansion.

We have shown in this section the applicability of the phase field method combined with corrosion-expansion in realistic heterogeneous structures of cementitious materials, obtained e.g. from segmented experimental images.

4.3 Corrosion cracking in optical-based image models with AI-based segmentation tools

Although the previous section was dedicated to applicability of phase field fracture modeling of corrosion-cracking simulation in general experimental image-based models of heterogeneous cementitious materials, the present section focuses on the use of optical images, which may easier to obtain in experimental studies as compared to tomography images. More specifically, the used images were obtained in EMGCU lab in Olfa Loukil's thesis [37]. The images were obtained using classical photos of concrete samples containing reinforcement steel bars. The samples were subjected to electric current to accelerate internal corrosion. After a given time, the samples were cut and internal cracks have been observed (see e.g. Fig. 49). These images will be used in the next chapter to make qualitative and quantitative validations of the numerical simulations.

One difficulty with optical images lies in the segmentation task. Although the images are in color, they often exhibit inconsistencies such as color diffraction, and poorly

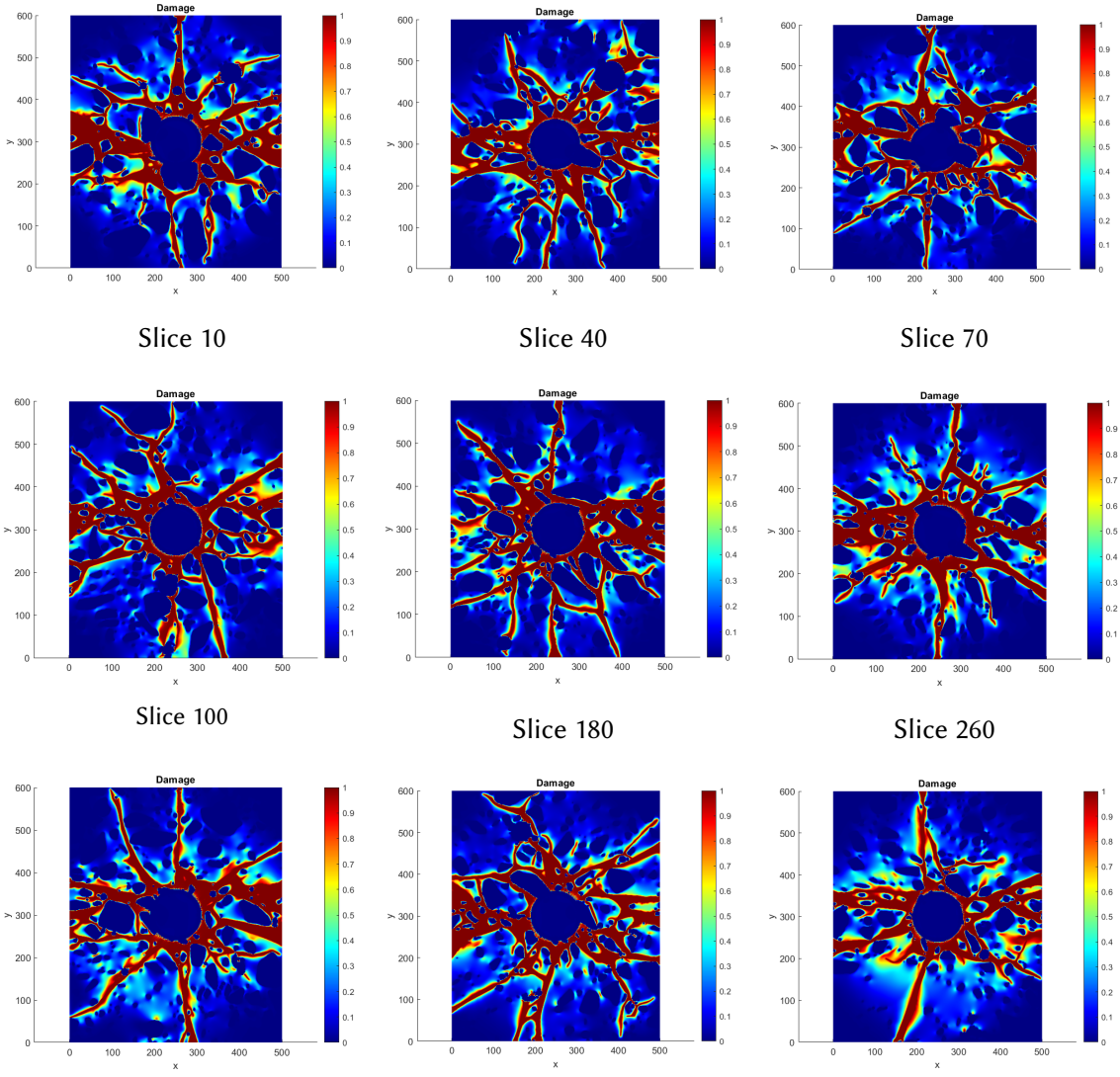

Figure 48: Damage patterns due to corrosion-induced expansion in nine heterogeneous concrete slices.

defined phase boundaries, which complicate accurate classification of material phases. Since the objective is to cluster pixel regions based on color to assign corresponding material indices (e.g., cement, aggregate, voids, steel), such disturbances interfere with reliable matrix extraction for meshing and simulation. To overcome these limitations, a dedicated preprocessing pipeline is using an AI-based software called Dragonfly ORS is presented below.

4.3.1 Dragonfly ORS Imaging Software

Dragonfly is a versatile software platform widely used for the advanced visualization, segmentation, and quantitative analysis of multidimensional datasets, particularly in materials science and medical imaging. In this study, Dragonfly was employed as a critical pre-processing tool to treat experimental tomography images of concrete specimens. Its robust segmentation capabilities enable the transformation of raw, complex image data into well-structured datasets suitable for simulation workflows. Dragonfly offers segmentation tools based on AI to train/apply models for 2D/2.5D/3D data. It includes deep-learning architectures (U-Net family, DeepLabV3+, PSPNet, etc.), image enhancement models for de-noising and super-resolution. It also supports classical ML (Random Forest, Gradient Boosting, etc.), sparse labeling, transfer learning, and import/export of pre-trained models.

The experimental tomography images used here are derived from reinforced concrete slices, such as the example shown in Figure 49. These raw images often exhibit color disturbances, inconsistent grayscale values, and blurred boundaries between material phases, which severely hinder direct data extraction for simulation purposes. Additionally, the overlapping hues and image noise make it difficult to distinguish between the concrete matrix, aggregates, voids, and steel rebar.

To overcome these issues, high-resolution photos of the cracked specimens were taken during this thesis and imported into Dragonfly for treatment. Using the *Segmentation Wizard*, a specialized module within Dragonfly, a machine learning-based pipeline was established to segment the images into discrete, well-defined regions. This tool utilizes techniques such as thresholding, region growing, and intensity-based classification to differentiate and label each material phase clearly. As a result, the software produced segmented images where cement, aggregates, voids, and steel were visually and computationally distinguishable.

This pre-processing step proved essential in enabling the successful application of clustering algorithms in later stages. By providing clean and consistent data matrices, Dragonfly ensures that the extracted pixel values correspond accurately to the underly-

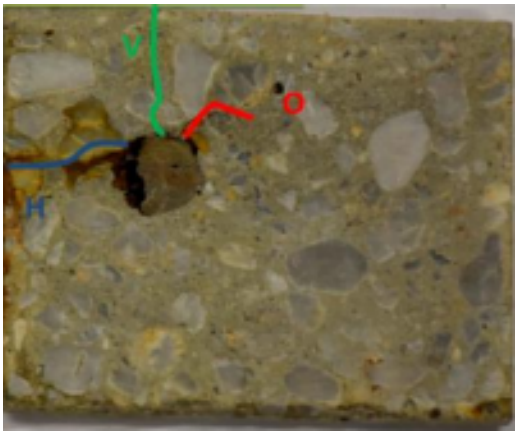

Figure 49: Original experimental slice: P11-d100-35j-T11-D [Concrete section with color disturbances and visual noise]

ing physical structure of the concrete specimen. This segmentation not only improves the fidelity of the simulation inputs but also standardizes the treatment across multiple images, thereby increasing the robustness and reproducibility of the simulation framework.

The following figures illustrate the evolution of this image-processing workflow. Figure 49 shows the raw experimental image used for simulation. This slice corresponds to a specimen denoted by P11-d100-35j-T11-D, obtained under conditions which as current density of 100 $\mu A/cm^2$ and a total applied load of 3500 $\mu A \cdot j/cm^2$. All treated slices in this study have dimensions of 125 mm × 100 mm. In figure 50(a), a failed attempt at direct segmentation is shown, highlighting the difficulty of classifying phases without image treatment. In contrast, figure 50(b) illustrates the improved output following segmentation, where distinct material phases are clearly identified and color-coded. In the following, we present a new step in the processing by using k-means clustering.

4.3.2 K-means Clustering for Phase Classification

Following segmentation in Dragonfly, the next step involves transforming the color-coded images into numerical data matrices suitable for simulation. This was achieved using the *k-means clustering* algorithm in MATLAB, which classifies pixels into $k = 4$ discrete groups corresponding to the four material phases: cement, aggregates, voids, and steel.

The clustering process is based on pixel color values, now made distinct by the prior segmentation step. As each phase is represented by a clearly defined and uniform color, the clustering algorithm can accurately group all pixels belonging to a specific material. The result is a numerical matrix in which each index represents a unique phase,

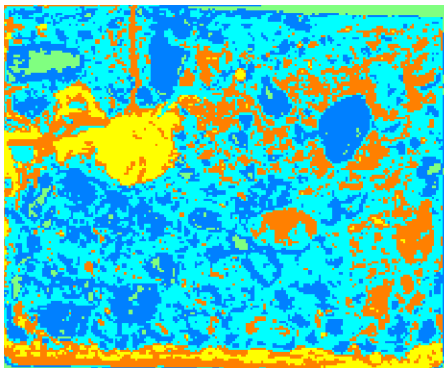

(a) Failed direct clustering (no segmentation)

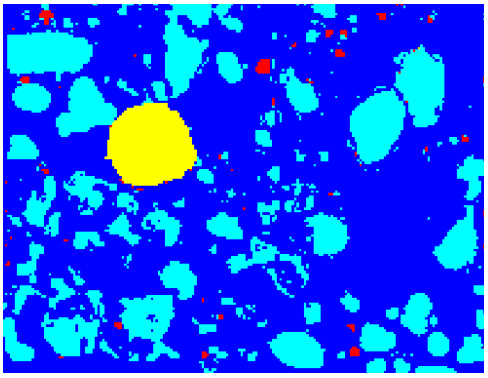

(b) Successfully segmented image using machine learning-based treatment

Figure 50: Comparison of image-based data extraction before and after pre-processing.

effectively converting the segmented image into simulation-ready data.

This matrix is then used to generate a regular mesh for finite element analysis, with each element inheriting the material properties corresponding to its matrix value (e.g., Young's modulus, fracture energy). The final data extraction process thus bridges the gap between experimental imaging and numerical modeling, offering a high-fidelity representation of the material microstructure.

The combination of Dragonfly's image preprocessing capabilities and clustering algorithm provides a robust and automated pipeline to convert real tomography slices into finite element inputs.

4.3.3 Mesh Construction

The simulation process continues with the construction of a computational mesh based on experimental tomography data. From the segmented image, a data matrix is extracted, where each pixel is assigned an index corresponding to one of the four material types. As in the previous section, this matrix serves as the input for mesh generation. A regular triangular mesh is then constructed by discretizing the image into square cells, where each pixel corresponds to a square that is subdivided into two triangular elements. These triangular elements inherit the material phase from the associated pixel, ensuring the mesh reflects the spatial distribution of materials captured in the segmented image. Additionally, material-specific element sets are defined, ensuring that each triangle in the mesh inherits the appropriate material property based on the underlying data.

The phase field to fracture as presented in section 3.2 is first applied to a traction test on the obtained mesh. A uniaxial tensile (traction) loading is applied to the specimen

slice to observe its deformation response and verify the correct mechanical behavior of the system. The boundary conditions are the same as described in Fig. 40. Results of crack paths corresponding to the image in Fig. 51 are presented for illustration.

Subsequently, a corrosion expansion scenario is simulated by introducing a corrosion layer (rust products) around the steel reinforcement. This is achieved by identifying and tagging the mesh elements that lie at the interface between steel and surrounding materials. As compared to the case presented in the previous section where a bar with idealized circular cross-section was introduced, here the cross-section of the reinforcement bar is not circular, and is directly defined by the image.

Then, the phase field fracture method combined with corrosion expansion is applied to the obtained mesh. The expansion parameter h is increased incrementally in the corrosion layer elements to induce fracture.

Starting with the slice presented in Fig. 51 (a), and denoted by *P11-d100-35j-T11-D*, the data is extracted and the mesh is constructed as follows. The generated mesh consists of 241,984 triangular elements. The physical size of each element is set to 0.003 mm, ensuring sufficient resolution to capture fine features of the material heterogeneity. The regularization length ℓ used in the phase-field model is taken as twice the element size, i.e., $\ell = 0.006\ mm$, ensuring numerical stability and adequate damage localization in the simulations. A vertical traction displacement of $\Delta U = 8 \times 10^{-4}$ mm was applied incrementally at the top boundary over 200 incrementations, resulting in a total imposed displacement of $U_{\text{max}} = 0.16$ mm.

The material properties of the different phases are described in Table 4.

Material Phase	**Young's Modulus, E (GPa)**	**Fracture Energy, g_c (kN/mm)**
Cement (matrix)	34.5	0.2
Aggregates	10^4	10^4
Voids	10^{-6}	10^4
Steel	210	5000

Table 4: Material properties used in the simulations for each phase in the heterogeneous reinforced concrete domain.

For the fracture energy g_c of steel, a value of $g_c = 5000$ kN/mm was adopted in the simulations. This choice was not based on direct literature assumptions but rather determined through preliminary numerical testing. In these trials, various values of g_c were applied to the steel region to identify the threshold beyond which the steel would remain uncracked under the imposed loading conditions. The selected value ensures that the steel reinforcement behaves as a non-fracturing phase during the simulations.

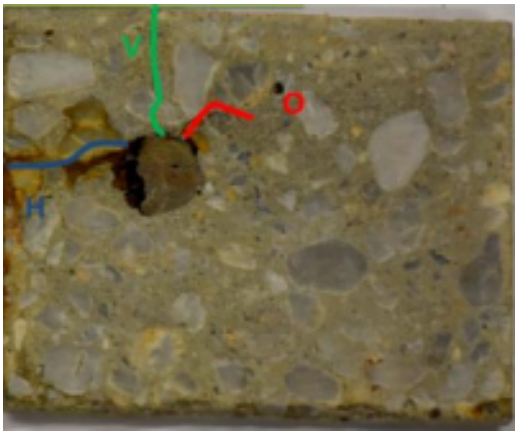

(a)

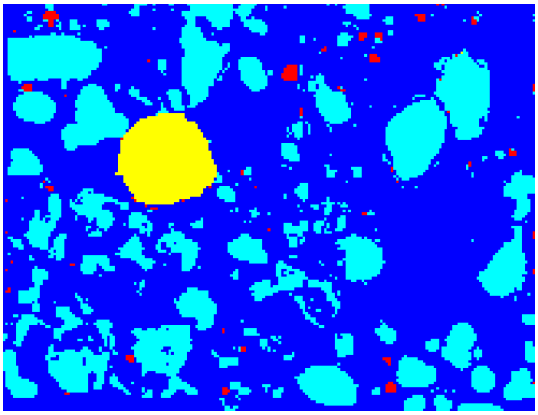

(b)

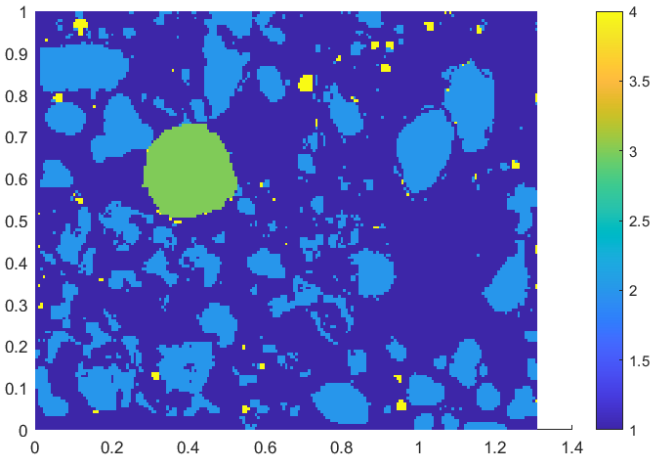

(c)

Figure 51: Experimental slice P11-d100-35j-T11-D (a), segmented image after preprocessing and classification of material phases (b), and the corresponding constructed triangular mesh (c) used for numerical simulation

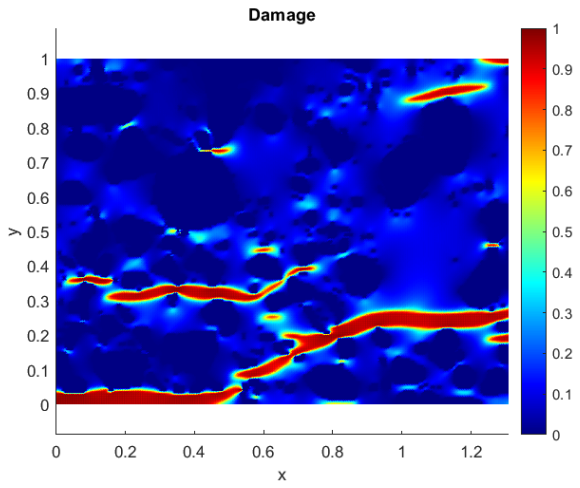

Figure 52: Damage pattern due to traction loading – Slice P11-d100-35j-T11-D

This pragmatic approach contrasts with the treatment of concrete fracture energy in the literature, where researchers such as Bažant and Becq-Giraudon [165] have emphasized the inherent variability of g_c in concrete due to its heterogeneous microstructure. Their work, which has informed other corrosion-induced cracking models using phase-field methods (e.g., Korec and Emilio [166, 167]), highlights that concrete fracture energy is not a fixed property but rather a statistical variable influenced by factors such as aggregate size, specimen dimensions, and testing procedures. In contrast, since the steel's fracture behavior was not the focus here, and no widely provided fracture energy values for steel in this context were available, a suitable g_c value was empirically calibrated to ensure numerical stability and physical consistency.

The resulting damage path are described in Fig. 52.

4.3.4 Corrosion-Induced Cracking Simulations

4.3.4.1 Uniform Expansion

In this section, corrosion-based fracture is applied to the present obtained segmented model and compared to experimental crack patterns as a preliminary qualitative validation of the approach. A more complete analysis of this approeach will be conducted in the next chapter. The main advantage of using the same images used for the experimental test than in the simulation allows to remove the stochastic influence of the microstructure. Again, image *P11-d100-35j-T11-D* was used.

Unlike previous meshes that were scaled representations of concrete slices (e.g., 1.25 mm × 1 mm), the current domain has physical dimensions of 125 mm × 100 mm, exactly matching the real experimental specimen. This ensures better realism and enables

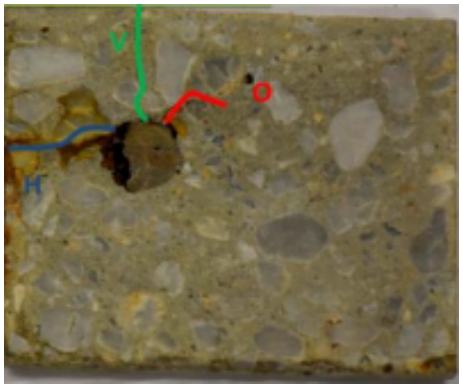

(a) Experimental photo

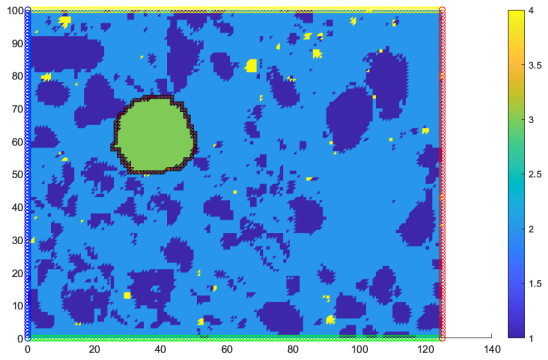

(b) Image-based mesh with new dimensions

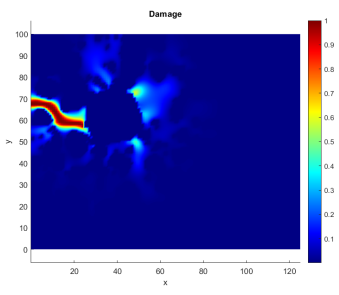

(c) Damage at $h_{max} = 0.5$

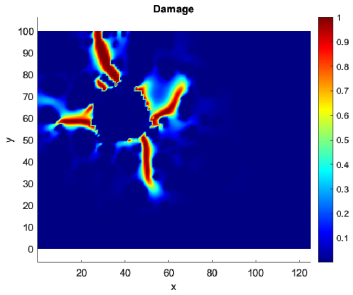

(d) Damage at $h_{max} = 1$

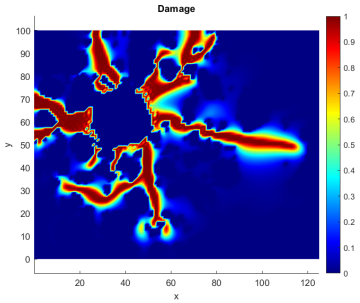

(e) Damage at $h_{max} = 5$

Figure 53: Validation of corrosion-induced cracking in slice P11-d100-35j-T11-D. Top row: experimental image and corresponding mesh. Bottom row: damage patterns from simulation for increasing expansion values.

meaningful comparisons with the actual photographed cracks.

The numerical setup is as follows. The mesh domain is 125 mm × 100 mm. The expansion parameter h is varied for different values: $h = 0.5, 1, 5$. The number of increments is 100. The regularization length is $\ell = 2$ mm and the element size is $h_e = 1$ mm. The material properties are the same than in the previous example.

Figure 53 presents the image-based mesh and the resulting damage patterns for three applied expansion values: $h_{\max} = 0.5$, 1, and 5, respectively. Each simulation was performed over 100 incrementations. It is worth noting that the applied maximum expansion here is smaller than that used in previous simulations (e.g., $h = 80$ in random sections), due to differences in mesh density and physical scaling, allowing clear crack propagation at smaller h values.

The damage fields shown in Fig. 53 illustrate the progressive development of corrosion-induced cracks for increasing values of internal expansion h. At a low expansion level ($h = 0.5$), crack initiation is observed near weak zones surrounding the steel-concrete

interface. However, damage remains localized, with limited propagation and minimal branching, indicating that the expansion pressure is not yet sufficient to cause widespread cracking.

As the expansion increases to $h = 1$, the damage becomes more pronounced, with several cracks branching out from the steel perimeter. These cracks interact with the heterogeneous matrix, where voids amplify local stress concentrations and aggregates deflect or obstruct crack paths. The result is a more tortuous and anisotropic crack network. Notably, at this level of expansion, the simulated damage pattern begins to qualitatively resemble the experimental observations, showing cracks in three principal orientations—horizontal, vertical, and oblique—similar to those captured in the experimental photograph (Fig. 53(a)).

Nevertheless, one additional crack orientation is observed in the numerical result that is not evident in the experimental specimen. This discrepancy is most likely a result of the *uniform expansion assumption* used in the current model, where the corrosion-induced pressure is applied evenly across the entire rust layer contour. Such a modeling choice leads to symmetric and isotropic crack propagation around the steel, which may not accurately represent the actual corrosion behavior in physical specimens.

When the expansion is further increased to $h = 5$, the crack network becomes significantly more complex and dense, with extensive branching and coalescence. While this stage captures the full potential of damage evolution, it does not correspond as closely with the experimental pattern in terms of crack orientation and extent.

Therefore, to refine the model's predictive capabilities and better replicate the experimental cracking behavior, a new approach is introduced in a coming section. Instead of assuming full, isotropic expansion along the rust interface, the *semi-uniform expansion* strategy selectively activates only specific angular sectors (dials) of the corrosion contour. This enables a more realistic simulation of directional corrosion growth and allows for better qualitative validation with experimental data.

Following the same modeling strategy, a second tomography-based specimen slice, P11-d100-35j-T12-D, extracted from prism P11-d100-35j, is analyzed. The numerical model replicates the corrosion-induced expansion around the steel reinforcement, and the resulting damage patterns are examined for multiple values of expansion effect h_{max}. Here, simulations were performed for three values of h_{max}: 0.5, 1, and 2, each applied incrementally over 100 steps. This variation in expansion accounts for the change in heterogeneous structure compared to the previous slice, influencing how the material accommodates stress and damage evolution.

The progression of damage fields with increasing h_{max} demonstrates a clear relation-

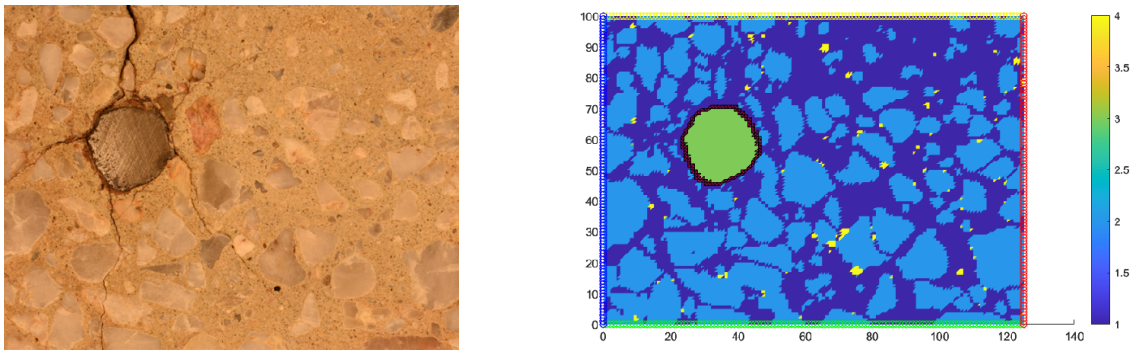

(a) Experimental photo

(b) Segmented mesh

Figure 54: Experimental slice and corresponding numerical mesh for P11-d100-35j-T12-D

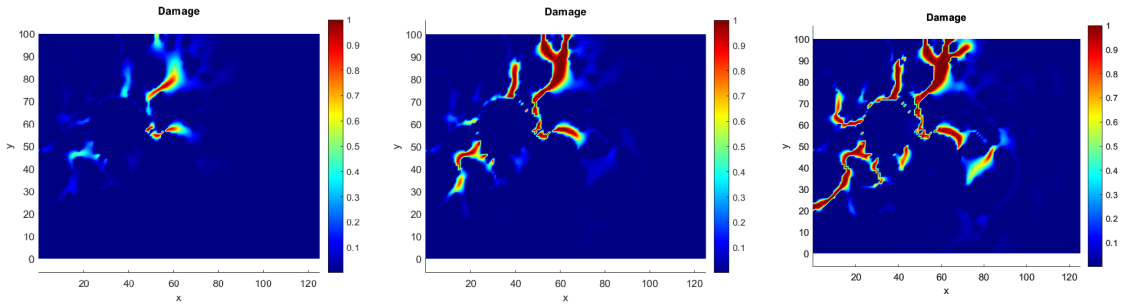

(a) Damage at $h_{max} = 0.5$

(b) Damage at $h_{max} = 1$

(c) Damage at $h_{max} = 2$

Figure 55: Damage field evolution under corrosion expansion for slice P11-d100-35j-T12-D at different h_{max} values.

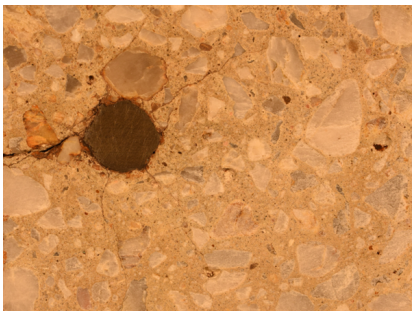

Figure 56: Experimental photo of P27-d50-70j-T15-D

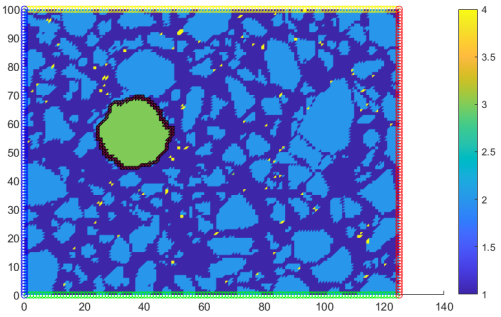

Figure 57: Segmented mesh for P27-d50-70j-T15-D

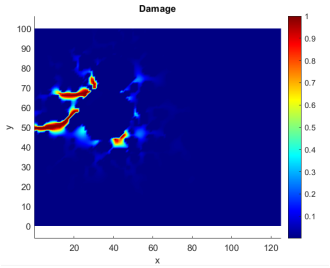

Figure 58: Damage at $h_{\max} = 0.5$

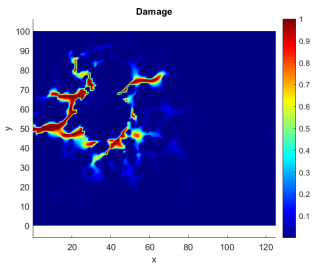

Figure 59: Damage at $h_{\max} = 1$

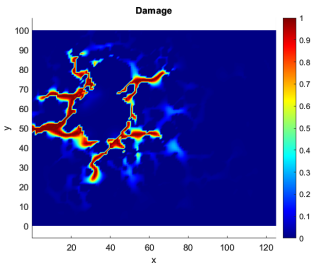

Figure 60: Damage at $h_{\max} = 1.5$

ship between expansion intensity and crack development. At $h_{max} = 0.5$, the damage remains localized near the steel boundary, showing minimal crack initiation. Increasing the expansion to $h_{max} = 1$ leads to more extended crack paths emerging from the steel and following preferred orientations guided by the heterogeneous microstructure. Finally, at $h_{max} = 2$, the cracks become significantly more developed, coalescing into a branching network with greater coverage across the specimen.

Comparing these numerical results to the experimental image (Fig. 54(a)), several crack orientations—vertical, oblique, and lateral—are qualitatively captured, particularly at higher expansion values. However, small discrepancies exist in crack directions and initiation points. These differences may be attributed to the idealized modeling of corrosion expansion as uniformly applied around the steel perimeter.

The third specimen slice under study is P27-d50-70j-T15-D, extracted from prism P027. It was subjected to a current density of 50 $\mu A/cm^2$ during 70 days equivalent to a total charge of 3500 $\mu A.j/cm^2$. Similar to the previous cases, this slice was simulated using uniform corrosion-induced expansion modeling. The expansion effects were tested for three different values of maximum expansion displacement: $h_{\max} = 0.5$, 1, and 1.5, all imposed over $N = 100$ increments.

The simulated damage fields for slice P27-d50-70j-T15-D reveal a progressive devel-

opment of cracks with increasing expansion values. At $h_{\max} = 0.5$, cracks are sparse and localized; as h increases to 1 and 1.5, the cracking patterns grow more extensive and interconnected. The case of $h_{\max} = 1.5$ demonstrates the closest qualitative agreement with the experimental photo, successfully capturing the main crack orientations radiating from the rebar. Minor discrepancies still appear, such as additional crack paths or deviations in crack orientations compared to experimental observations. These inconsistencies are partly attributed to the assumption of uniform expansion around the entire rust contour, but more critically, they can stem from the sensitivity of the tomography-based image processing and mesh generation procedure. In the image segmentation stage, small misclassifications—such as merging two adjacent aggregates into a single larger one or slightly overestimating aggregate boundaries—can alter the spatial distribution of material phases. These changes may unintentionally block an expected crack path or redirect it by modifying local mechanical resistance. As a result, a crack that experimentally propagates in one direction may numerically shift toward a different orientation. Such discrepancies underline the importance of accurate phase decomposition and the inherent influence of the real slice heterogeneity on crack initiation and propagation.

4.3.4.2 Semi-Uniform Expansion Approach

Determination of cracking expansion: inverse type approach

While the uniform expansion model provides a simplified representation of corrosion-induced cracking, it does not reflect the actual behavior observed in experimental and real-world scenarios. In practice, corrosion does not develop uniformly around the entire steel perimeter. Instead, the accumulation of corrosion products tends to be highly localized due to variations in environmental exposure, chloride penetration, material properties, and electrochemical activity. As a result, the thickness and distribution of rust layers are non-uniform, leading to localized expansion pressures at specific regions of the steel-concrete interface.

To better capture this realistic behavior, a semi-uniform expansion approach is introduced. This method selectively applies expansion to specific angular regions (referred to as dials) along the rebar perimeter rather than enforcing uniform pressure around the full contour. The objective is not to determine where cracks initiate, but rather to identify the dials where corrosion is likely to have accumulated in the experiment—those that, when expanded in simulation, reproduce crack patterns closely resembling the experimental observations. This inverse-type approach enables a more accurate replication of the damage and improves the model's physical relevance in predicting corrosion-induced cracking.

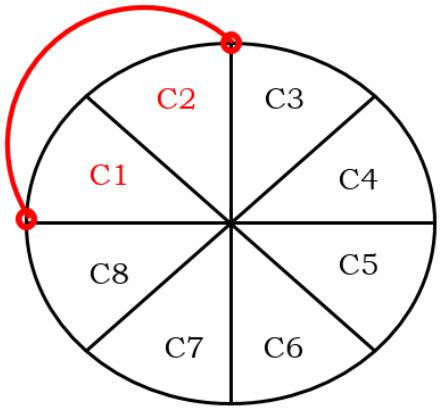

Figure 61: Division of the steel–concrete interface into eight corrosion dials (C1–C8), where each dial represents a zone between two adjacent points on the steel perimeter. This segmentation enables selective application of expansion in semi-uniform modeling [37].

The semi-uniform expansion approach follows an inverse-type strategy based on iterative testing and comparison. The key steps are as follows:

1. **Dial-Based Segmentation:** The steel-concrete interface is divided into eight equal angular sectors or "dials" (C1 to C8). Each dial corresponds to a specific region of the circular boundary of the steel rebar.

2. **Controlled Expansion Application:** Instead of expanding the entire contour, expansion (h_{max}) is applied selectively to one or more dials during each simulation. All other dials are kept inactive (i.e., no expansion), allowing localized effects to be studied in isolation.

3. **Iterative Simulation and Analysis:** A series of simulations are conducted for different dial configurations—individually and in selected combinations (e.g., C1, C2, C1+C2, etc.). The resulting crack patterns are compared against the experimental damage patterns.

4. **Dial Identification and Validation:** The simulations that best reproduce the experimental crack orientations and locations are identified. These indicate the likely zones of dominant corrosion pressure and help validate the model's predictive capability.

This methodology allows for a focused investigation of the spatial effects of corrosion-induced expansion and provides insight into how specific rebar zones influence crack morphology. Ultimately, this approach refines the link between material heterogeneity,

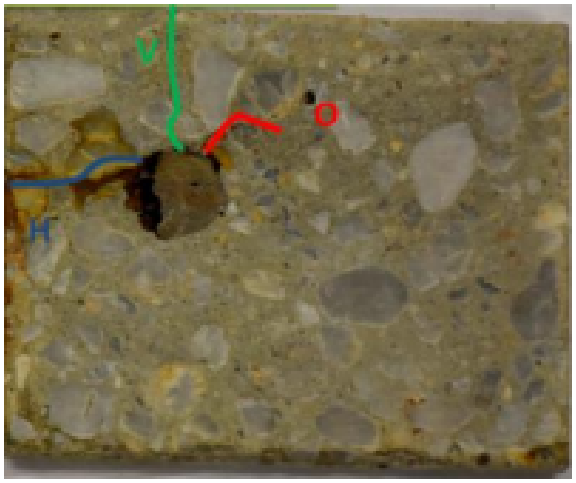

Figure 62: Slice: P11-d100-35j-T11-D (experimental crack pattern)

localized corrosion, and the resulting structural damage, leading to more accurate and physically representative simulations.

As an application of the semi-uniform expansion approach, slice P11-d100-35j-T11-D is examined to compare the effects of applying expansion over the full rust contour versus certain dials only. As shown in the experimental image (Fig. 62), the crack pattern exhibits strong directional behavior, primarily with three crack orientations—vertical, oblique, and horizontal—emerging from the steel-concrete interface.

The simulation using uniform expansion across the entire rebar perimeter ($h_{\max} = 1$) results in a more symmetric and over-distributed crack pattern (Fig. 63), with four dominant propagation directions. While some of these match the experimental directions, others appear artificially induced due to the uniformity of expansion, which does not reflect the true localized nature of corrosion.

Alternatively, when expansion is limited to only the C1–C2 dials (top-left quadrant, see Fig. 61), the resulting damage pattern (Fig. 64) aligns more closely with experimental observations. This pattern presents more focused crack initiation and directional propagation, resembling the top-vertical, right-oblique and left-horizontal cracks visible in the experimental slice. The reduction in symmetry and noise improves the physical realism of the numerical results and supports the hypothesis that corrosion is often localized rather than uniformly distributed. This application highlights the strength of the semi-uniform expansion strategy in isolating key corrosion zones that drive damage and validates its potential in inverse identification of corrosion-prone regions.

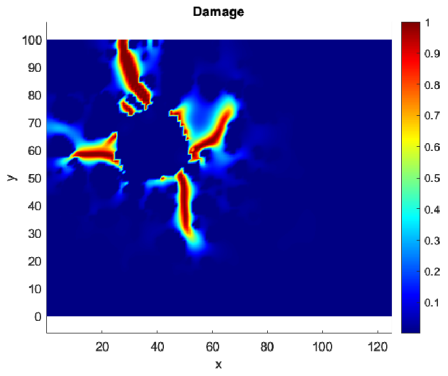

Figure 63: Expansion Creating Cracking (whole rust contour); $h_{max} = 1$

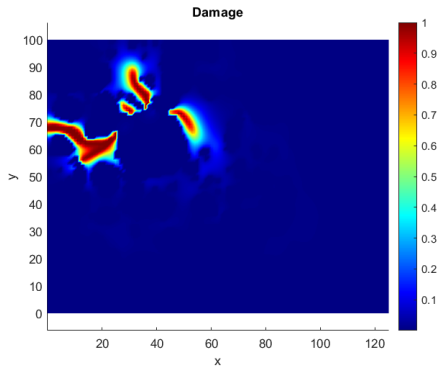

Figure 64: Expansion Creating Cracking (C1C2); $h_{max} = 1$

4.4 Conclusion

In this chapter, we have shown the applicability of corrosion-induced crack simulations based on phase field in realistic image-based models of concrete or cementitious microstructures, for the first time to our best knowledge. First, a general procedure has been developed based on available segmented experimental images, such as obtained from tomography images. The corrosion cracking model based on the expansion of a corrosion layer developed in the previous chapter has been applied in 2D segmented images, which have been converted to meshes and where idealized reinforcement bars and corrosion layers have been introduced. Convergence analyses with respect to domain sizes, and analyses on several samples have been conducted, showing the interest of such simulations in capturing the variability of realistic experiments. Second, a procedure has been developed to segment 2D optical images, which are more commonly obtained in experiments on larger samples, not adapted to tomography. A dedicated AI-based segmentation procedure combining machine learning and clustering has been developed and applied to experimental photos of corrosion-induced cracked specimens to provide direct comparisons between simulations and experiments. It was demonstrated that this procedure can qualitatively capture crack patterns. Finally, a methodology differentiating corrosion width along the reinforcement has been tested to investigate its influence on the crack propagation directions. In the next chapter, the present procedure will be applied to identify time-dependent corrosion models and quantitatively assess the corrosion-induced crack model.

Chapter 5
Modeling of the corrosion kinetics: Time-dependent corrosion-induced expansion

5.1 Introduction

In this chapter, the focus is placed on incorporating the time variable into the modeling of corrosion-induced expansion, with the objective of accounting for corrosion kinetics in a more realistic and time-dependent manner. Unlike static approaches that consider corrosion product buildup as an instantaneous or linear process, this study introduces a dynamic framework where the evolution of corrosion product thickness is directly related to time. By establishing this time-dependent relationship, it becomes possible to predict not only the growth of corrosion products but also the consequent development of crack openings in reinforced concrete (RC) specimens as corrosion progresses. This approach enables a more accurate simulation of the deterioration process in RC structures due to steel reinforcement corrosion, offering valuable insights into the timeline of damage initiation and propagation. The overall strategy consists of deriving a general evolution law that governs corrosion-induced expansion in relation to the thickness of corrosion products. To achieve this, a series of numerical simulations is carried out to compute the crack opening (CO) and to evaluate its progression over time. The resulting numerical predictions are then compared to Loukil's experimental results [37] obtained under accelerated corrosion conditions and chloride contamination, enabling the calibration and validation of the model.

5.2 Approach description of the modelling of the corrosion kinetics

In previous simulations, the expansion of corrosion products was introduced by applying an eigenstrain to the boundary elements surrounding the reinforcement. Specifically, the corrosion-induced expansion was modeled using a predefined strain tensor, $\varepsilon_h = h\mathbf{I}$, where h denotes the final expansion magnitude and $\mathbf{I}$ is the identity matrix. This strain was added directly to the elastic strain to compute the total strain in the material, resulting in $\varepsilon_{\text{total}} = \varepsilon_{\text{elastic}} + \varepsilon_h$. While effective in generating corrosion-induced stresses, this approach implicitly assumes a volumetric expansion distributed throughout the

affected elements and not directly tied to physical corrosion thickness measurements.

In the current approach, the expansion is introduced by prescribing a radial displacement U on the boundary nodes located at the concrete–steel interface as illustrated in Fig. 65, where U_{max} denotes the final imposed displacement. This displacement reflects the accumulated corrosion layer thickness and acts as a kinematic boundary condition, such that the resulting strain and stress fields develop naturally in response to the material's stiffness and boundary constraints. Notably, in this case, the total strain is purely elastic, i.e., $\varepsilon_{\text{total}} = \varepsilon_{\text{elastic}}$.

Although both methods apply the expansion effect at the interface, they differ in their mechanical interpretation and implementation. The strain-based approach imposes an internal expansion over a finite element region, producing a relatively rapid and widespread stress buildup. In contrast, the displacement-based method initiates expansion at the nodal level, resulting in a more localized deformation response and, consequently, slower and less intense crack development for the same expansion magnitude (when U_{max} is taken equal to h_{max}).

It is important to note that this difference in crack evolution was expected, as it stems from the fundamental difference in the nature of the imposed quantities. The maximum strain h_{max} is a dimensionless quantity, while the maximum displacement U_{max} has a physical unit of length (e.g., mm). As such, the same numerical value applied in both formulations does not represent the same physical effect.

This approach was adopted for the remainder of the study due to its alignment with physical reality. By directly linking the imposed displacement to the corrosion layer thickness, the model allows for a more explicit and measurable representation of corrosion-induced expansion. Although the exact relationship between the imposed displacement and the corrosion product thickness is not assumed to be one-to-one at this stage, this relationship will be further examined and calibrated in later sections. This modeling strategy ultimately facilitates a more robust comparison between numerical predictions and experimental results, particularly in terms of crack initiation and crack opening evolution.

This section presents the modeling approach developed to simulate corrosion-induced expansion in a time-dependent framework. The methodology involves first determining the evolution of corrosion product thickness $h(t)$ for each current density. The corresponding mechanical expansion $U(t)$ is then computed using a calibrated scaling factor β and the evolution function of corrosion products $h(t)$, ensuring that the numerical crack opening evolution aligns with experimental observations. This framework enables both qualitative and quantitative comparison with experimental data through damage patterns and crack width measurements.

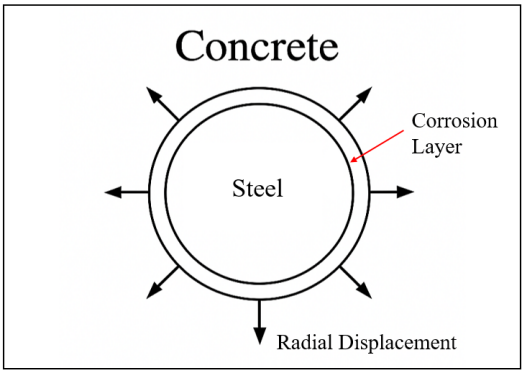

Figure 65: Radial Displacement Scheme

5.2.1 Radial Displacement: A non-linear exponential model

To model the time-dependent growth of the corrosion layer, an exponential growth function of the form $h(t) = A(1 - e^{-Bt})$ is used, where $h(t)$ is expressed in micrometers at time t (in days), A represents the asymptotic (maximum) corrosion thickness, and B controls the rate of growth. The parameters A and B are to be identified using nonlinear regression based on the experimental data corresponding to each imposed current density.

The resulting curve shape of this model is intended to be similar to the one illustrated in Figure 66. Once the corrosion layer thickness $h(t)$ is defined, the resulting radial

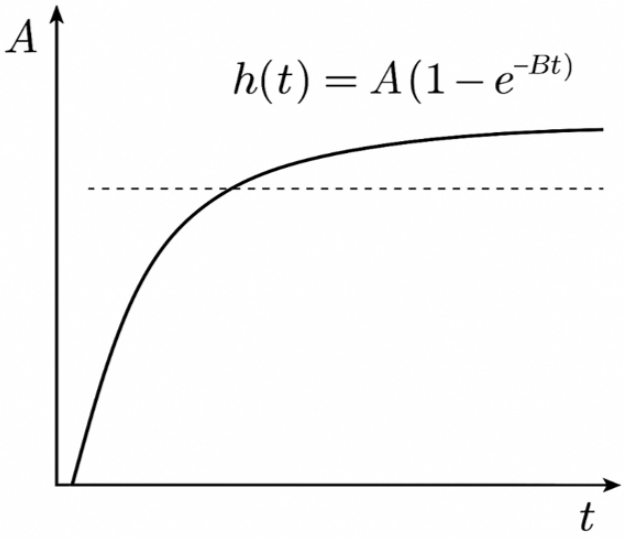

Figure 66: Exponential growth model used to describe corrosion layer thickness over time

displacement imposed on the concrete–steel interface is expressed as $U(t) = \beta h(t)$ where β is a dimensionless calibration parameter that relates the corrosion product layer to the corrosion-induced expansion evolution. Unlike the analytical expression for $h(t)$, the value of β cannot be prescribed a priori and must instead be determined numerically. It is calibrated such that the mechanical response of the model - the observed crack opening and damage evolution - matches our reference experimental benchmarks.

5.2.2 Crack Opening Finding Methodology

It has been established that there is a correlation between corrosion-induced expansion and structural degradation, and consequently, cracking. In this framework, the crack opening has been identified as a quantitative indicator of damage progression, offering a direct measurement of the progression of concrete damage. To validate the corrosion expansion model against experimental results qualitatively and quantitatively, it is essential to compare the predicted crack opening over time with that which has been observed through experimental tests.

Since the phase-field damage variable d is diffuse, the crack is not explicitly discrete, so the opening must be inferred from the displacement field in the damaged region. In this framework, crack opening (CO) is to be evaluated by extracting the relative displacement in this region.

The crack opening is computed by evaluating the vertical displacement jump Δu between selected nodes located just above and below the most damaged region at the left boundary, where the crack emerges. This was done directly at the nodal level, based on the displacement field u obtained from the simulation.

The identification of these nodes is a sensitive step. Since damage in phase-field models is diffuse, the definition of the "crack front" depends on the threshold chosen for the damage variable d. For example, using a high threshold like $d \geq 0.98$ focuses the calculation on the most degraded nodes, while a slightly lower threshold such as $d \geq 0.95$, which is being assumed in our simulations, includes nodes from the surrounding zone. This choice directly influences the computed crack opening, especially in early stages when the damage zone is still evolving.

The vertical displacement difference between the selected upper and lower nodes was computed, and the maximum such value was retained at each time step. This process was repeated over time to generate the crack opening evolution curve.

This method provides a physically meaningful estimate of the crack opening in the diffused phase-field representation and allows comparison with experimental measurements.

5.3 Necessary experimental data for the modeling

To define the corrosion-induced radial expansion used in the numerical model, we rely on accelerated-corrosion experiments previously done during the thesis of Loukil [37] which were performed on reinforced-concrete prisms tested at several impressed current densities (e.g., 50, 100, 200 $\mu A\,cm^{-2}$) and over distinct exposure durations. For each prism and time, the corrosion product thickness around the rebar is observed on multiple slices and samples, and read at eight angular sectors (C1–C8) to capture the accumulated thickness (minimum/maximum) on the circumference. The resulting time–thickness pairs per current density form the experimental basis for constructing the expansion input data $U(t)$ used later in the crack-opening simulations (see Fig. 67).

5.3.1 Corrosion product thickness

Before analyzing the evolution of crack opening over time, it is first necessary to establish a realistic input for the corrosion-induced expansion to be used in the numerical simulations. This input is derived by extracting the time-dependent evolution of corrosion product thickness (PdC) from experimental measurements reported in Loukil's thesis [37]. The aim of this step is to construct a thickness–time relationship for various current densities, which will then serve as a foundation for applying radial expansion at the steel–concrete interface within the numerical model.

The needed experimental data from Loukil's thesis [37] are the minimum and maximum corrosion product thicknesses (colored green and red respectively) measured at eight dials (C1 to C8) around steel reinforcement bars embedded in concrete prisms. These measurements have been obtained under accelerated corrosion conditions, using three different current densities: 50, 100, and 200 $\mu A/cm^2$, and for different corrosion durations which are 14, 28 and 70 days, 7, 14, 21, 28 and 35 days and 3.5, 7 and 17.5 days for the current densities 50, 100, and 200 $\mu A/cm^2$ respectively.

The introduction of the evolution of corrosion thickness in the modelling based on the experimental data has the capacity to more realistically reproduce the mechanical effects of corrosion in consequence, the concrete cracking.

Prism reference/ current density (µA/cm²)/ Corrac duration (days)	Sample	Dials	C1	C2	C3	C4	C5	C6	C7	C8
P23-d50-14j	E10	Max	0	0	0	0	0	0	205	638
		Min	0	0	0	0	0	0	54	338
	E13	Max	560	167	0	0	0	0	266	393
		Min	437	50	0	0	0	0	164	127
	E16	Max	302	1 502	0	159	209	181	952	180
		Min	151	107	0	63	97	85	211	110
P25-d50-28j	E10	Max	344	345	412	150	103	75	434	530
		Min	126	115	163	84	29	34	132	329
	E13	Max	690	220	493	0	0	0	277	483
		Min	218	118	177	0	0	0	132	96
	E16	Max	640	158	494	336	257	0	0	828
		Min	340	134	156	93	96	0	0	347
P27-d50-70j	E10	Max	710	873	157	194	135	267	242	566
		Min	474	173	127	84	31	81	152	370
	E13	Max	402	152	557	422	323	309	241	445
		Min	149	73	153	228	115	152	35	171
	E16	Max	100	211	702	329	841	123	342	550
		Min	23	104	104	336	383	53	187	80

Table 5: Maximum and minimum thicknesses (µm) of corrosion products for a current density of 50µA/cm² (reproduced from Table IV-1 from Loukil's thesis [37])

Prism reference/ current density (µA/cm²)/ Corrac duration (days)	Sample	Dials	C1	C2	C3	C4	C5	C6	C7	C8
P31-d100-7j	E10	Max	100	89	102	263	0	0	0	139
		Min	25	22	49	65	0	0	0	61
	E13	Max	300	225	417	227	150	82	107	175
		Min	25	59	304	118	88	22	101	27
	E16	Max	338	736	370	180	0	0	0	250
		Min	250	221	150	53	0	0	0	50
P05-d100-14j	E10	Max	440	507	375	0	0	0	0	0
		Min	392	102	57	0	0	0	0	0
	E13	Max	531	827	433	0	0	0	0	0
		Min	320	300	116	0	0	0	0	0
	E16	Max	374	173	0	0	0	0	0	0
		Min	215	36	0	0	0	0	0	0
P08-d100-21j	E10	Max	142	342	300	0	0	0	0	80
		Min	124	180	160	0	0	0	0	29
	E13	Max	511	617	236	0	0	0	0	0
		Min	36	461	168	0	0	0	0	0
	E16	Max	227	358	0	0	0	0	0	152
		Min	140	215	0	0	0	0	0	32
P09-d100-28j	E10	Max	0	708	450	284	206	0	0	0
		Min	0	213	102	82	94	0	0	0
	E13	Max	871	200	515	0	0	0	0	1 041
		Min	354	96	144	0	0	0	0	695
	E16	Max	364	726	342	0	0	0	0	1 112
		Min	336	374	189	0	0	0	0	436
P11-d100-35j	E10	Max	431	655	666	0	0	0	0	0
		Min	111	158	190	0	0	0	0	0
	E13	Max	481	594	500	0	0	0	628	1 584
		Min	187	394	204	0	0	0	0	797
	E16	Max	906	528	408	468	0	0	0	0
		Min	328	158	238	145	0	0	0	0

Table 6: Maximum and minimum thicknesses (µm) of corrosion products for a current density of 100µA/cm² (reproduced from Table IV-2 from Loukil's thesis [37])

Prism reference/ current density (µA/cm²)/ Corrac duration (days)	Sample	Dials	C1	C2	C3	C4	C5	C6	C7	C8
P14-d200-3.5j	E10	Max	1287	259	263	0	0	0	0	646
		Min	365	74	200	0	0	0	0	465
	E13	Max	872	710	0	0	0	0	0	0
		Min	86	84	0	0	0	0	0	0
	E16	Max	831	967	334	132	154	517	908	947
		Min	75	136	148	64	50	143	98	348
P16-d200-7j	E10	Max	795	990	487	551	235	200	368	1374
		Min	668	217	101	135	164	100	105	231
	E13	Max	880	672	680	0	0	0	880	447
		Min	602	103	224	0	0	0	189	230
	E16	Max	648	654	529	420	250	373	1000	584
		Min	335	352	209	122	115	221	425	290
P17-d200-17.5j	E10	Max	731	783	519	200	500	416	884	761
		Min	491	382	271	28	175	152	597	391
	E13	Max	340	552	501	1006	785	214	390	619
		Min	100	256	109	226	191	129	139	101
	E16	Max	738	782	1228	198	378	325	313	733
		Min	282	498	614	125	101	108	121	162

Table 7: Maximum and minimum thicknesses (µm) of corrosion products for a current density of 200µA/cm² (reproduced from Table IV-3 from Loukil's thesis[37])

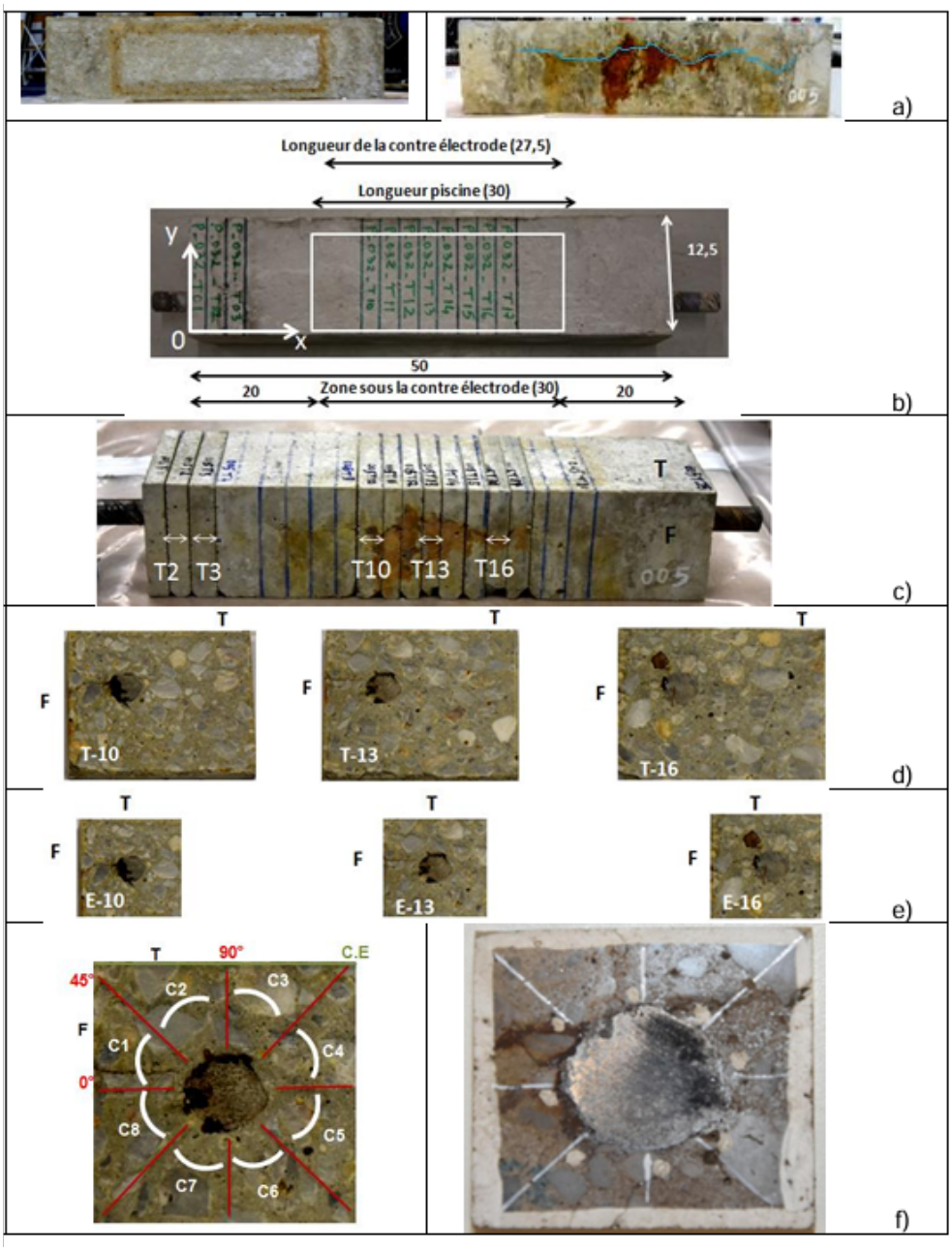

Figure 67: a) External cracking (Faces T and F), b) Reinforced prism cutting plan (100x12.5x10, dimensions in cm), c) Slice location, d) Slices T10, T13 and T16 (12.5x10), e) Samples E10, E13 and E16 (4x4), f) Dial delimitation methodology from C1 to C8 (reproduced from Loukil's thesis [37], Fig. II-18.)

5.3.2 Data Processing Methodology

To calculate the average corrosion product thickness along the entire contour of the reinforcement bar for each prism at each time instant, the following procedure was applied individually to each specimen:

1. **Average per sample:** For each sample (E10, E13, E16), the mean of the minimum and maximum values is computed at each dial (C1, C2,...,C8).

2. **Average per prism:** For each prism (e.g., P23-14d-50), the average thickness at each dial is calculated across the three samples.

3. **Global average:** The final average thickness for a given prism and time is computed as the mean of the values across all eight dials.

4. **Time–thickness pair:** For each prism, the corrosion duration (e.g., 14, 28, or 70 days) is paired with its associated global average thickness at each instant to create a point on the corrosion thickness–time curve.

This procedure is repeated for each of the three current densities (50, 100, and 200), resulting in three distinct corrosion thickness–time curves (figure 68).

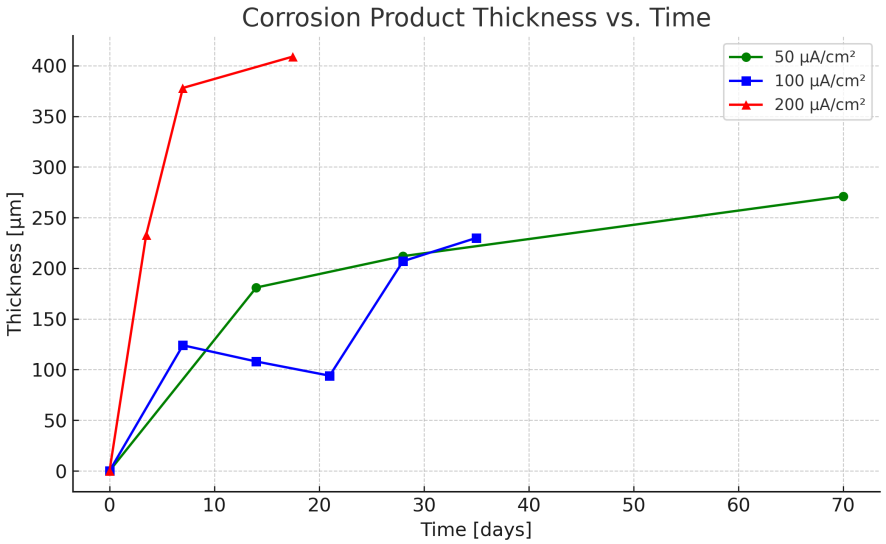

Figure 68: Evolution of average corrosion product thickness over time for three current densities (50, 100, and 200$\mu A/cm^2$)

5.3.3 Comparison Across Current Densities

In order to obtain a more profound comprehension of the experimental evolution of the thickness and its subsequent reproduction in a numerical context, an investigation was conducted on the experimental average corrosion product thickness under varying current densities and temporal durations. As expected, an overall increasing trend of rust layer thickness with time was observed for all tested current densities ($50\,\mu A/cm^2$, $100\,\mu A/cm^2$, and $200\,\mu A/cm^2$), though the rates and patterns of increase varied notably (tables 5, 6, 7 and figure 68).

At the lowest density ($50\,\mu A/cm^2$), corrosion proceeded gradually, with the thickness reaching approximately $271\,\mu m$ after 70 days, indicating a relatively slow and steady expansion characteristic of milder corrosion environments. In contrast, the $200\,\mu A/cm^2$ tests showed a rapid increase in rust product thickness, reaching $233\,\mu m$ in just 3.5 days and $409\,\mu m$ by day 17.5, demonstrating aggressive and early-stage corrosion due to the high current density.

The $100\,\mu A/cm^2$ case presented a more complex behavior: although corrosion initially increased ($124\,\mu m$ at day 7), a temporary reduction in average thickness was recorded at days 14 and 21, followed by a renewed increase toward $230\,\mu m$ at day 35.

This confirms that the corrosion kinetics are strongly governed by the applied current density. These findings provide a direct physical correlation between the imposed current density and the degradation rate of the steel reinforcement [168], where higher current accelerates the expansion but may also introduce more complex failure mechanisms.

In order to facilitate the study of corrosion product thickness in a comparable way between the three current densities, an analysis was performed as a function of the total charge Q (multiplication of the current density and the experimental test duration). Indeed, each duration was found to be associated with an impressed current density to achieve a targeted value of the total charge.

For instance, at a total charge of $700\,\mu Ad/cm^2$, the corresponding exposure durations were 14 days for $50\,\mu A/cm^2$, 7 days for $100\,\mu A/cm^2$, and 3.5 days for $200\,\mu A/cm^2$. Despite this equivalence in charge, the resulting average corrosion product thicknesses differed notably: around $181\,\mu m$, $124\,\mu m$, and $233\,\mu m$, respectively (figure 69).

This variation suggests that corrosion product accumulation is influenced not only by the total charge but also by the current intensity and the corrosion exposure duration. Higher current densities may lead to more aggressive local corrosion behavior even over short durations, possibly due to faster chloride ion migration and steel oxidation kinetics [168]. In addition, spatial heterogeneity around the reinforcement bar—such as

variations in exposure along the eight dials—may contribute to differences in average thickness, especially when comparing slices from different prisms or orientations.

The observations presented here provide support for the hypothesis that the implementation of an exponential law for the modelling of corrosion-induced expansion, in which the data manifest saturation behaviour over time, is an optimal approach (Figure 69).

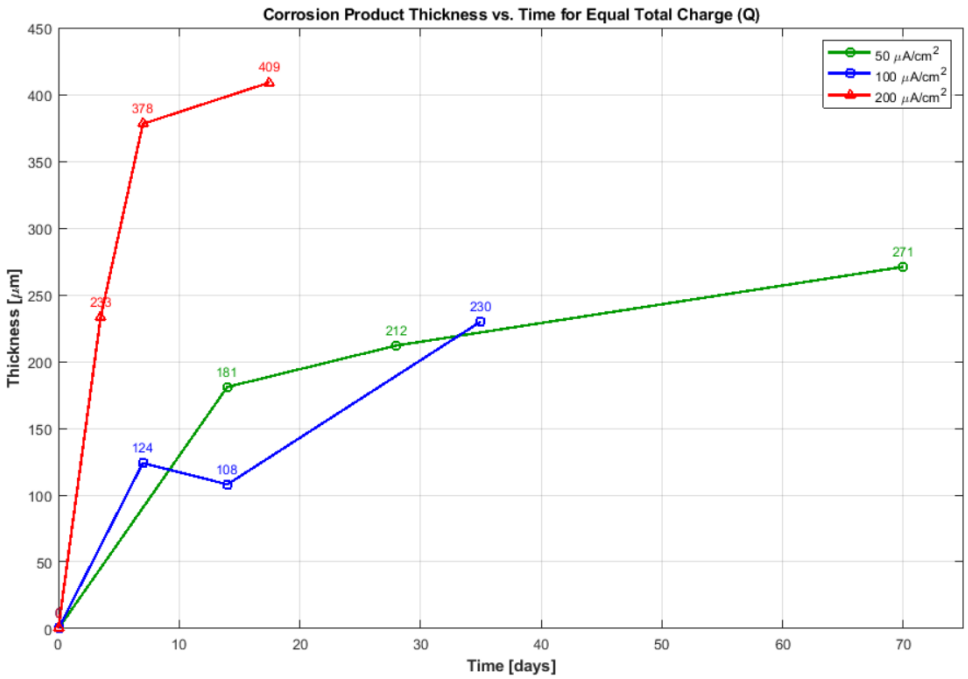

Figure 69: Corrosion Product Thickness vs. Time for Equal Total Charge (Q = 700 $\mu Ad/cm^2$)

5.3.4 Selection of Experimental Slices for Numerical Modeling and Validation

In order to construct the numerical model and validate it, a selection of 2D slices was directly taken from the work of Loukil [37]. These slices, prepared and analyzed in her thesis, correspond to reinforced concrete prisms subjected to various corrosion durations and current densities. In the context of the present study, a rigorous approach has been adopted to select the slices that are to be analyzed. This process involves the selection of slices corresponding to each instant t, with the caveat that only those slices displaying a horizontal crack on the left side of the specimen are to be considered. This choice ensures consistency in the comparison, as horizontal cracks are the most frequently observed in the experimental data, and crack openings were predominantly measured for this type of cracking. In our work, each slice is then processed

and transformed into a regular mesh using tomography-based image processing tools as shown in the previous chapter. In doing so, the heterogeneous nature of the concrete is captured, allowing the model to incorporate local variations in material composition and structure.

The use of multiple slices corresponding to different durations and current densities allows us to simulate the effect of varying corrosion progression and heterogeneous microstructures. These simulations are later used to compare both the morphology and evolution of the cracks with the experimental results. Specifically, the comparison will be conducted qualitatively, by visually comparing the simulated and experimental crack patterns, and quantitatively, by evaluating the crack opening evolution over time. The corresponding results and validation steps will be illustrated in the following sections.

1 Current Density of 50 $\mu A/cm^2$:

1.a Corrosion exposure duration of 14 days:

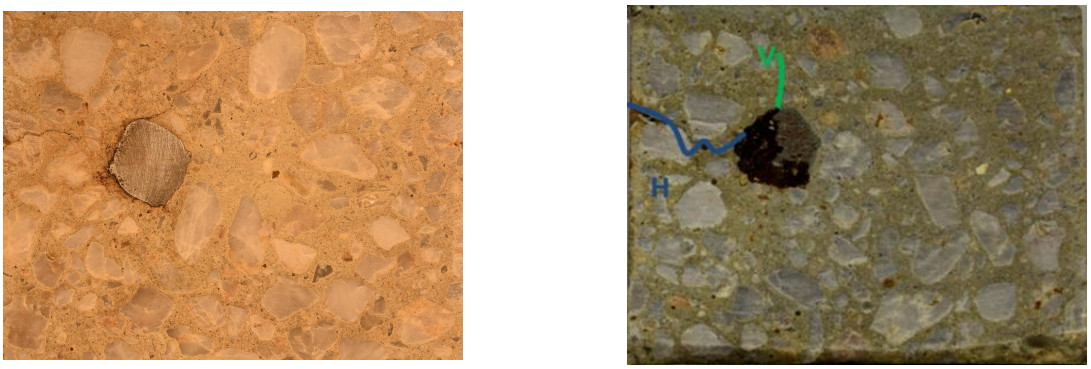

(a) **(b)**

Figure 70: Experimental slices for prism P23 (a) P23-d50-14d-T12-D and (b) P23-d50-14d-T13-D

1.b Corrosion exposure duration of 28 days:

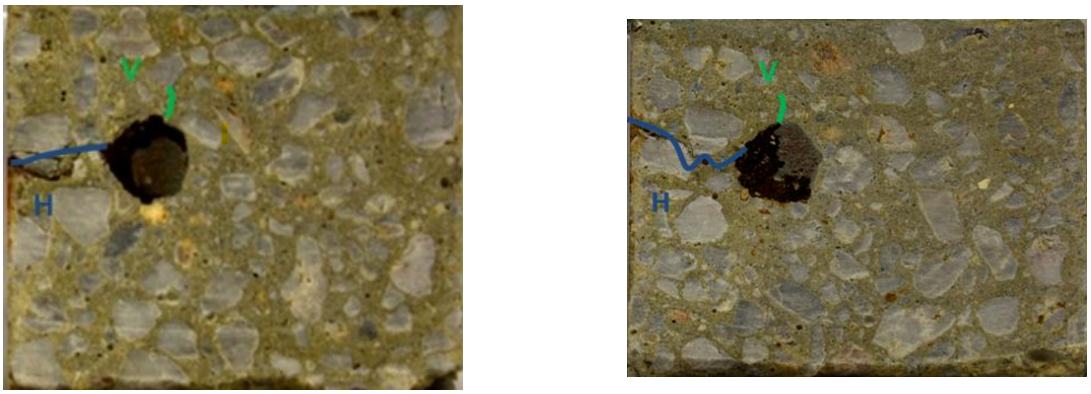

(a) (b)

Figure 71: Experimental slices for prism P25 (a) P25-d50-28d-T16-D and (b) P25-d50-28d-T13-D

1.c Corrosion exposure duration of 70 days:

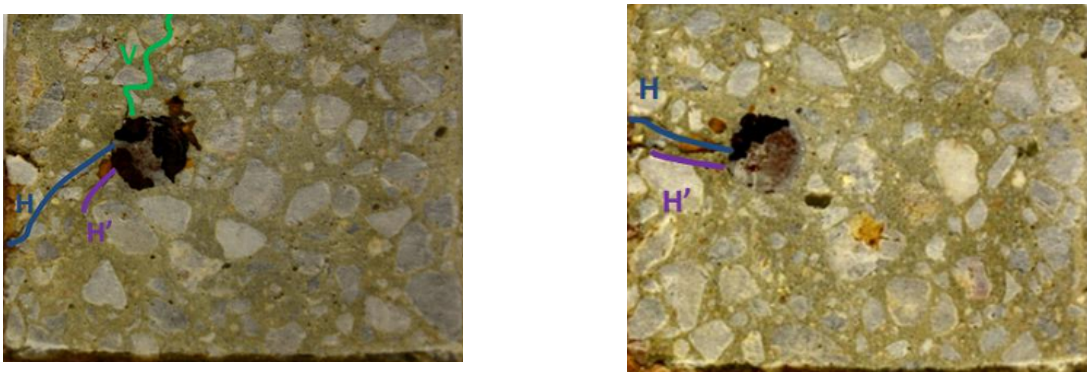

(a) (b)

Figure 72: Experimental slices for prism P27 (a) P27-d50-70d-T9-D and (b) P27-d50-70d-T13-D

2 Current Density of 100 $\mu A/cm^2$:

2.a Corrosion exposure duration of 7 days:

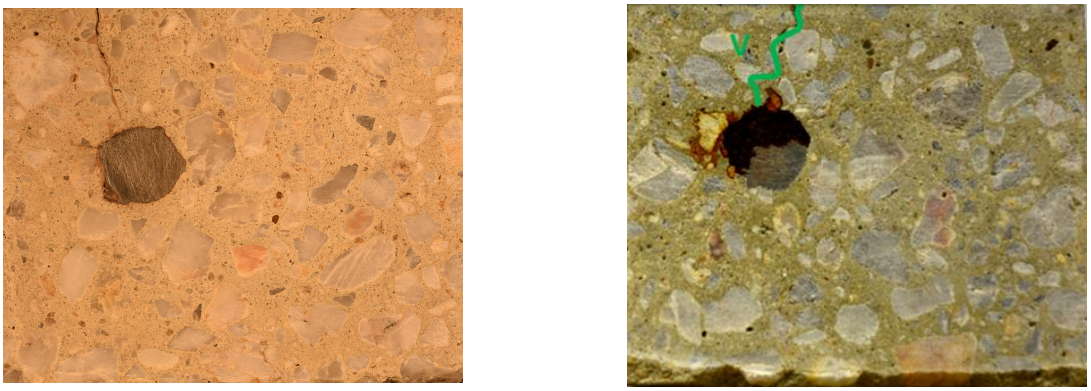

(a) (b)

Figure 73: Experimental slices for prism P31 (a) P31-d100-7d-T11-D and (b) P31-d100-7d-T16-D

2.b Corrosion exposure duration of 14 days:

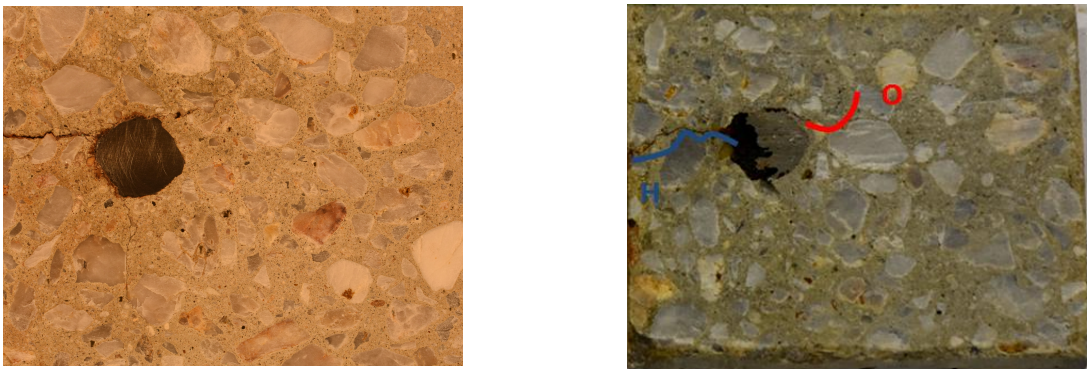

(a) (b)

Figure 74: Experimental slices for prism P05 (a) P05-d100-14d-T14-D and (b) P05-d100-14d-T10-D

2.c Corrosion exposure duration of 21 days:

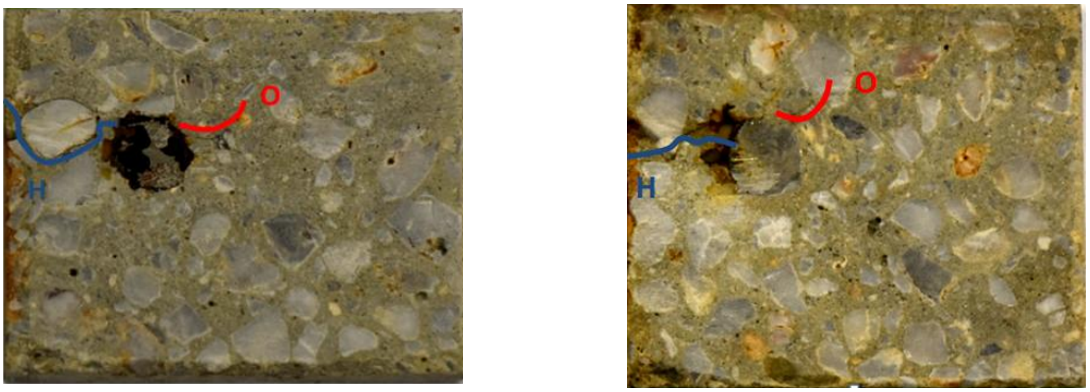

(a) (b)

Figure 75: Experimental slices for prism P08 (a) P08-d100-21d-T12-D and (b) P08-d100-21d-T17-D

2.d Corrosion exposure duration of 28 days:

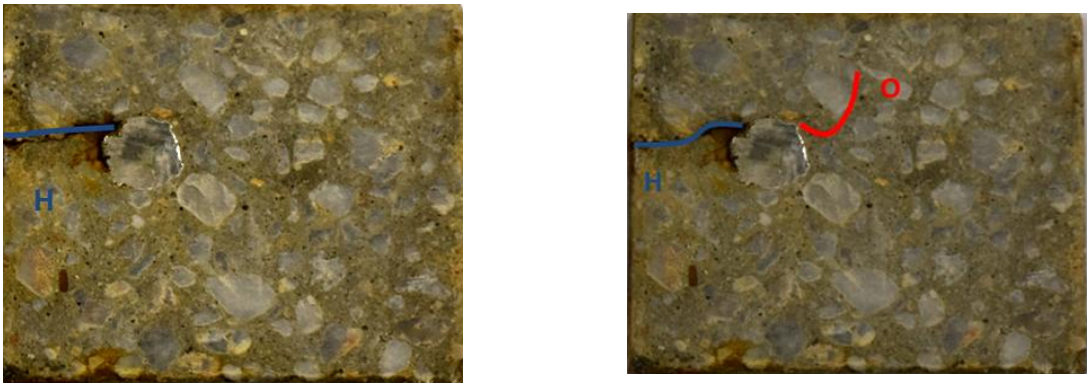

(a) (b)

Figure 76: Experimental slices for prism P09 (a) P09-d100-28d-T10-D and (b) P09-d100-28d-T15-D

2.e Corrosion exposure duration of 35 days:

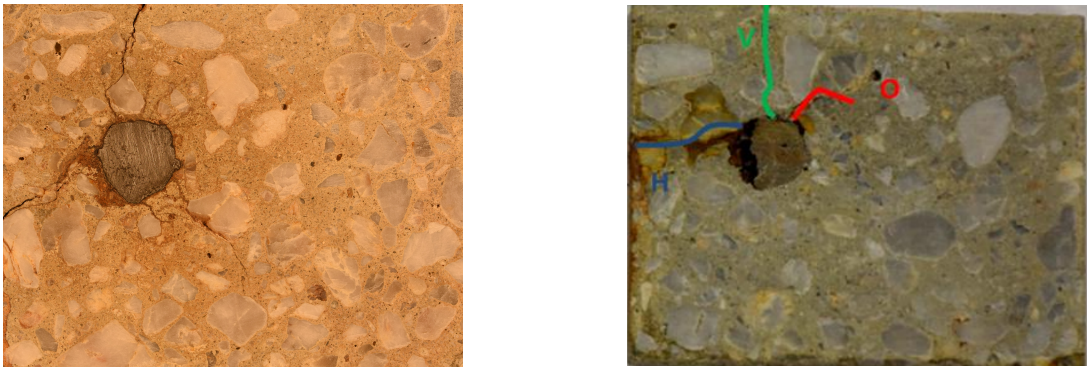

(a) (b)

Figure 77: Experimental slices for prism P11 (a) P11-d100-35d-T14-D and (b) P11-35d-T11-D

3 Current Density of 200 $\mu A/cm^2$:

3.a Corrosion exposure duration of 3.5 days:

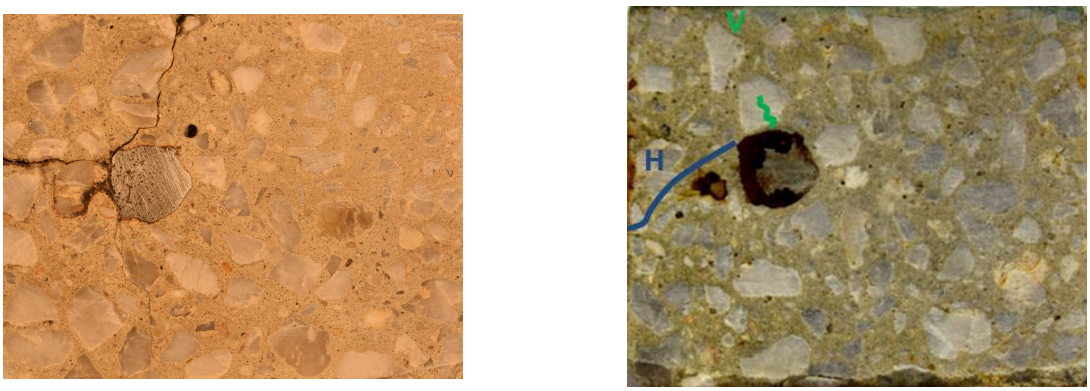

(a) (b)

Figure 78: Experimental slices for prism P14 (a) P14-d200-3.5d-T11-D and (b) P14-d200-3.5d-T10-D

3.b Corrosion exposure duration of 7 days:

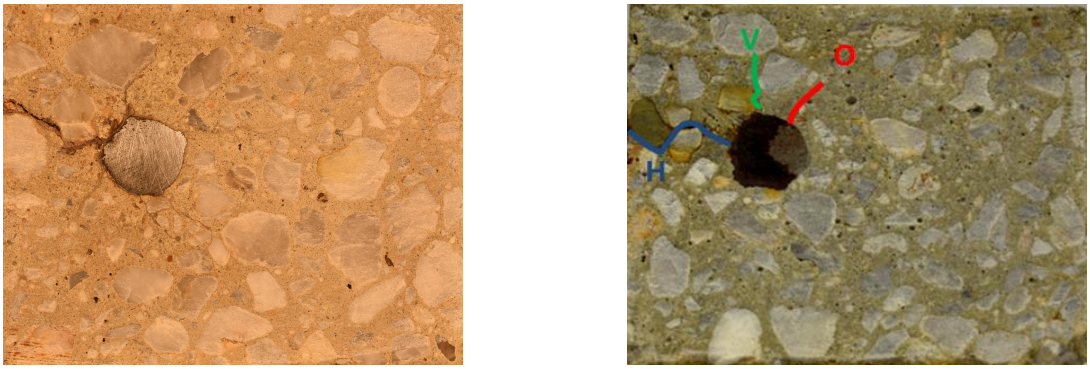

(a) (b)

Figure 79: Experimental slices for prism P16 (a) P16-d200-7d-T14-D and (b) P16-d200-7d-T16-D

3.c Corrosion exposure duration of 17.5 days:

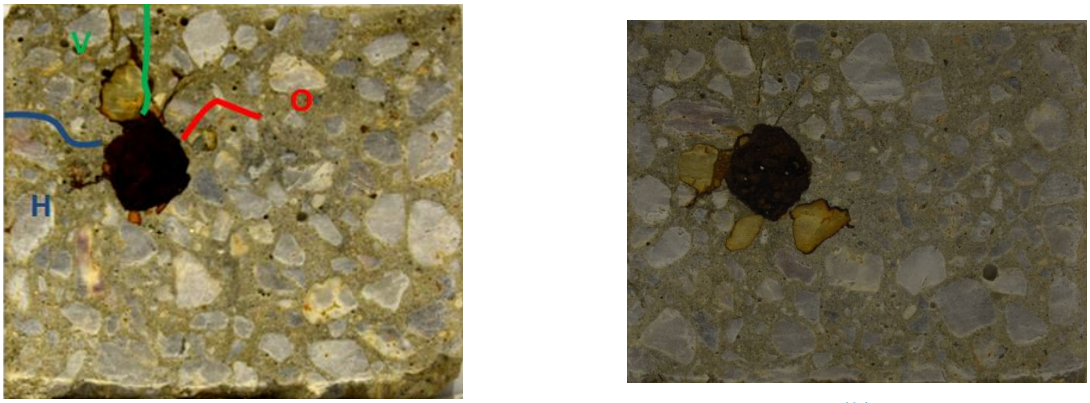

(a) (b)

Figure 80: Experimental slices for prism P17 (a) P17-d200-17.5d-T16-D and (b) P17-d200-17.5d-T13-D

5.3.5 Experimental evaluation of horizontal crack widths

Figure 81, extracted from Loukil's data [37], presents the maximum widths of the longitudinal cracks observed on both faces T and F of reinforced concrete prisms after undergoing accelerated corrosion testing. These results indicate that, beyond specific corrosion durations—70 days for $50\,\mu A\,cm^{-2}$ (Figure 81(a)), 28 days for $100\,\mu A\,cm^{-2}$ (Figure 81(b)), and 7 days for $200\,\mu A\,cm^{-2}$ (Figure 81(c))—the observed crack openings typically range between 0.4 mm and 0.7 mm.

Interestingly, for $50\,\mu A\,cm^{-2}$, when cracks are present on both faces T and F, the opening on face F is generally larger than that on face T. Conversely, for 100 and $200\,\mu A\,cm^{-2}$, this trend reverses: face T tends to exhibit wider cracks than face F when both are

cracked. This is likely due to the faster penetration of chloride ions through cracks in face T, accelerating corrosion product formation and leading to greater crack opening.

Due to the interaction between the corrosion products and the electrolyte solution during testing, it was not possible to follow the exact chronological order of crack appearance on faces T and F, making surface tracking challenging.

Based on final crack width observations across all prisms, four distinct cracking scenarios can be hypothesized:

- Cracks initiate in face F and then appear in face T (e.g., prisms P26–28j, P27–70j, P28–70j). In such cases, openings in face F (e.g., 0.3 mm) are greater than those in face T (e.g., 0.1 mm).
- Cracks initiate in face T and then appear in face F (e.g., prism P11–35j), with larger openings in T (0.7 mm) than F (0.4 mm).
- Cracking occurs only in face F, with significant openings (e.g., prism P29–78j at 0.5 mm, P19–19.5j at 0.6 mm, and P20–19.5j at 0.7 mm).
- Cracking occurs only in face T, and the openings are typically larger than those of similar prisms cracked only in face F (e.g., prism P06–14j in T at 0.2 mm vs. P05–14j in F at 0.1 mm).

These observations further reinforce the variability of corrosion-induced cracking depending on both face exposure, the corrosion exposure time and current density, and they provide useful reference points for the subsequent validation of numerical simulations.

To better capture the temporal evolution of the horizontal crack openings, the average crack width was calculated across all prisms subjected to the same corrosion duration. This allowed the construction of a crack opening–time curve, as shown by the plotted points in Fig. 82.

In this study, only horizontal (F-type) cracks were considered for the average crack width calculation. The rationale behind this choice is set out in subsection 5.3.4. The horizontal crack results will serve as the primary reference point for both qualitative and quantitative comparisons with numerical simulations presented in the following sections.

A comprehensive concluding comparison of crack opening evolution under the three applied current densities—50, 100, and 200 µA/cm²—reveals a strong influence of corrosion intensity on both the timing and distribution of cracking.

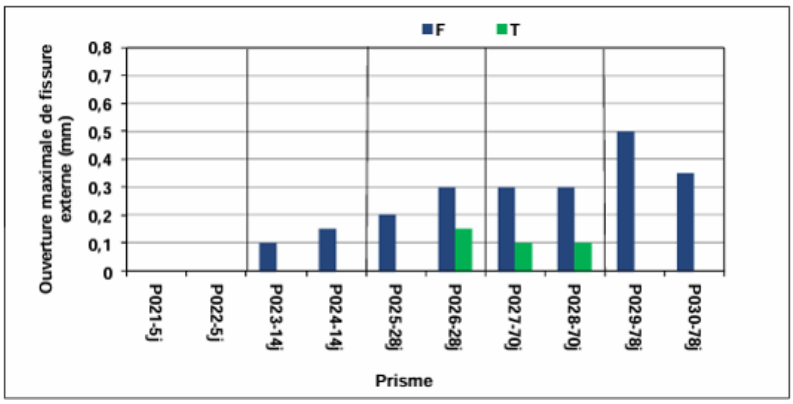

(a)

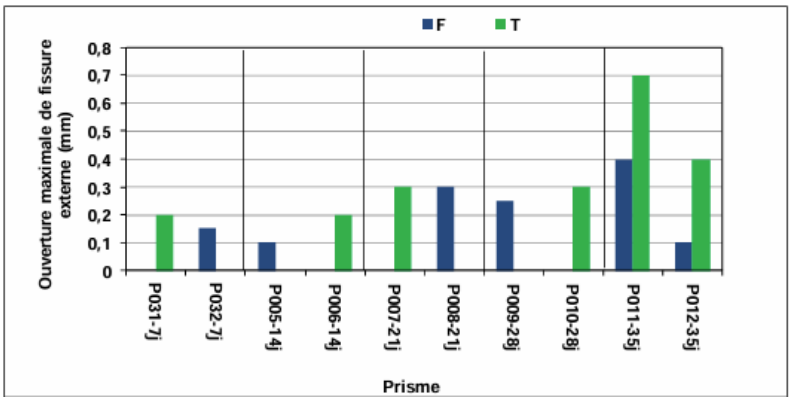

(b)

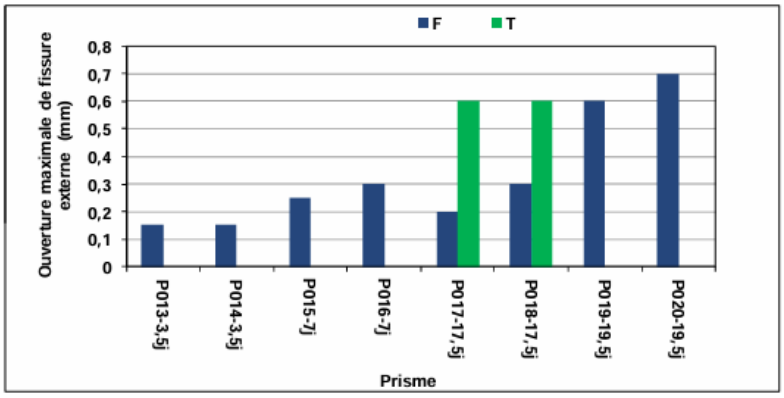

(c)

Figure 81: Location (in T and/or F) and maximum opening of the external crack for the current densities: (a) 50 µA/cm², (b) 100 µA/cm², (c) 200 µA/cm².

At 200 µA/cm², cracks initiate very early, with a crack width of 0.15 mm already reached by 3.5 days, increasing to 0.275 mm by 7 days, as shown in Figure 82c. However, a slight decline to 0.25 mm is observed at 17.5 days. While this may initially suggest crack closure due to compaction or rust filling, an alternative explanation is the initi-

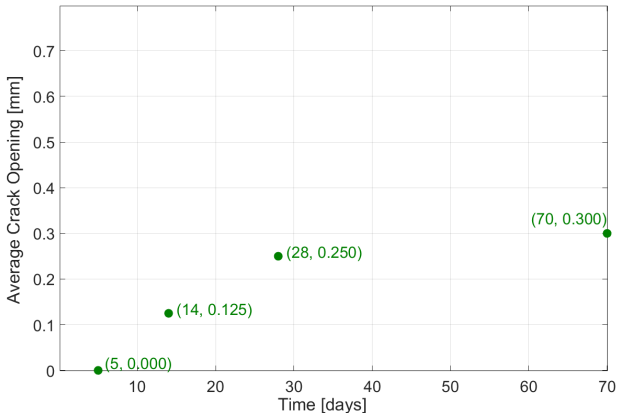

(a)

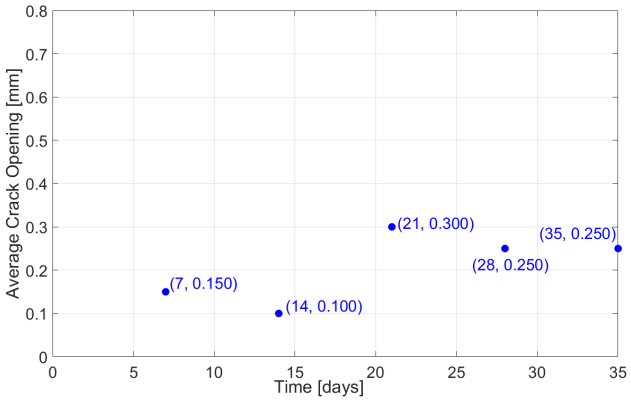

(b)

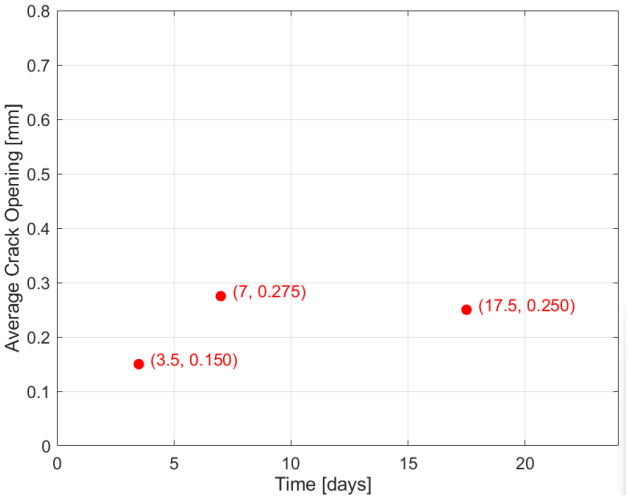

(c)

Figure 82: Average horizontal crack openings over time for the current densities: (a) 50 µA/cm², (b) 100 µA/cm², (c) 200 µA/cm².

ation of vertical cracks, which relieve internal stresses and reduce the need for further opening on horizontal faces. This redistribution of damage likely explains the observed stabilization or slight drop in horizontal crack width.

This interpretation is further supported by the bar plot in Figure 81-c, where significant vertical cracking is evident, particularly near the end of the corrosion duration. These findings imply that the apparent plateau or reduction in horizontal crack openings reflects a shift in crack propagation direction, rather than material healing.

In the case of 100 µA/cm² (Figure 82b), the evolution of horizontal crack width appears less consistent compared to the other current densities. The crack opening increases to a peak of approximately 0.3 mm at 21 days, but then declines to about 0.25 mm by 35 days and then arises to 0.4 mm by 35 days, indicating a non-monotonic trend. Unlike the lowest current density (50 µA/cm²), this evolution does not follow a smooth or progressive pattern.

Closer inspection of the corresponding bar chart (Figure 81-b) reveals that, in contrast to the 50 µA/cm² and 200 µA/cm² cases, vertical cracks are already present from the early stages of corrosion, and their development persists throughout the testing period. This early and simultaneous presence of both horizontal and vertical cracks suggests a more complex and possibly heterogeneous damage mechanism.

Conversely, for the lowest current density of 50 µA/cm², the evolution is continuous and monotonic, as shown in Figure 82a. The crack width increases steadily from 0.125 mm at 14 days to 0.425 mm at 78 days, with no significant reductions.

Key Comparative Insights:

- **Higher current densities** lead to earlier crack initiation, compressing the corrosion damage process into a shorter time window.
- These conditions also promote multi-directional cracking, especially the emergence of vertical cracks that may reduce horizontal crack openings in later stages.
- **Lower current densities** produce a more gradual and predictable crack opening trend, with damage predominantly observed on the horizontal surface.
- The presence of vertical cracks alters the interpretation of horizontal crack data, as the stress relief they provide can falsely suggest healing or stabilization on the horizontal plane.
- Full understanding of crack development therefore requires not just single-face monitoring but multi-directional and 3D assessment to capture the true damage evolution.

These findings underscore the importance of considering the directionality and redistribution of cracking in corrosion-induced damage assessments. Higher corrosion intensities introduce more complex fracture mechanisms that go beyond simple one-dimensional measurements, highlighting the necessity for integrated experimental and modeling approaches.

5.4 Application of the approach: Test case

To demonstrate the practical implementation of the proposed numerical methodology, this section presents a detailed application to a selected reinforced concrete microstructure. The chosen specimen, referred to as P14-d200-3.5j-T11-D, was subjected experimentally to an accelerated corrosion regime under a current density of 200 μA/cm² for a duration of 3.5 days. This microstructure was initially selected arbitrarily, as a first attempt to validate and test the full workflow of the modeling strategy on real experimental data. The choice of this specific current density is further justified by its consistent exponential evolution of corrosion product thickness over time, which aligns well with the analytical formulation adopted for the imposed corrosion product expansion.

In this section, all the steps of the methodology are illustrated and applied comprehensively. This includes the digital extraction and preprocessing of the microstructure, the generation of the regular mesh from tomography data, the definition of the corrosion contour, the numerical imposition of time-dependent radial displacement, and finally the computation and tracking of crack opening evolution over time. Qualitative results in terms of crack patterns are compared to experimental observations, while quantitative comparisons are made based on the evolution of crack width, thus providing a robust validation of the approach.

This case study is presented as a foundationl example to illustrate and substantiate the computational pipeline. In the subsequent sections, the analysis will be extended to other microstructures, durations, and current densities in order to assess the generalisability and sensitivity of the approach across different experimental scenarios.

5.4.1 Numerical Analysis of a Selected Microstructure

The simulation is based on a two-dimensional (2D) cross-sectional representation of the selected specimen, specifically extracted from slice T11-D (figure 83a). This slice captures the steel reinforcement embedded in the heterogeneous concrete matrix, including the corrosion layer that develops at the steel–concrete interface.

To accurately reflect the physical microstructure, the geometry was constructed di-

rectly from the digitized image of the experimental slice. A triangular finite element mesh was then generated based on the pixel matrix, allowing for spatially resolved simulation of mechanical response within the heterogeneous medium (figure 83b). The mesh constructed from the experimental microstructure captures the main material phases, including cement paste, aggregates, voids, and the steel reinforcement as figure 83b shows. However, the corrosion layer was not explicitly extracted from the experimental image. It was extracted from SEM measurements and modeled implicitly through the application of radial displacements at the boundary nodes located along the corrosion products-concrete interface. These boundary nodes were identified as the location of final corrosion product expansion. Accordingly, it was hypothesised that the surrounding boundary elements of the steel are considered to represent the corrosion layer boundary, where the imposed displacement simulates the effect of corrosion-induced volumetric growth.

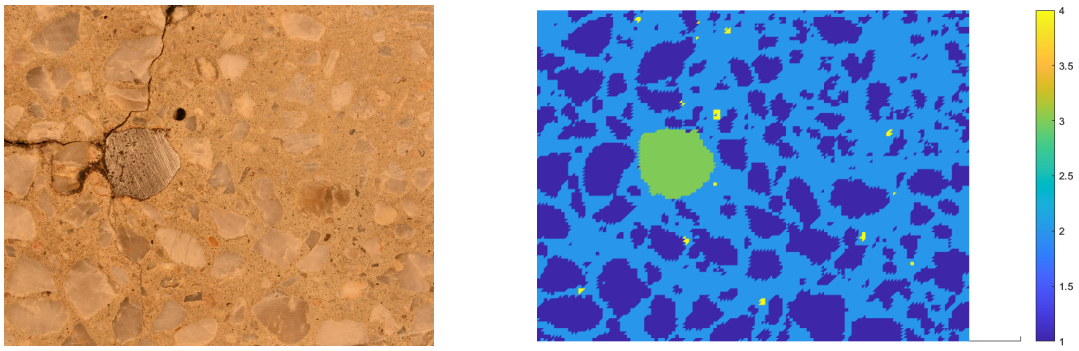

(a) **(b)**

Figure 83: Experimental slice P14-d200-3.5j-T11-D (a) and its corresponding mesh (b)

5.4.2 Qualitative Comparison of Simulated and Experimental Crack Patterns

In this section, all the geometrical and material characteristics, model parameters, and boundary conditions are adopted being identical to those described previously in section 4.3.4.1 (Chapter 4). In particular, the same assumptions regarding the corrosion-induced expansion, a uniform expansion applied within the corrosion layer, are maintained here. Figures 84a and 84b present a visual comparison between the experimental microstructure exhibiting corrosion-induced cracking and the simulated damage pattern respectively. It was observed that the cracks initiate radially around the steel bar and propagate outward into the surrounding concrete matrix.

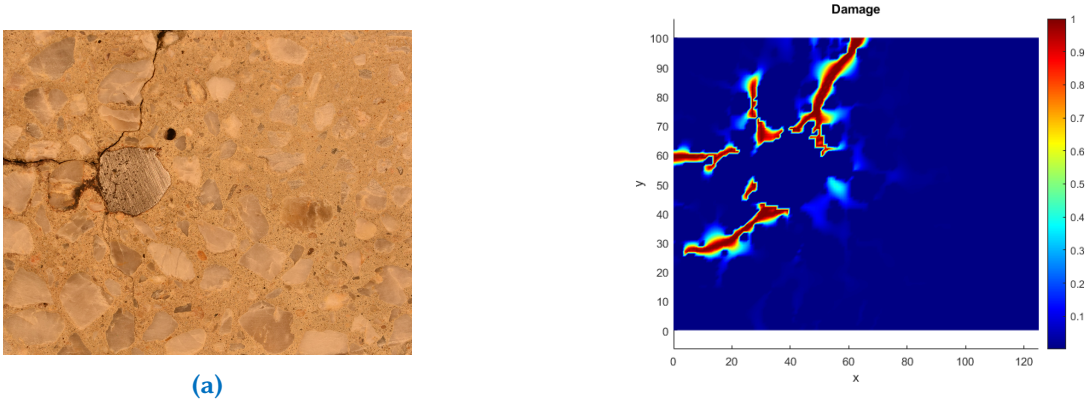

(a) (b)

Figure 84: (a) Experimental Cracks, (b) Numerical Damage Pattern

The orientations and trajectories of the main cracks also exhibit a noticeable similarity between the numerical and experimental observations particularly with respect to the emergence and branching of cracks from the steel–concrete interface. In both the numerical and experimental results, significant horizontal and diagonal crack paths are visible, indicating the development of tensile stresses consistent with corrosion-induced expansion. However, slight discrepancies can be noted in the exact orientation and extent of certain cracks. For instance, in figure 84b, some cracks appear to follow slightly altered paths compared to their experimental counterparts.

These deviations observed between the numerical and experimental crack patterns are mainly due to the assumption of a uniform expansion of corrosion products adopted in the numerical model. However, the corrosion product thicknesses obtained experimentally show a non-uniform distribution around the steel surface, which significantly influence the initiation and propagation of cracks. Consequently, the simulated crack morphology differs from the experimental observations, particularly in terms of crack orientation and distribution.

Additionally, these deviations are also affected by the image processing procedures used to digitize and prepare the microstructure for simulation. Local heterogeneities in the concrete—such as aggregates, pores, or voids—alter the crack propagation paths in the experimental specimen. These features can obstruct or redirect the cracks, producing discrepancies between the experimental and simulated crack networks.

This qualitative agreement serves as a foundation for the quantitative analysis to follow, where the evolution of crack opening over time will be examined. The accuracy of these numerical predictions, however, is influenced by several modeling parameters that govern the imposed corrosion expansion and damage evolution. These parameters and their effects will be systematically investigated in the next section through a dedicated

parametric sensitivity analysis.

5.4.3 Quantitative Comparison and Parametric Sensitivity

This section focuses on quantitatively comparing the numerical simulations with experimental observations in terms of crack opening evolution over time. While earlier sections established qualitative agreement between simulated and experimental crack patterns, the goal here is to verify and calibrate the numerical results by reproducing the experimentally observed crack openings quantitatively. To achieve this, the crack opening is computed numerically at each corrosion exposure duration and compared to the experimentally measured values. This allows for both point-by-point comparison and an overall assessment of the entire crack opening–time evolution. The numerically obtained curve is plotted and assessed against the experimental reference curve in terms of individual values as well as the general shape, growth rate, and asymptotic behavior. This comparison forms the basis for the model calibration process and evaluation of parameter influence.

In this section, the comparison is based on a representative microstructure extracted after 3.5 days of accelerated corrosion. Although this microstructure corresponds to an early stage of degradation, the simulation was extended up to 17.5 days to align with the full duration covered by the experimental reference curve. This temporal extension enables a meaningful comparison between the numerically computed crack opening and the experimentally measured evolution, not only at individual time points but also in terms of the overall shape of the crack opening–time curve. This approach serves as a foundational validation step before applying the model to additional microstructures and corrosion scenarios.

In order to facilitate this comparison, the numerical simulations are carried out by using the imposed expansion function $U(t) = \beta \cdot A(1-e^{-Bt})$ up to the maximum corrosion exposure duration, despite the microstructure representing an earlier corrosion state. As was stated in the preceding paragraph, the present density of 200 $\mu A/cm^2$ has a duration of 17.5 days. The assumption is that each microstructure continues to evolve under prolonged corrosion exposure until the maximum duration is reached. This allows the numerical model to predict how the damage pattern—and particularly the crack opening—would progress if the corrosion process continued, thereby enabling extrapolation toward the full experimental timeline.

This approach is applied consistently for each tested microstructure, ensuring that the numerical crack opening reaches the value observed experimentally. The extended simulation then facilitates comparison of the crack opening's temporal shape, growth

rate, and asymptotic behavior with the experimental data.

To understand the influence of the model formulation on the results, four key parameters governing the imposed displacement and material response are analyzed in the following subsections:

- the exponential law parameters A and B, which control the magnitude and rate of imposed radial expansion;
- the regularization length ℓ, affecting crack resolution and initiation timing;
- the scaling factor β, which scales the displacement intensity;
- the fracture energy g_c, defining the material's resistance to fracture.

These parameters are systematically varied to calibrate the numerical curves against experimental observations and to evaluate the model's sensitivity. The insights gained will guide the selection of parameters for future simulations by considering the different current densities and various heterogeneous microstructures.

Exponential Growth Parameters A and B

The corrosion-induced expansion applied at the steel–concrete interface is defined using the following exponential function:

$$U(t) = \beta \cdot A \left(1 - e^{-Bt}\right) \tag{5.1}$$

where:

- A represents the maximum possible radial expansion due to corrosion products, and is directly tied to the experimentally measured corrosion layer thickness. It defines the upper limit (asymptotic value) of the expansion over time.
- B governs the temporal evolution of the expansion function. It controls how quickly the expansion increases and, more specifically, determines the time required for the simulated crack opening to reach a value comparable to that observed experimentally.
- β is a dimensionless scaling factor that adjusts the overall magnitude of the expansion. Since $U_{\text{max}} = \beta \cdot A$, tuning β allows the model to match the observed crack opening magnitude, while keeping A physically consistent with experimental corrosion thickness measurements.

To reduce the number of free variables and to maintain a physically grounded approach, the amplitude parameter A was fixed directly from experimental measurements. For the microstructure P14-d200-3.5j-T11-D extracted at 3.5 days under a current density of 200 $\mu A/cm^2$, the average corrosion product thickness was measured to be:

$$A = 0.233 \text{ mm}$$

With A fixed, the product $\beta \cdot A$ becomes the principal factor controlling the total expansion. As such, the scaling parameter β is to be calibrated to achieve a qualitative validation of the crack pattern — i.e., the spatial location and morphology of the cracks in the simulation are to be compared visually with experimental observations. A range of values of β is tested, and the one producing the closest match with the observed crack trajectories is retained.

Once this qualitative agreement is established through the calibration of β, the time-evolution parameter B is then adjusted to achieve a quantitative agreement with experimental crack opening data. In this context, B does not simply control the speed at which $U(t)$ reaches its asymptotic value; rather, it dictates the temporal alignment between the simulated and observed crack openings. Specifically, it ensures that the numerical simulation reproduces the experimentally observed crack opening (e.g., 0.15 mm at 3.5 days) by or before the same experimental time.

This calibration process is illustrated in Figure 85, where the effect of varying β on the crack opening evolution is shown. In all cases, the exponential parameters were set to $A = 0.233$ mm and $B = 0.2$. The results highlight that reducing β below a certain threshold (e.g., $\beta = 30$) led to a complete absence of cracks on the left side of the slice face. In such cases, no qualitative validation could even be attempted, as cracking did not occur.

To overcome this limitation and allow for smaller β values and thus finer calibration of crack opening magnitudes, it was necessary to adjust another parameter which is a key component in the phase field model, the regularization length ℓ in the phase-field model. The influence of this adjustment is explored in the next subsection.

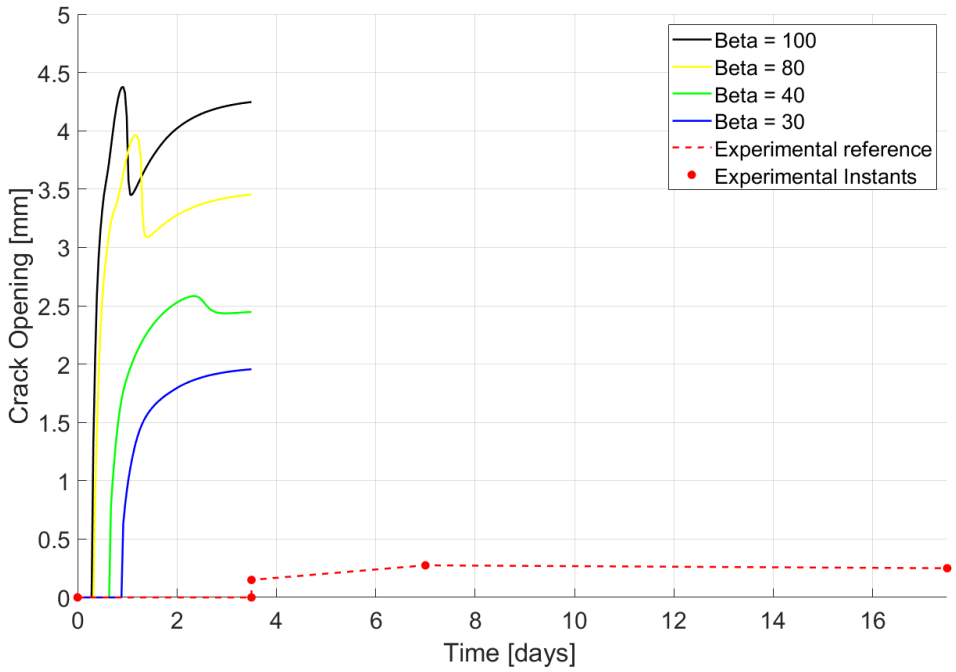

Figure 85: Crack opening over time for different values of β (with fixed $A = 0.233$ mm and $B = 0.2$), ℓ = 2*element size and before extension of curve duration range. The red curve represents the experimental results curve for $200\mu A/cm^2$.

Regularization Length ℓ

In the context of phase-field fracture modeling, the choice of the regularization length ℓ has a direct impact on the resolution and evolution of cracks (as illustrated in chapter 3). Although the theoretical role and formulation of ℓ are well-established in the literature, its practical selection remains a key numerical consideration, particularly when aiming to compare simulation results with experimental observations.

A general guideline, supported by works based on Miehe's formulation [146, 156], recommends that ℓ should be at least twice the element size in order to adequately resolve the smeared crack zone, which spans approximately a width of 2ℓ. If the mesh is too coarse relative to ℓ, the fracture zone cannot be properly captured. In earlier simulations presented in previous chapters, ℓ was taken as the lower bound (i.e., $\ell = 2 *$element size) in order to obtain sharper cracks that align well with the experimentally observed crack geometries.

However, in the current simulations, we have also sought a better agreement in the timing of crack initiation when compared to experimental results. To this end, a larger value of ℓ is adopted, specifically $\ell = 3 *$element size. As shown in figure 86, increasing ℓ promotes earlier crack initiation and smoother damage growth, which helps align the numerical crack opening curve with experimental trends. In particular, when attempting

to reduce the β parameter (scaling the expansion), crack opening on the left slice side failed to initiate below a certain threshold (e.g., $\beta = 30$) (figure 85). This limited our flexibility in achieving quantitative agreement with experimental crack openings, which were significantly lower in magnitude.

A larger ℓ, which is applied here, effectively lowers the critical strain required for damage to initiate, thereby enabling the model to produce cracks under smaller displacements. This adjustment allowed further reduction of β, facilitating better control over crack propagation and more accurate representation of the crack opening evolution. The effect of this updated modeling setup is illustrated in figure 86, where simulations using increased ℓ and extended time duration (up to 17.5 days) demonstrate better crack initiation and reduced crack opening magnitudes at lower β values, such as $\beta = 12.2$, which closely matches the experimental reference.

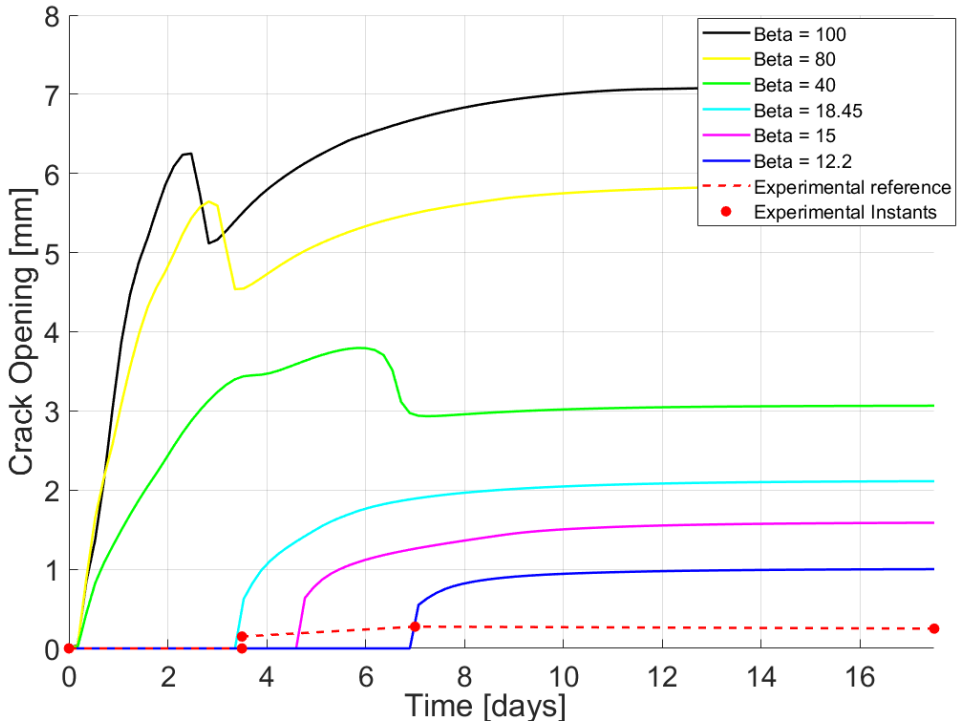

Figure 86: Crack opening evolution over time for various values of β with increased regularization length ($\ell = 3\times$ element size) and extension of curve duration. The red curve represents the experimental results curve for $200\mu A/cm^2$.

Effect of Scaling Factor β

The scaling factor β plays a pivotal role in determining the intensity of the corrosion-induced expansion applied at the steel–concrete interface. β is thus the primary param-

eter controlling the overall magnitude of expansion $U(t)$, and thereby the extent of crack opening. The product $\beta \cdot A$ determines the maximum imposed expansion, making β a direct modulator of crack initiation and growth.

Rather than calibrating A (already grounded in physical measurements), numerical simulations focused on adjusting β to reproduce experimentally observed crack openings. In this context, the value of β was tuned until the simulated crack opening evolution curve aligned both qualitatively (in terms of crack pattern and morphology) and quantitatively (in terms of magnitude and timing) with experimental results.

As illustrated previously in Figure 86 (included under the Regularization Length subsection), the effect of β on crack opening evolution is significant. Higher values of β (e.g., 80, 100) led to earlier crack initiation and larger crack openings, often overestimating the experimental reference. Conversely, lower values of β delayed cracking and produced more restrained damage evolution. For instance, a value of $\beta = 12.2$ yielded a crack opening evolution that closely matched the experimental reference curve in both shape and magnitude, making it a strong candidate for further simulations. However, alterations to other parameters such as the B parameter can be implemented to fasten crack initiation and better-match both the experimental and numerical curves.

These findings underscore the importance of carefully calibrating β, particularly when the amplitude parameter A is held constant. Moreover, the influence of β must be considered in conjunction with other modeling parameters such as the regularization length ℓ, which promotes earlier crack initiation, and the rate parameter B, which governs the timing of crack development. As will be discussed in the next section, the fracture energy g_c also plays a critical role in enabling further reduction of β by lowering the material's resistance to cracking, thereby improving better agreement with the experimental reference curve.

Fracture Energy g_c

The fracture energy g_c fundamentally controls the material's resistance to crack formation and propagation in phase-field models. In the context of phase-field modeling, the critical strain at which fracture initiates is estimated as in [169]:

$$\epsilon = \sqrt{\frac{g_c}{3 * \ell * E}} \tag{5.2}$$

From the expression (5.2), it is clear that decreasing g_c leads to a lower critical strain. In practical terms, this means that the material will fracture under smaller strain levels. Since the expansion is defined as $U(t) = \beta h(t)$, a lower critical strain implies that a smaller expansion is sufficient to initiate cracking. As a result, lower values of β be-

come capable of triggering fracture. This gives us greater flexibility in reducing β and adjusting the numerical mechanical response.

By decreasing g_c, we are therefore able to reduce the necessary expansion amplitude (i.e., β), which in turn leads to smaller maximum crack openings. This approach was particularly effective in calibrating the model against experimental data from Loukil's work. By carefully selecting a lower g_c value and adjusting β accordingly, we achieved crack opening curves in better agreement with experimental observations, both in terms of timing and magnitude of crack opening.

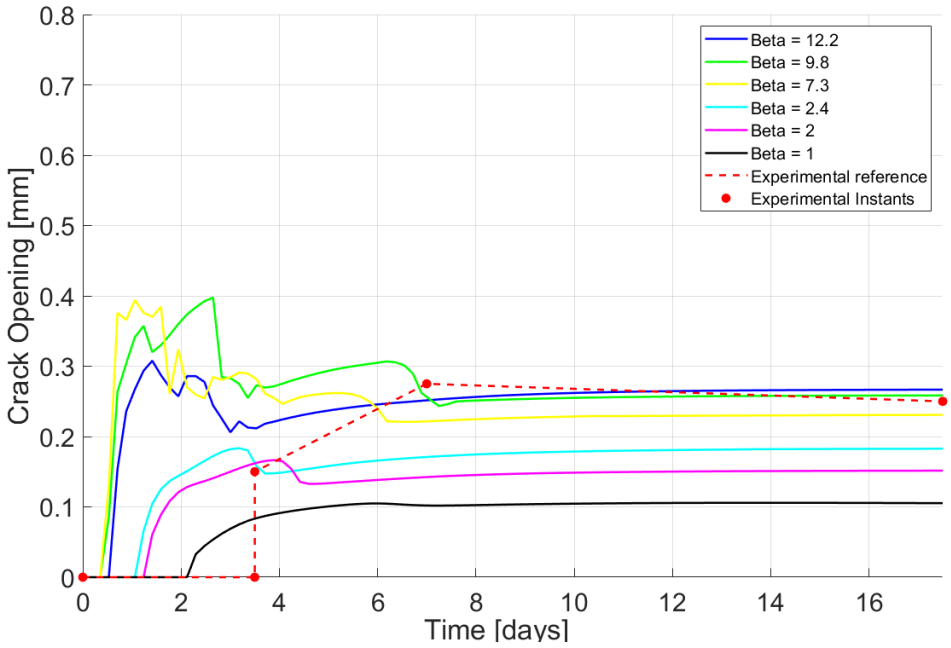

Figure 87: Crack opening over time for smaller g_c value

Among the numerical simulations conducted using different values of the parameter β—with $A = 0.233$ mm being constant and $B = 0.2$ after several numerical trials—the values $\beta = 9.8$ and $\beta = 12.2$ yielded the closest agreement with the experimental reference curve, as shown in Figure 87. To refine the match further, an intermediate value of $\beta = 11.6$ was tested. The resulting curve (Figure 88) demonstrated excellent agreement with the experimental data in both magnitude and timing.

Quantitatively, the numerical crack opening reached the experimentally observed value of 0.15mm at approximately 1.24 days, which is before the actual microstructural cut-off time of 3.5 days fulfilling a key validation criterion. Moreover, the value of 0.275mm, observed experimentally at 7 days, was reproduced numerically at around 4.3 days. The maximum crack opening predicted by the model was 0.3219 mm, occurring at 6.19 days, closely mirroring the overall trend of the experimental data.

This final configuration $A = 0.233$mm (corrosion product thickness), $B = 0.2$, $\beta = 11.6$, and $g_c = 250 \times 10^{-6}$kN/mm provides a well-calibrated baseline capable of capturing the crack opening evolution with high fidelity. These parameters were obtained after carefully balancing the effects of amplitude, growth rate, and material resistance to fracture, and will serve as reference values for future simulations on other microstructures and corrosion conditions.

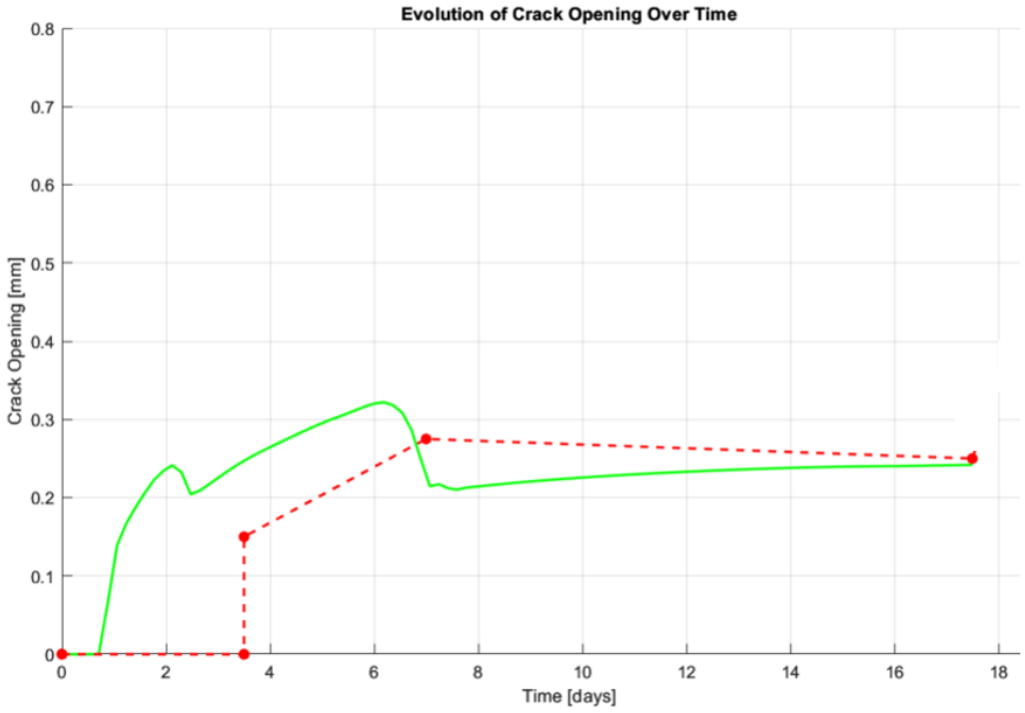

Figure 88: Close correlation between the simulated curve (β = 11.6) and the experimental reference

5.5 Results for the three current densities

In the previous sections, a single microstructure at high current density (200 µA/cm²) was investigated to establish the methodology. In this section, the analysis is extended by systematically examining a wider range of current densities: 200, 100, and 50 µA/cm², each corresponding to different levels of corrosion rate and total charge passed.

The total charge is calculated as the product of the imposed current density i and the exposure duration t, following the relation:

$$Q(t) = i \cdot t$$

where i is the applied current density (in $\mu A/cm^2$) and t is the time (in days).

This provides a unified basis for comparing specimens subjected to different current intensities.

For each current density:

- Several microstructures were simulated, each representing a different corrosion duration (3.5 to 70 days).
- Parameters A, B, and β were calibrated based on corrosion thickness and crack opening data.
- Final results (mesh, damage pattern, and crack opening curve) are presented for each case.

This enables direct comparison across time and current intensity, and provides insight into the kinetics of corrosion-induced cracking.

5.5.1 Current Density: 200 µA/cm²

The experimental average crack openings measured during Loukil's thesis [37] for all prisms tested at 200 µA/cm² are summarized in figure 82c. This current density represents the most aggressive corrosion in our study. Although the maximum total charge reached in the tests is the same across all current densities, here it is achieved in a much shorter period of time (17.5 days) due to the higher applied density. This allows us to observe early crack initiation, mid-stage propagation, and finally a stage where the crack opening stabilizes and no longer evolves significantly, all within a few weeks.

The final parameters of the corrosion-induced expansion (corrosion kinetics) have been determined in the preceding subsection and are presented in Table 8 for a current density equal to 200 $\mu A/cm^2$.

As demonstrated in the preceding section, the methodology outlined enabled the successful generation of the meshes, numerical damage patterns and crack opening-time curves (Figures 89 and 90).

Microstructure designation	Corrosion expansion parameters				
	A (mm)	B (day^{-1})	β	g_c (kN/mm)	ℓ
P14-d200-3.5j-T11-D	0.233	0.20	11.6	2.5×10^{-5}	3 × element size
P16-d200-7j-T14-D	0.378	0.25	5.3	2.5×10^{-5}	3 × element size
P17-d200-17.5j-T16-D	0.409	0.45	1.83	2.5×10^{-5}	3 × element size

Table 8: Corrosion expansion parameters calibrated for the microstructures extracted from experimental specimens exposed to a current density of 200 $\mu A/cm^2$.

The combined plot of all simulated crack opening curves, overlaid with the experimental reference curve, allows direct comparison of each microstructure's predictive performance. All three simulations P14-d200-3.5j-T11-D, P16-d200-7j-T14-D, and P17-d200-17.5j-T16-D exhibit the characteristic phases of crack evolution observed experimentally: initiation, progressive growth, and final saturation. However, these phases occur at slightly different rates and times across the specimens. This variation arises from the different heterogeneity and local composition of each microstructure — such as variations in aggregate distribution, cement matrix density, and porosity — which influence the local stiffness and corrosion-induced stress development.

As corrosion progresses and the total charge increases, the calibrated expansion factor (A×β) — where A is fixed to the experimental corrosion product thickness and β acts as an amplification factor — decreases (Figure 91). Early in the process, when cracks are just forming, a larger A×β (around 2.7 mm) is required to overcome the tensile strength of the concrete and initiate crack growth. Over time, the rust layer thickens and the crack becomes fully developed. At this stage, the structural restraint is reduced: the crack lips separate more easily, so less displacement is needed to produce the same increase in crack width. This is why A×β falls to about 0.75 mm at high total charges — corrosion continues, but the extra mechanical force needed to widen the crack further is minimal. This trend reflects a saturation effect, where once the main crack has opened substantially, additional corrosion has a progressively smaller impact on crack widening.

5.5.2 Current Density: 100 µA/cm²

The experimental average crack openings measured during Loukil's thesis [37] for all prisms tested at 100 µA/cm² are summarized in figure 82b. This current density represents an intermediate corrosion acceleration rate. The maximum total charge which is the same across all current densities (approximately 3500 $\mu A \cdot day/cm^2$), is achieved over a longer period (up to 35 days) than in 200 µA/cm². In the case of this current den-

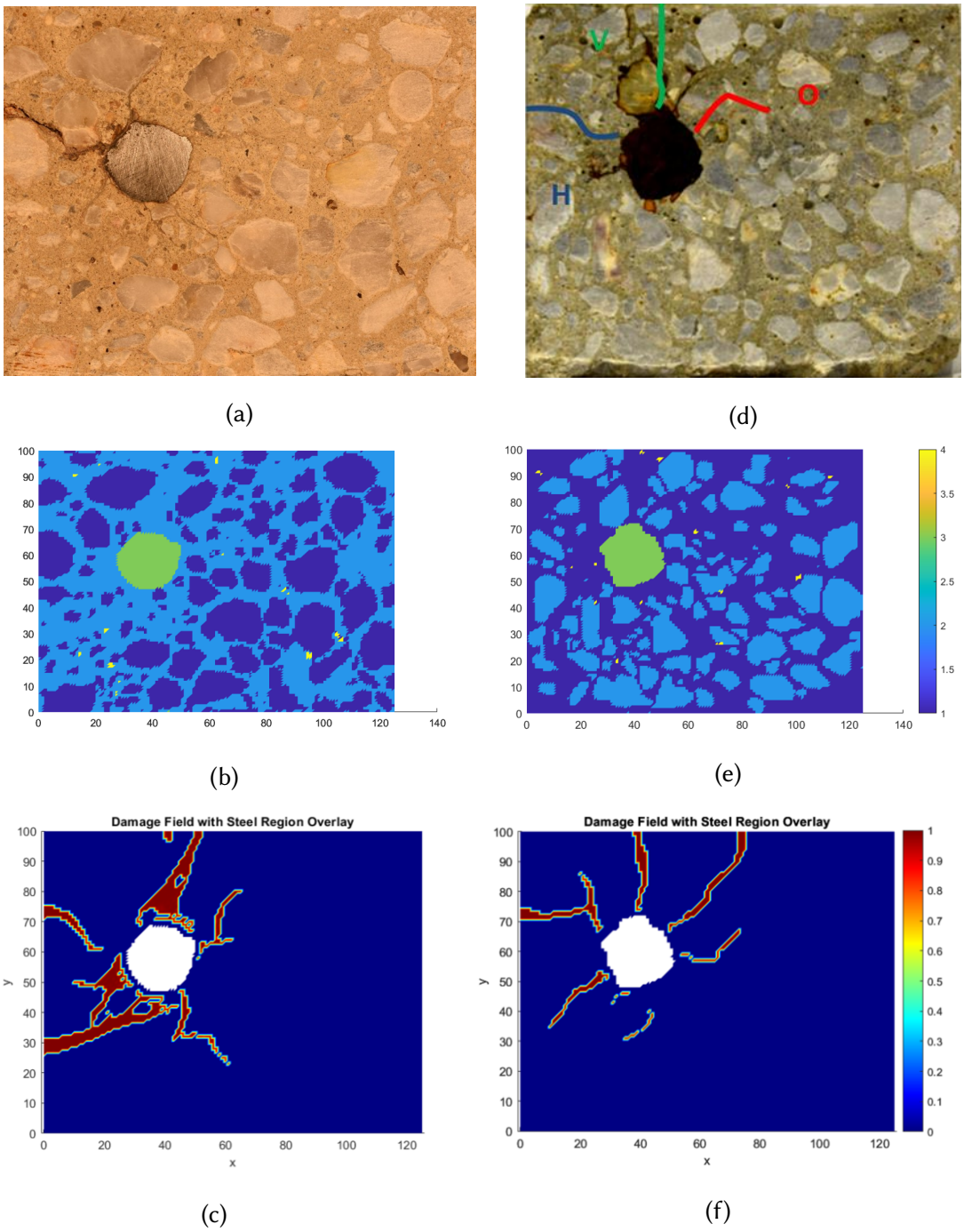

Figure 89: Comparison of experimental, meshed, and numerical damage pattern for two different slices P16–T14–D (a, b, c) and P17–T16–D (d, e, f) after 7 and 17.5 days of corrosion respectively under 200 $\mu A/cm^2$.

sity, a greater number of microstructures were analysed in order to reflect the effect of local heterogeneity.

Throughout this section, we focus on reproducing the *crack opening–time* behavior

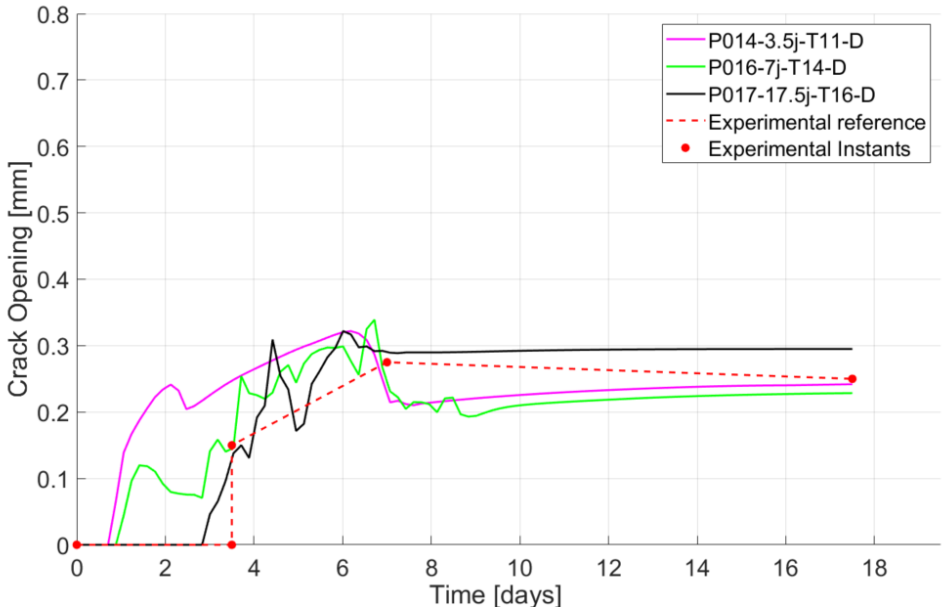

Figure 90: Combined crack opening curves of all slices with the experimental results curve for the current density equal to 200 $\mu A/cm^2$.

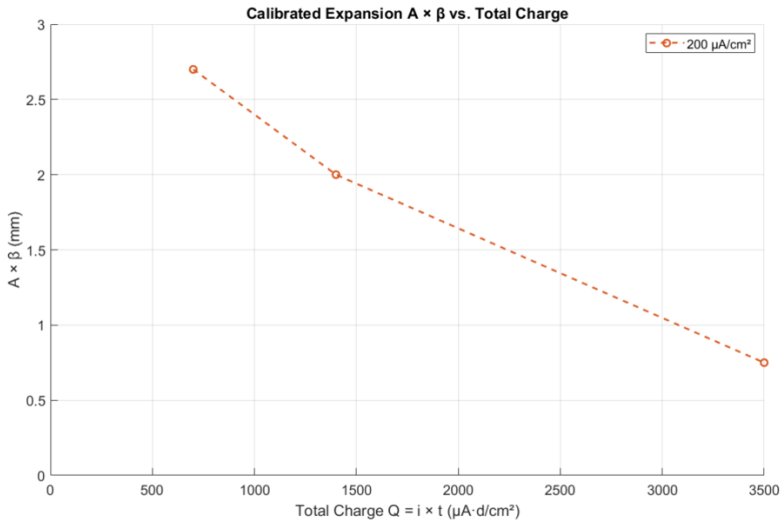

Figure 91: Calibrated expansion A×β vs. total charge for 200 µA/cm².

(reference curve), even when the thickness–time evolution shows local variability.

Based on the methodology outlined in the preceding section, Figures 92, 93, 94 and 95 present the experimental crack patterns as well as the associated microstructure meshes and numerical damage patterns. The employed parameters and associated with microstructures for a current density equal to 100 $\mu A/cm^2$ are presented in Table 9.

Microstructure designation	Corrosion expansion parameters				
	A (mm)	B (day^{-1})	β	g_c (kN/mm)	ℓ
P05-d100-14j-T10-D	0.108	0.30	8.33	2.5×10^{-6}	3 × element size
P05-d100-14j-T14-D	0.108	0.35	15.3	2.5×10^{-6}	3 × element size
P08-d100-21j-T12-D	0.094	0.25	8.5	2.5×10^{-6}	3 × element size
P08-d100-21j-T17-D	0.094	0.25	8.5 / 21.3	2.5×10^{-6}	3 × element size
P09-d100-28j-T10-D	0.207	0.60	6.5	2.5×10^{-6}	3 × element size
P09-d100-28j-T15-D	0.207	0.60	3.38	2.5×10^{-6}	3 × element size
P11-d100-35j-T11-D	0.230	0.28	3.48	2.5×10^{-6}	3 × element size
P11-d100-35j-T14-D	0.230	0.48	3.3	2.5×10^{-6}	3 × element size

Table 9: Corrosion expansion parameters calibrated for the microstructures extracted from experimental specimens exposed to a current density of 100 $\mu A/cm^2$.

In both of the microstructures that were studied (P08-d100-21j-T12-D and P08-d100-21j-T17-D), no damage paths were identified that went towards the left boundary. This could be attributable to a local microstructural blockage and/or limited path continuity within the region in question. Such a blockage or absence of continuity would arise from minor problems with the arrangement of the data, which occur during the preparation step for the tomography. This preparation step includes procedures such as establishing an image threshold and separating phases. Indeed, the presence of small artificial inclusions or merged aggregate regions can appear, locally stiffening the mesh and preventing crack initiation in these zones. Furthermore, the absence of damage pathways towards the left boundary could be also attributable to the way in which corrosion product expansion is applied. Indeed, the expansion is imposed uniform while the distribution of corrosion products is not. In summary, the observations may be attributable to minor numerical discrepancies arising from image-based reconstruction and the implementation of expansion.

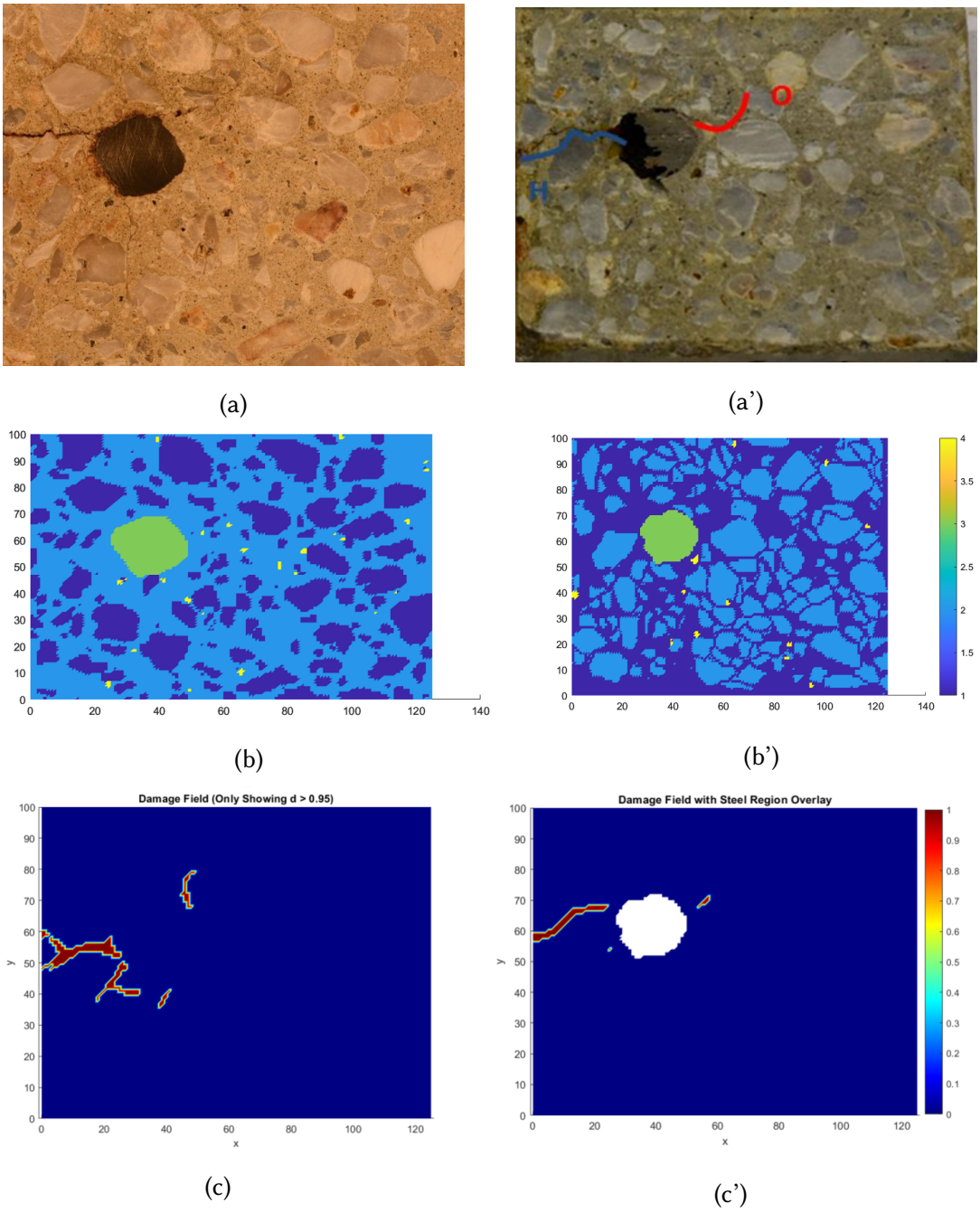

Figure 92: Comparison of experimental, meshed, and numerical damage pattern for two different slices P05–T14–D (a, b, c) and P05–T10–D (a', b', c') after 14 days of corrosion under 100 $\mu A/cm^2$.

The combined plot shows that the model captures the late-stage plateau and the temporary reduction in horizontal opening due to orthogonal cracking. Slice-to-slice spread at the same duration quantifies heterogeneity effects (blocked vs. open horizontal paths). However a drop in measured horizontal opening is observed in some slices

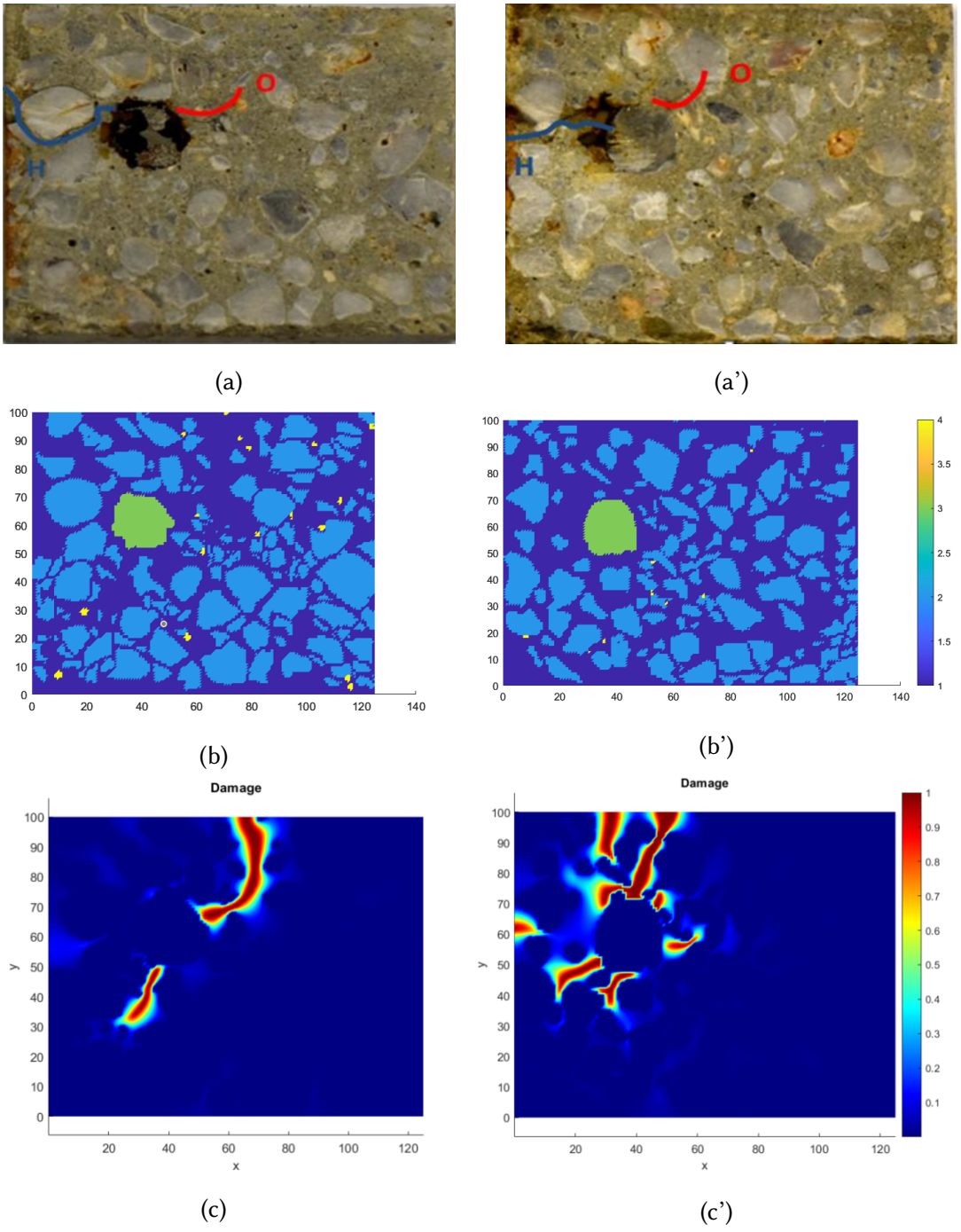

Figure 93: Comparison of experimental, meshed, and numerical damage pattern for two different slices P08–T12–D (a, b, c) and P08–T17–D (a', b', c') after 21 days of corrosion under 100 $\mu A/cm^2$.

due to *vertical crack nucleation* (stress relief along the horizontal crack). Both 35-day slices reproduce the saturation level and the vertical-crack effect on horizontal measurements.

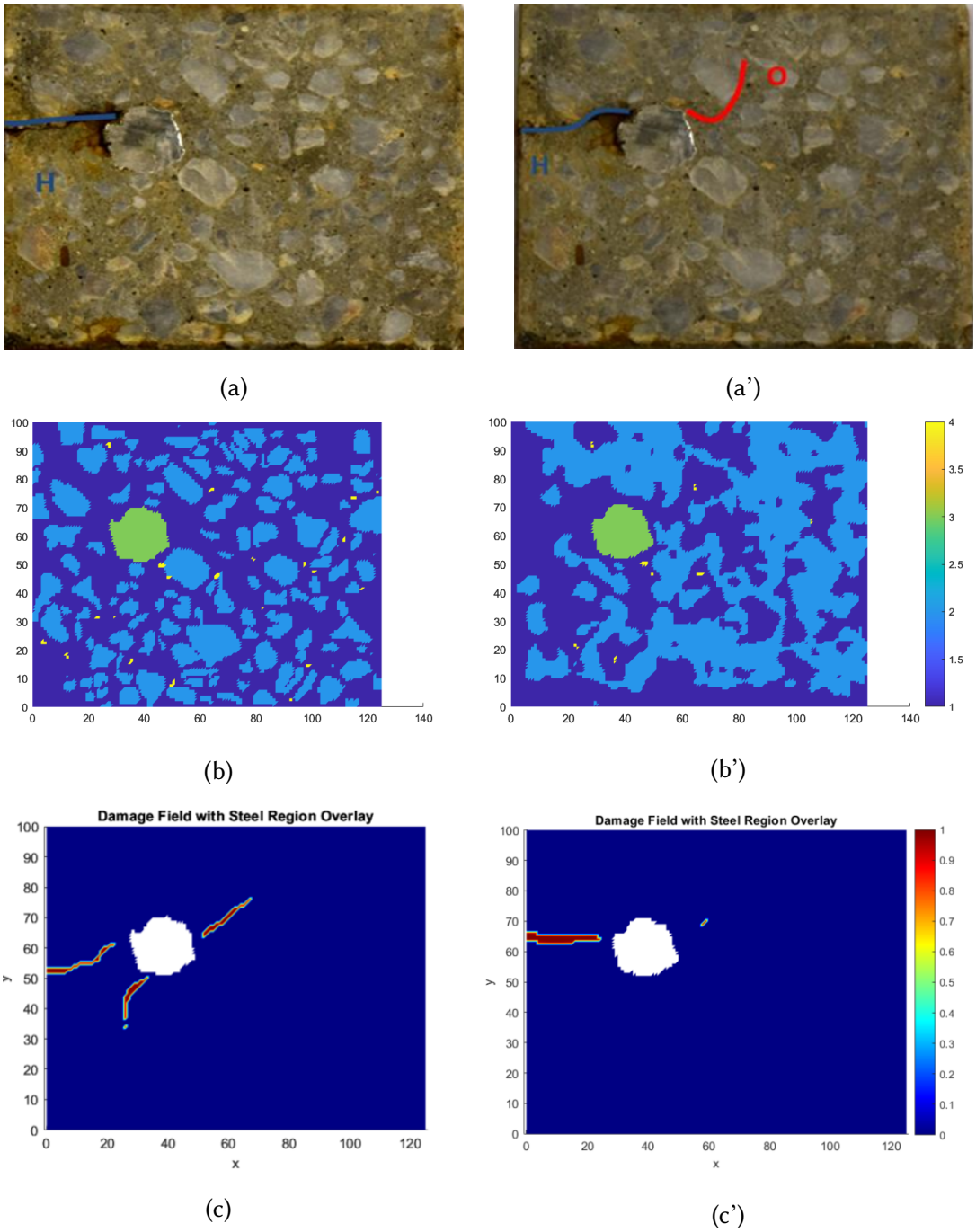

Figure 94: Comparison of experimental, meshed, and numerical damage pattern for two different slices P09-T10-D (a, b, c) and P09-T15-D (a', b', c') after 28 days of corrosion under 100 µA/cm^2.

A×β decreases with total charge: using slice-averaged values across 100 µA/cm²,

$$Q_{100} = \{1400\,\mu\text{A d cm}^{-2},\ 2800\,\mu\text{A d cm}^{-2},\ 3500\,\mu\text{A d cm}^{-2}\}, \quad A\beta_{100} \approx \{1.275\,\text{mm},\ 1.025\,\text{mm},\ 0.78\,\text{mm}\}.$$

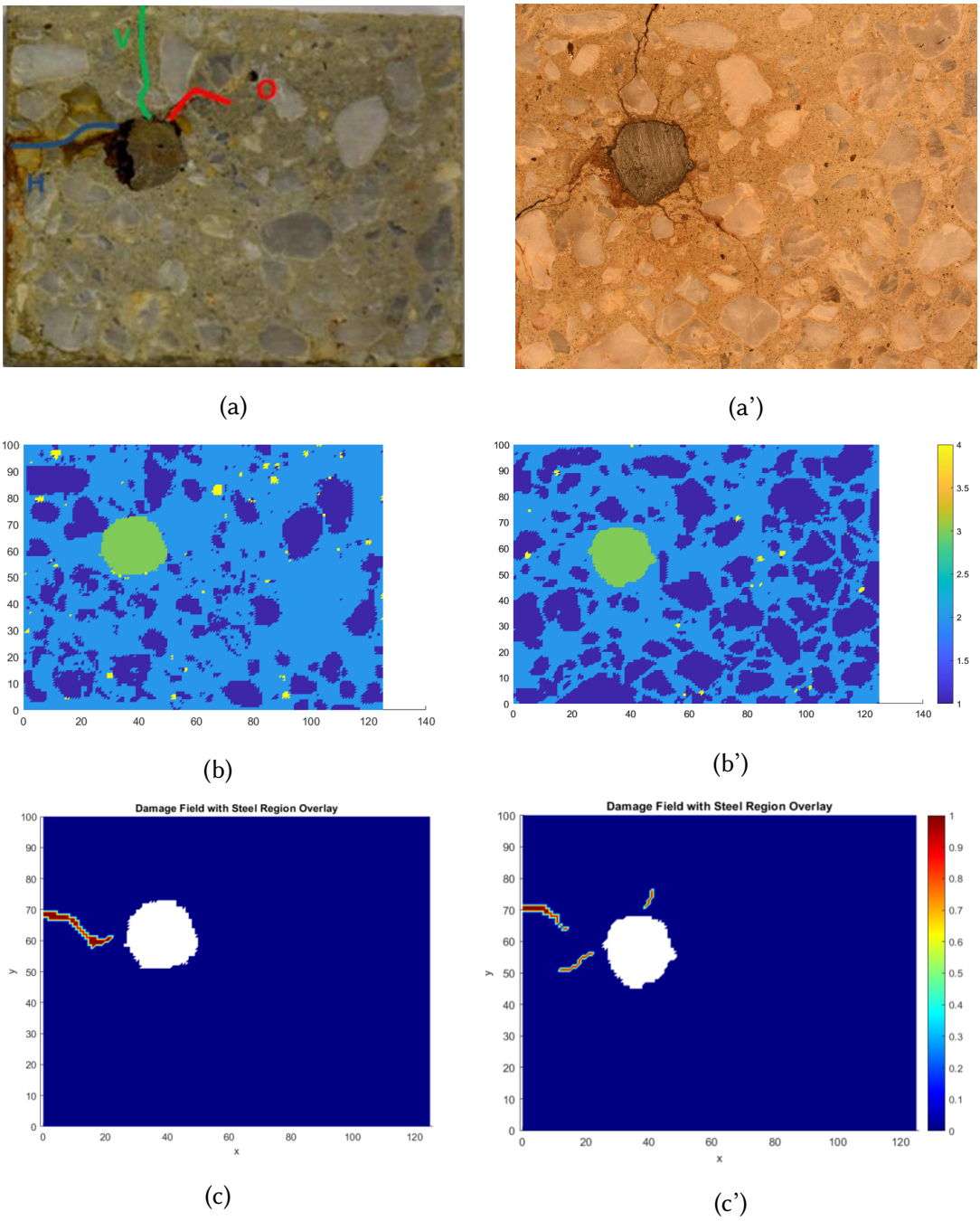

Figure 95: Comparison of experimental, meshed, and numerical damage pattern for two different slices P11-T11-D (a, b, c) and P11-T14-D (a', b', c') after 35 days of corrosion under 100 $\mu A/cm^2$.

As demonstrated in Figure 91, which illustrates the current density of 200 $\mu A/cm^2$, Figure 97 shows that the calibrated expansion factor ($A \times \beta$) decreases with both corrosion and total charge. The asymptotic approach toward $\sim$ 0.75–0.8 mm is consistent with saturation behavior, and the decay is smoother than at 200 $\mu A/cm^2$, in line with

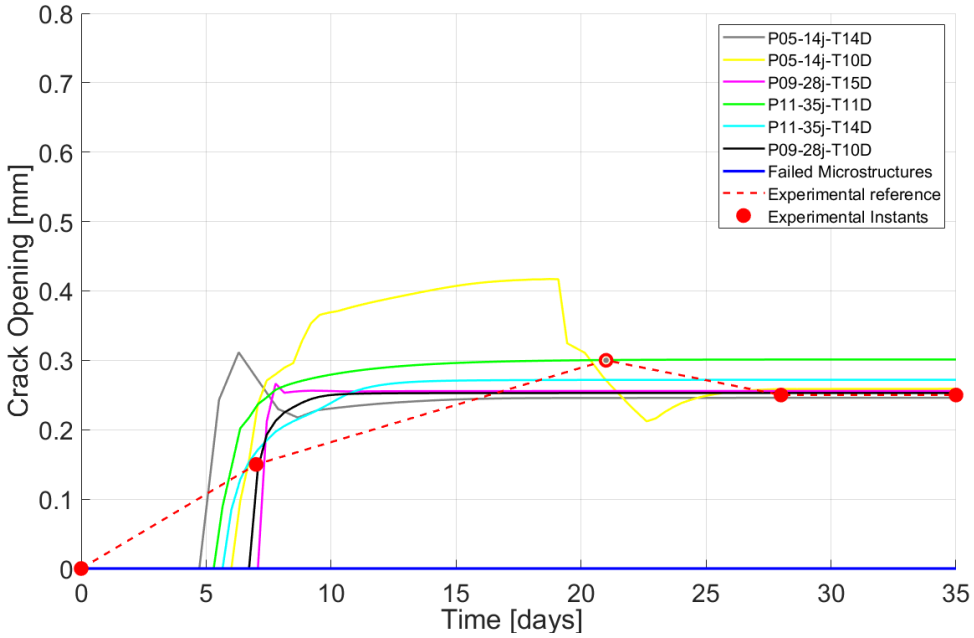

Figure 96: Combined crack opening curves of all slices with the experimental results curve for the current density equal to 100 µA/cm².

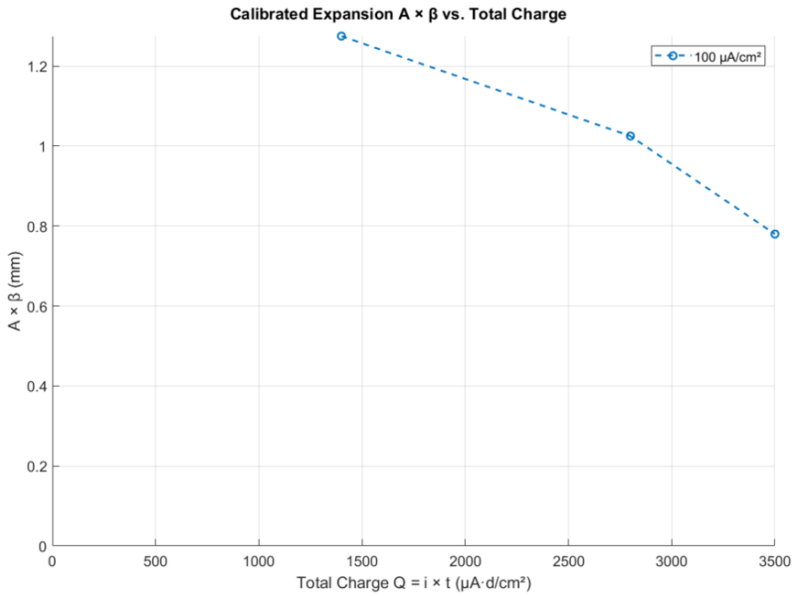

Figure 97: Calibrated expansion A×β vs. total charge for 100 µA/cm².

the slower kinetics.

5.5.3 Current Density: 50 µA/cm²

This current density is consistent with the slowest accelerated corrosion scenario in the present study. The maximum total charge which is the same across all current densities (approximately 3500 µA. days/cm²), is achieved over a longer period (up to 70 days) than in 100 and 200 µA/cm². The lower corrosion rate allows a gradual growth of corrosion products and a clearer view of the transition from initiation to saturation, with strong expression of microstructural heterogeneity. In order to consider the effect of real heterogeneity, the focus is directed towards the analysis of certain microstructures. It turned out that a smaller number of microstructures is analysed in the case of 50 µA/cm² than in the case of 100 µA/cm². However, this number is the same one observed in the 200 µA/cm² case.

The experimental crack openings measured during Loukil's thesis for all prisms tested at 50 µA/cm² are summarized in 82a.

Horizontal cracks dominate the earliest observations. With time, *vertical* cracks can nucleate and intersect the horizontal ones, temporarily stabilizing the measured horizontal opening. Continued rust expansion then *re-increases* the horizontal opening. This behavior (rise the standard then rise) is visible in several prisms and is important for interpreting the horizontal crack opening–time curves used as reference.

Based on the methodology outlined in the preceding section, Figures 98, 99 and 100 present the experimental crack patterns as well as the associated microstructure meshes and numerical damage patterns for a current density of 50 µA/cm². The employed parameters and associated with microstructures are presented in Table 10.

Microstructure designation	**Corrosion expansion parameters**				ℓ
	A (mm)	**B (day^{-1})**	β	g_c (kN/mm)	
P23-d50-14j-T13-D	0.181	0.25	6.6	2.5×10^{-6}	3 × element size
P25-d50-28j-T16-D	0.212	0.10	4.2	2.5×10^{-6}	3 × element size
P27-d50-70j-T9-D	0.271	0.08	3.3	2.5×10^{-6}	3 × element size

Table 10: Corrosion expansion parameters calibrated for the microstructures extracted from experimental specimens exposed to a current density of 50 µA/cm^2.

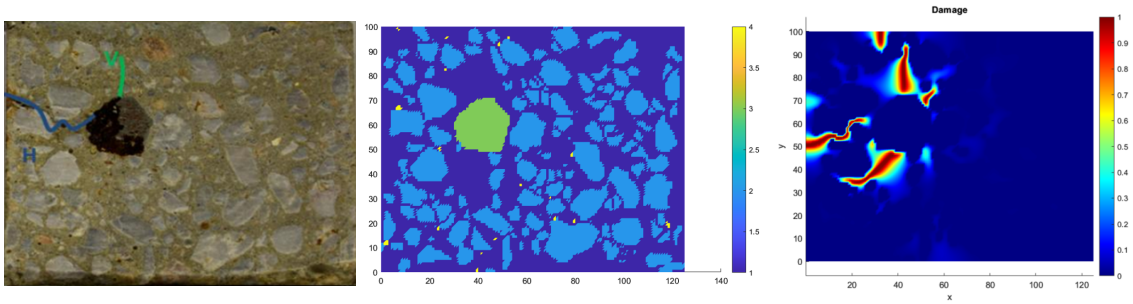

(a) Experimental slice **(b)** Image-based mesh **(c)** Numerical damage pattern

Figure 98: Experimental slice, image-based mesh, and numerical damage pattern for microstructure P23–T13-D after 14 days of corrosion under 50 $\mu A/cm^2$.

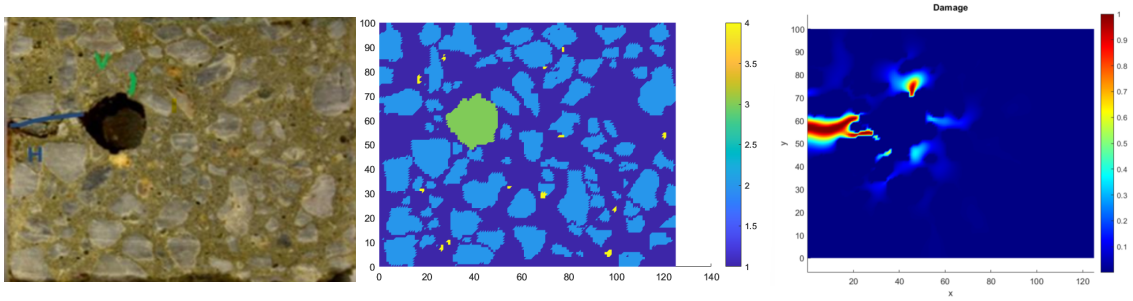

(a) Experimental slice **(b)** Image-based mesh **(c)** Numerical damage pattern

Figure 99: Experimental slice, image-based mesh, and numerical damage pattern for microstructure P25–T16-D after 28 days of corrosion under 50 $\mu A/cm^2$.

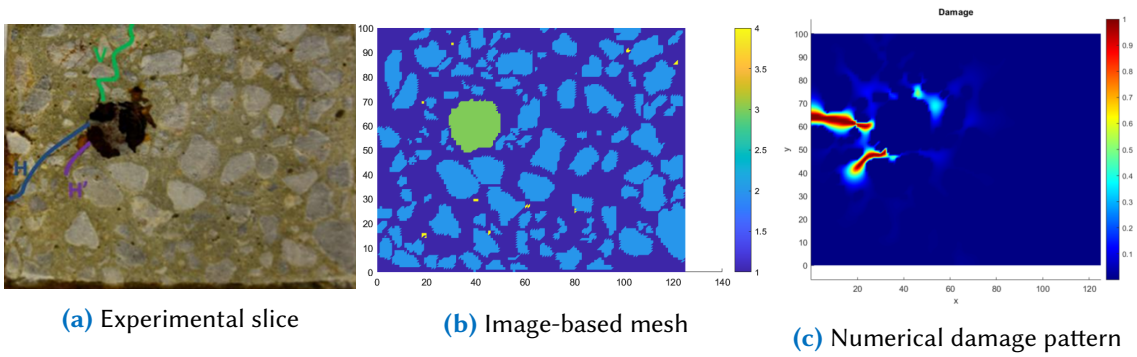

(a) Experimental slice **(b)** Image-based mesh **(c)** Numerical damage pattern

Figure 100: Experimental slice, image-based mesh, and numerical damage pattern for microstructure P27–T9-D after 70 days of corrosion under 50 $\mu A/cm^2$.

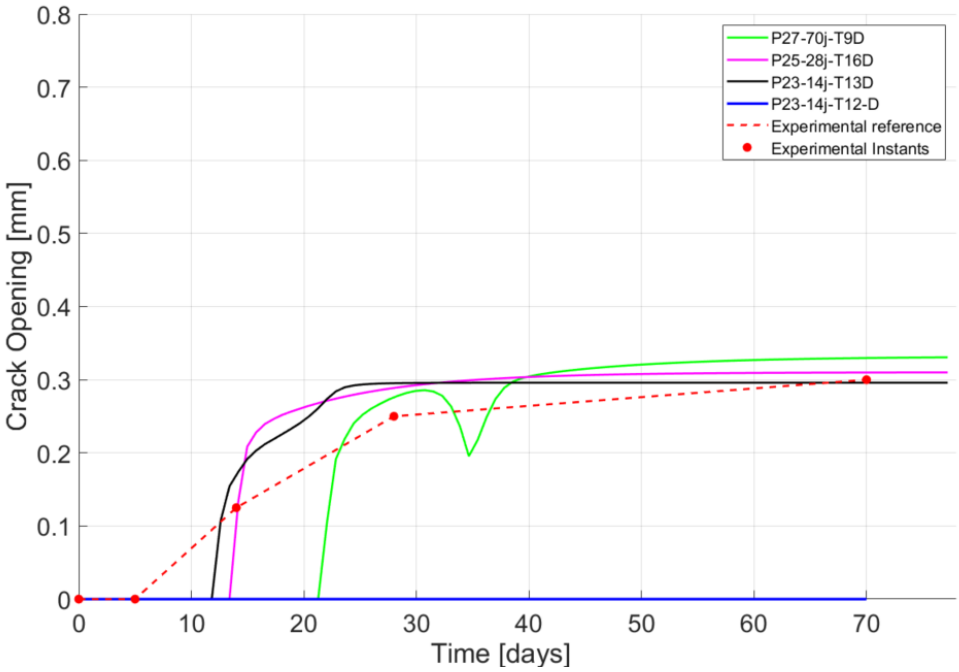

Figure 101: Combined crack opening curves of all slices with the experimental results curve for the current density equal to 50 µA/cm².

The same trend is observed as in Figures 91 and 97: the calibrated expansion factor (A×β) decreases with both corrosion and total charge. The trend of A×β with total charge at 50 µA/cm² is smooth and mildly decreasing. Since A is fixed to the measured thickness, the decrease in A×β reflects diminishing β as cracks are formed and structural restraint lowers. Compared to the 200 and 100 µA/cm² cases, the decay is more gradual in this instance, which is consistent with the hypothesis that corrosion kinetics are slower and damage evolution is more distributed.

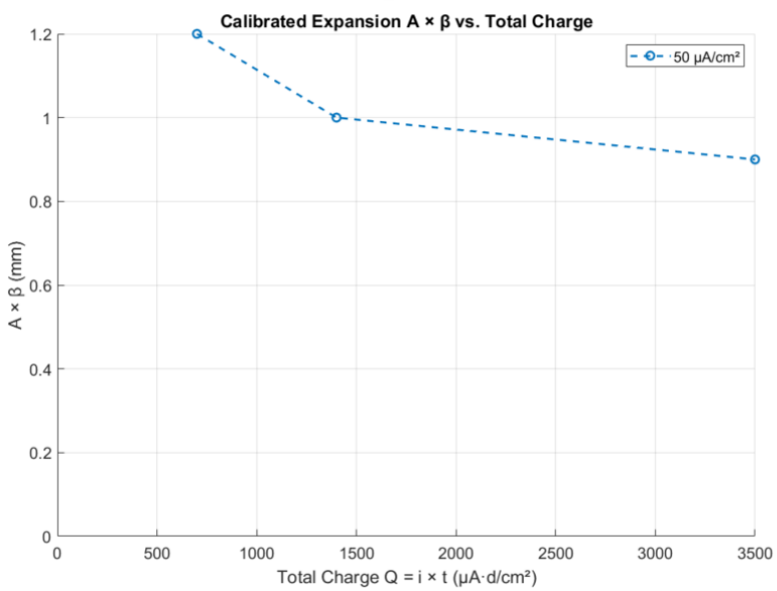

Figure 102: Calibrated expansion A×β vs. total charge for 50 µA/cm².

5.6 Generalized Model

5.6.1 Introduction and motivation

The deterioration of reinforced concrete structures due to steel corrosion represents one of the most critical degradation mechanisms affecting service life and structural safety. When reinforcement corrodes, the electrochemical transformation of metallic iron into expansive corrosion products (principally oxides and hydroxides) generates volumetric expansion at the steel–concrete interface. This expansion induces internal tensile stresses that progressively lead to cracking, loss of bond strength, and eventual spalling of the concrete cover. Capturing this process accurately within a numerical framework is of paramount importance for predictive modelling of durability and structural performance. To accurately reproduce these processes in numerical simulations, it is essential to represent the nonlinear kinetics of corrosion product expansion through a physically meaningful and experimentally calibrated formulation and the mechanically coupled response of the concrete matrix as cracking develops. In this work, the corrosion-induced radial displacement is represented by a time-dependent exponential function that intrinsically accounts for the asymptotic buildup of corrosion products and their mechanical interaction with the surrounding concrete:

$$U(t) = A \cdot \beta(1 - e^{-Bt}) \tag{5.3}$$

where A, β and B are the amplitude, scaling, and rate parameters, respectively. This formulation provides a physically interpretable and flexible means to impose corrosion expansion within a mechanical model, allowing for direct calibration against experimental observations of both corrosion kinetics and crack propagation.

5.6.2 Physical interpretation and calibration of model parameters

Each parameter in Equation (5.3) has a distinct physical meaning and role in the representation of corrosion-induced expansion:

- Amplitude Parameter A: The parameter A represents the asymptotic radial displacement corresponding to the fully developed corrosion layer. It is determined directly from experimental measurements of corrosion product thickness and therefore reflects the volumetric expansion associated with corrosion product formation. As expected, A increases with the total charge Q, consistent with the progressive conversion of steel mass into corrosion products. At higher current densities, equivalent A values are attained over shorter durations due to accelerated anodic dissolution, confirming that A is primarily a function of cumulative corrosion products and therefore exposure time and current density intensity.

- Scaling Parameter β: While A captures the physical expansion potential, the scaling factor β is introduced to adjust the magnitude of the imposed displacement to match the experimentally measured crack openings. The product $A.\beta$ thus defines the effective mechanical expansion transmitted to the concrete, which directly governs the initiation and propagation of cracks. The calibration process revealed that although A increases with Q, the effective product $A.\beta$ exhibits a decreasing trend with increasing total charge. This counterintuitive behavior can be explained by the progressive loss of stiffness and strength in the concrete matrix as corrosion advances. Once microcracking and damage have developed, smaller displacements are sufficient to reproduce observed crack widths. Consequently, as the material degrades, the mechanical system becomes more compliant, and its sensitivity to corrosion-induced expansion increases.

- Rate Parameter B: Calibrated to match the timing of crack opening, B does not exhibit a clear monotonic trend with Q. Rather, its variability is more strongly influenced by local microstructural geometry, volume fraction of aggregates and the interaction between vertical and horizontal cracks. In particular, larger B values were required in configurations where early vertical cracking occurred, suggesting a localized acceleration of mechanical response linked to damage patterns.

5.6.3 Relationship between effective expansion and total charge

Figure 103 illustrates the evolution of the calibrated effective displacement, $A.\beta$, as a function of the total charge Q for all tested current densities (50, 100, and 200 µA/cm²). Despite the differing corrosion rates, the data points appear to coalesce around a single point, converging at a value of approximately 0.75 mm at a Q-value of 3500 µAd/cm². This convergence provides convincing evidence that the effective expansion governing crack formation is primarily a function of the total charge until a certain point. Physically, this implies that the mechanical degradation of the steel–concrete system depends on the total charge and therefore the accumulated corrosion products that has occurred during the designated exposure time. Thereafter, a stabilisation of the global damage is attained. The decay of $A.\beta$ with increasing Q reflects a fundamental transition in system behavior: from an initially stiff and undamaged response, where large expansions are required to initiate cracking, to a progressively weakened and microcracked state, where smaller additional displacements suffice to sustain damage propagation.

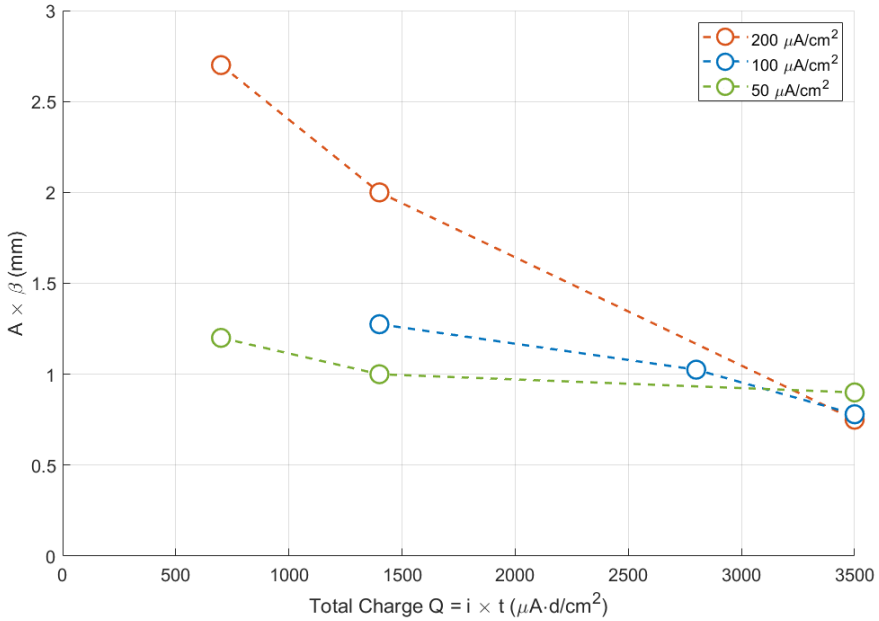

Figure 103: Calibrated effective displacement ($A \cdot \beta$) versus total charge Q for the three current densities.

5.6.4 Generalized modelling framework

The systematic convergence of $A \cdot \beta$ across all current densities establishes the basis for a generalized empirical model of corrosion-induced mechanical expansion. By expressing the effective expansion, $A \cdot \beta$ which is a significant parameter of the expression

of the expansion function $U(t)$, as a function solely of the total charge Q, the model overcomes the need for case-specific calibration with respect to corrosion rate, enabling consistent and scalable predictions across different acceleration regimes. This finding emphasizes the dominant role of cumulative corrosion-induced damage in governing the mechanical response of reinforced concrete. The approach effectively couples the kinetics governed by current density from the mechanical manifestation of damage governed by accumulated corrosion products, offering a unified framework for the simulation of corrosion-driven cracking phenomena. The following subsection formalizes this concept by deriving an empirical expression for $A \cdot \beta$ based on the observed convergence trend, enabling the incorporation of this generalized expansion law into the numerical model for predictive analysis of corrosion-induced damage evolution.

5.6.5 Formulation of a physically-based generalized exponential law

Experimental calibration of the effective displacement $A \cdot \beta$ across multiple corrosion rates revealed a systematic monotonic decay with increasing total charge Q, tending toward a common asymptotic plateau. This decay reflects a mechanically saturating response, where additional corrosion produces a diminishing in displacement due to progressive stiffness degradation and crack coalescence within the concrete. To capture this nonlinear saturation behavior, the following exponential model is proposed:

$$A\beta(i, Q) \;=\; a_1(i)\, e^{-\,a_2(i)\,Q} \;+\; a_3, \qquad Q = i\,t, \tag{5.4}$$

where:

- i is the impressed current density (μA/cm^2);
- t is the corrosion exposure duration (days), so $Q = i\,t$ has units $\mu\text{A} \cdot \text{day/cm}^2$;
- A is the measured corrosion-product thickness (mm);
- β is a dimensionless amplification factor calibrated to reproduce the measured crack-opening curves;
- $a_1(i)$ (mm) is the current-dependent *initial excess* expansion above the plateau;
- $a_2(i)$ ($(\mu\text{A} \cdot \text{day/cm}^2)^{-1}$) is the current-dependent *decay rate*;
- a_3 (mm) is the common asymptotic plateau approached at large Q.

This expression explicitly couples corrosion kinetics (via total charge Q) with mechanical degradation, thus offering a physical interpretation.

5.6.6 Parameter identification and model validation

At early corrosion stages (low Q), the system consisting of steel, steel–concrete interface and concrete is highly confined; thus, a relatively large imposed expansion $A\beta$ is necessary to overcome restraint and initiate cracking. As corrosion progresses, cracking and internal damage gradually reduce mechanical confinement, allowing smaller expansions to produce similar mechanical effects. Consequently, $A\beta$ decreases exponentially and approaches the steady-state plateau a_3, which corresponds to a fully cracked, damage-saturated configuration. To incorporate the influence of corrosion intensity, the parameters $a_1(i)$ and $a_2(i)$ are expressed as power laws of current density:

$$a_1(i) = \alpha\, i^m, \qquad a_2(i) = \kappa\, i^n. \tag{5.5}$$

where α, κ, m, and n are empirical coefficients derived from regression analysis. Substituting Eq. (5.5) into Eq. (5.4) yields:

$$A\beta(i, Q) = a_3 + \alpha\, i^m \, \exp\Big[- \, \kappa\, i^n \, Q \Big]. \tag{5.6}$$

and equivalently as a function of exposure time:

$$A\beta(i, t) = a_3 + \alpha\, i^m \, \exp\Big[- \, \kappa\, i^{n+1} \, t \Big]. \tag{5.7}$$

This formulation provides a quantitative bridge between the current density and the resulting mechanical displacement, encapsulating both the rate-dependent corrosion kinetics and the mechanical evolution of cracking within a single analytical law.

At small total charge Q (early corrosion), mechanical restraint is high and a larger imposed displacement ($A\beta$) is required to initiate/propagate cracking. As corrosion proceeds, restraint diminishes and the mechanical demand decreases exponentially toward a saturated state. The plateau a_3 represents a regime where additional corrosion produces only marginal increases in crack opening demand—consistent with a damage-saturated configuration once cracking is established. The dependence $a_1(i) \propto i^m$ captures the fact that higher current densities start from a larger excess above the plateau, while $a_2(i) \propto i^n$ captures the faster decay (i.e., quicker approach to saturation) at higher i.

The model parameters were calibrated using the experimental data (Q, $A\beta$) for three current densities (i = 50, 100, 200 μA/cm²), with the plateau fixed at a_3 = 0.75 mm. For any two points ($Q1$, y1) and ($Q2$, y2) at fixed i:

$$a_2(i) = -\frac{1}{Q_1 - Q_2}\,\ln\!\left(\frac{y_1 - a_3}{y_2 - a_3}\right), \qquad a_1(i) = (y_1 - a_3)\,e^{\,a_2(i)\,Q_1}. \tag{5.8}$$

Applying (5.8) to the three current densities yields

i (μA/cm^2)	$a_1(i)$ (mm)	$a_2(i)$ $\left((\mu\text{A}\cdot\text{day/cm}^2)^{-1}\right)$
50	0.592233	3.9236×10^{-4}
100	3.538762	1.36295×10^{-3}
200	5.755051	1.54607×10^{-3}

A log–log regression yields:

$$\alpha = 1.2019 \times 10^{-3}, \qquad m = 1.6403, \qquad \kappa = 9.8654 \times 10^{-6}, \qquad n = 0.9892.$$

With $a_3 = 0.75$ mm, the *final* generalized expressions are:

$$A\beta(i, Q) = 0.75 + \left(1.2019 \times 10^{-3}\right) i^{\,1.6403}\,\exp\!\Big[-\left(9.8654 \times 10^{-6}\right) i^{\,0.9892}\,Q\Big] \quad \text{(mm)}, \tag{5.9}$$

$$A\beta(i, t) = 0.75 + \left(1.2019 \times 10^{-3}\right) i^{\,1.6403}\,\exp\!\Big[-\left(9.8654 \times 10^{-6}\right) i^{\,1.9892}\,t\Big] \quad \text{(mm)}. \tag{5.10}$$

Here i is in μA/cm^2, Q in $\mu\text{A}\cdot\text{day/cm}^2$, and t in days.

The reconstructed points correspond to the experimental data within experimental uncertainty, validating the predictive consistency of the model (Figure 104).

To further explore the robustness of the generalized law, two additional current densities 75 μA/cm^2 and 150 μA/cm^2 were tested by plotting their corresponding $A\beta$ values within the same Q-based framework. These values were not individually calibrated, but rather used as test cases to evaluate the predictive power of the established model. As illustrated in Figure 104, both data series align reasonably well with the decay trend identified from the main dataset, further reinforcing the idea that total charge Q influences the corrosion product expansion across different current densities. In the calibrated datasets ($i = 50, 100, 200$ μA/cm^2) the decay curves were observed to *decrease monotonically and converge* toward a common plateau near $A.\beta \simeq 0.75$ mm as the accumulated charge approached

$$Q^{\star} = 3500\ (\mu\text{A}\cdot\text{day/cm}^2).$$

Residual differences between datasets seem to be systematic and minor, arising from current-dependent corrosion product distribution and local cracking kinetics. The con-

vergence at $A.\beta \simeq 0.75$ across all current densities demonstrates that mechanical degradation is governed by cumulative corrosion product damage, the current density intensity and the exposure time.

The purpose of the extended validation is therefore to test this generalized model on other new densities (i.e. $i = 75$ and 150 μA/cm^2) and to see if they also attain the same endpoint when brought to the same dose $Q^\star$.

The predicted values of the effective expansion at common total charges are presented in Table 11.

i (μA/cm^2)	50	75	100	150	200
$A\beta(i, 700)$ (mm)	1.278	1.622	1.938	2.420	2.689
$A\beta(i, 1400)$ (mm)	1.129	1.282	1.366	1.376	1.276
$A\beta(i, 2800)$ (mm)	0.946	0.948	0.915	0.838	0.788
$A\beta(i, Q^* = 3500)$ (mm)	0.891	0.871	0.836	0.783	0.761

Table 11: Computed values of the corrosion expansion parameter $A\beta(i, Q)$ for different current densities i and corrosion charges Q.

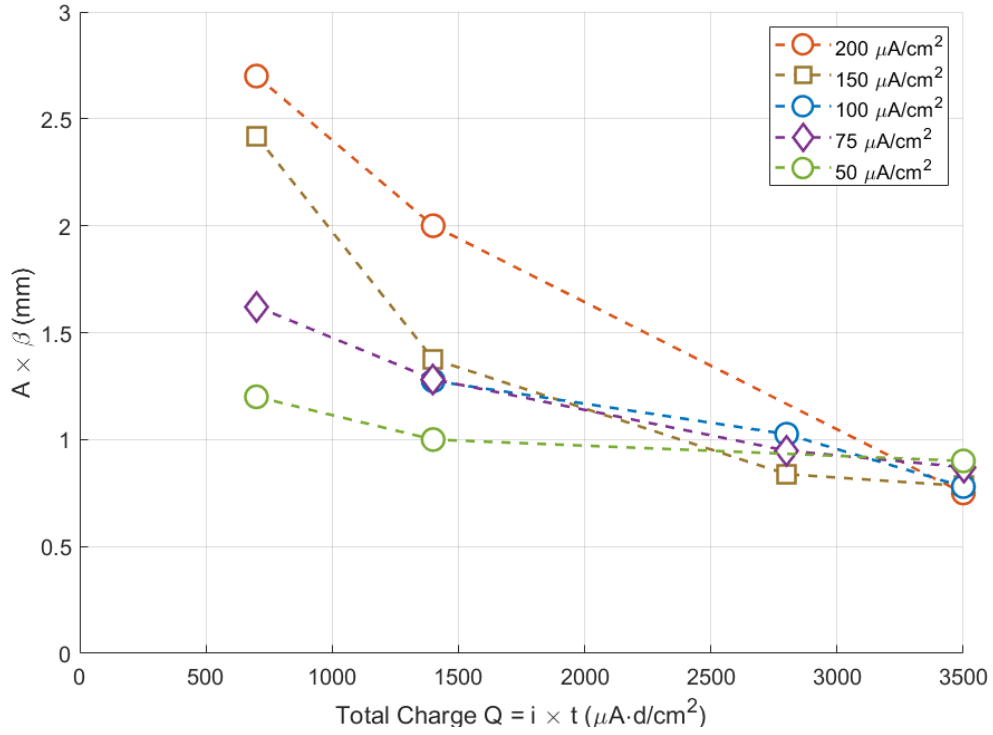

Figure 104: Verification of the generalized $A\beta(Q)$ model for two new current densities (75 and 150 μA/cm^2)

The inverse form of the model offers a practical way to estimate the required me-

chanical expansion to initiate cracking, using purely experimental inputs. Given a corrosion test with known parameters — the current density i, exposure time t, and measured corrosion product thickness A — all of which are directly obtainable from experimental data, one can compute the total charge as:

$$Q = i \cdot t \quad \left(\mu\text{A} \cdot \text{day/cm}^2\right)$$

Then, the generalized law is used to evaluate the corresponding displacement demand $A\beta(Q)$. From this, the amplification factor β — which scales the imposed displacement in numerical models — can be computed as:

$$\beta = \frac{A\beta(Q)}{A(t,i)}$$

This process effectively bridges experimental observations with numerical implementation. It allows to infer the mechanical displacement required to replicate experimental cracking behavior, without resorting to trial-and-error calibration. In this way, the generalized law becomes a powerful tool for guiding simulation setups across varying corrosion conditions.

This generalized law effectively consolidates the behavior of corrosion-induced expansion demand across multiple current densities and durations. It highlights that the total charge ($Q = i \cdot t$), expressed in μA·day/cm², serves as a physically meaningful and unifying parameter for corrosion modeling. The exponential decay behavior not only captures the observed reduction in expansion need over time but also provides a predictive tool for estimating β values for any future corrosion scenario.

The corrosion-induced radial expansion is, finally, represented by the following expression:

$$U(t) = (0.75 + \left(1.2019 \times 10^{-3}\right) i^{1.6403} \exp\left[- \left(9.8654 \times 10^{-6}\right) i^{1.9892} t \right]).(1 - e^{(-Bt)}) \quad . \tag{5.11}$$

5.7 Conclusion

This chapter has presented a comprehensive investigation into the modeling and calibration of corrosion-induced cracking in reinforced concrete, leveraging both experimental data and numerical simulations. Starting from the temporal evolution of corrosion product thickness, the study established a foundation for quantifying the mechanical impact of corrosion as a function of time and current density. These thickness

measurements provided the basis for defining the corrosion-induced expansion at the steel–concrete interface in the phase-field fracture simulations.

Quantitative crack opening curves were extracted from simulations across multiple microstructures, corrosion test durations and current densities, enabling direct comparison with experimental observations. To ensure consistency, the numerical results were extrapolated over the full experimental duration using an exponential displacement function. Key modeling parameters—such as the exponential growth rate B, amplification factor β, regularization length ℓ, and fracture energy g_c—were systematically calibrated. Their influence on crack initiation timing and opening magnitude was thoroughly assessed, highlighting the necessity of coordinated tuning for accurate reproduction of the experimental behavior.

A critical insight from this work is the identification of total charge Q as an effective physical parameter governing the mechanical expansion demand. The effective displacement ($A\beta$) required to reproduce the observed cracking patterns and openings was shown to collapse onto a single decaying curve across all current densities when plotted against Q. This led to the formulation of a generalized exponential model for $A\beta(Q)$, capturing the transition from early crack formation to saturation.

This empirical law not only simplifies the calibration process but also enables predictive modeling across a wide range of corrosion scenarios. Furthermore, it allows the inversion of the model to compute β based purely on experimental inputs—namely, i, t, and A—making it a powerful bridge between experimental characterization and simulation setup.

The methodologies and findings developed here set the stage for future investigations involving more complex geometries, heterogeneous microstructures, and extended loading conditions. The generalized model offers a scalable framework to simulate and predict corrosion-induced damage in reinforced concrete with both accuracy and efficiency.

Chapter 6
General Conclusions and Perspectives

This thesis has addressed the modeling of corrosion-induced cracking in reinforced concrete (RC) structures through the development and application of a phase-field approach. The research has combined numerical modeling with experimental insights to contribute to the understanding and simulation of damage mechanisms driven by corrosion of steel reinforcements.

First a review of existing modeling strategies for corrosion-induced cracking was proposed in Chapter 2, ranging from empirical formulations and classical fracture models to advanced numerical approaches. Through this review, the phase-field method emerged as a promising and thermodynamically consistent tool capable of overcoming the limitations of traditional techniques. Unlike discrete models that require explicit ad-hoc calibrations or cohesive models which are associated with numerical convergence issues, the phase-field approach employs classical Finite Element Method, naturally regularizes solutions with respect to the mesh size, and can handle initiation and propagation of complex, multiple cracks topologies. These features make it a method of choice in the numerical modeling of corrosion-induced cracking in reinforced concrete (RC) structures.

In Chapter 3, the phase field method was implemented and validated using standard reference cases. The model was then extended to account for corrosion-induced expansion using a formulation based on an eigenstrain deformation, enabling the simulation of crack nucleation and propagation due to the accumulation of corrosion products. Numerical investigations focused on assessing the influence of key modeling aspects, such as energy split formulations (Amor vs. Miehe's models), mesh sensitivity, and boundary conditions. Results demonstrated that Miehe's spectral decomposition better captured complex cracking patterns like branching and was more adapted to corrosion-induced cracking problems. Additionally, various non-uniform expansion modes—such as unidirectional and elliptical distributions—were introduced to reflect semi-realistic corrosion geometries, showing significant impact on crack directionality. Parametric studies also confirmed the critical role of rebar positioning and concrete cover thickness in influencing crack initiation zones and their subsequent development.

The contribution of Chapter 4 focused on extending corrosion-induced cracking simulations to realistic concrete microstructures derived from experimental imaging. Using segmented two-dimensional tomography-based images processed via an Artificial Intelligence (AI)-based tool, a framework was developed to incorporate realistic hetero-

geneities into the phase-field model. These image-based models captured the irregular distribution of aggregates and the presence of voids, providing a more representative basis for simulating damage in cementitious materials. Multiple microstructures were simulated to explore how local heterogeneities affect crack initiation and propagation. The resulting crack patterns were qualitatively compared to experimental observations, enabling insights into the influence of aggregate positioning, interfacial voids, and local constraints on crack morphology. While not intended for quantitative validation, this approach served as a useful interpretative tool to better understand the variability of cracking behavior in heterogeneous concrete sections. This investigation demonstrated the added value explicitly incorporating heterogeneities in the corrosion cracking modeling. However, it also pointed to the need for careful handling of image segmentation steps and the high dependency to the uncertainties. As the preprocessing pipeline involves both manual treatment and AI-assisted classification, some limitations may arise in the accurate reconstruction of internal features. These aspects could influence the simulated crack paths and suggest directions for refinement in future imaging and modeling efforts.

In Chapter 5, the time-dependency of corrosion-induced cracking was explicitly addressed. By correlating the growth of the corrosion layer with electrochemical parameters such as current density and total charge, an expansion law was proposed to model the evolution of crack opening over time. Simulations were calibrated using experimental results, and the parameters of a time-dependent model were related to the current density applied to accelerate the corrosion in the experiments. The proposed formulation, identified through measurable experimental quantities, was validated on several configurations and constituted a contribution to the modeling of time-dependent corrosion-induced cracking.

In conclusion, this work has introduced robust numerical simulation tools such as the phase field method for corrosion-induced cracking in RC structures. It has also explored for the first time the identification of time-dependent corrosion expansion models from experiments. The developed models introduced explicitly the heterogeneities such as observed by experimental imagery techniques to provide one-to-one relationship between simulations and experiments. Even though constituting a first tentative in this area, this work paved the way for improvements and future studies, as described in the following. It has laid the groundwork for future enhancements toward truly predictive and experimentally validated models. The coupling of physical insights, experimental data, and numerical modeling opens new opportunities for robust durability assessment and maintenance planning in civil infrastructure.

Perspectives

Several promising avenues for future research emerged from the findings and limitations discussed throughout the thesis:

- **Refinement of the model of corrosion expansion**. The models developed in this work for describing the expansion of the corrosion product require to be further explored, to better take into account the chloride concentration gradients due to exposure conditions, and geometry. Future studies should incorporate spatially varying expansion profiles to better reflect experimental conditions and assess their influence on crack patterns and damage evolution.
- **Improvement of experimental time-dependent crack observations** A key limitation of the study performed in this thesis in the identification of time-dependent models was the lack of data in time regarding experiments, usually involving only a few time snapshots on a few samples, and no clear knowledge about the time when the crack opens on the boundary of the sample. Future works should include more experimental data, and explore new experimental methodologies, such as in-situ monitoring or time-lapse imaging, to track crack evolution in a single sample over time.
- **Modelling of uncertainties** Both experiments and numerical simulations showed a strong influence of the heterogeneities on the crack paths and location of crack opening on the external boundaries of the sample. Taking into account the stochastic nature of this process both in the modelling and in the identification of the model parameters regarding the experiments is a broad scope of research for the future.
- **Extension to 3D modeling, multiphysics coupling and inverse identification:** The models developed in this thesis are two-dimensional. Extending the phase-field corrosion models to 3D will provide more realistic predictions of cracking behavior, especially regarding the influence of heterogeneities, which can induce non-planar cracks. Furthermore, coupling the phase-field fracture model with transport models (e.g., chloride ingress or carbonation diffusion) could enable fully predictive durability simulations over the entire lifecycle of RC structures. Such developments will require efficient numerical strategies to solve the associated 3D, time-dependent, stochastic problems, coupled with experimental observation for inverse identification of parameters.

- **Model parameter identification and calibration:** Developing more robust calibration procedure for the time-dependent models, e.g. using AI tools, could help to automatize the identification procedure of the numerical morels with respect to the experimental result in a stochastic context and improve model predictive capacity.

References

[1] Ba-Thanh Vu, The-Truyen Tran, and Huy-Cuong Nguyen. “Phase-field method of fracture for experimental validation to simulate damage caused by reinforcement corrosion in clam-shell concrete beams”. In: *Construction and Building Materials* 454 (2024), p. 139065.

[2] Sénat Français. *Rapport d’information n°609 (2018–2019): Sécurité des ponts*. 2019. URL: https://www.senat.fr/rap/r18-609/r18-609.html.

[3] Sénat Français. *Rapport d’information n°669 (2021–2022): Suivi de la mission d’information « sécurité des ponts »*. 2022. URL: https://www.senat.fr/rap/r21-669/r21-669.html.

[4] Christoph Gehlen et al. *Condition Control and Assessment of Reinforced Concrete Structures Exposed to Corrosive Environments (Carbonation/Chlorides)*. fib Bulletin No. 59. State-of-the-Art Report. Lausanne, Switzerland: International Federation for Structural Concrete (fib), 2011, p. 80. ISBN: 978-2-88394-099-4.

[5] K. Tuutti. *Corrosion of Steel in Concrete*. Tech. rep. CBI Research Report 4:82. CBI Research Report No. 4.82. Stockholm, Sweden: Swedish Cement and Concrete Research Institute, 1982.

[6] Pietro Pedeferri and Luca Bertolini. *Corrosion Science and Engineering*. 2nd. Cham, Switzerland: Springer, 2018. ISBN: 978-3-319-97624-2. DOI: 10.1007/978-3-319-97625-9.

[7] NACE International. *International Measures of Prevention, Application, and Economics of Corrosion Technologies (IMPACT 2016)*. Houston, TX, USA: NACE International, 2016.

[8] L. Bertolini et al. “Front Matter”. In: *Corrosion of Steel in Concrete*. Weinheim, Germany: Wiley-VCH Verlag GmbH & Co. KGaA, 2003.

[9] D. Addari, B. Elsener, and A. Rossi. “Electrochemistry and surface chemistry of stainless steels in alkaline media simulating concrete pore solutions”. In: *Electrochimica Acta* 53.27 (2008), pp. 8078–8086.

[10] Vagelis G. Papadakis, Costas G. Vayenas, and Michael N. Fardis. “Experimental investigation and mathematical modeling of the concrete carbonation problem”. In: *Chemical Engineering Science* 46.5–6 (1991), pp. 1333–1338.

[11] J. Kropp and H. K. Hilsdorf. *Performance Criteria for Concrete Durability*. London: E & FN Spon, 1995.

[12] Francesco Freddi and Lorenzo Mingazzi. “Phase-field simulations of cover cracking in corroded reinforced concrete beams”. In: *Engineering Fracture Mechanics* 252 (2021), p. 107811.

[13] H. Yang et al. “A phase-field approach for portlandite carbonation and application to self-healing cementitious materials”. In: *Materials and Structures* 55.7 (2022), p. 128.

[14] Z. Wei, C. Wojnar, and Y. Wu. “Hydro-chemo-mechanical phase field formulation for corrosion-induced cracking in reinforced concrete”. In: *Cement and Concrete Research* 146 (2021), p. 106474.

[15] Wen Yao et al. “Simulation of corrosion cracking in reinforced concrete based on multi-phase multi-species electrochemical phase-field modeling”. In: *Materials* 18.16 (2025), p. 3742.

[16] Mario Collepardi. “A state-of-the-art review on the causes of deterioration of concrete in the sea environment”. In: *Cement and Concrete Research* 2.3 (1972), pp. 449–461. DOI: 10.1016/0008-8846(72)90062-0.

[17] C. Andrade and C. L. Page. “Pore solution chemistry and chloride ion penetration in concrete”. In: *Materials and Structures* 19.6 (1986), pp. 437–442. DOI: 10.1007/BF02472021.

[18] Emilio Bastidas-Arteaga. “Reliability of reinforced concrete structures subject to corrosion-fatigue and climate change”. In: *Engineering Structures* 56 (2013), pp. 2288–2298. DOI: 10.1016/j.engstruct.2013.08.038.

[19] D. A. Hausmann. “Steel corrosion in concrete: How does it occur?” In: *Materials Protection* 6.11 (1967), pp. 19–23.

[20] G. K. Glass and N. R. Buenfeld. “The presentation of the chloride threshold level for corrosion of steel in concrete”. In: *Corrosion Science* 39.5 (1997), pp. 1001–1013.

[21] C. Alonso, M. Castellote, and C. Andrade. “Chloride threshold dependence of pitting potential of reinforcements”. In: *Electrochimica Acta* 47.21 (2002), pp. 3469–3481.

[22] R. E. Melchers and C. Q. Li. “Reinforcement corrosion initiation and activation times in concrete structures exposed to severe marine environments”. In: *Cement and Concrete Research* 39.11 (2009), pp. 1068–1076.

[23] U. M. Angst et al. “Critical chloride content in reinforced concrete — A review”. In: *Cement and Concrete Research* 39.12 (2009), pp. 1122–1138.

[24] C. Chalhoub, R. François, and M. Carcasses. “Critical chloride threshold values as a function of cement type and steel surface condition”. In: *Cement and Concrete Research* 134 (2020), p. 106086.

[25] C. Li, L. Jiang, and S. Li. “Effect of limestone powder addition on threshold chloride concentration for steel corrosion in reinforced concrete”. In: *Cement and Concrete Research* 131 (2020), p. 106018.

[26] Nelson Silva. “Chloride Induced Corrosion of Reinforcement Steel in Concrete: Threshold Values and Ion Distributions at the Concrete–Steel Interface”. Thesis for the Degree of Doctor of Philosophy. PhD thesis. Gothenburg, Sweden: Department of Civil and Environmental Engineering, Chalmers University of Technology, 2013. ISBN: 978-91-7385-808-3.

[27] U. M. Angst et al. “Chloride induced reinforcement corrosion: Electrochemical monitoring of initiation stage and chloride threshold values”. In: *Corrosion Science* 53.4 (2011), pp. 1451–1464.

[28] Marcel Pourbaix and Roger W. Staehle. *Lectures on Electrochemical Corrosion*. Classic reference on electrochemical corrosion theory and Pourbaix diagrams. New York, USA: Plenum Press, 1973. ISBN: 9780306306352.

[29] A. Pourbaix. “Corrosion Chemistry within Pits, Crevices and Cracks”. In: *Corrosion Chemistry within Pits, Crevices and Cracks*. Ed. by A. Turnbull. Invited lecture chapter. Teddington, Middlesex, UK: National Physical Laboratory, 1984, pp. 1–15.

[30] Allen J. Bard and Larry R. Faulkner. *Electrochemical Methods: Fundamentals and Applications*. 2nd. Published December 2002. New York, USA: John Wiley & Sons, 2001. ISBN: 9780471405214.

[31] S. Ahmad. “Reinforcement corrosion in concrete structures, its monitoring and service life prediction — A review”. In: *Cement and Concrete Composites* 25.4–5 (2003), pp. 459–471.

[32] U. M. Angst et al. “Concrete cover cracking owing to reinforcement corrosion – theoretical considerations and practical experience”. In: *Materials and Corrosion* 63.12 (2012). Dedicated to Professor Dr. Bernhard Elsener on the occasion of his 60th birthday, pp. 1069–1077.

[33] Robert Baboian. *Corrosion Tests and Standards: Application and Interpretation*. 2nd. West Conshohocken, PA: ASTM International, 2005.

[34] Y. Zhao et al. “Comparison of uniform and non-uniform corrosion induced damage in reinforced concrete based on a Gaussian description of the corrosion layer”. In: *Corrosion Science* 53.9 (2011), pp. 2803–2814.

[35] Y. Zhao, X. Xu, and W. Jin. “Concrete cracking process induced by steel corrosion: A review”. In: *Construction and Building Materials* 25.9 (2011), pp. 3859–3871.

[36] B.-T. Vu et al. “Phase-field modeling for investigating the effect of rebar positioning and uniform versus non-uniform corrosion on concrete fracture”. In: *Fracture and Structural Integrity* 19.73 (2025), pp. 166–180.

[37] Olfa Loukil. “Etude expérimentale et numérique de la dégradation d’éléments structurels en béton armé par corrosion sous courant imposé”. Theses. Université Paris-Est, Oct. 2017. URL: https://theses.hal.science/tel-01759295.

[38] Olfa Loukil et al. “Investigation of Corrosion Product Distribution and Induced Cracking Patterns in Reinforced Concrete Using Accelerated Corrosion Testing”. In: *Applied Sciences* 14.23 (2024), p. 11453.

[39] Olfa Loukil et al. “Experimental and Numerical Analysis of Corrosion-Induced Cracking in Reinforced Concrete”. In: *Applied Mechanics* 6.3 (2025), p. 57.

[40] C. Tongning et al. “Simulation of chloride ion transport in concrete under the coupled effects of a bending load and drying–wetting cycles”. In: *Construction and Building Materials* 241 (2020), p. 118045.

[41] I. G. Ogunsanya and C. M. Hansson. “Detection of the critical chloride threshold of carbon steel rebar in synthetic concrete pore solutions”. In: *RILEM Technical Letters* 3.1 (2019), pp. 75–83.

[42] C. Cao and M. M. S. Cheung. “Non-uniform rust expansion for chloride-induced pitting corrosion in RC structures”. In: *Construction and Building Materials* 51.2 (2014), pp. 75–81.

[43] Y. Zhao et al. “Critical thickness of rust layer at inner and outer surface cracking of concrete cover in reinforced concrete structures”. In: *Corrosion Science* 59.6 (2012), pp. 316–323.

[44] Q.-F. Liu, R. K. L. Su, and F. Xu. “Quantification of the actual expansion and deposition of rust in reinforced concrete”. In: *Construction and Building Materials* 297.32 (2021), p. 123760.

[45] F. Chen, H. Baji, and C.-Q. Li. “A comparative study on factors affecting time to cover cracking as a service life indicator”. In: *Construction and Building Materials* 163.6 (2018), pp. 681–694.

[46] G. Malumbela, P. Moyo, and M. Alexander. "Longitudinal strains and stiffness of RC beams under load as measures of corrosion levels". In: *Engineering Structures* 35.2 (2012), pp. 215–227.

[47] J. Rodriguez, L. Ortega, and J. Casal. "Load carrying capacity of concrete structures with corroded reinforcement". In: *Construction and Building Materials* 11.4 (1997), pp. 239–248.

[48] P. Turcry et al. "Vieillissement naturel du béton armé: expérimentations in situ du PN PERFDUB". In: *Academic Journal of Civil Engineering* (2022). URL: https://journal.augc.asso.fr/index.php/ajce/article/view/3243.

[49] A. A. Torres-Acosta, S. Navarro-Gutiérrez, and J. Terán-Guillén. "Residual flexural capacity of corroded reinforced concrete beams". In: *Engineering Structures* 29.6 (2007), pp. 1145–1152.

[50] R. K. Biswas et al. "Effect of non-uniform rebar corrosion on structural performance of RC structures: A numerical and experimental investigation". In: *Construction and Building Materials* 230 (2020), p. 116908.

[51] S. Robuschi et al. "Bond of naturally corroded, plain reinforcing bars in concrete". In: *Structure and Infrastructure Engineering* 17.6 (2020), pp. 792–808.

[52] C. Van Steen et al. "On-site inspection of a reinforced concrete structure deteriorated due to corrosion by means of acoustic emission and other techniques". In: *Proceedings of the Structural Faults and Repair Conference*. Paper presented at the Structural Faults and Repair Conference. Edinburgh, Scotland, May 2018, pp. 14–17.

[53] D. De Domenico, D. Messina, and A. Recupero. "A Combined Experimental–Numerical Framework for Assessing the Load-Bearing Capacity of Existing PC Bridge Decks Accounting for Corrosion of Prestressing Strands". In: *Materials* 14.17 (2021), p. 4914.

[54] W. Zhu and R. François. "Corrosion of the reinforcement and its influence on the residual structural performance of a 26-year-old corroded RC beam". In: *Construction and Building Materials* 51.2 (2014), pp. 461–472.

[55] M. Otieno et al. "Acceleration of steel corrosion in concrete by cyclic wetting and drying: effect of drying duration and concrete quality". In: *Materials and Structures* 52.2 (2019), p. 50.

[56] H. Ye et al. "Performance of reinforced concrete beams corroded under sustained service loads: A comparative study of two accelerated corrosion techniques". In: *Construction and Building Materials* 162.5 (2018), pp. 286–297.

[57] C. Andrade and A. Castillo. “Evolution of reinforcement corrosion due to climatic variations”. In: *Materials and Corrosion* 54.6 (2003), pp. 379–386.

[58] J. O’Flaherty et al. “Effect of under-reinforcement on the flexural strength of corroded beams”. In: *Materials and Structures* 41.2 (2007), pp. 311–321.

[59] A. Almusallam. “Effect of degree of corrosion on the properties of reinforcing steel bars”. In: *Construction and Building Materials* 15.8 (2001), pp. 361–368.

[60] M. Elgarf. “The effect of reinforcement corrosion on the structural performance of concrete flexural members”. PhD Thesis. Aberdeen, UK: University of Aberdeen, Department of Engineering, 1994.

[61] L. Hariche et al. “Effects of reinforcement configuration and sustained load on the behaviour of reinforced concrete beams affected by reinforcing steel corrosion”. In: *Cement and Concrete Composites* 34.10 (2012), pp. 1202–1209.

[62] Y. Lu et al. “Effects of simultaneous fatigue loading and corrosion on the behavior of reinforced beams”. In: *Construction and Building Materials* 181.24 (2018), pp. 85–93.

[63] H. Seok So and G. Millard. “On-site measurements on corrosion rate of steel in reinforced concrete”. In: *ACI Materials Journal* 104.6 (2007), pp. 638–642.

[64] S. A. Alghamdi and S. Ahmad. “Service life prediction of RC structures based on correlation between electrochemical and gravimetric reinforcement corrosion rates”. In: *Cement and Concrete Composites* 47.3 (2014), pp. 64–68.

[65] C. Andrade et al. “On-site corrosion rate measurements: 3D simulation and representative values”. In: *Materials and Corrosion* 63.12 (2012), pp. 1154–1164.

[66] C. Andrade, C. Alonso, and J. Sarria. “Corrosion rate evolution in concrete structures exposed to the atmosphere”. In: *Cement and Concrete Composites* 24.1 (2002), pp. 55–64.

[67] C. Andrade et al. “Estimating corrosion attack in reinforced concrete by means of crack opening”. In: *Structural Concrete* 17.4 (2016), pp. 533–540.

[68] T. El Maaddawy and K. Soudki. “Effectiveness of impressed current technique to simulate corrosion of steel reinforcement in concrete”. In: *Journal of Materials in Civil Engineering* 15.1 (2003), pp. 41–47.

[69] G. Malumbela, P. Moyo, and M. Alexander. “A step towards standardising accelerated corrosion tests on laboratory reinforced concrete specimens”. In: *Journal of the South African Institution of Civil Engineering* 54.2 (2012), pp. 78–85.

[70] W. Feng et al. “Methods of accelerating chloride-induced corrosion in steel-reinforced concrete: A comparative review”. In: *Construction and Building Materials* 289.23 (2021), p. 123165.

[71] T. Liu and R. E. Weyers. “Modeling the time-to-corrosion cracking in chloride contaminated reinforced concrete structures”. In: *Cement and Concrete Research* 28.3 (1998), pp. 365–379.

[72] S. J. Pantazopoulou and K. D. Papoulia. “Modeling cover-cracking due to reinforcement corrosion in RC structures”. In: *Journal of Engineering Mechanics* 127.4 (2001), pp. 342–351.

[73] G. Williamson and L. A. Clark. “Pressure required to cause cover cracking of concrete due to reinforcement corrosion”. In: *Magazine of Concrete Research* 52.6 (2000), pp. 387–398.

[74] K. Bhargava et al. “Modeling of time to corrosion-induced cover cracking in reinforced concrete structures”. In: *Cement and Concrete Research* 35.11 (2005), pp. 2203–2218.

[75] C. Lu, W. Jin, and R. Liu. “Reinforcement corrosion-induced cover cracking and its time prediction for reinforced concrete structures”. In: *Corrosion Science* 53.4 (2011), pp. 1337–1347.

[76] J. A. Mullard and M. G. Stewart. “Corrosion-induced cover cracking: New test data and predictive models”. In: *ACI Structural Journal* 108.1 (2011), pp. 71–79.

[77] Y. Zhao and W. Jin. “Modeling the amount of steel corrosion at cracking of concrete cover”. In: *Corrosion Science* 48.6 (2006), pp. 1779–1792.

[78] W. Zhang, A. Castel, and R. François. “The corrosion pattern of reinforcement and its influence on serviceability of reinforced concrete members”. In: *Materials and Structures* 43 (2010), pp. 533–546.

[79] R. Roshn, N. Noel, and B. Martin-Perez. “Validation of the thick-walled cylinder analogy for modeling corrosion-induced cracking in reinforced concrete”. In: *Construction and Building Materials* 263 (2020), p. 120180.

[80] S. Liu et al. “Corrosion-induced cracking behavior of lightweight aggregate concrete”. In: *Construction and Building Materials* 373 (2023), p. 130857.

[81] P.A. Cundall and O.D.L. Strack. “A discrete numerical model for granular assemblies”. In: *Géotechnique* 29.1 (1979), pp. 47–65.

[82] L. Rothenburg and R.J. Bathurst. "Influence of particle eccentricity on micromechanical behavior of granular materials". In: *Mechanics of Materials* 16.1-2 (1993), pp. 141–152.

[83] F.A. Tavarez and M.E. Plesha. "Discrete element method for modelling solid and particulate materials". In: *International Journal for Numerical Methods in Engineering* 70.4 (2007), pp. 379–404.

[84] P. Jiradilok, K. Nagai, and K. Matsumoto. "Meso-scale modeling of non-uniformly corroded reinforced concrete using 3D discrete analysis". In: *Engineering Structures* 185 (2019), pp. 305–321.

[85] Di Qiao et al. "Experimental and analytical evaluation of concrete cover spalling behavior due to local corrosion". In: *Journal of Structural Engineering A (JSCE)* 61A (2015). Available via J-STAGE, pp. 707–719.

[86] L. M. Kachanov. "Time of the rupture process under creep conditions". In: *Izv. Akad. Nauk SSSR Otd. Tekh. Nauk* 8 (1958). In Russian, pp. 26–31.

[87] Y. N. Rabotnov, F. A. Leckie, and W. Prager. "Creep Problems in Structural Members". In: *Journal of Applied Mechanics* 37 (1970), pp. 249–249.

[88] J. Lemaitre. "A continuous damage mechanics model for ductile fracture". In: *Journal of Engineering Materials and Technology* 107 (1985), pp. 83–89.

[89] S. Murakami. "Mechanical modeling of material damage". In: *Journal of Applied Mechanics* 55 (1988), pp. 280–286.

[90] J. W. Ju. "Isotropic and anisotropic damage variables in continuum damage mechanics". In: *Journal of Engineering Mechanics* 116.12 (1990), pp. 2764–2770.

[91] K. E. Løland. "Continuous damage model for load-response estimation of concrete". In: *Cement and Concrete Research* 10 (1980), pp. 395–402.

[92] J. Mazars. "A description of micro- and macroscale damage of concrete structures". In: *Engineering Fracture Mechanics* 25 (1986), pp. 729–737.

[93] I. Zreid and E. Brühwiler. "Modeling of corrosion-induced concrete cover cracking using continuum damage mechanics". In: *Materials and Structures* 45.9 (2012), pp. 1347–1355.

[94] T. Pan. "Continuous damage of concrete structures due to reinforcement corrosion: A micromechanical and multi-physics based analysis". In: *Journal of Building Engineering* 83 (2024), p. 108058.

[95] B. Zeng et al. "Corrosion-induced cracking pattern analysis of RC beams under sustained load". In: *Buildings* 12.12 (2022), p. 2256.

[96] S. C. Seetharam et al. “A mesoscale framework for analysis of corrosion induced damage of concrete”. In: *Construction and Building Materials* 223 (2019), pp. 718–734.

[97] D. Qiao et al. “Modeling of corrosion-induced damage in reinforced concrete considering electro-mechanical coupling”. In: *Journal of Advanced Concrete Technology* 14.11 (2016), pp. 664–678.

[98] A.L. Gurson. “Continuum theory of ductile rupture by void nucleation and growth: Part I—Yield criteria and flow rules for porous ductile media”. In: *Journal of Engineering Materials and Technology* 99 (1977), pp. 2–15.

[99] Bhasker Paliwal and K.T. Ramesh. “An interacting micro-crack damage model for failure of brittle materials under compression”. In: *Journal of the Mechanics and Physics of Solids* 56.3 (2008), pp. 896–923.

[100] N. Kinoshita and T. Mura. “Elastic fields of inclusions in anisotropic media”. In: *Physica Status Solidi (a)* 5.3 (1971), pp. 759–768.

[101] T. Mori and K. Tanaka. “Average stress in matrix and average elastic energy of materials with misfitting inclusions”. In: *Acta Metallurgica* 21.5 (1973), pp. 571–574.

[102] B. Budiansky and R.J. O’Connell. “Elastic moduli of a cracked solid”. In: *International Journal of Solids and Structures* 12.2 (1976), pp. 81–97.

[103] H. Horii and S. Nemat-Nasser. “Overall moduli of solids with microcracks: Load-induced anisotropy”. In: *Journal of the Mechanics and Physics of Solids* 31.2 (1983), pp. 155–171.

[104] Z. Hashin. “The differential scheme and its application to cracked materials”. In: *Journal of the Mechanics and Physics of Solids* 36.6 (1988), pp. 719–734.

[105] R.W. Zimmerman. “Elastic moduli of a solid containing spherical inclusions”. In: *Mechanics of Materials* 12.1 (1991), pp. 17–24.

[106] Q.Z. Zhu, J.F. Shao, and D. Kondo. “A micromechanics-based thermodynamic formulation of isotropic damage with unilateral and friction effects”. In: *European Journal of Mechanics - A/Solids* 30 (2011), pp. 316–325.

[107] Q.Z. Zhu and J.F. Shao. “A refined micromechanical damage–friction model with strength prediction for rock-like materials under compression”. In: *International Journal of Solids and Structures* 60-61 (2015), pp. 75–83.

[108] Q.Z. Zhu, L.Y. Zhao, and J.F. Shao. "Analytical and numerical analysis of frictional damage in quasi brittle materials". In: *Journal of the Mechanics and Physics of Solids* 92 (2016), pp. 137–163.

[109] L.Y. Zhao, J.F. Shao, and Q.Z. Zhu. "Analysis of localized cracking in quasi-brittle materials with a micro-mechanics based friction-damage approach". In: *Journal of the Mechanics and Physics of Solids* 119 (2018), pp. 163–187.

[110] Ha-Won Song et al. "A Micro-mechanics Based Corrosion Model for Predicting the Service Life of Reinforced Concrete Structures". In: *International Journal of Electrochemical Science* 2 (2007), pp. 341–354.

[111] Eduardo R. Rios. "A micro-mechanics model of corrosion-fatigue crack growth in steels". In: *Fatigue & Fracture of Engineering Materials & Structures* 19.11 (1996), pp. 1437–1450.

[112] D. S. Dugdale. "Yielding of steel sheets containing slits". In: *Journal of the Mechanics and Physics of Solids* 8.2 (1960), pp. 100–104.

[113] G. I. Barenblatt. "The mathematical theory of equilibrium cracks in brittle fracture". In: *Advances in Applied Mechanics* 7 (1962), pp. 55–129.

[114] A. Hillerborg, M. Modéer, and P.-E. Petersson. "Analysis of crack formation and crack growth in concrete by means of fracture mechanics and finite elements". In: *Cement and Concrete Research* 6.6 (1976), pp. 773–781.

[115] Xun Xi, Shangtong Yang, and Chun-Qing Li. "A non-uniform corrosion model and meso-scale fracture modelling of concrete". In: *Cement and Concrete Research* 108 (2018), pp. 87–102.

[116] Zdeněk P Bažant and Jaime Planas. *Fracture and size effect in concrete and other quasibrittle materials*. Boca Raton, FL: CRC press, 1998. ISBN: 9780849382840.

[117] J. Alfaiate, G.N. Wells, and L.J. Sluys. "On the use of embedded discontinuities for plasticity and damage". In: *Computers & Structures* 81.6 (2003), pp. 691–701.

[118] Nicolas Moës, John Dolbow, and Ted Belytschko. "A finite element method for crack growth without remeshing". In: *International journal for numerical methods in engineering* 46.1 (1999), pp. 131–150.

[119] G.N. Wells and L.J. Sluys. "A new method for modelling cohesive cracks using finite elements". In: *International journal for numerical methods in engineering* 50.12 (2001), pp. 2667–2682.

[120] Santiago Guzmán, Jaime C. Gálvez, and José M. Sancho. "Modelling of corrosion-induced cover cracking in reinforced concrete by an embedded cohesive crack finite element". In: *Engineering Fracture Mechanics* 93 (2012), pp. 92–107.

[121] Shangtong Yang et al. "Numerical modeling of nonuniform corrosion-induced concrete crack width". In: *Journal of Structural Engineering* 144.8 (2018).

[122] T. Belytschko and T. Black. "Elastic crack growth in finite elements with minimal remeshing". In: *International Journal for Numerical Methods in Engineering* 45.5 (1999), pp. 601–620.

[123] G. Zi, T. Rabczuk, and W. Wall. "Extended meshfree methods without branch enrichment for cohesive cracks". In: *Computational Mechanics* 40 (2007), pp. 367–382.

[124] Ravindra Duddu, Nithyanand Kota, and Siddiq M. Qidwai. "An Extended Finite Element Method Based Approach for Modeling Crevice and Pitting Corrosion". In: *Journal of Applied Mechanics* 83.8 (2016), p. 081003.

[125] Hao Jin and Shuo Yu. "Study on corrosion-induced cracks for the concrete with transverse cracks using an improved CDM-XFEM". In: *Construction and Building Materials* 318 (2022), p. 126173.

[126] M. J. Mirzaee, Farshid J. Alaee, and M. Hajsadeghi. "Modeling of cracks induced by corrosion of reinforcing bars in marine structures using XFEM". In: *11th International Conference on Coasts, Ports and Marine Structures (ICOPMAS)*. 24–26 Nov. 2014. Tehran, Iran, 2014.

[127] J. Oliver, A. E. Huespe, and P. J. Sánchez. "A comparative study on finite elements for capturing strong discontinuities: E-FEM vs X-FEM". In: *Computer Methods in Applied Mechanics and Engineering* 195.33-36 (2006), pp. 4732–4752.

[128] D. Dias-da-Costa et al. "A comparative study on the modelling of discontinuous fracture by means of enriched nodal and element techniques and interface elements". In: *International Journal of Fracture* 161 (2010), pp. 97–119.

[129] M. Ortiz. "A constitutive theory for the inelastic behavior of concrete". In: *Mechanics of Materials* 4.1 (1985), pp. 67–93.

[130] X. P. Xu and A. Needleman. "Numerical simulations of fast crack growth in brittle solids". In: *Journal of the Mechanics and Physics of Solids* 42.9 (1994), pp. 1397–1434.

[131] E. N. Dvorkin, A. M. Cuitiño, and G. Gioia. “Finite elements with displacement-interpolated embedded localization lines insensitive to mesh size and distortions”. In: *International Journal for Numerical Methods in Engineering* 30.3 (1990), pp. 541–564.

[132] J. C. Simo, J. Oliver, and F. Armero. “An analysis of strong discontinuities induced by strain-softening in rate-independent inelastic solids”. In: *Computational Mechanics* 12.5 (1993), pp. 277–296.

[133] A. E. Huespe et al. “Strong discontinuity approach in dynamic fracture simulations”. In: *Mecánica Computacional*. Vol. 25. AMCA (Asociación Argentina de Mecánica Computacional). 2006, pp. 1997–2018.

[134] F. Armero and C. Linder. “Numerical simulation of dynamic fracture using finite elements with embedded discontinuities”. In: *International Journal of Fracture* 160 (2009), pp. 119–141.

[135] J. Y. Wu, F. B. Li, and S. L. Xu. “Extended embedded finite elements with continuous displacement jumps for the modeling of localized failure in solids”. In: *Computer Methods in Applied Mechanics and Engineering* 285 (2015), pp. 346–378.

[136] K. Pham and J.-J. Marigo. “Approche variationnelle de l’endommagement: I. les concepts fondamentaux”. In: *Comptes Rendus Mécanique* 338.4 (2010), pp. 191–198.

[137] R.H.J. Peerlings et al. “Gradient-enhanced damage modelling of concrete fracture”. In: *Mechanics of Cohesive-frictional Materials* 3.4 (1998), pp. 323–342.

[138] Z.P. Bažant and T. Belytschko. “Wave propagation in a strain-softening bar: exact solution”. In: *Journal of Engineering Mechanics* 111.3 (1985), pp. 381–389.

[139] Zdeněk P Bažant and Gilles Pijaudier-Cabot. “Nonlocal continuum damage, localization instability and convergence”. In: *Journal of Applied Mechanics* 55.2 (1988), pp. 287–293.

[140] C. Giry, F. Dufour, and J. Mazars. “Stress-based nonlocal damage model”. In: *International Journal of Solids and Structures* 48.25 (2011), pp. 3431–3443.

[141] Gilles Pijaudier-Cabot and Zdeněk P Bažant. “Nonlocal damage theory”. In: *Journal of Engineering Mechanics* 113.10 (1987), pp. 1512–1533.

[142] Timon Rabczuk. “Computational methods for fracture in brittle and quasi-brittle solids: State-of-the-art review and future perspectives”. In: *International Scholarly Research Notices* 2013.1 (2013), p. 849231.

[143] M. Matallah, C. Laborderie, and O. Maurel. "A practical method to estimate crack openings in concrete structures". In: *International Journal for Numerical and Analytical Methods in Geomechanics* 34 (2010), pp. 1615–1633.

[144] R.H.J. Peerlings et al. "Gradient enhanced damage for quasi-brittle materials". In: *International Journal for Numerical Methods in Engineering* 39.19 (1996), pp. 3391–3403.

[145] Hanen Amor, Jean-Jacques Marigo, and Corrado Maurini. "Regularized formulation of the variational brittle fracture with unilateral contact: Numerical experiments". In: *Journal of the Mechanics and Physics of Solids* 57.8 (2009), pp. 1209–1229.

[146] C. Miehe, M. Hofacker, and F. Welschinger. "A phase field model for rate-independent crack propagation: Robust algorithmic implementation based on operator splits". In: *Computer Methods in Applied Mechanics and Engineering* 199 (2010), pp. 2765–2778.

[147] Luigi Ambrosio and Vincenzo M. Tortorelli. "Approximation of functionals depending on jumps by elliptic functionals via Γ-convergence". In: *Communications on Pure and Applied Mathematics* 43.8 (1990), pp. 999–1036.

[148] Blaise Bourdin, Gilles A Francfort, and Jean-Jacques Marigo. "The Variational Approach to Fracture". In: *Journal of Elasticity* 91.1 (2008), pp. 5–148.

[149] Marreddy Ambati, Tymofiy Gerasimov, and Laura De Lorenzis. "A review on phase-field models of brittle fracture and a new fast hybrid formulation". In: *Computational Mechanics* 55.2 (2015), pp. 383–405.

[150] T.T. Nguyen et al. "A phase field method to simulate crack nucleation and propagation in strongly heterogeneous materials from direct imaging of their microstructure". In: *Engineering Fracture Mechanics* 139 (2015), pp. 18–39.

[151] Gilles A Francfort and Jean-Jacques Marigo. "Revisiting brittle fracture as an energy minimization problem". In: *Journal of the Mechanics and Physics of Solids* 46.8 (1998), pp. 1319–1342.

[152] Christian Miehe and Marcus Lambrecht. "Algorithms for computation of stresses and elasticity moduli in terms of Seth–Hill's family of generalized strain tensors". In: *Communications in Numerical Methods in Engineering* 17.5 (2001), pp. 337–353.

[153] Zakaria Chafia et al. “Massively parallel phase field fracture simulations on supercomputers: towards multi-billion degree-of-freedom computations”. In: *Advanced Modeling and Simulation in Engineering Sciences* 11.1 (2024), p. 25. DOI: 10.1186/s40323-024-00280-4.

[154] Jian-Ying Wu et al. “Phase-field modelling of fracture”. In: *International Journal of Fracture* 242.2 (2023), pp. 157–187.

[155] Jonas Rudshaug, Tore Børvik, and Odd Sture Hopperstad. “Modeling brittle crack propagation for varying critical load levels: a dynamic phase-field approach”. In: *Computational Mechanics* 64.2 (2019), pp. 331–356.

[156] X. Lu et al. “Crack propagation simulation in brittle elastic materials by a phase field method”. In: *Theoretical and Applied Mechanics Letters* 9 (2019), pp. 339–352.

[157] F. Vicentini et al. “On the energy decomposition in variational phase-field models for brittle fracture under multi-axial stress states”. In: *International Journal of Fracture* 247 (2024), pp. 291–317.

[158] F.J. Molina, C. Alonso, and C. Andrade. “Cover cracking as a function of rebar corrosion: Part 2 Numerical model”. In: *Materials and Structures* 26.9 (1993), pp. 532–548.

[159] M. Dekoster. “Etude du comportement mécanique des structures en béton armé dégradé par la corrosion”. PhD thesis. Université de Lille 1, 2003.

[160] X. Du, L. Jin, and R. Zhang. “Modeling the cracking of cover concrete due to non-uniform corrosion of reinforcement”. In: *Corrosion Science* 89 (2014), pp. 189–202.

[161] B.S. Jang and B.H. Oh. “Effects of non-uniform corrosion on the cracking and service life of reinforced concrete structures”. In: *Cement and Concrete Research* 40 (2010), pp. 1441–1450.

[162] B. Šavija et al. “Cracking of the concrete cover due to reinforcement corrosion: a two-dimensional lattice model study”. In: *Construction and Building Materials* 44 (2013), pp. 626–638.

[163] C. Cao and M. Cheung. “Non-uniform rust expansion for chloride-induced pitting corrosion in RC structures”. In: *Construction and Building Materials* 51 (2014), pp. 75–81.

[164] Y. Yuan and Y. Ji. “Modeling corroded section configuration of steel bar in concrete structure”. In: *Construction and Building Materials* 23.6 (2009), pp. 2461–2466.

[165] Zdeněk P. Bažant and Emilie Becq-Giraudon. “Statistical prediction of fracture parameters of concrete and implications for choice of testing standard”. In: *Cement and Concrete Research* 32.4 (2002), pp. 529–556.

[166] Evžen Korec et al. “A phase-field chemo-mechanical model for corrosion-induced cracking in reinforced concrete”. In: *Cement and Concrete Research* 169 (2023), p. 107393.

[167] Evžen Korec et al. “Phase-field chemo-mechanical modelling of corrosion-induced cracking in reinforced concrete subjected to non-uniform chloride-induced corrosion”. In: *Computer Methods in Applied Mechanics and Engineering* 419 (2024), p. 116343.

[168] Sabine Caré and André Raharinaivo. “Influence of impressed current on the initiation of damage in reinforced mortar due to corrosion of embedded steel”. In: *Cement and Concrete Research* 37.12 (2007), pp. 1598–1612.

[169] T.T. Nguyen et al. “On the choice of parameters in the phase field method for simulating crack initiation with experimental validation”. In: *International Journal of Fracture* 197.2 (2016), pp. 213–226.